

---

# Microstructure and grain boundary evolution in titanium thin films

---

Dissertation

zur

Erlangung des Grades Doktor-Ingenieur

der

Fakultät für Maschinenbau

der Ruhr-Universität Bochum

von

**Vivek Devulapalli**

aus

Bhilai, Indien

Bochum 2022

Dissertation eingereicht am:	29.08.2022
Tag der mündlichen prüfung:	04.11.2022
Vorsitz:	Prof. Dr.-Ing. Jan T. Sehart
Erstgutachter:	Prof. Dr. Gerhard Dehm
Zweitgutachter:	Prof. Dr. Jochen M Schneider

# Declaration of Authorship

I, Vivek Devulapalli, declare that this thesis titled, “Microstructure and grain boundary evolution in titanium thin films” and the work presented in it are my own. I confirm that:

- This work was done wholly while in candidature for a research degree at this University.
- Where I have consulted the published work of others, this is always clearly attributed.
- Where I have quoted from the work of others, the source is always given. With the exception of such quotations, this thesis is entirely my own work.
- I have acknowledged all main sources of help.
- Where the thesis is based on work done by myself jointly with others, I have made clear exactly what was done by others and what I have contributed myself.

Signed:

---

Date:

---



To the two authors who have shaped the thinking of millions.

*“Questions you cannot answer are usually far better for you than answers you cannot question.”*

– Yuval Noah Harari, *Sapiens*

*“The nitrogen in our DNA, the calcium in our teeth, the iron in our blood, the carbon in our apple pies were made in the interiors of collapsing stars. We are made of starstuff.”*

– Carl Sagan, *Cosmos*



# *Abstract*

## **Microstructure and grain boundary evolution in titanium thin films**

Vivek Devulapalli

Titanium (Ti) is the fourth most abundant metal that is commercially used mainly for its high specific strength and corrosion resistance. Similar to iron, the allotropic transition in Ti is responsible for a wide variety of alloys that can be synthesized. Different heat treatments and alloying elements can vary the hexagonal close packed (hcp) and body centered cubic (bcc) phase fractions along with the microstructure, which can have dramatic influence on its properties. Similar to bulk phases, grain boundaries (GBs) have been demonstrated in both metals and ceramics to constitute a 'phase' whose existence is confined by the abutting grains. GB phases, sometimes termed as 'complexions,' are poorly understood, especially in hcp materials. Much work has been done in recent years to increase our understanding of GBs and interfaces. It is well understood that all material properties depend not only on the bulk of the material but also, and perhaps more importantly, on the interfaces. While the presence of GBs can have an adverse effect on the corrosion properties or strength of the material, it has been demonstrated that suitable alloying additions can mitigate the harm. To engineer materials such that they contain only the innocuous GBs requires their complete understanding. This involves our ability to investigate their atomic structure and the role of chemistry in it. This thesis attempts to investigate the titanium GBs in depth, taking into account the importance of both titanium and GBs. To achieve this, first the thin film deposition techniques are established to obtain poly/-nanocrystalline, bicrystalline and single crystalline films. Next, the GBs in the thin films are characterized at a macroscale. Lastly, the GBs of interest are investigated at atomic scale.

Firstly, we discuss the thin films of Ti that were deposited using e-beam evaporation on multiple single crystalline substrates like NaCl, silicon and sapphire. It was observed that Ti grew as nanocrystalline films on Si and NaCl while epitaxial single crystalline films were obtained on three differently orientated sapphire substrates. A single crystalline Ti film on r-plane sapphire is reported for the first time. HRTEM imaging was used to determine the orientation relationship (OR) between the film and the substrate. Overall, the influence of changing deposition parameters on the microstructure and texture of the films is established. The role of GBs in increased

resistivity of the films is also shown by comparing the resistivity of a single crystalline film to that of a nanocrystalline film.

Next, we discuss additional Ti thin films that were deposited on SrTiO<sub>3</sub> substrate using pulsed magnetron sputtering. Again, the role of deposition parameters like the pulse duration and post-annealing duration on the film microstructure is explored. Electron backscatter diffraction is used to analyse the film texture and microstructure which revealed a large population of coincident site lattice (CSL) GBs. Increasing the annealing time increased the  $\Sigma 13$  [0001] GB population. All of the observed GBs in the 8 h annealed film are identified as  $\Sigma 13$  with [0001] tilt axis. The film forms a meandering microstructure with a strong (0001) texture and only two in-plane rotations. The two orientation relationships are identified by examining the film cross-section in TEM. The prime goal of depositing these films was to devise thin films with GBs that grew perpendicular to the surface of the substrate. This is due to the limitations on the types of GBs that are appropriate for atomic resolution investigation. The cross-section analysis verified the presence of such GBs. In the TEM, the macroscopically curved GBs are observed to be faceted into symmetric GB segments. Iron, which is a common impurity element in Ti is seen to be segregated to every alternate GB facet. Although it is observed that the density of CSL sites is lower on the GBs that have Fe-segregation, we conclude that there isn't sufficient evidence to reason the influence of planar CSL density on Fe-segregation. This necessitates additional investigation at higher spatial resolution. Finally, using atom probe tomography, the GB solute excess is quantified.

To understand the anomalous Fe-segregation to  $\Sigma 13$  [0001] GBs, in the next chapter, the GBs are investigated at the atomic scale. First, the 'clean' symmetric  $\bar{7}520$  GB is observed to be composed of several repeating structural units (SUs). A 2.8° deviation from the exact CSL results in some defects in the periodicity. Topological characterisation of the GBs is carried out by constructing a circuit around the SUs and mapping the burger circuit to a dichromatic pattern. This reveals the GB-SUs to have a pure edge dislocation-like character. Next, Fe segregation to the same symmetric GBs is seen to result in a complete rearrangement of atomic columns to form new cage-like SUs that are periodically arranged in a zig-zag manner with a uniform spacing of 0.9 nm in the GB plane. The new SU is also observed to also have an edge-dislocation-like defect character. Next, the asymmetric GBs are observed to be faceted on a nano-scale into the two symmetric variants. Also in the nano-scale, every alternate segment is observed to constitute the SUs with and without Fe. In another instance, the asymmetric GB with Fe-segregation is observed to have a larger spacing between the Fe-columns than the symmetric GB with Fe-segregation. Energy dispersive X-ray



spectroscopy (EDS) is performed at 120 kV to obtain a near-atomically resolved EDS map that confirms the presence of Fe in the column trapped inside of the Ti-cage.

Overall, this thesis discusses in detail the influence of various thin film deposition parameters and substrates on the film microstructure. The GBs in the thin films are characterized on the atomic-scale and the structural unit model is shown to be applicable in an hcp metallic GBs for the first time. Beyond finding novel SUs, this thesis reports the first observation of a segregation-induced GB phase transition.



# *Publications*

The main results and discussion contained within this thesis are based on the following publications/manuscripts:

## Publication 1

**Influence of substrates and e-beam evaporation parameters on the microstructure of nanocrystalline and epitaxially grown Ti thin films**

Vivek Devulapalli, Hanna Bishara, Matteo Ghidelli, Gerhard Dehm, Christian H. Liebscher

*Applied Surface Science* 562 (2021), 150194

Contribution: Thin-film depositions, sample preparation, experiments, data analysis and writing.

## Publication 2

**Microstructure, grain boundary evolution and anisotropic Fe segregation in (0001) textured Ti thin films**

Vivek Devulapalli, Marcus Hans, Prithiv T Sukumar, Jochen M Schneider, Gerhard Dehm, Christian H. Liebscher

*Acta Materialia* 238 (2022), 118180

Contribution: Designing and planning, sample preparation, characterization, data analysis and writing.

## Publication 3

**Segregation induced grain boundary phase transition in titanium**

Vivek Devulapalli, Marcus Hans, Jochen M Schneider, Gerhard Dehm, Christian Liebscher

*Manuscript to be submitted*

Contribution: Conceptualization, methodology, sample preparation, characterization, data analysis, visualization and writing.



## *Acknowledgements*

It is impossible to write an exhaustive list of beings that I would wish to acknowledge. In theory, the position and momentum of every single atom in the universe put together can be held responsible for all our thoughts and actions. I wonder if I could acknowledge them all. However, we have built a system to give names to certain blobs of atoms that we tend to call as friends and family. Some of them deserve a special mention here.

I would firstly like to acknowledge Prof. B S Murty, my master thesis supervisor, who was the first person to have introduced me to the field of research. Hailing from a university nowhere nearly equipped with the state-of-the-art machinery, I had no exposure whatsoever to the world of material science. His freely available online lectures have not just inspired me but an entire generation of material scientists in India. Without a doubt, his fascinating way of lecturing makes one want to binge-watch them like a Netflix series. But beyond a great teacher, he is an amazing human being and I stay indebted to him for shaping my academic career.

Being a small town boy who never crossed his national borders until four years ago, the international atmosphere of MPIE was a massive learning experience for me. After I started my PhD, I heard a lot of horror stories from other graduate students about how difficult life can be if you can't get along with your adviser. I couldn't have been more fortunate in this regard. In Dr. Christian Liebscher, I had the best of the supervisors. He has the skill to have the perfect balance of guidance and freedom that a PhD student would desire. My skill set was relatively restricted when I started my PhD studies. But he never showed signs of displeasure, and even when I failed to complete simple tasks, he remained upbeat. His microscopy expertise is incredible, but what's even more impressive is his humility in the face of it. I've taken numerous mental notes on how to approach a variety of problems in the professional manner that he does. I can only hope that when the time comes, I will be able to emulate some aspect of him.

Prof. Gerhard Dehm is one of the most modest and competent supervisors I could have anticipated. His ever smiling face and the warmth that he shares with his students is remarkable. I am especially grateful to him for his prompt and effective supervision, which included not only the correction of thesis and paper manuscripts but also his critical advice on our research ideas. For a person as busy as him, it is amazing how quickly he managed to respond to every request for a discussion/ meeting I had. Undoubtedly, I find myself highly fortunate to have his supervision for accomplishing this thesis.

I would like to thank Prof. Jochen M Schneider and Dr. Marcus Hans for their support in the thin film depositions without which this work would not have been possible. For their unwavering support from the beginning of my master's degree to the conclusion of my PhD, they and all the kind colleagues at MCh, Aachen have my sincere gratitude.

My friends, Lena and Saba, certainly deserve a special mention. Always available for the good and bad times, there is a lot that I learnt from them. I would take this opportunity to also thank my good friend Niels for pushing the entire group towards the ideals of open-access and introducing me to the world of Python. My office colleagues, Chunhua, Reza, Nico and more recently Nina were some of the nicest colleagues I have had the fortune to work with. Even in the middle of pandemic, I was always given the opportunity to have the comfort of working at office for which I am thankful to them. They always maintained a cheerful and yet calming office atmosphere. Also, I would like to thank Prithiv, with whom I believe I spent the majority of my PhD time with.

I thank all the people who have provided their selfless contribution to build the open-access resources that are the backbone of making science diverse and inclusive.

My appreciation for the scholarly works of Dr. APJ Abdul Kalam, Yuval Noah Harari, Carl Sagan, and Stephen Hawking for authoring some wonderful books that have shaped the thoughts of millions. In addition, I owe a debt of gratitude to Eden Hazard, N'Golo Kante, and Chelsea FC for the exquisite football that energised my evenings and helped me preserve sanity during lonely times.

Lastly, I would like to acknowledge my parents, my sister and my wife who are my horcrux. I owe them my life for their endless love and trust. I would never be where I am not without their support and there is nothing that I could write to thank them enough.

# Contents

<b>Declaration of Authorship</b>	<b>iii</b>
<b>Abstract</b>	<b>vii</b>
<b>Acknowledgements</b>	<b>xiii</b>
<b>1 Introduction</b>	<b>1</b>
1.1 Introduction . . . . .	1
1.2 Aim and outline of the thesis . . . . .	2
<b>2 Background</b>	<b>5</b>
2.1 Thin film deposition . . . . .	5
2.1.1 e-beam evaporation . . . . .	6
2.1.2 Direct current magnetron sputtering . . . . .	7
2.1.3 Pulsed magnetron sputtering . . . . .	9
2.2 Titanium and its alloys . . . . .	11
2.2.1 Introduction and phase transitions . . . . .	11
2.2.2 Alloying and segregation behaviour in titanium . . . . .	13
Iron in Ti . . . . .	14
Oxygen in Ti . . . . .	16
2.3 Titanium thin films . . . . .	18
2.3.1 Nano-/ polycrystalline films . . . . .	19
2.3.2 Epitaxial and single crystalline films . . . . .	22
2.4 Grain boundaries . . . . .	24
2.4.1 Description and role of grain boundaries in materials . . . . .	24
2.4.2 Coincident site lattice theory . . . . .	26
Dichromatic pattern and the topological theory . . . . .	28
2.4.3 Grain boundary atomic structure . . . . .	30
Experimental observation of grain boundary structures . . . . .	32
Grain boundaries in hcp materials . . . . .	35
2.5 Characterization . . . . .	45

2.5.1	X-Ray diffraction . . . . .	46
2.5.2	Thin film resistivity measurement . . . . .	46
2.5.3	Scanning electron microscopy . . . . .	46
	Electron backscatter diffraction . . . . .	48
2.5.4	Focused ion beam . . . . .	49
2.5.5	Transmission electron microscopy . . . . .	50
	High-resolution transmission electron microscopy . . . . .	51
2.5.6	Scanning transmission electron microscopy . . . . .	52
	Coherent and incoherent imaging . . . . .	54
	Aberration correction . . . . .	57
	Energy dispersive X-ray spectroscopy . . . . .	58
<b>3</b>	<b>Experimental Details</b>	<b>61</b>
3.1	Thin film depositions . . . . .	61
3.2	Material characterization . . . . .	63
3.3	Software . . . . .	68
<b>4</b>	<b>Results</b>	<b>69</b>
4.1	Ti thin film deposition using e-beam evaporation . . . . .	69
4.1.1	e-beam deposition parameters . . . . .	69
4.1.2	Deposition on $\text{SiN}_x$ and NaCl . . . . .	70
4.1.3	Deposition on sapphire substrate . . . . .	76
4.1.4	Resistivity measurements . . . . .	80
4.2	Microstructure, grain boundary faceting and anisotropic Fe-segregation	82
4.2.1	Evolution of thin film microstructure and grain boundaries . . .	83
4.2.2	Grain size and grain growth measurement . . . . .	91
4.2.3	Coincident site lattice and GB planes . . . . .	95
4.2.4	Grain boundary faceting . . . . .	99
4.2.5	Anisotropic Fe segregation in symmetric GB facets . . . . .	102
4.2.6	Discussion . . . . .	105
	Thin film deposition and texture evolution . . . . .	105
	Grain boundary faceting . . . . .	107
	Grain boundary segregation . . . . .	110
4.3	STEM investigation of atomic-scale structural transitions in Ti grain boundaries . . . . .	114
4.3.1	Thin film characterization . . . . .	114
4.3.2	Structural unit model for 'clean', symmetric $\Sigma 13$ GB . . . . .	115
	Defect content of the experimentally observed structural units .	116



4.3.3	GB structural transition due to segregation . . . . .	119
	Change of GB Fe concentration . . . . .	121
4.3.4	Atomic structure of Fe-segregated asymmetric GBs . . . . .	123
4.3.5	Dislocation on hcp basal plane . . . . .	126
4.3.6	Near-atomically resolved energy dispersive spectrometry . . . . .	126
4.3.7	Discussion . . . . .	126
	Structural units and their defect content . . . . .	126
	Grain boundary phase transitions due to segregation . . . . .	129
<b>5</b>	<b>Summary and conclusions</b>	<b>133</b>
5.1	Ti thin film deposition using e-beam evaporation . . . . .	133
5.2	Grain boundary evolution and anisotropic Fe segregation in (0001) textured Ti thin films . . . . .	134
5.3	(S)TEM investigation of $\Sigma$ 13 grain boundaries in Ti . . . . .	135
<b>6</b>	<b>Conclusions and outlook</b>	<b>137</b>
	<b>Bibliography</b>	<b>139</b>
	<b>Curriculum Vitae</b>	<b>171</b>



# List of Figures

2.1	Schematic of an e-beam evaporation setup used to deposit thin films. Redrawn in modified form from [18]. . . . .	6
2.2	Schematic of a direct current sputtering setup used to deposit thin films. The plasma of $\text{Ar}^+$ ions and $e^-$ is confined in front of the target due to the magnetic field around the cathode. Redrawn from [25]. . . . .	8
2.3	Overview of the classification of dcMS and pulsed magnetron sputtering based on the duty cycle and the peak power density. Adapted from [30].	11
2.4	Ball and stick models of hcp and bcc Ti unit cells with highlighted basal plane and the lattice parameters. . . . .	12
2.5	Phase diagram of Ti-Fe system showing all the possible intermetallics, their composition range and phase transitions at various temperatures [72]. . . . .	16
2.6	Ti-O phase diagram showing wide solubility range of O in $\alpha$ Ti [86]. . .	17
2.7	Crystal structure of sapphire a) and expanded 2D arrangement of $\text{Al}^{3+}$ and $\text{O}^{2-}$ ions on the surface of b) $(11\bar{2}0)$ A-plane, c) $(0001)$ C-plane, and d) $(10\bar{1}0)$ M-plane sapphires. Adapted from [112] . . . . .	21
2.8	The five macroscopic degrees of freedom that stem from the misorientation between the grains (the angle and axis of rotation) and the GB plane. Taken from [4] . . . . .	24
2.9	Tilt and twist GB are defined by the rotation axis being perpendicular and parallel to the GB plane normal, respectively. . . . .	25
2.10	The first report on the dependence of grain boundary energy on the misorientation angle for any cubic lattice with arbitrary lattice parameters. Taken from [160]. . . . .	30
2.11	a) b) The structure of a $\Sigma 19[110]$ $(311)$ gold GBs that shows repeating periodic units that match with the structure predicted using EAM potential [172]. c) Tilt GB in molybdenum that has a misorientation of $\sim 13^\circ$ . As expected from the SUM, the GB appears to be a mixture of $\Sigma 25$ and $\Sigma 41$ that are the two favoured GBs that it is bounded by [175].	33

2.12	A plot of the change in GB energy calculated using MD for changing tilt angles in Ti, Mg and Zr. Taken from [207]. . . . .	36
2.13	Atomic configuration of $\Sigma 13$ symmetric tilt GB in ZnO. a) HAADF-STEM image, b) stable structure from first-principles. Taken from [231].	44
2.14	The structural units made of 5,7- atom rings that make the [0001] wurtzite tilt GBs exhibit two pronounced minima at rotation angles corresponding to $\Sigma 7$ and 13. Taken from [234]. . . . .	44
2.15	The structural units made of 5,7- atom rings that make the [0001] wurtzite tilt GBs exhibit two pronounced minima at rotation angles corresponding to $\Sigma 7$ and 13. Taken from [234]. . . . .	45
2.16	Overview of the interaction volume of the incident electron beam with a crystalline sample in an SEM. Adapted from [242]. . . . .	47
2.17	A schematic ray diagram showing the equivalence between STEM and TEM according to the principle of reciprocity. Redrawn from [255]. . .	52
2.18	An overview showing the relative position of high-angle annular dark field (HAADF), annular dark field (ADF), annular bright field (ABF) and bright field (BF) detectors in a STEM. . . . .	54
3.1	Evolution of the target voltage and current during a single cycle of pulsed magnetron sputtering. A strong voltage overshoot is observed during ignition followed by a steady state of voltage for 200 $\mu s$ resulting in a peak target power of 20 kW and peak target power density of 46 W $cm^{-2}$ . The pulse period was 2 ms. . . . .	63
3.2	The stages for preparing a plane-view sample using FIB are presented in chronological sequence. . . . .	66
4.1	Light optical microscope image of Ti film deposited on $SiN_x$ substrate at 200°C at a deposition rate of 2.5 Å/s (sample #Si1) exhibiting crack and porosity free surface . . . . .	70
4.2	Grazing-Incidence XRD (Cu-K $\alpha$ source) of a 75 nm thick Ti thin film deposited at 200°C on $SiN_x$ (100) (sample #Si1) and NaCl (100) (sample #N3). Both films exhibit a polycrystalline microstructure. The film deposited on $SiN_x$ shows a strong (10 $\bar{1}$ 0) texture; the film grown on NaCl a (10 $\bar{1}$ 1) texture. . . . .	72

4.3	TEM bright field image showing the microstructure of the Ti thin film deposited a) at 200° C on SiN <sub>x</sub> substrate (cross section, sample #Si1) and c) at RT on NaCl (100) substrate (plane view, sample #N1), with respective selected area diffraction patterns in b) and d) verifying the nanocrystalline hcp α-Ti structure. . . . .	74
4.4	Plane view TEM bright field image of a Ti thin film deposited at a) 0.8 Å/s at RT (#N2) and b) 2.5 Å/s at 200°C on NaCl(100) (#N3). The corresponding selected area diffraction patterns are shown in c) and d), respectively, both exhibiting a strong (10 $\bar{1}$ 1) texture. . . . .	77
4.5	Grazing-Incidence XRD of 90 nm thick Ti thin films deposited at RT on a) C-plane sapphire with only the (0002) peak present (Co-Kα source), b) C-plane with a 2° miscut(C <sub>2mis</sub> ), A-plane and R-plane sapphire displaying multiple diffraction peaks (Cu-Kα source . . . . .	77
4.6	Inverse pole figure (IPF) obtained from EBSD of Ti thin films deposited at 400°C on (a) C <sub>2mis</sub> -plane (b) A-plane and (c) R-plane sapphire at low magnification to display uniform orientation over the entire wafer. . . . .	79
4.7	HRTEM image of cross-section of Ti thin film deposited on C-plane sapphire shows a 90 nm thick Ti film deposited using e-beam evaporation at RT (sample #S3) observed in [11 $\bar{2}$ 0] zone axis orientation of the sapphire substrate. The insets show fast Fourier transforms (FFTs) of the film and substrate, respectively, which are used to determine the ORs	80
4.8	Resistivity values of films grown on C-plane sapphire and A-plane at varying T <sub>dep</sub> . The nanocrystalline film shows higher resistivity of ~ 95 μ Ω cm while all SC films show resistivity of ~ 60 μ Ω cm . . . . .	81
4.9	Ti film deposited using DC Sputtering at 600°C and post annealed at 600°C for 2 h. . . . .	84
4.10	Ti film deposited using DC Sputtering at 600°C and post annealed at 600°C for 4 h. . . . .	85
4.11	Orientation map and the point-to-origin misorientation plot of the film deposited at 600° and annealed at 600° for 8 h. . . . .	86
4.12	Ti film deposited using DC Sputtering at 600°C and post annealed at 600°C for 8 h. . . . .	87

4.13	a), b) and c) Bright field TEM micrographs acquired at low magnification from three different lamellae lifted out from the Ti thin film deposited on SrTiO <sub>3</sub> at 600°C and annealed at 600°C for 8h. The selected area apertures used to capture the SADPs are marked in yellow circles. d), e) and f) The corresponding [0001] zone axis SADPs confirm the 30° [0001] misorientation. . . . .	89
4.14	Bright and dark field micrographs of cross-section of the film with their corresponding diffraction patterns. . . . .	90
4.15	STEM-EDS of the film-substrate interface. . . . .	92
4.16	EBSD images showing the increasing area fraction of OR I with increasing annealing duration. . . . .	94
4.17	A Σ13 dichromatic pattern is constructed using two grains, μ (cyan) and λ (red). The CSL unit cell (PQRS) is marked. The shorter and longer diagonals are the GB planes {75̄20} and {43̄10}, respectively. The circuit used to index the GB planes is marked in white. . . . .	96
4.18	A Σ13 dichromatic pattern is constructed by rotating the two basal planes by 32.2° instead of 28.8° as observed in the previous case. The CSL unit cell (PQRS) is marked. The shorter and longer diagonals are the GB planes {75̄20} and {43̄10}, respectively. . . . .	98
4.19	a) HAADF-STEM image of Σ13 [0001] Ti GB in the pulse magnetron sputtered film deposited at 600°C and post-annealed at 600°C for 8 h showing a faceted GB with symmetric GB facets. Each GB plane is represented by a different colour. b) Fast Fourier transform (FFT) of the HAADF-STEM image in a). c) HAADF-STEM image of from a different region showing asymmetric GB facets. d) FFT from the HAADF-STEM image shown in c). The dashed brown line is a symmetric facet present between the two asymmetric facets. . . . .	100
4.20	High angle annular dark field (HAADF), low angle annular dark field (LAADF), annular bright field (ABF) and bright field (BF) images of the Σ13 GB captured simultaneously showing the variation in GB contrast with the change of collection angle. . . . .	101
4.21	a) STEM annular-BF image showing GB facets with symmetric {75̄20} GB planes. EDS reveals segregation of b) Fe in alternate GB facet, c) depletion of Ti in the Fe rich region. The Fe rich GBs are found to be planes with lower CSL density. d), e) Net-intensity line profile across the two symmetric facets revealing a strong segregation of Fe in only the (2̄570) facet. . . . .	102

4.22	APT demonstrating Fe segregation to one of the GB facet, while the neighbouring facet is depleted of Fe. A ladder diagram is drawn to calculate the Gibbsian GB excess. . . . .	104
4.23	Schematic of $\Sigma 13$ GB with planes a) $\{\bar{7}520\}$ and $\{\bar{5}7\bar{2}0\}$ consisting of highest and second highest planar coincident site density (PCSD), respectively leading to reduction of GB energy. b) $\{2\bar{1}\bar{1}0\}$ and $\{10\bar{1}0\}$ have a lower PCSD but higher effective d-spacing ( $d_{eff}$ ) leading to the second most frequently observed GB facet plane. . . . .	108
4.24	Overview of characterization performed using SEM for the film annealed for 8 h at $600^{\circ}\text{C}$ . . . . .	115
4.25	Symmetric $\Sigma 13$ $[0001]$ $\{\bar{7}5\bar{2}0\}$ GB in Ti imaged using HAADF-STEM demonstrates periodic arrangement of structural units ('ABC'). The FFT in the inset shows the $30^{\circ}$ misorientation that is $2.2^{\circ}$ away from the exact $\Sigma 13$ misorientation. . . . .	117
4.26	a) Symmetric $\Sigma 13$ $[0001]$ $\{\bar{7}5\bar{2}0\}$ GB in Ti imaged using HAADF-STEM demonstrates periodic arrangement of structural units ('ABC'). The Burgers circuit is drawn connecting the two periodic atomic positions. b) The same circuit is retraced on a dichromatic pattern. . . . .	119
4.27	The dichromatic pattern seen in Fig. 4.26 (b) is used to draw the vectors that represent the equivalents of mapped GB circuits to subsequently calculate the projected primary and secondary defect content of the $\Sigma 13$ $[0001]$ GB SUs. . . . .	120
4.28	a) Symmetric $\Sigma 13$ $[0001]$ $\{\bar{7}520\}$ GB in Ti imaged using HAADF-STEM demonstrates periodic Fe segregation that are uniformly spaced apart. b), c) The structural rearrangement caused by Fe segregation is observed to follow the SUM, with repeating 'PQ' units. The atomic column rich in Fe is highlighted in yellow. . . . .	122
4.29	Symmetric $\Sigma 13$ $[0001]$ $\{\bar{7}520\}$ GB with greater Fe-rich columns per unit GB length than Fig. 4.28 demonstrates periodicity in clustering of the 'PR' units to form '4P-2R' units. . . . .	123
4.30	Asymmetric $\Sigma 13$ $[0001]$ $\{10\bar{1}0\}$ GB in Ti imaged using HAADF-STEM demonstrates GB faceting at atomic scale into the two symmetric variants, $\{\bar{5}7\bar{2}0\}$ and $\{\bar{4}310\}$ . . . . .	124
4.31	Asymmetric $\Sigma 13$ $[0001]$ $\{10\bar{1}0\}$ GB in Ti imaged using HAADF-STEM shows Fe-rich columns spaced farther apart than in symmetric GB. 'ABC' units also present periodically at the GB were seen to have an additional bright Fe-rich column within the 'C' unit. . . . .	125

- 4.32 Two edge dislocations with Burgers vector,  $b = 1/3 [11\bar{2}0]$  are observed to have bright contrast indicating Fe segregation. The dislocation core appears to have a 'cage-like' structure with Fe trapped in the core. . . . 127
- 4.33 a) HAADF-STEM signal acquired during the EDS scan at 120 kV for a symmetric  $\Sigma 13 [0001] \{\bar{7}520\}$  GB in Ti. b) The bright atomic columns in HAADF are verified to be Fe using STEM-EDS. The line-integral along the GB length depicts the Fe-K counts obtained from the EDS spectrum. 128
- 4.34 The 'ABC' structure of the solute-free  $\Sigma 13 [0001] \{\bar{7}520\}$  is magnified to label the 11 atoms that form the 'B' and the 'C' units. The addition of Fe transforms the GB unit 'P' and 'R' units where Fe-rich column is highlighted in yellow. . . . . 131



# List of Tables

2.1	Sputtering yield of Ti, Cu and Au for ions having 500 eV. [23] . . . . .	7
2.2	Studies on hcp grain boundary atomic structure grouped by the material and the chronological order. . . . .	38
2.3	CSL misorientations with $\Sigma < 50$ for grain boundaries with a [0001] rotation axis in the hexagonal system . . . . .	43
3.1	FIB parameters used for STEM sample preparation to obtain samples of the thickness of $< 100$ nm. . . . .	67
4.1	List of deposited films using e-beam deposition with their deposition parameters. . . . .	71
4.2	Grain size distribution of Ti thin films deposited on NaCl (100) by varying substrate temperature and deposition rate . . . . .	75
4.3	Deposition conditions, OR I/ OR II grain size and $\Sigma 13$ GB length of the pulsed magnetron sputtered films. . . . .	93



# List of Abbreviations

<b>APT</b>	<b>A</b> tom <b>P</b> robe <b>T</b> omography
<b>bcc</b>	<b>b</b> ody- <b>c</b> entered <b>c</b> ubic
<b>BF</b>	<b>B</b> right <b>F</b> ield
<b>BSD</b>	<b>B</b> ack- <b>S</b> cattered <b>E</b> lectron <b>D</b> etector
<b>BSE</b>	<b>B</b> ack- <b>S</b> cattered <b>E</b> lectron
<b>CCD</b>	<b>C</b> harge- <b>C</b> oupled <b>D</b> evice
<b>dcMS</b>	<b>d</b> irect <b>c</b> urrent <b>M</b> agnetron <b>S</b> puttering
<b>CSL</b>	<b>C</b> oincident <b>S</b> ite <b>L</b> attice
<b>CCSL</b>	<b>C</b> onstricted <b>C</b> SL
<b>DCFI</b>	<b>D</b> rift <b>C</b> orrected <b>F</b> rame <b>I</b> ntegration
<b>DF</b>	<b>D</b> ark <b>F</b> ield
<b>DFT</b>	<b>D</b> ensity <b>F</b> unctinal <b>T</b> heory
<b>DME</b>	<b>D</b> omain <b>M</b> atching <b>E</b> pitaxy
<b>DP</b>	<b>D</b> iffraction <b>P</b> attern
<b>EAM</b>	<b>E</b> MBEDDED <b>A</b> tom <b>M</b> ethod
<b>EDS</b>	<b>E</b> nergy <b>D</b> ispersive <b>X</b> -ray <b>S</b> pectroscopy
<b>EELS</b>	<b>E</b> lectron <b>E</b> nergy <b>L</b> oss <b>S</b> pectroscopy
<b>fcc</b>	<b>f</b> ace- <b>c</b> entered <b>c</b> ubic
<b>FFT</b>	<b>F</b> ast <b>F</b> ourier <b>T</b> ransform
<b>FIB</b>	<b>F</b> ocused <b>I</b> on <b>B</b> eam
<b>FM</b>	<b>F</b> rank- <b>v</b> an der <b>M</b> erwe
<b>FWHM</b>	<b>F</b> ull <b>W</b> idth at <b>H</b> alf <b>M</b> aximum
<b>GB</b>	<b>G</b> rain <b>B</b> oundary
<b>HAADF</b>	<b>H</b> igh <b>A</b> n timer <b>A</b> nnular <b>D</b> ark <b>F</b> ield
<b>hcp</b>	<b>h</b> exagonal <b>c</b> lose <b>p</b> acked
<b>HPPMS</b>	<b>H</b> igh <b>P</b> ower <b>P</b> ulsed <b>M</b> agnetron <b>S</b> puttering
<b>HR</b>	<b>H</b> igh <b>R</b> esolution
<b>LAADF</b>	<b>L</b> ow <b>A</b> n timer <b>A</b> nnular <b>D</b> ark <b>F</b> ield
<b>LOM</b>	<b>L</b> ight <b>O</b> ptical <b>M</b> icroscope
<b>nc</b>	<b>N</b> ano- <b>c</b> rystalline
<b>OA</b>	<b>O</b> bjective <b>A</b> perture
<b>OIM</b>	<b>O</b> rientation <b>I</b> maging <b>M</b> icroscopy
<b>PCA</b>	<b>P</b> rincipal <b>C</b> omponent <b>A</b> n timer
<b>PF</b>	<b>P</b> ole <b>F</b> igure
<b>ROI</b>	<b>R</b> egion of <b>I</b> nterest
<b>RT</b>	<b>R</b> oom <b>T</b> emperature
<b>SAA</b>	<b>S</b> elect ed <b>A</b> rea <b>A</b> perture
<b>SADP</b>	<b>S</b> elect ed <b>A</b> rea <b>D</b> iffraction <b>P</b> attern

<b>SC</b>	<b>S</b> ingle <b>C</b> rystalline
<b>SDD</b>	<b>S</b> ilicon <b>D</b> rift <b>D</b> etector
<b>SE</b>	<b>S</b> econdary <b>E</b> lectron
<b>SEM</b>	<b>S</b> canning <b>E</b> lectron <b>M</b> icroscopy
<b>SK</b>	<b>S</b> transki- <b>K</b> rastanov
<b>STEM</b>	<b>S</b> canning <b>T</b> ransmission <b>E</b> lectron <b>M</b> icroscopy
<b>STGB</b>	<b>S</b> ymmetric <b>T</b> ilt <b>G</b> rain <b>B</b> oundary
<b>SU</b>	<b>S</b> tructural <b>U</b> nit
<b>SUM</b>	<b>S</b> tructural <b>U</b> nit <b>M</b> odel
<b>TEM</b>	<b>T</b> ransmission <b>E</b> lectron <b>M</b> icroscopy
<b>VM</b>	<b>V</b> olmer- <b>W</b> eber
<b>XRD</b>	<b>X</b> - <b>R</b> ay <b>D</b> iffraction

# List of Symbols

$\vec{b}$	Burger vector	
$C_{2mis}$	2° deviation (miscut) from C-plane	
$C_s$	Spherical aberration coefficient	nm
$d_{eff}$	Effective interplanar spacing	Å
$d_{Sch}$	Scherzer defocus	
V	Voltage	kV
I	Current	A
$I_{BF}$	Intensity of bright-field	
$I_{ion}$	Peak ion current	A
$P_{13}$	Transformation matrix to generate $\Sigma 13$ misorientation	
$t_{on(off)}$	On(off)-time	$\mu s$
$t(\mu)$	translation vector in $\mu$ -grain	
$T_{dep}$	Deposition temperature	°C
Z	Atomic number	
$\alpha$ -Ti	Hexagonal close packed-Ti	
$\beta$ -Ti	Body centered cubic-Ti	
$\delta$	Misfit	
$\delta\theta$	Deviation from desired misorientation	
$\Gamma$	Planar coincidence site density	
$\Gamma_{Fe}$	Interfacial excess of Fe (solute)	at/nm <sup>2</sup>
$\lambda$	Wavelength	
$\Omega$	Solid angle	
$\rho$	Sheet resistivity	
$\phi(R)$	Phase shift	
$\sigma$	Interaction constant	
$\Sigma$	Coincident site density	



*To all the countless species that have been lost to human  
greed . . .*





# Chapter 1

## Introduction

### 1.1 Introduction

Understanding the structure-property correlation is at the heart of material science. The essence of material engineering is the manipulation of the chemistry, structure, and spatial distribution of various microstructure components. Metals were paramount to the advancement of human civilisation and decisive in the industrial revolution during the last three centuries [1]. Undoubtedly, metals have been investigated at greater depth with the progress in material characterization tools. The invention of X-ray diffraction was earliest to reveal the crystal structure and lattice parameters of crystalline materials [2]. Soon electron diffraction allowed similar investigation with greater precision and higher spacial resolution. Investigation of failed materials under the microscope revealed that cracks seem to propagate along specific regions called grain boundaries (GBs). GBs are a 3-dimensional network of defects that form the interface between differently orientated crystallites in polycrystalline metals and are critical to many of the properties of the material [3]. From the failure of boilers in power plants and submarines to the advancement of energy storage in batteries and the prevention of spallation in nuclear power plants, GBs are known to play a critical role everywhere. This necessitates that we have a thorough understanding of the structure and chemistry of the GBs, just as we do of the grains' interiors.

It was quickly realised that because GBs are grain interfaces, they are similar to surfaces. Therefore, the thermodynamics of surfaces that was known since Gibbs in 19th century could be readily translated to the GBs. However, the nanometre length scales involved provided an experimental verification problem, as did the limitless types of GBs that may be produced even in a single-phase pure material. Analogous to all other fields of science, the advent of high-resolution microscopy and computer simulations in the latter half of the previous century, led to tremendous progress. Today's engineering challenges include the design of process parameters to obtain specific GBs, termed GB

engineering (GBE) [4]. Foreign elements segregating to the GB can often lead to catastrophic failure, but in some cases can also strengthen the material. In recent years, many experimental and theoretical studies have been used to reveal at the atomic level the behaviour of GBs [5–8]. GBs are increasingly dealt with as a defect-phase and not a 2-dimensional sheet having negligible width. Potential engineering benefits have resulted in a surge in GB research. Here we identify a massive void that remains in our understanding of GBs in hexagonal close packed (hcp) materials. Therefore, this thesis aims to push the limits of our understanding of GBs in hcp metals with a particular focus on Ti GBs.

## 1.2 Aim and outline of the thesis

Titanium and its alloys are commercially important structural materials. However, because of the hcp structure of Ti, it has been relatively less studied than the cubic elements that are more abundant in nature. In particular, when it comes to GBs, most of the fundamental work was performed for cubic elements, and relatively lesser literature is available on hcp metals.

The primary aim of this work was to study in detail the GB structures in Ti. Traditionally, GB structures have been studied using bicrystals that are custom made by joining the desired planes of two single crystals. Due to the allotropic transition in Ti, which results in loss of control in desired orientation during single crystal growth, obtaining such bicrystals in Ti is extremely difficult. Therefore, to analyse the GBs, it was necessary to establish a route for obtaining them. Following a review of the literature, thin film deposition was chosen as the preferred method. Thin film deposition has many process parameters, and it is often necessary to grow numerous films to understand the influence of a single deposition parameter. Therefore, the first challenge was to provide a template for growing perfectly columnar grains such that their GBs are aligned in a practical way for high-resolution microscopic investigations. It is known to be tricky to reproduce thin films. Therefore, one of the main aims of the thesis was to establish control of the deposition parameters and to understand the various mechanisms that govern Ti thin film growth. The apparent next aim was to explain the microstructure of the film, both in plan-view and cross-section, by underscoring the importance of the thin film route to obtain GBs. The succeeding step was to revert back to our fundamental objective of investigating the atomic structure of GBs in depth using high-resolution scanning transmission electron microscopy (HRSTEM).

Another key objective of this thesis was to analyse the influence of impurities or alloying elements in the atomic-level modification of the GB structure upon alloying.

Ti is almost always used in all commercial applications in an alloyed form. Therefore, it is of great interest to know the influence of alloying on the GB structure. Because Fe is an abundant economic alloying element and because Ti-Fe alloys and intermetallics are of keen commercial interest, the determination of the influence of Fe on the GB atomic structure was targeted.

The following chapters of the thesis are divided as follows: The second chapter provides necessary background for understanding the results and discussion section. Initially, thin film deposition technology is briefly discussed with greater emphasis on e-beam evaporation and pulsed magnetron sputtering. Then, phase transformations in Ti and the role of commonly used alloying elements in phase stability are reviewed. Next, the microstructure of Ti thin films and its dependence on the varying deposition parameters are discussed. This is followed by a section of the description of various GBs. Two sub-sections are written on the atomic structure analysis of the GBs in cubic elements that have been explored more often in the literature, and hcp GBs that are scarcely investigated, respectively. To wind-up the background chapter, a brief review of the characterization techniques that are used in obtaining the results is provided. The next chapter provides the experimental parameters used in thin film deposition and their characterization. The results chapter is divided into three sections based on the three manuscripts that were written as a result of this work. In the last chapter, the findings are concluded and suggestions for some promising projects that the current effort may lead to are discussed.



## Chapter 2

# Background

### 2.1 Thin film deposition

Thin film is a term that has been loosely defined to refer to a thin layer of material deposited onto a substrate. The thickness of the layer can vary anywhere between a few atomic layers up to about 10  $\mu\text{m}$ . There is no strict upper limit, although the properties of thin films can vary with thickness. The science of thin films has hugely expanded since its inception in the late 19<sup>th</sup> century [9]. In the present day, thin films are used for a wide variety of applications like high-frequency amplifiers and high-power transistors in the field of telecommunications, flat-panel displays, reflectors, and solar cells due to their optical properties, interconnects, and ohmic contacts in microelectronics, anti-abrasive coatings, barriers for diffusion, corrosion protective coatings, nanofiltration membranes, and so on [10, 11]. Basically, better understanding of thin film technology opens new ways for advancement in most fields of science. Although there are numerous ways to deposit thin films, all the methods are broadly classified into physical vapor deposition (PVD) and chemical vapor deposition (CVD). In PVD, the material to be coated is evaporated using various means and guided to a substrate where it condenses upon contact. In contrast, in CVD, a chemical reaction occurs between a carrier gas and a precursor and the reaction product deposits on to the substrate surface. CVD is used industrially for high-throughput applications, such as in the semiconductor industry or the deposition of refractory materials on turbine blades. One of the major differences between PVD and CVD is that PVD is a line of sight process, which means that the deposition takes place from a specific direction whereas in CVD the reaction products can reach the substrate from any direction. Because of the directionality, relatively complex-shaped substrates can be employed in CVD, which are not feasible via PVD. In the present work, all films were deposited using three different PVD methods which are briefly described below.

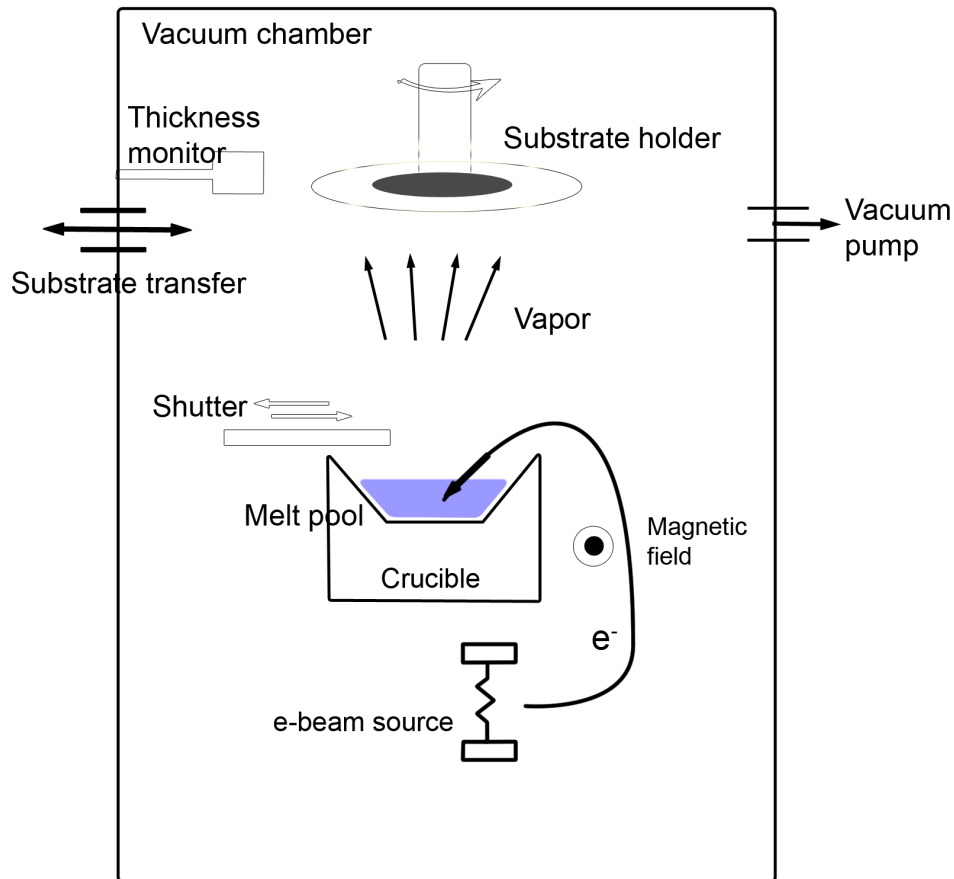


**Figure 2.1** Schematic of an e-beam evaporation setup used to deposit thin films. Redrawn in modified form from [18].

### 2.1.1 e-beam evaporation

Electron-beam (e-beam) evaporation is a PVD process in which the target material that is intended to be deposited is typically placed in a copper cooled crucible and evaporated using a high energy e-beam inside a vacuum chamber [12, 13]. The e-beam is usually generated using a thermionic source and is accelerated towards the target material. As shown in Fig. 2.1, the e-beam source has to be placed behind the target to maintain a better vacuum near it. A magnetic field is applied to direct the beam towards the targeted crucible. Upon collision of the electrons with the target material, the kinetic energy of the e-beam is converted to thermal energy, and a local melt pool forms. This leads to evaporation of the target material, which then condenses on to the substrate, forming a thin film. The substrate holder is usually rotated at 10-20 rpm to obtain uniform thickness of the film. The desired mean free path for the evaporated species of few tens of centimeters (which is the typical target to substrate distance) is obtained with a vacuum of  $\sim 10^{-7}$  mbar or lower [14]. Several reviews have detailed the history, development and utility of e-beam evaporation techniques [15–17].

**Table 2.1** Sputtering yield of Ti, Cu and Au for ions having 500 eV. [23]

Ions	Ti (48)	Cu (64)	Au (197)
He <sup>+</sup> (4 amu)	0.07	0.24	0.07
Ne (20 amu)	0.43	1.80	1.08
Ar <sup>+</sup> (40 amu)	0.51	2.35	2.40
Kr <sup>+</sup> (84 amu)	0.48	2.35	3.06
Xe <sup>+</sup> (131 amu)	0.43	2.05	3.01

### 2.1.2 Direct current magnetron sputtering

Direct current magnetron sputtering (dcMS) is a versatile sputtering method used extensively in the semiconductor industry [10, 18, 19]. In this process, a high voltage is applied across two electrodes, the target and the substrate, in the presence of a non-reactive gas at low pressure. The gas under high potential and low pressure generates a plasma that is a mixture of electrons and gas ions in a high-energy state. Usually, argon (Ar) is employed to generate the plasma. The target is the negative electrode which gets continuously bombarded with the positively charged ions (Ar<sup>+</sup>) present in the plasma. When the high-energy ions hit the target, they eject ions from the target material with energy that is sufficient to travel from the target to the substrate [20]. The ratio of sputtered atoms to the incident ions is called sputter yield. It depends on the atomic mass, momentum, angle of incidence of the carrier gas, and surface binding energy. The soft metals like Ag, Au, and Cu have a larger sputter yield than harder transition metals like Fe and Ti due to the filled d-orbitals [21]. The sputter yields of Ti, Cu and Au for all the noble gases is enlisted in Table 2.1. It can be seen that Ar leads to high sputter yield due to its higher atomic mass than He and Ne. However, when using Kr and Xe, which have a higher atomic mass, the implantation of ions in the target increases due to their higher momentum and the sputter yield plateaus/reduces [22]. Ar is also less expensive than the heavier noble gases, hence it is the most commonly used process gas.

The bombardment of the target with Ar<sup>+</sup> also generates secondary electrons (SE). The SE are attracted towards the anode and on their way collide with Ar atoms to form new Ar<sup>+</sup> ions. Ar<sup>+</sup> ions are again attracted towards the cathode. This cascading effect leads to a stable plasma, given that the pressure of the gas is adjusted so that the electron collides with another gas atom before hitting the anode [24]. However, if the pressure is maintained too high, the electrons may not attain enough velocity/momentum to cause ionisation when the collision occurs.

In dcMS, a magnetic field is obtained by using permanent or electromagnets behind

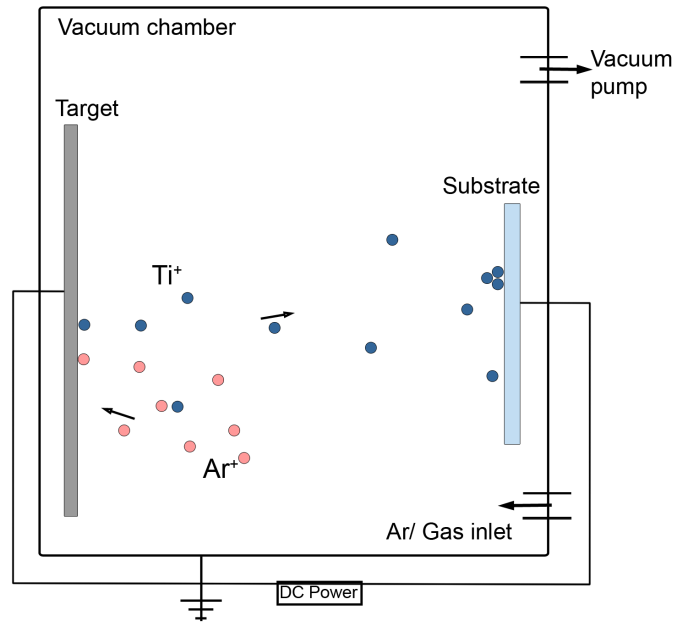


**Figure 2.2** Schematic of a direct current sputtering setup used to deposit thin films. The plasma of  $\text{Ar}^+$  ions and  $e^-$  is confined in front of the target due to the magnetic field around the cathode. Redrawn from [25].

the target. This brings according to the Lorentz force the electrons on a spiral path and prevents the SE from flying away and increases the ionisation of the plasma. Because of the increased ion availability, dcMS can be performed at a gas pressure much lower than that of a DC diode sputtering. This leads to higher deposition rates [25].

There are several other deposition parameters that can influence the deposition process. The voltage applied between the electrodes determines the acceleration of ions toward the target and thus the current originating from the target ions, called target-ion current ( $I_s$ ). A substrate bias of several hundred volts can be applied to influence the  $I_s$  that can largely change the thin film microstructure, porosity, and texture [10]. The dcMS consists of two electrodes that are kept under certain potential difference throughout the deposition process. This necessitates that the target used in dcMS must be conductive to avoid charge accumulation. If there is charge build up on the surface of the target, the incoming ions are deflected away. Therefore, to deposit films of insulating materials or to perform chemical reactions before/during film deposition, numerous modifications have been made to the setup seen in Fig. 2.2. One such modification is to pulse the sputter target that is discussed in the next section.

The target ions condense onto the substrate upon contact and form a thin film, just as in other physical vapour deposition methods. However, the complete formation of the film is a multistep process. In some cases, the incoming ions can condense and



re-evaporate from the substrate. At other times, they can migrate to the substrate surface and meet other groups of atoms that are condensed as well. The critical size of such groups of atoms is called a nucleus. The addition of more atoms, called adatoms, leads to the growth of the island. When several islands meet each other, the process is called coalescence [20]. The rate of migration of adatoms on the substrate surface depends on factors such as the wetting angle between the adatoms and the substrate, the substrate temperature and the substrate surface. At higher substrate temperature, the diffusion of adatoms is eased, often leading to larger grains or epitaxial films. When high energetic ions are bombarded on the growing film, the physical properties of the film can be altered. Metastable phases can form due to higher energy [26]. The high energy ions can also move the deposited atoms into the substrate, thereby improving the adhesion of the film [13]. As can be seen, all of the process parameters are linked, making PVD a very adaptable technology with a wide range of film microstructure possibilities on the one hand, but also making precise control of these numerous process parameters in an industrial scale a major challenge.

### 2.1.3 Pulsed magnetron sputtering

In dcMS, the introduction of a magnetic field near the cathode increases the plasma density and the sputter yield [20]. But the density of plasma near the substrate surface is rather low for high-throughput industrial requirements. In addition, increasing the power density to deposit low-conducting materials can lead to arcing. In the case of reactive sputtering, for example, to deposit TiN or TiO<sub>2</sub>, the Ti metal target is used and a certain partial pressure of oxygen or nitrogen is maintained near the substrate for the reaction between the adatoms and the gas to occur. However, this can also lead to the formation of an insulating layer over the target surface and result in arcing due to charge build-up [27]. RF sputtering (radio frequency, usually 13.56 MHz) can produce similar high-quality films, but the deposition rate of few  $\mu\text{m}/\text{h}$  which is too low for commercial utility [28].

To overcome these challenges, in the 1980s, unipolar pulsing of the magnetron power source was introduced [29]. In this technique, in a cyclic manner, the power supply operates at a low or near-zero power for a certain duration and is shot to high power for the remainder of the cycle. The manner in which these pulses are applied influences the sputtering behaviour [25]. In asymmetric bipolar magnetron sputtering the target voltage is alternated between negative and positive potential. The positive potential is often only a small fraction (10 to 20%) of the negative potential. And the width of the

positive pulse is much shorter, approximately 10% of the width of the negative pulse. Therefore, the target stays in the sputtering mode for most of the pulse duration. During the short reversal of the target, the electrons from the plasma get attracted to the target to first neutralize and then negatively charge it. When the cycle reverses and the ions from the plasma are attracted to the cathode, the ions are accelerated more strongly than in dcMS. This increases the sputter yield while also preventing charge build-up and arcing. Based on the ratio of the positive and negative potential, the pulsing is termed as symmetric or asymmetric [27].

The ratio of 'pulse-on-time' to the total duration of a pulse is expressed as duty cycle.

$$\text{Duty cycle} = \frac{t_{ON}}{t_{ON} + t_{OFF}}. \quad (2.1)$$

The pulse-on-time can range from a few microseconds to a few milliseconds or longer. Due to the large variation in the plasma properties based on the duty cycle, pulsed magnetron sputtering is classified into several categories as seen in Fig. 2.3 [25]. High-power unipolar pulse with a power-density higher than  $0.5 \text{ kW cm}^{-2}$  is called high power pulsed magnetron sputtering (HPPMS). To achieve a high power density, the duty cycle is shortened to about 1–3% while maintaining the same time averaged power at the cathode target. The high electron density in the discharge also leads to high ionisation of the sputtered species. As seen in Fig. 2.3, the peak power loading in dcMS is of the order of few tens of  $\text{W cm}^{-2}$  where as the power loading during pulsing can be as high as  $10 \text{ kW cm}^{-2}$ .

The energy of the sputtered positive ions can be controlled by biasing the substrate [31]. Therefore, the applied bias voltage is another parameter that can influence the thin film microstructure. Their energy influences the desorption of physically absorbed adatoms and promotes surface migration. The increased surface migration is necessary to fill the surface steps and to avoid micro-cracks. The main properties that determine the film microstructure are the ratio of the fluxes of incoming ions to the deposited ions, the energy of the incoming ions and the homologous temperature [32]. The rate of deposition in dcMS is proportional to the power applied to the target. However, in HPPMS the back-attraction of the sputtered ions increases as a result of increased ionisation. Therefore, for the same power input, the deposition rate in HPPMS is lower than dcMS [30].

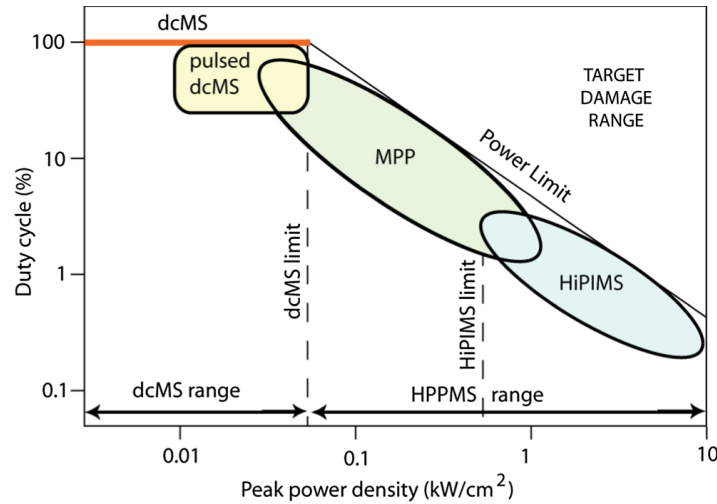


**Figure 2.3** Overview of the classification of dcMS and pulsed magnetron sputtering based on the duty cycle and the peak power density. Adapted from [30].

## 2.2 Titanium and its alloys

### 2.2.1 Introduction and phase transitions

Titanium (Ti) was discovered by W. Gregor in the UK in 1791 and was named after the Titans, the Greek mythological pre-Olympic gods [33]. Since then, our understanding of Ti has come a long way, making it one of the most prominent metals of commercial importance. As of 2020, the world production of Ti sponge metal is estimated to be 341,000 tons and TiO<sub>2</sub> pigment production of 8 million tons [34]. Therefore, more than 95% of current-day Ti consumption is in the form of TiO<sub>2</sub>. Due to its high refractive index, TiO<sub>2</sub> has wide commercial utility in the production of paints, paper, toothpastes, and sunscreen creams. However, metallic Ti is also an important structural material due to its high strength-to-weight ratio and high corrosion resistance [35, 36]. Ti is used most widely in the aerospace industry. Its high production cost has confined its usage to higher-priced applications, despite the fact that it has the same strength as steel and weighs half as much. It is commonly used for steam turbine blades, condenser tubes for fuel plants, and biomedical devices. Most oxidising acids do not have an effect on Ti. Therefore, it is used extensively for handling salt and acid solutions. Ti is most widely used in the form of Ti-6Al-4V (Ti-64) alloy in the aerospace industry [37]. Ti-64 is expensive due to the high cost of vanadium. There is an increasing interest to develop Ti alloys having lean and economic alloying additions. This has led to increased interest in the understanding of pure and micro-alloyed Ti.

Pure Ti can exist in two crystal structures, hcp ( $\alpha$ ) and body-centered cubic (bcc) ( $\beta$ ), based on the temperature [38].  $\alpha$ -Ti is the room-temperature allotrope of Ti

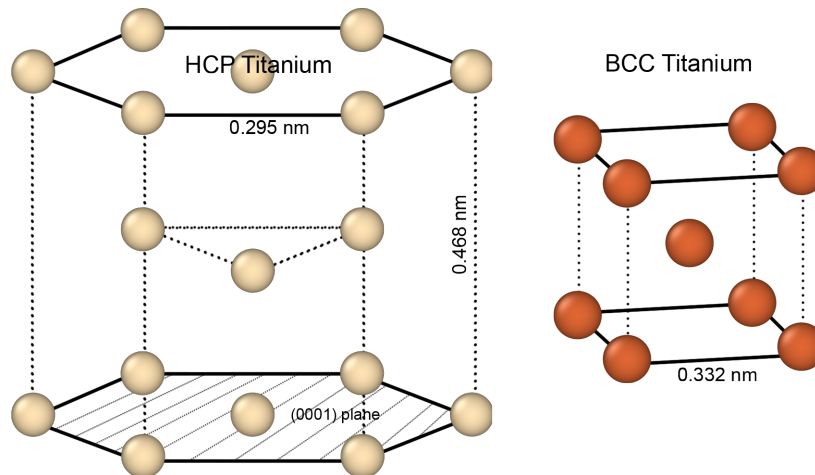


**Figure 2.4** Ball and stick models of hcp and bcc Ti unit cells with highlighted basal plane and the lattice parameters.

that transforms to  $\beta$ -Ti when heated to about  $882^{\circ}\text{C}$ . It has lattice parameters of  $c = 0.468$  nm,  $a = 0.295$  nm, leading to a  $c/a$  ratio of 1.586 that is slightly less than the ideal hcp  $c/a$  ratio of 1.633 [39]. As seen in Fig. 2.4, an hcp Ti crystal is made by adding a two-atom motif to the hexagonal primitive lattice. The two atoms are located at  $(0\ 0\ 0)$  and  $(1/3\ 2/3\ 1/2)$  positions [40].

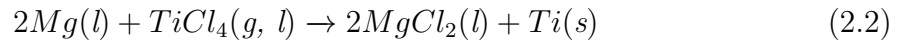
Due to its hcp crystal structure,  $\alpha$ -Ti has low cold-formability. A close packed plane of  $\{0002\}$  and a close packed direction of  $\langle 11\bar{2}0 \rangle$  leads to only 4 independent slip systems which according to Von-Mises criterion are insufficient for plastic deformation [35]. However, due to the possibility of mechanical twinning, a moderate ductility can still be obtained in  $\alpha$ -Ti. Like most polycrystalline materials, grain size strongly determines the mechanical properties of pure  $\alpha$ -Ti. Additional heat treatments and cold working are effective in further tuning the properties. For example, water quenching an equiaxed large grain microstructure after 1 h of annealing at  $1000^{\circ}\text{C}$  produces small grains with serrated GBs. This doubles the yield strength while maintaining the ductility and toughness [41]. Therefore, heat-treatments and material processing methods can largely modify the microstructure and determine the final material properties.

Additionally, the formation of  $\beta$ -Ti, due to the allotropic transition, can be used to generate several other alloys. The bcc lattice has a lattice parameter of 0.332 nm [42]. Because of its more open structure, the self diffusivity of Ti is 310 times higher in bcc than in hcp Ti [43]. As a result,  $\alpha$ -Ti exhibits better creep resistance than  $\beta$ -Ti. However, bcc Ti offers higher short-term strength and better fabricability [41]. Implants inside the human body are one of the most significant uses of  $\beta$ -Ti. In order to avoid attrition of bone to which the implant is attached to, and to distribute the

load on bone and implant uniformly, it is necessary that the elastic modulus of the bone and implant are nearly the same. While human bones roughly have stiffness of 20 GPa,  $\alpha$ - and  $\beta$ -Ti have a modulus of 100 GPa and 65 GPa, respectively, making  $\beta$ -Ti highly desirable as an implant material [44]. Aerospace industry also extensively uses  $\beta$ -Ti alloys, like Ti-13V-11Cr-3Al, which was the first commercially used  $\beta$ -Ti alloy [45]. Many alloying elements can be added to Ti to stabilise either of the phases and obtain a desired phase fraction. Similar to steel, the allotropic phase transition in Ti leads to a a myriad of achievable properties.

### 2.2.2 Alloying and segregation behaviour in titanium

Ti is one of the metals that is difficult to extract, mainly due to its high melting point (1668°C), high chemical reactivity and high thermodynamic stability of the ores (oxides).  $\text{TiO}_2$  which is converted to  $\text{TiCl}_4$  is reduced by magnesium in a closed reactor under an inert gas atmosphere in the Kroll's process [46]. The reduction of titanium chloride can be written as follows:



The exothermic reduction process generates enough heat to keep the magnesium chloride molten. But,  $\text{TiCl}_4$  and Mg have very low solubility in  $\text{MgCl}_2$ . As a result, it is generally assumed that metallic Ti is formed during the reduction process by direct contact of  $\text{TiCl}_4$  with metallic Mg. Some of the titanium tetrachloride gets partially reduced resulting in formation of titanium dichloride [45]. The spontaneous reduction of titanium dichloride is an exothermic reaction. The reaction can be written as follows:



When this exothermic reaction occurs inside a steel reaction container, the molten titanium metal tends to react with iron. This is a major source of iron impurity that is commonly present in titanium [46]. Because of the very high reactivity of Ti, the sponge Ti metal often has a large number of impurities.

All of the major impurities and alloying additions to Ti can be classified as either hcp or bcc phase stabilisers [40]. If an element delays the  $\alpha$ - $\beta$  transition, it is an  $\alpha$  stabiliser, while the elements that hasten the transition are  $\beta$  stabilisers. The most common  $\alpha$  stabilisers are aluminium (Al), oxygen (O), nitrogen (N), and carbon (C). Of these, O and N are particularly notorious as they are present in abundance in the air and often

gets dissolved in the metal during the process of melting and ingot formation. The most common  $\beta$  forming elements are iron (Fe), chromium (Cr), niobium (Nb), molybdenum (Mo), tantalum (Ta), vanadium (V), and tungsten (W) [45]. Some elements do not influence the transition temperature and are categorised as neutral elements. The commonly alloyed neutral elements are Zr, Sn and Si. A comprehensive list of all commercially available titanium alloys can be found in [41].

### Iron in Ti

Iron (Fe) is one of the most common impurities observed in Ti [47]. The addition of Fe can result in its segregation at GBs,  $\beta$ -phase formation, or precipitation of intermetallic compounds [48, 49]. The ratio of  $\alpha$  and  $\beta$  phase usually depends on other alloying additions.

In the case of  $\alpha$ -Ti, as indicated in Fig. 2.5, the maximum solubility of Fe is less than 0.05 at.% [50, 51]. Consequently, Fe either forms secondary phases or segregates at the GBs. Although extensive studies have been performed on GB segregation in many fcc and bcc metals and alloys, limited reports have discussed GB segregation of Fe in Ti or other hcp metals. Recently, density functional theory (DFT) calculations also confirmed the presence of a high driving force for Fe to segregate at  $\alpha$ -Ti GBs [47]. However, it is unclear how Fe pins the GBs and whether or not secondary phases contribute to this.

The  $\beta$ -phase in Ti alloys improves its corrosion resistance, fracture toughness and yield strength but reduces the ductility [52]. Therefore, Fe has attracted plentiful attention for being the most cost-effective  $\beta$  stabilizing alloying element [53–55]. One of the major usage of  $\beta$  Ti on a commercial scale was on the landing gear forgings of Boeing 777 aircraft. For this application, Ti-10V-2Fe-3Al (Ti-10-3-2) alloy was initially used [56]. Formation of fine-scale  $\alpha$  Ti precipitates (20–200 nm) results in a large  $\alpha$ - $\beta$  interface that acts as dislocation barriers and improves the strength [57]. However, due to superior strength and a wider processing window, Ti-5Al-5Mo-5V-3Cr (Ti-5-5-5-3) replaced Ti-10-3-2 as the recommended  $\beta$  Ti alloy in the recent years [58]. When Fe-rich  $\beta$  Ti is cooled down from at higher temperatures to below eutectic temperatures, based on the rate of cooling, we obtain a mixture of Ti-Fe intermetallics and super-saturated  $\beta$  Ti. While  $\beta$  Ti improves the corrosion resistance, fracture toughness and yield strength, excess of  $\beta$ -flakes at the GBs can be deleterious to the material properties [59]. Therefore, the right mixture and microstructure of the two phases have been utilized to obtain a combination of high strength and high hardness [60]. The role of alloying elements, especially Fe, in the nucleation and growth of  $\beta$ -Ti is of a great commercial interest. In  $\beta$ -Ti, Fe and Cr have been shown to segregate at the GBs and

act as grain refiners when cooling [61]. The segregation of Fe at Ti GBs has repeatedly been suggested to be responsible for pinning the GBs, leading to remarkably stable nanocrystalline Ti [47, 62].

The Ti-Fe system forms two intermetallics, TiFe which has an ordered B2 structure (Space group:  $Pm\bar{3}m$ ) and  $TiFe_2$  which is a laves phase with C14 structure (MgZn<sub>2</sub> type) [63]. Fe segregation at GBs in Ti alloys can lead to the formation of both of these intermetallic compounds [64]. The lattice parameter of TiFe, which varies continuously in the composition range of 47 to 51 at. %, is comparable to that of the FeAl intermetallic system [65]. The amount of ordering can vary based on the rate of cooling or rate of phase transition. TiFe is interesting for hydrogen storage due to its strong affinity for hydride formation [66]. However, the hydrogen activation process of TiFe is hindered by the formation of titanium oxide layer. Both high-pressure and high temperature are required to achieve a reproducible absorption/desorption of the maximum amount of hydrogen in the compound that is nearly 1.90 wt. % [67]. Amorphous TiFe achieved by mechanical alloying (ball-milling) has been shown to absorb higher H-content than crystalline TiFe [68]. As expected for intermetallics, TiFe is highly brittle and has limited use as structural material. However, several alloying additions have proven to dramatically improve the mechanical properties of TiFe with high compressive strength higher than 2.5 GPa and ductility of about 10% have been shown [69]. Some of these alloying additions include, TiFe(Sn), TiFe(Co), and TiFe(B).

The C14 structure of the Laves phase  $TiFe_2$  can be visualized as a closed packed structure of Ti atoms in which half of the tetrahedral sites are occupied by Ti and the other half by tetrahedrons of Fe atoms [63]. Ferromagnetic clusters of Fe inside of the antiferromagnetic matrix have been observed in  $TiFe_2$  [70]. Similarly, the magnetic behaviour of the laves phase has also been studied using first principles [71].

Ti-Fe alloys have also been extensively used to fabricate near-net shape parts using the blended elemental powder metallurgy (BEPM) route to achieve cost reduction [73, 74]. Attempts to partially or completely replace V or other expensive  $\beta$ -stabilizers with Fe have been successfully undertaken [75, 76]. The addition of Fe in the powder blend enhances the sinterability of Ti alloys because of its high diffusivity [52, 77].

Additionally, two metastable phases,  $\alpha'$ -Ti (hcp), and  $\omega$ -Ti(Fe), have been observed during martensitic transformation of Ti-Fe alloys [78–82]. The  $\omega$ -Ti(Fe) is a high-pressure Ti phase which is retained at low pressure in Ti-Fe alloys.

Overall, a multitude of phase transitions have been realized in Ti-Fe alloys. Many of them appear to have commercially attractive properties, with the greatest attraction

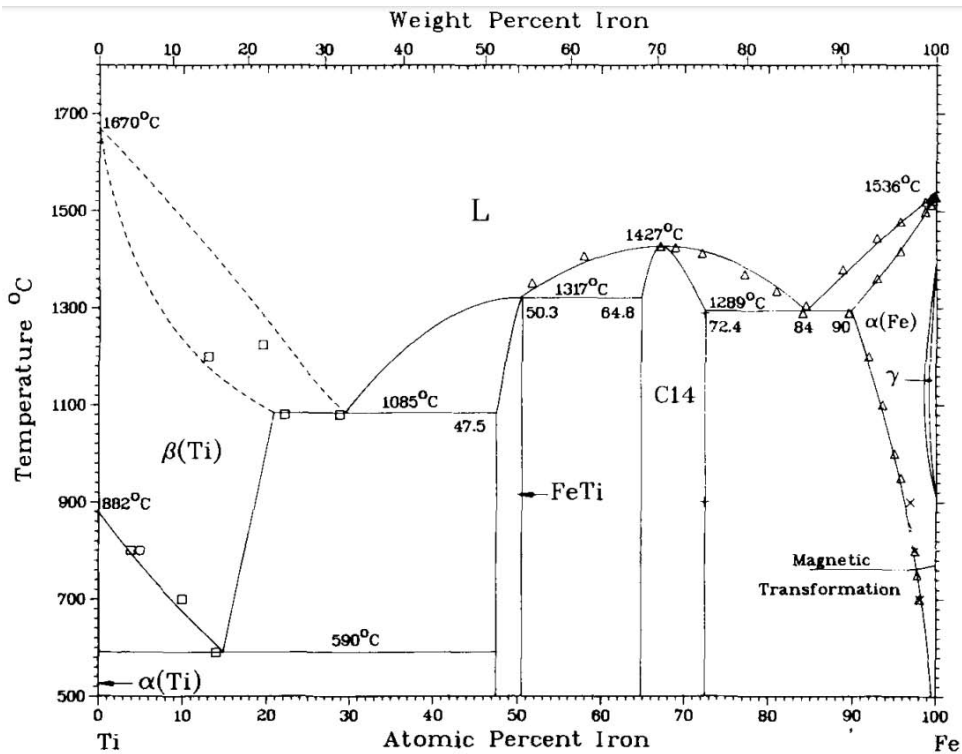


**Figure 2.5** Phase diagram of Ti-Fe system showing all the possible intermetallics, their composition range and phase transitions at various temperatures [72].

being the economic viability of Fe to reduce the usual high cost of Ti alloys. However, numerous questions on how Fe influences these phase transformations remain unanswered and is a hot subject of research [83].

## Oxygen in Ti

Titanium has a very high affinity for oxygen. Because of its high reactivity, Ti immediately forms an oxide layer that remains impenetrable. The oxide layer is hard and smooth and therefore, does not allow for any foreign particles to stick to the surface. The oxide layer results in excellent corrosion resistance of Ti that makes it attractive for many demanding applications such as in marine environment. However, Ti has limited resistance to oxidation at temperatures greater than 650°C. Oxygen dissolves interstitially even at 430°C.

Pure-Ti has low strength but high toughness. A small addition of oxygen can improve the strength. By increasing the oxygen content from 0.2 at.% to 0.6 at.% the strength of Ti can be increased from 250 MPa to 450 MPa. The former is the grade-I Ti and the latter is grade-IV. While a small amount of oxygen appears to be beneficial to strength, it is necessary to strictly limit the oxygen content. On one hand, the formation of oxide particles in the matrix are known to reduce the fatigue strength and



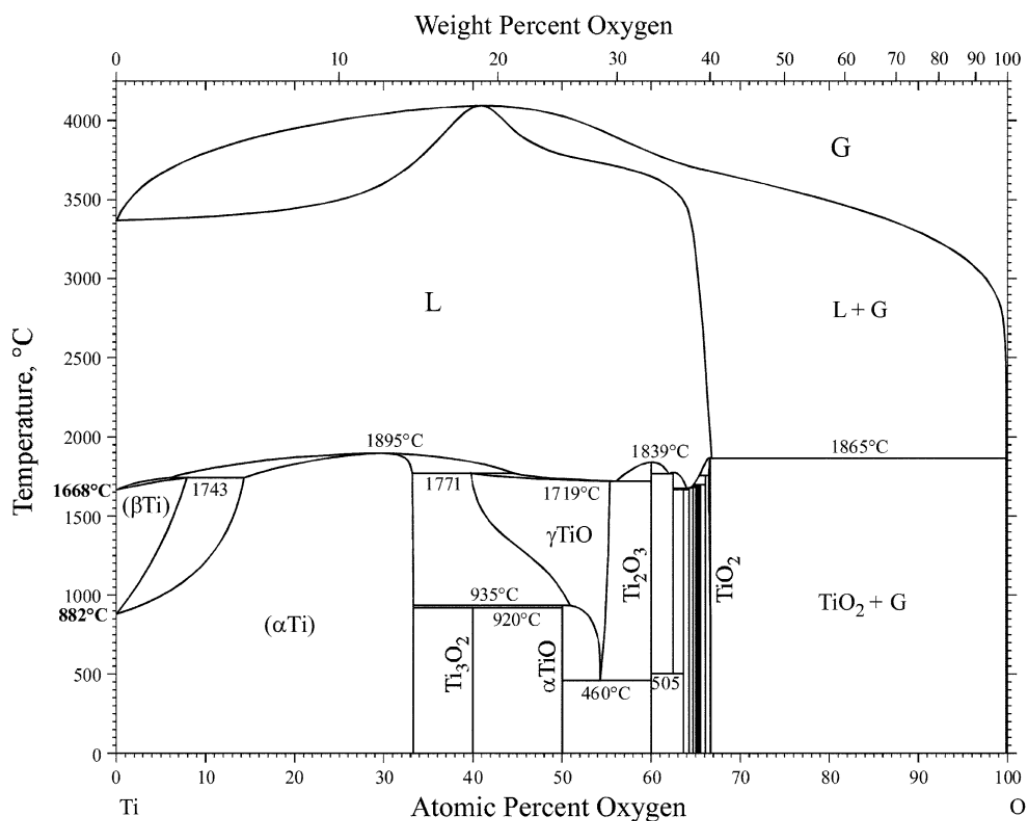


**Figure 2.6** Ti-O phase diagram showing wide solubility range of O in  $\alpha$  Ti [86].

act as the fracture initiating sites and therefore can be detrimental to the mechanical properties [84], and on the other hand, the presence of interstitial oxygen also impairs the mechanical properties severely. When a material is plastically deformed, a wavy slip band is generated when the slip occurs in multiple slip planes and directions. If the slip is restricted to a particular slip plane, the slip bands are rather planar. This can strongly limit the amount of plasticity in a material. The interstitial oxygen hops between the octahedral and hexahedral sites in hcp Ti when slip occurs and causes resistance to the dislocation motion. The kinetics of the hopping which are determined by temperature and strain rate are responsible for the switch between planar and wavy slip [85]. Overall, it is well established that even very small amounts of oxygen in the interstitial sites of Ti can cause large change in its plasticity.

As can be seen from the phase diagram in Fig. 2.6, the solubility of oxygen in Ti can be as high as 30 at.%. The oxygen is dissolved in the octahedral voids of  $\alpha$ -Ti in a disordered manner. At lower temperatures, many oxides can form. The high solubility of oxygen in Ti is one of the reasons for the high cost of Ti production. Because during Ti production, a thick layer of oxide forms on the surface, which is difficult

to chemically deoxygenate. Thermodynamically, reducing titanium oxides by adding another reducing element is feasible. However, the challenge is to get the oxygen out from the solid solution. To remove the oxygen that is dissolved into the interstitial sites is kinetically hindered. Therefore, this layer has to be chipped off/ removed by machining, resulting in a lower net-output. To make the process economical, the generated scrap is deoxygenated using several methods such as calcium molten salt deoxygenation, hydrogen-assisted Mg deoxygenation, and calcium vapor deoxygenation [87]. High-value Ti powder is obtained from it that can be used for powder metallurgy or additive manufacturing.

Several other developments have been made in terms of understanding and utilizing the Ti-O alloy system. The surface hardness and wear resistance of Ti alloys have been improved by performing surface laser gas oxidation in dilute oxygen environment by mixing the gas with Ar [88]. By using post-processing methods such as solution heat treatment and thermomechanical processing, the discarded powders from additive manufacturing or powder metallurgy containing higher oxygen content have been used to make alloys that exhibit  $\geq 6\%$  elongation. The improved ductility in high oxygen Ti alloys stem from the transformation of  $\beta$ -Ti into  $\alpha'$ -Ti (martensite). The  $\alpha'$ -martensite formed between the oxygen rich  $\alpha$ -Ti can accommodate large strains during tension [89]. Additionally, oxygen and carbon have been shown to weakly segregate at the Ti GBs although oxygen has a high solubility in  $\alpha$ -Ti [47, 90].

In summary, although the vital role of oxygen in Ti in improving its strength and corrosion resistance is well-understood but improving the toughness of high-oxygen alloys is necessary. Using Ti-O alloys will result in economic viability of Ti and this makes it an important subject of research.

## 2.3 Titanium thin films

Apart from its conventional bulk applications, there are emerging advancements to use Ti in microelectromechanical systems (MEMS) devices and hydrogen storage applications [91–93]. Due to its corrosion resistant properties, thin films of Ti are also attractive as a protective coating. They can also be used as an adhesive bonding layer to grow films of Pt, GaN, and Cu thin films [94–96]. Depending on the application, thin films of varied properties are required. This demands the film to have a preferred microstructure, for example a nanocrystalline film would exhibit high strength and fatigue resistance whereas a single crystalline film would exhibit better corrosion resistance. Therefore, it is necessary to understand the influence of deposition parameters on the various film microstructures that are obtainable.

Apart from the deposition parameters, the lattice matching, symmetry of surface planes, substrate miscut, and the planes forming terraces and steps on the substrate surface [97] are variables that can alter the orientation and morphology of thin films, while maintaining substrate chemistry. The adaptation of an orientation relationship (OR) between a substrate and a film is a complex phenomenon [98]. Even with a known substrate surface symmetry and chemical composition, it is in most cases not possible to predict the preferred OR [99].

The effect of deposition parameters on Ti thin films deposited using DC sputtering have been investigated earlier, which are predominantly reported to be nanocrystalline [100–102]. However, when using e-beam evaporation a range of microstructures and orientations have been observed. For example, when using e-beam evaporation, a high deposition rate of 350 Å/s resulted in a (10 $\bar{1}$ 0) and (11 $\bar{2}$ 0) single crystalline (SC) films on sapphire substrate [103]. However, a growth rate of 20 Å/s on the same sapphire substrate resulted in a (0001) SC films [104]. As a misconception, 6 Å/s was stated to be the lower limit of deposition rate to obtain a SC film [104], but Dehm *et al.* [105] reported SC Ti at much lower deposition rate of 0.15 Å/s at substrate temperatures ( $T_{dep}$ ) ranging from 373 K to 473 K for up to 100 nm thick films on (0001) sapphire. A further decrement of the deposition rate down to  $\sim$ 0.03 Å/s lead to a polycrystalline film with 3D island growth [106]. Interestingly, the reduction of Al<sub>2</sub>O<sub>3</sub> by formation of Ti<sub>3</sub>Al at the interface in sputter deposited Ti at room temperature (RT) with a deposition rate of 0.4 Å/s has also been reported [107]. Overall, these studies illustrate that a wide range of film microstructures can be obtained. This necessitates a thorough investigation of the effect of deposition parameters on thin film microstructure.

### 2.3.1 Nano-/ polycrystalline films

Owing to the surface energy anisotropy in hcp materials, most of the Ti thin films are textured. Many studies have discussed the role of deposition parameters on changing the film texture. Using a DC sputtering setup a change in texture of nanocrystalline Ti thin film was reported [108]. The nanocrystalline film with a grain size of 5-15 nm was obtained on (100) single crystalline Si substrate. By increasing the substrate bias, the kinetic energy of the incoming ions/ adatoms can be increased. This enhances its diffusivity but also causes sputtering of the deposited ions. The authors reported a weakening of texture from (0002) at 0 V to a mixture of (0002), (10 $\bar{1}$ 0) and (10 $\bar{1}$ 1) at 150 V bias.

The effect of target power and chamber pressure on the properties of Ti thin films prepared by DC magnetron sputtering has been studied by many authors [100, 109,

110]. The triode sputtering setup includes the introduction of an additional positive grid to maintain a discharge event at low pressure and voltages. In one study, the authors were able to show that by keeping all the deposition parameters constant they systematically varied the target power between 60 W to 120 W. Only when using high power, the films were observed to be crystalline and had a (0002) texture. At lower target power of 80 W, the film exhibited no visible peaks in XRD and were considered to be nearly amorphous. However, when the deposition pressure is reduced, due to increased mean-free path, the (0002) textured crystalline films were obtainable with 80 W power [110]. The triode (supporting mesh) setup has been shown to increase the target current substantially even at low chamber pressures and thus results in a high-density film [109]. Additionally, the same film morphology that was attainable at 400°C for diode can be obtained at 100°C for triode resulting in lower substrate temperatures.

In another study, the influence of changing incidence angles on the film microstructure and texture was evaluated. At normal incidence angle deposition, the film was observed to have a (0002) fiber texture, which means, all the grains had a (0002) surface plane with an arbitrary in-plane rotation. When the deposition angle (incoming flux angle) was inclined, porous inclined columns formed. With an increase in inclination, biaxial texture with two competing tilt axis,  $[10\bar{1}0]$  and  $[2\bar{3}10]$  are observed. The change of texture and inclination of the columns is attributed to the shadowing effect which dominates the diffusivity [111]. The change in microstructure with inclination angle is essential to understand the coating of components having complex shapes.

Nanocrystalline Ti films have been reported on NaCl [113], which is a water-soluble substrate. It is extensively used as a growth substrate or as an intermediate sacrificial film for ultra-thin metallic films. It has a wide variety of applications like transfer-printing, nanotexturing, and fabrication of metallic nanostructures for transparent flexible electrodes [114]. Furthermore, under certain deposition conditions, both, the co-existing hcp and fcc phases and entirely nanocrystalline hcp phase, have been reported on NaCl substrates [113, 115]. Nanocrystalline Ti films have also been proposed as an attractive material for hydrogen storage. It is expected that higher defect density increases the hydrogen storage capacity. Therefore, growing a nanocrystalline film is favourable. Tarnawski et al. [91] grew nanocrystalline Ti on Si(111) and SiO<sub>2</sub> substrates using DC sputtering at 250°C. When comparing Ti with thin films, it was found that Ti exhibited a hydrogen storage capacity of up to 50 at.% compared to 30 at.% for Ti-V-Ni film and 20 at.% for V<sub>2</sub>O<sub>5</sub> films. The affinity for hydrogen specially increases at higher temperatures reaching more than 50 at.% at 600°C. In a multilayer deposition of Ti/TiO<sub>2</sub>/Ti/Si(111) with Pd layer capping, it was shown that hydrogen is

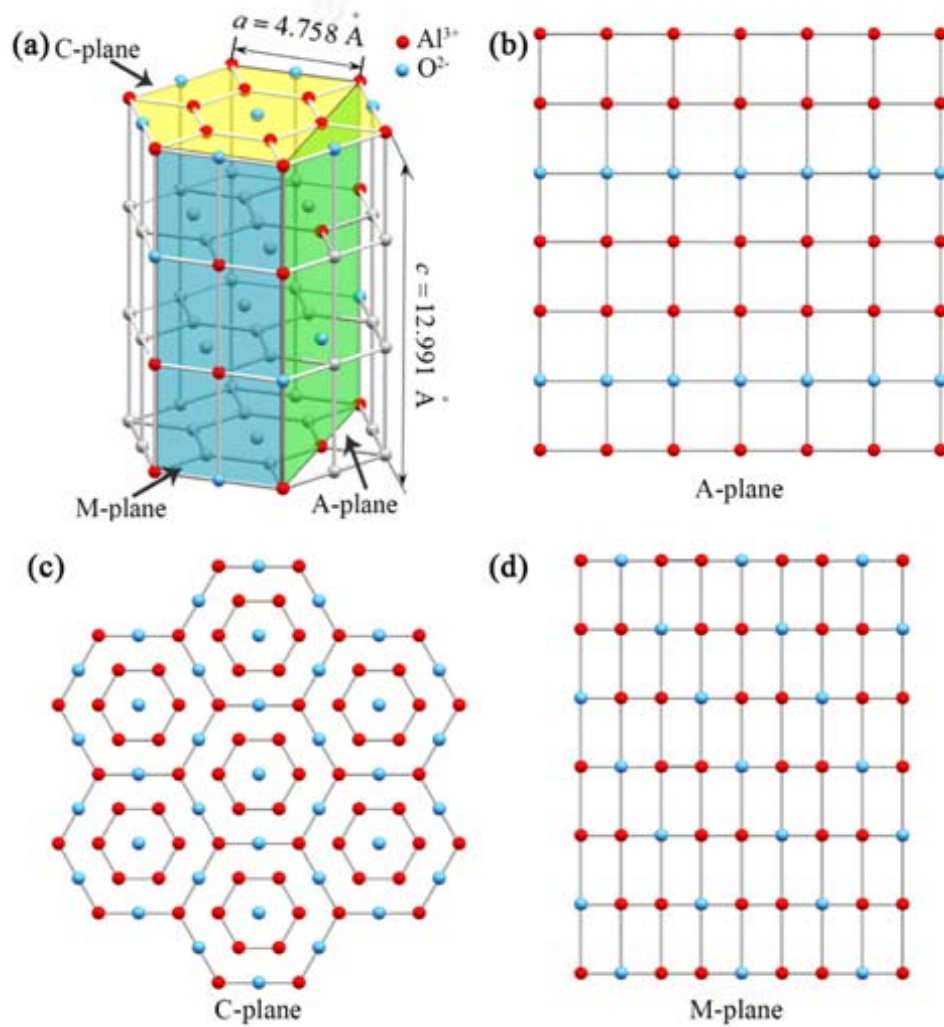


**Figure 2.7** Crystal structure of sapphire a) and expanded 2D arrangement of Al<sup>3+</sup> and O<sup>2-</sup> ions on the surface of b) (11 $\bar{2}$ 0) A-plane, c) (0001) C-plane, and d) (10 $\bar{1}$ 0) M-plane sapphires. Adapted from [112]

adsorbed on both the layers with no adsorption in the  $\text{TiO}_2$  layer [91]. In another study of hydrogen storage in nanocrystalline Ti thin films, the film texture was observed to change the hydrogen storage capacity [116]. The (0002) orientated film had lower residual stress and had an elastic deformation on hydrogen charging until a certain limit before plastically deforming due to the hydride formation. While the (10 $\bar{1}$ 0) orientated film does not deform plastically as no dislocations are seen around the hydrides. It is identified that the hydrides forming on c-plane and prism plane Ti have different stoichiometry. In fact, hydrides that are not observed in bulk can be obtained in thin films, likely due to the high amount of stresses. Bandyal *et al.* reported  $\text{TiH}_3$  in thin films of Ti evaporated over Ru (0001) [117] when the Ti film is sufficiently thin. For thicker films, the hydride was seen to approach the bulk composition of  $\text{TiH}_2$ .  $\text{TiH}_2$  thin film has also been used in supermirrors that are used to guide the neutron beam. Because of the higher refraction indices, fewer layers of Ti-H film are required to achieve the same reflectivity as pure Ti film. Nanocrystalline Ti films using DC sputtering have also been deposited as barrier coatings on the TiNi shape memory alloys that are used in bio-implants. It is known that Ni can leach out into biological tissues and cause damage. Therefore, applying a strong adhesive barrier coating can prevent this [102].

In summary, polycrystalline and nanocrystalline thin films for titanium are of a great interest for many applications and therefore we discuss in detail the influence of several deposition parameters on film microstructure in Section 4.1 and Section 4.2.

### 2.3.2 Epitaxial and single crystalline films

Highly epitaxial films tend towards single-crystal-like behaviour, which is of great interest especially for next-generation nano- and power electronics, optical and magnetic devices. Due to the allotropic transition, solidification from the melt is not a viable way to obtain SC Ti. For applications such as coating medical devices with Ti to improve their bio-compatibility and wear resistance, epitaxial films to obtain a SC surface is highly attractive [107].

As discussed earlier, due to the surface energy anisotropy of Ti, it is prone to form a highly textured/ orientated films. When the right substrate and deposition conditions are provided, it is expected that Ti would form single crystals. The same has been observed in numerous occasions using many deposition methods and on various substrates [104, 118–121]. Although the (0002) plane of Ti has the lowest surface energy, making it the dominant surface plane, Ti films have been reported to grow with at least six other surface plane orientations [122]. High quality SC of Ti in six distinct orientations were obtained on substrates that are chemically similar but

different in geometry. The six orientations were (0001) basal plane, the (11 $\bar{2}$ 0) slip plane perpendicular to it, and the prismatic planes, (10 $\bar{1}$ l), where  $l = 0, 1, 2, 3$  [99]. A good 2D-registry between Ti (10 $\bar{1}$ 3) and Mo (211), and similarly Ti (10 $\bar{1}$ 0) and Ta (211) result in epitaxial growth. In both cases the high quality bcc metals were first grown on sapphire substrates. In a similar manner other epitaxial growths can simply be explained by 2D-registry. In another similar metal-on-metal deposition, Ti thin films were deposited on (111) Cu and (111) Pt that were grown on (111) single crystal Si [123]. Similarly, strongly textured (0001) Ti films have also been reported to grow on (111) textured Al thin films [124].

Sapphire is a good choice as a substrate for depositing epitaxial thin films due to its hexagonal symmetry [104, 125]. Single crystalline Ti on sapphire was first reported by O'Neal *et al.* on c-plane sapphire at 200–400°C by e-beam evaporation. They concluded that even at higher temperatures r-plane sapphire is not conducive of single crystalline growth. Similarly, Dehm *et al.* deposited Ti on c-plane sapphire and a Ti film having Cu interlayer (Ti/Cu/Al<sub>2</sub>O<sub>3</sub>) to investigate the growth behaviour. They obtained films of near single crystal quality and reported the orientation relationship. They observed atomically smooth interface between Ti and sapphire and reported no reaction layer at the interface [126]. However, in another study for a different orientation of sapphire, the interface reaction between (1 $\bar{1}$ 02) plane of sapphire and Ti film was studied using photo-emission spectroscopy to reveal that Ti reacts with oxygen in the sapphire to form Ti-O bond and reduce Al<sup>3+</sup> to metallic Al [127].

Epitaxial Ti films have also been reported on mica [128]. Mica has often been used due to its hexagonal surface plane that can be readily cleaved to obtain a fresh unexposed surface. Superconductive properties of epitaxial Ti films have been studied to show that films with very low thickness can be contaminated with impurities arising from mica resulting in higher resistivity than thicker films. But, promising low resistivity values for SC Ti films have been reported [129]. Epitaxial Ti thin films have also been reported on thermally oxidised Si wafers having (0002) orientation. The orientation could be modified to develop a fiber texture of (10 $\bar{1}$ 0) prismatic or (10 $\bar{1}$ 1) pyramidal planes by varying the Ar pressure during DC sputtering [130]. In summary, a large amount of study on epitaxial growth of Ti on various substrates has been carried on. Apart from the film microstructure, many properties of the films like hydrogen storage capacity, improved corrosion resistance and resistivity have been studied. But a better understanding of the mechanisms of epitaxial growth and combinations of other substrates and deposition parameters are yet to be explored.

## 2.4 Grain boundaries

### 2.4.1 Description and role of grain boundaries in materials

A grain boundary (GB) is the interface region that separates two crystallites that are oriented differently but have the same lattice parameters and chemistry [4]. The role of GBs in materials was felt even before we knew that they were present in crystalline materials. In nineteenth century, material failure due to embrittlement led to modifications in the ore refinement and casting methods. It was later understood that GB segregation was the culprit. Over the last century, GBs have risen to great importance in all of material science. We now know that GBs influence all properties of material such as mechanical, electrical, and chemical [3]. Basically, understanding of GBs is essential in mitigating most of the engineering challenges related to crystalline materials. The emergence of nanocrystalline materials that have a large volume fraction made of GBs has made GB research even more important.

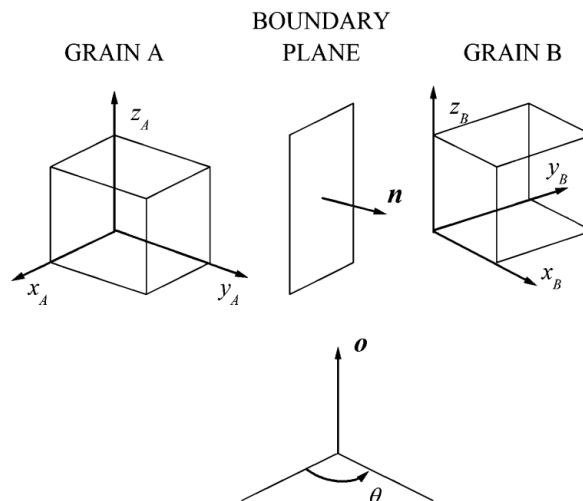


**Figure 2.8** The five macroscopic degrees of freedom that stem from the misorientation between the grains (the angle and axis of rotation) and the GB plane. Taken from [4]

Any GB can be uniquely defined by specifying the GB plane and the misorientation of the abutting grains, as shown in Fig. 2.8 [4]. The GB plane (or any plane) is defined by its normal that needs two parameters to uniquely define it. We require another three parameters to define the misorientation between grains that can be expressed in many equivalent ways. One way is to define the angle and axis of rotation, commonly written as  $[uvw]/\theta$ . The same can also be described in the form of misorientation matrix, Euler angles, Rodrigues vector or quaternions [3]. The GB plane normal and the



misorientation form the five macroscopic degrees of freedom required to define a GB. Using them a GB can be formally denoted as  $\theta^\circ[h_0k_0l_0]/(h_ak_al_a)(h_bk_b l_b)$ , where 'a' and 'b' indicate the two grains. Additionally, the two grains can perform rigid translation along and perpendicular to the GB plane, giving rise to three microscopic degrees of freedom. The lateral shift in position of a GB while maintaining the misorientation between the grains is the ninth parameter that can modify the nature of the GB. The microscopic parameters are not independent of the macroscopic parameters [3]. The relaxation of GBs often leads to cusps in the GB energy vs misorientation plots. This limits the choice of microscopic parameters that a GB can adapt.

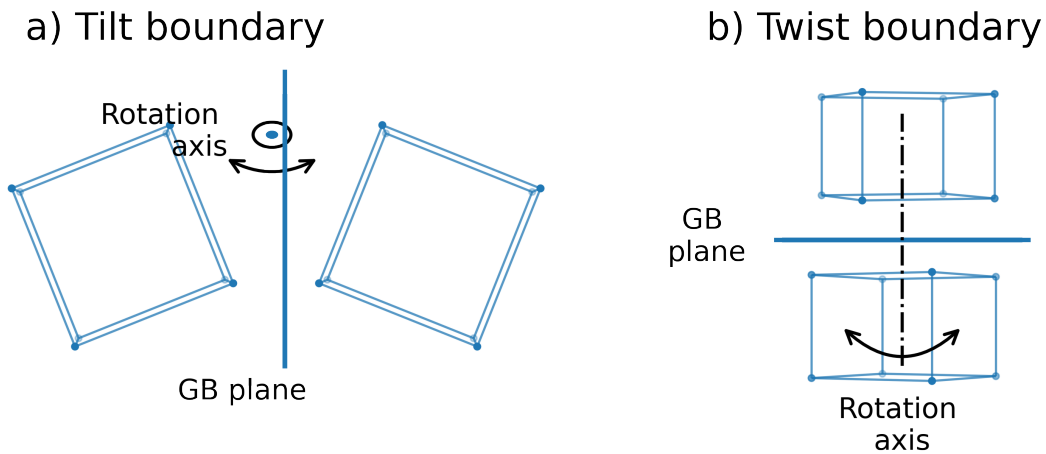


**Figure 2.9** Tilt and twist GB are defined by the rotation axis being perpendicular and parallel to the GB plane normal, respectively.

GBs can be classified in many ways based on these parameters. As shown in Fig. 2.9, if the GB plane normal is parallel to the axis of rotation it is called a twist GB, while if it is perpendicular it is called a tilt GB. A tilt GB needs four degrees of freedom and twist needs three. A low-angle GB (LAGB) is one in which the angle of misorientation is less than  $\sim 15$  degrees, while the rest are high angle GBs [4]. When the GB plane for both grains is the same, the grain is said to be symmetric. And when the GB planes vary for each of the grain, the GB is called asymmetric. Apart from these, in the literature there are also two common terminologies that are used with respect to defining GBs, general/random GBs and special GBs. Any high angle GB having low energy or having a peculiar property distinct from its neighbours have been loosely termed as *special GBs* [3, 4]. The massive parameter space of the GBs makes their complete characterization challenging. Two GBs may share four of the five macroscopic parameters, with one variable resulting in radically distinct properties. Therefore, unless all

the GB parameters are characterized, attributing material properties to specific GB types can lead to erroneous conclusions and is often observed in the literature.

### 2.4.2 Coincident site lattice theory

For a certain misorientation between two grains, the lattice sites are positioned such that when the two lattices are superimposed, they lead to several coinciding points. The periodically arranged coinciding points create a unit-cell of their own which is termed as coincident site lattice (CSL). The CSL theory was introduced mathematically in as early as 1948 [131] albeit with no relation to interfaces. They tried to give an equation for how cubic lattices can be rotated around a certain axis to obtain coincident points, and called them 'cubic tessellations'. In the following year, it was suggested that such coincidence in lattices might be responsible for secondary recrystallization texture in copper [132]. Although they did not introduce a 'sigma' value yet, they presented that based on different rotation angles along [001] axis, the size of the CSL varies and called them *special GBs*. Dunn [133] present detailed tables of all possible CSLs for cubic system with  $\langle 001 \rangle$ ,  $\langle 110 \rangle$  and  $\langle 111 \rangle$  tilt axis. Within the next years, physical phenomenon like GB migration in lead [134] and GB structure of diamond [135] were explained using CSL lattice theory. The Greek letter,  $\Sigma$  is used to denote the ratio of the volume of the coincidence unit-cell to the primitive crystal unit cell.

$$\Sigma = \frac{\text{Volume of coincidence unit-cell}}{\text{Volume of primitive crystal unit-cell}} \quad (2.4)$$

Brandon et al. in a series of seminal papers [136–138], expanded the CSL theory to include not only the misorientation of mathematically exact coincidence angles but also its nearby orientations. They proposed that a GB that deviates from the exact CSL misorientation will still act as a CSL GB with additional dislocations superimposed on the underlying CSL to compensate for the deviation. The GB energy hence is a sum of the CSL GB energy, the energy from dislocations and the interaction of the two. They also predicted that in a CSL GB, the selection of GB plane would be such that the GB plane contains highest density of coincident sites. If the GB plane deviates from this, it would form a stepped structure made of ledges and dislocations. The so-called *Brandon criterion* is used to determine the deviation ( $\Delta\theta$ ) from exact-CSL misorientation for a GB to belong to a certain CSL.

$$\Delta\theta = \frac{15^\circ}{\sqrt{\Sigma}} \quad (2.5)$$

From the Eq. (2.5), when  $\Sigma$  is 1, the accepted deviation is 15 degrees which is the upper-limit of LAGBs. With increasing size of the coincidence lattice and increasing  $\Sigma$  value, the  $\Delta\theta$  reduces. Although there is no theoretical upper limit to the  $\Sigma$  value, in practice, there is limited utility in defining CSL GBs with  $\Sigma$  larger than 100. The ease and simplicity of CSL theory has since then led to an ever increasing volume of work in relating properties of materials with CSL GBs. Fully automated routines to identify the CSL GBs using electron backscatter diffraction (EBSD) in an SEM has invited non-crystallography community as well to classify GBs into *special and random*. The question however is, if the  $\Sigma$  value has a significance other than being just a short hand notation. Several bicrystals with specific CSL misorientation have been explored to better understand this. The inter-granular corrosion tests have shown that low  $\Sigma$  GBs are less susceptible to corrosion compared to random GBs [139, 140]. A significant improvement in arresting the crack growth during high cycle fatigue tests was observed in a nickel based superalloy with increased population of special GBs [141]. Creep in austenitic and ferritic-martensitic alloys has been demonstrated to be dependent on the CSL fraction and can be explained by a boundary's capacity to absorb lattice dislocations [142]. Creep test performed at  $0.6 T_m$  in polycrystalline copper exhibited preferential damage occurring on random GBs as opposed to special GBs [143]. Besides the value of  $\Sigma$ , their spacial distribution has an influence [144].

There have been several efforts to obtain desired GBs in engineering materials by modifying processing parameters to improve material properties in what is called as *GB engineering* (GBE) [145]. The relationship between thermomechanical treatment parameters and a high fraction of  $\Sigma 3^n$  GBs have been shown [146]. They demonstrate how a  $\Sigma 27$  decomposes into a  $\Sigma 3$  and a  $\Sigma 9$ . In another region, a  $\Sigma 51$  decomposes into  $\Sigma 3$  and a  $\Sigma 17_b$  and  $\Sigma 87$  decomposes into  $\Sigma 3$  and  $\Sigma 29$  [146]. Straining and annealing cycles to increase the percentage of special GBs has also been shown in copper, austenitic stainless steel and nickel alloys [147]. One of the main aims of such studies has been to break the network of random GBs by introducing special GBs between them. However, as noted already by Brandon in 1966, it is the boundary coincidence that is expected to influence the properties more than mere lattice coincidence. It appears that the field of GBE has consistently overlooked this over the years [148].

Criticizing the practice of calling every CSL GB as a special GB, Wolf pointed out that while energy cusps are present for  $\Sigma 3 \langle 111 \rangle$  and  $\Sigma 11 \langle 311 \rangle$ , no cusps in energy are seen in  $\Sigma 3 \langle 211 \rangle$ ,  $\Sigma 9 \langle 211 \rangle$  and  $\Sigma 9 \langle 114 \rangle$  CSL GBs. They argued that  $\Sigma$  value of CSL is a purely volumetric concept, whereas interplanar spacing of the GB plane ( $d_{h,k,l}$ ) is a planar quantity and might strongly affect the interfacial properties. In an unrelaxed

bicrystal, it is the  $d_{h,k,l}$  that determines how close the atoms from the either side of the interface come to each other. According to Pauli's exclusion principle, when two atoms come closer than their equilibrium spacing the energy increases exponentially. Clearly, the GB plane that have the largest interplanar spacing will be preferred in such situations. While the misorientation and therefore the  $\Sigma$  value remains the same, only certain GB planes will lead to energy cusps and others will not. Since the above conclusion stems from atomic interactions, it is true for all kinds of interfaces, may it be symmetric, asymmetric or a phase boundary. For a symmetric GB, the interplanar spacing would be same as  $d_{h,k,l}$ , and for an asymmetric GB the effective interplanar spacing ( $d_{eff}$ ) can be given by the following equation:

$$d_{eff} = \frac{d_{h_1,k_1,l_1} + d_{h_2,k_2,l_2}}{2} \quad (2.6)$$

From the above discussion, we can enlist some of the parameters that can be used to predict the GBs that could be favoured due to their low energy [3].

1. Small volume of coincidence unit lattice or small  $\Sigma$  number.
2. High planar density of coincidence sites ( $\Gamma$ ).
3. Larger interplanar spacing ( $d_{eff}$ ).

These are overly simplified criteria and neither of them explains in entirety the presence of all the cusps in the energy vs misorientation plots and there are several examples where each of the criteria fails. Sutton and Balluffi [149] discussed this in detail giving several examples of why these simple geometric models are not sufficient for the prediction of preferred GB planes or the GB energy calculations. The high  $\Gamma$  model is particularly flawed because it ignores that while having few lattice sites of good fit, one cannot ignore other atoms that excessively overlap at the interface. These overlapping regions would lead to rigid translation along the interface. They propose that any GB prediction models must include the atomic structure and the nature of local bonding. The inability of these simple models to explain the presence or absence of cusps in the GB energy vs misorientation profiles is the leading motivation behind the present work that deals with our need to understand the GB structure at atomic level.

### Dichromatic pattern and the topological theory

Pond and Bollmann [150] formulated a theory such that bicrystals can be classified based on the point/space group of the component crystals. They stated that understanding of the symmetry of the abutting crystals holds the key to the analysis of GB

structure multiplicity [151]. For this, they introduced the idea of use of dichromatic patterns to simplify the identification of equivalent structures in a bicrystal. They stated that while the bicrystals themselves might have low symmetry, the GB structures can have high symmetry. The symmetry of the dichromatic pattern governs the symmetry of all the possible bicrystals that can be created out of it. Dichromatic pattern was shown to be useful to determine the Burger vector of the interfacial dislocations [150]. The method treats any bicrystalline interface by using the principle of symmetry of composites systems, where the composite comprises of two elements of varying crystal symmetry or orientations. For a phase boundary, where the two grains have different structures, the interface symmetry is an intersection of the two components. This leads to lower symmetry, called dissymmetrization. Because the crystal symmetry is same on both sides of a GB, its symmetry is higher than the intersection of the two grains [150]. This addition of new symmetry elements is termed as symmetrization. Pond and Vlachavas [151] further discussed that the summation or intersection of the symmetry of the two composite elements is not enough to predict the symmetry of the interface for non-holosymmetric and non-symmorphic structures. However, because our present study involves only hcp GBs, a dichromatic pattern is sufficient to determine the interface defect content.

It has been noted that although first-order phase transitions in GBs are of interest, it is necessary to use topological theory that links the observed structure and GB properties to the defect nature of the GB [152]. The goal of topological theory is to start with creations of the highest degree of symmetry and then take subsequent symmetry breaking into account when constructing real structures [153]. The circuit is formulated by fixing the crystals and transporting a hypothetical observer on an excursion through the crystal based on the symmetry operations. An arbitrary origin can be chosen based on the convenience. Because the movement is based on the symmetry operations, every stop for the observer appears to be an identical location [154]. In a dichromatic pattern, the symmetry operations that relate atoms of a given colour to another atom of the same colour are called 'ordinary operations'. The operations that relate two atoms of different colours are referred to as 'anti-symmetry operations' [151]. Using these two kinds of operations, a circuit can be drawn on an experimental image and the same can be mapped on the dichromatic pattern to measure the defect content inside of the circuit. The dichromatic constructions serve as perfect reference lattices for circuit operations to not only identify primary but also secondary interface defects. This methodology to investigate the GB structures has been frequently employed for materials of all crystal structures [153, 155]. In the following, we extensively

refer to this methodology when applied to ZnO and GaN, both of which have wurtzite structure [156, 157].

### 2.4.3 Grain boundary atomic structure

When two materials with a periodic structure are brought together, the interface can naively be expected to have a certain structure as well. However, about a century ago, when materials were understood to be crystalline by XRD, it was predicted that the interfaces are likely amorphous [158]. Later, Mott in his seminal paper suggested that GBs should only be a region of two crystalline surfaces meeting as best as they could given their orientation difference, but not be amorphous. To conclude this, he calculated the intercrystalline slip velocity for aluminium with and without the amorphous layer impeding the slip [159]. Read and Shockley determined the GB energy assuming that they are made of arrays of dislocations and converged to the experimentally measured values [160]. Fig. 2.10 shows a misorientation vs GB energy plot, adapted from [160], that was the first of its kind to isolate one the GB parameters. It is interesting to note that although they assumed the GBs to be exclusively made of dislocations they found cusps in their plot. The imagined that the cusps represent the regions of good fit from both the lattices. Therefore, the very nature of how we came to understand the crystalline nature of GBs gives us an insight that GBs massively influence mechanical and chemical properties of materials.

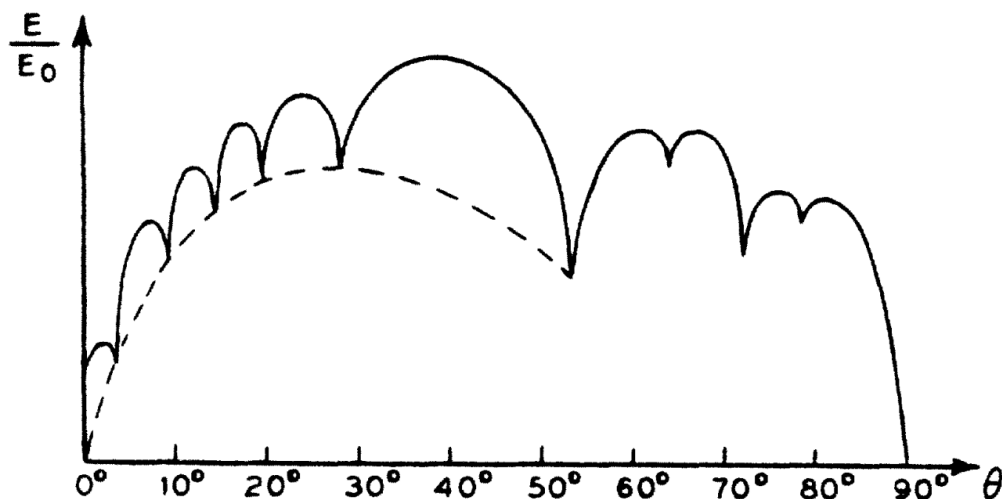


**Figure 2.10** The first report on the dependence of grain boundary energy on the misorientation angle for any cubic lattice with arbitrary lattice parameters. Taken from [160].

Weinberg in his 1959 review of GBs mentioned that LAGBs appear to have structure that breaks down above  $\sim 15^\circ$  of misorientation angle [161]. He predicted that GBs might be disordered at higher angles. However, Bishop *et al.* showed that high-angle symmetrical tilt GBs are not disordered, but can be described as a two-dimensional array of coincidence atoms or ledges or dislocations or their combination in the GB plane [162]. This idea was modified by Chalmers by stating that the low-energy in GB need not necessarily stem from coincident sites. Using computer simulations, they minimised the GB energy by allowing rigid translation of the grains along the GB plane. The two coinciding lattices were considered as an arbitrary starting configuration. The translation led to small periodic units along the length of the GB. They concluded that the physical criterion for the special properties of coincidence GBs is not coincidence per se but the small, periodically repeating units of the structure [163]. They also predicted that GBs that depart away from the exact coincidence orientation result in having 'mixing' of units that correspond to the neighbouring coincidence orientations. Promptly, using pairwise central force interaction between the atoms (computer simulations), several periodic units were shown that form symmetric tilt GBs in copper with a tilt axis of [100] and [111] [164]. Similar molecular statics simulations revealed that in aluminium, many low energy structures may be obtained for the same GB [165]. Because the intermediate misorientations are a mixture of the two preferred GBs, it was hypothesised that there could be multiple metastable *mixture-states* of GB [5]. This observation was overlooked and is discussed in the following section.

In a series of papers from Sutton *et al.*, atomistic calculations of the structures of symmetric and asymmetric tilt boundaries in aluminium and copper were performed [166, 167]. They coined the use of the term 'structural units' (SUs) to define the building blocks of GBs. They demonstrated that certain preferred boundaries are made up of a contiguous sequence of fundamental units of a single kind. These units are assumed to be their ideal or the 'undistorted' state. When the misorientation is changed, secondary GB dislocations can help in accommodating the favoured units in the non-favoured boundaries. However, the favoured boundary units are expected to be distorted in these non-favoured GBs. By varying the angle of misorientation, they observed the change in structure of the boundary from one favoured to the next. Regarding CSL theory, they also determined that in symmetrical tilt boundaries, favoured boundaries are not always associated with low  $\Sigma$  values. As a corollary, it was proven that CSL is a geometrical concept and that not all CSL GBs necessarily result in special properties. Furthermore, they observed that for the same GB and the same crystal structure, different GB structures could be obtained. Therefore, the GB structure was found to depend on the inter-atomic potentials and not just on the geometry.

When considering the symmetric GBs, the number of macroscopic degrees of freedom reduces from 5 to 3. A vast majority of the symmetric GBs are twist boundaries and an infinitely small subset of them ( $180^\circ/m$  symmetry) are tilt boundaries. However, from experiments we know that an abundance of tilt GBs are present in materials. Using the embedded-atom-method (EAM) potentials it was shown that it is the GB energy that plays a vital role in determining the selection of specific twist GBs that can also be defined as tilt GBs [168]. It was reasserted that the cusps in the GB energy plots arise from the small unit cells in the GB plane.

### Experimental observation of grain boundary structures

As seen in the above section, 1980s saw a great increase in the theoretical understanding of the GB atomic structures. With the development of high-voltage electron microscopes operating at 1250 keV, the imaging resolution necessary for lattice imaging was nearly achieved. Initially, ceramics or oxides with large lattice parameters were investigated. The first direct determination of the structure of a high-angle tilt GB was a Ge GB viewed end-on on a [011] zone axis [169]. Soon after, the first atomic resolution image of a GB in metal was published for the Au film deposited on the NaCl substrate [170].

Subsequently, a number of similar studies were carried out mainly on copper, gold, and aluminium [171–176]. Fig. 2.11 shows two sample GB atomic structures out of many that were investigated during this period. The common theme observed in all of these experiments was that they were all carried out on bicrystalline specimens. In most cases the bicrystallinity was obtained by thin films deposition on NaCl substrate of varying orientations and intermediate layers. The authors stressed on two major inadequacies that: a) obtaining bicrystalline samples of desired GBs is challenging and b) only tilt GBs can be investigated.

Vitek *et al.* proposed multiple possible structures for the same GB using computer simulations [5]. The same was attempted to be verified experimentally, but with no success. The authors reported that only one stable GB structure was observed [177].

EAM calculations predicted two possible structures of  $\Sigma 3$  112 twins in aluminium [178]. However, only the higher-energy structure of the two predicted structures was experimentally observed [176]. The two structures varied in the rigid body translation along the GB. The observed segment with higher energy structure was bound by a 111 twin disabling the rigid body translation. It was noted that if the observed segment was not bound by another GB, the low-energy structure could also have been observed, which would indicate that the structure of a GB depends not only on the parameters that define the GB but also on other GBs that it is bounded by.



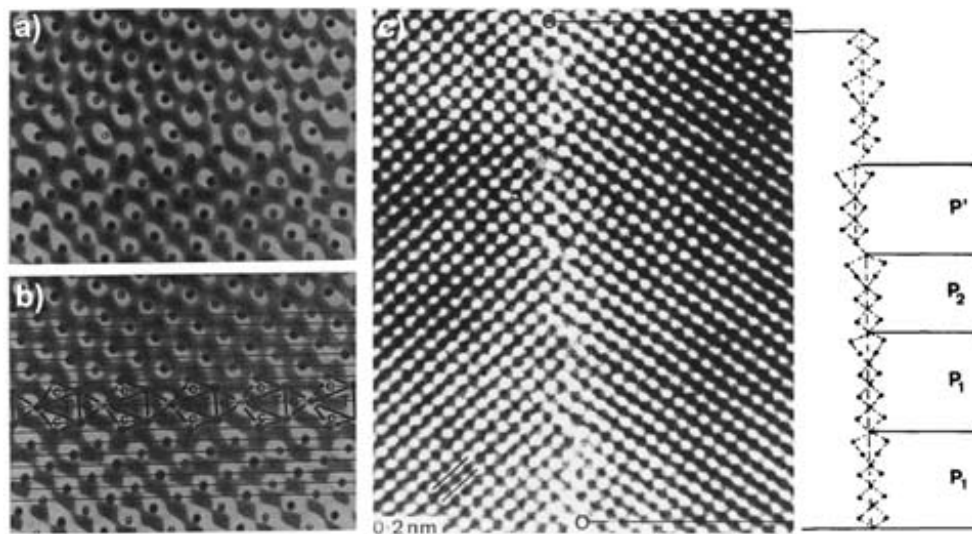


**Figure 2.11** a) b) The structure of a  $\Sigma 19[110]$  (311) gold GBs that shows repeating periodic units that match with the structure predicted using EAM potential [172]. c) Tilt GB in molybdenum that has a misorientation of  $\sim 13^\circ$ . As expected from the SUM, the GB appears to be a mixture of  $\Sigma 25$  and  $\Sigma 41$  that are the two favoured GBs that it is bounded by [175].

Mills *et al.* observed the coexistence of two GB phases in  $\Sigma 11$  [011] ( $2\bar{2}1$ ) GB in Au, a notable achievement in the increasing understanding of GBs in the 90s [179]. Good agreement was observed between the experimentally observed images and the ones simulated using the EAM potential. Rigid body translation parallel to the GB as well as local atomic relaxations were observed to match between experiments and simulation. GB excess energy was calculated using the EAM potential, and the GB excess volume was measured using the experimental images for multiple low  $\Sigma$  GBs. The higher GB energy corresponded to a larger excess volume. This meant that a larger deviation from the atomic arrangement inside the grain leads to higher energy, which one would intuitively expect. A summary of the observed GB structures using HRTEM and their comparison with the simulated structures was provided by [180]. The introduction of HRTEM led to direct experimental observation of GB-related phenomena such as multiple structures, GB dissociation, faceting, microfaceting, and their relation to GB energy, GB constraints, defects, and steps in GBs, misfit localisation, the role of stacking faults in GB relaxations in fcc metals, the misorientation dependence of atomic structures in CSL and incommensurate GBs [181]. HRTEM also revealed a general propensity to build atomically well-matched structures with strong coherency across the interface. As a result, the majority of reported structures in fcc systems were linked by the trend to maximize the GB volume (length) that is well-coordinated atomically at the expense of localized misfit patches. This was observed not just in symmetric GBs but also in asymmetric and incommensurate GBs [180].

As discussed in detail in Section 2.5, with the introduction of FEGs that quickly replaced thermionic sources in most of the instruments, the coherency and the obtainable current in an electron probe improved. It was noted that the main advantage of ADF imaging over HRTEM is the ability to acquire rapid, immediately interpretable pictures of grain boundary or defect structures thanks to improved chemical sensitivity and lower susceptibility to instrumental and scattering errors [182]. They also pointed out that studying the GB structure using STEM instead of TEM gives the advantage of collecting electron energy loss spectroscopy (EELS) signal. This can be used to map light elements but also find the bonding characteristics. A change in bond length shifts the core energy loss signal. Such detailed information on change in band gaps due to bonding changes at the GB region can be used to relate the GB properties such as intergranular cracking or diffusion with the observed structure. For example, in a Ni-23at.% Si alloy, EELS was used to observe the change in the bonding nature at GB. Ni enrichment was found in the GB region. The d bands of Ni at Ni-rich GBs were smaller than those in the bulk, indicating less hybridization and bonding at the GBs than in the bulk [183]. In Ni-Al alloy, addition of boron was shown using EELS to change the bonding nature at GB similar to the bulk, and thereby enhancing the GB cohesive strength and improving the fracture properties [184]. Many similar investigations combined the power of STEM imaging and EELS/ EDS to relate the structure and properties of the GB at atomic scale [185].

Many studies were also performed on the structural analysis of the GBs using aberration corrected STEM imaging. STEM annular bright field (ABF) imaging was used to observe the GB atomic structure in MgO  $\Sigma 5$  (410) GB [186]. Coexistence of multiple SUs in the same GB was observed using HAADF-STEM imaging in  $\Sigma 19b$  [111] GBs of Cu [8]. Multiple GB phases have also been reported in TiO<sub>2</sub> (001)/(100) GB [187]. The authors suggested a first-order phase transition between the three coexisting GB phases. The same group has reported several observations of GB phase transitions in ceramics upon segregation [188–190]. In another study, Ag segregation induced nano-faceting in Cu was also observed with HAADF-STEM imaging [191]. Misorientation dependence of the structure and Cu segregation to Al  $\langle 111 \rangle$  GBs has been recently investigated [192]. A direct observation of GB migration in Al<sub>2</sub>O<sub>3</sub> was recently reported [193]. The authors observed a change in GB structural arrangement that facilitates the GB mobility. Overall, there is a rapidly increasing volume of work in using STEM to investigate structure and structural transitions in GBs.

Similar progress has also been made on the computational/ simulation front to complement the experimental techniques. In a molecular statics study of 125 symmetric tilt GBs (STGB) in Fe, H was introduced into the GB to study the influence of GB plane

and structure of H-embrittlement. The segregation and embrittlement were found to be controlled by competing interactions between the GB structures, the H-defect interactions, and the H location in the GB. A strong correlation between the GB character and the saturation limit of H was observed [194]. Asymmetric tilt GBs in Al have been shown to facet into STGBs as well [195]. First-order phase transition has been observed in a Ni-doped Mo asymmetric GBs transitioning into two variants of bi-layer adsorption of Ni. [196]. Segregation induced GB transitions have also been modelled on Cu-Zr GBs. It was shown that based on the initial GB structure, the arrangement of solute/ dopant can vary [197]. A summary on the role of GB phase transitions on GB mobility using MD simulations was provided by Mishin *et al.* [198]. Segregation of Mg on various Al GBs was studied using Monte Carlo - Molecular dynamics (MC-MD) combination to reveal a strong dependence of segregation on the kind of GB [199]. In summary, there is a very vastly growing literature on the fast developing techniques to simulate various GB properties. However, the experimental validation to the computer simulations is still lacking in most cases.

It is expected that lower symmetry might lead to more complicated SUs. Campbell *et al.* observed  $\Sigma 5$  (310) [110] GB in molybdenum (Mo), which has bcc crystal structure, using HRTEM [200, 201]. They observed the simulated structures to agree well with experimentally observed low-energy structures using angular-force interatomic potentials developed from model generalized pseudopotential theory (MGPT). They found disagreement of the structure with predictions based on radial-force potentials, such as EAM potentials. MGPT accounted for many-body angular forces through explicit three- and four-body potentials. The modified analytic EAM potentials, that are used nowadays, take this into account and are extensively used for lower symmetry elements. The key take away based on the requirement to use modified potentials for 'non-fcc' materials is that their GB structure simulations are more elaborate than fcc elements [202].

### Grain boundaries in hcp materials

The literature for GB structures of materials with non-cubic symmetry is relatively scarce compared to cubic. However, there is still a wealth of research on hcp GBs that is intended to be summarized here, with a focus on atomic structure of hcp GBs.

As pointed out by Bruggeman [203], for hcp materials, a perfect CSL lattice can only be formed for a rotation along [0001] axis unless  $c^2/a^2$  is a rational fraction which would also result in CSLs. For real materials this is seldomly true. Any deviation from

the rational fraction would mean additional strain on the lattice to accommodate the mismatch. This imposition of small strain on materials having near CSL interfaces has been termed as constrained CSL (CCSL) model. Any additional deviation from the ideal CCSL misorientation can be also accommodated by the DSC dislocations [203]. Chen and King provided an extensive list of all the possible CCSLs upto  $\Sigma 50$  in hcp system [204]. They also prepared zinc bicrystals and examined an exact-CSL and seven CCSL GBs. They found that all the secondary dislocations in the GB followed the theoretically expected DSC vectors.

However, in a critical reassessment of the model, MacLaren *et al.* pointed out certain key weaknesses. It was established that the interfacial dislocations anticipated by the CCSL technique were only roughly comparable to those that would separate interface regions for the same crystallographic parameters [205]. They formed extensive calculations to derive that the long-range strain induced in the grains due to CCSL cannot be relieved by dislocation arrays unless the material is nanocrystalline. A vicinal high angle GB of mixed tilt-twist character was investigated in a deformed and annealed pure Ti using TEM [206]. They showed that the reference structure predicted by CCSL is not experimentally observed. Instead a 2D periodic arrangement of common  $(0\bar{1}11)$  planes at the interface nearly represents the observed structure. They suggested that a more appropriate approach to the geometrical modelling of vicinal HAGBs is to consider the high planar density of coincident sites ( $\Gamma$ ) planes as the GBs. Others have emphasized that this criterion is only pure geometric and is insufficient [167]. Therefore, the CCSL approach to explain the hcp GBs remains unsettled.

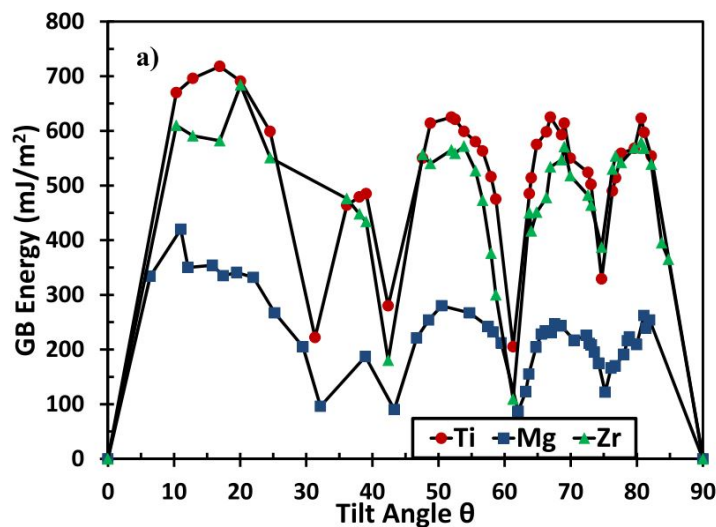


**Figure 2.12** A plot of the change in GB energy calculated using MD for changing tilt angles in Ti, Mg and Zr. Taken from [207].

While the earlier discussion was emphasized on the arrangement of primary and secondary dislocations at the hcp GBs, there were simultaneous theoretical developments to explain the hcp GBs using the SUM. EAM simulations were presented for the symmetric  $[1\bar{1}00]$  tilt GBs in Ti and Co. Both of them were shown to have similar structural units although their energies varied by a factor of 2 [208]. As seen in Fig. 2.12, for the  $[11\bar{2}0]$  tilt axis, the GB energy is shown to vary in a similar manner for most hcp metals (Ti, Zr and Mg) using MD simulations [207]. Furthermore, for hcp CSL GBs, if the GB plane (the plane with the largest  $\Gamma$  value) remains the same, changing the  $c/a$  ratio changes the  $\Sigma$  value but the GB structure remains the same. This is similar to how the direction perpendicular to the twin plane has no effect on the twin structure [208]. Concerning the debate on constriction of CSLs in hcp, it was shown using the SUM that similar to cubic, hcp GBs also follow the SUM where a GB may contain another structural unit as a 'defect' in order to accommodate any deviation from either the exact disorientation angle or the  $c/a$  ratio. Also, the structural units were shown to be independent of the interatomic potential used for  $[11\bar{2}1]$  tilt GBs [209]. Atomic structure of a host of symmetric tilt GBs having  $[11\bar{2}0]$  tilt axis were reported by Wang *et al.* [210]. Four minimum energy GB planes were identified and all of them could be explained using the SUM. As one would expect, other GBs that deviated from these planes were observed to have periodic array of DSC dislocations [210]. Enlisted below, a wealth of literature exists on twins in hcp [108, 153], however more work is needed on other GBs.

A significant work on the hcp GBs are on ionic crystals. Due to the ionic nature of the bonding, the GBs in ceramics are more complicated than in metals. The charge neutrality and charge transfers also acts as an additional parameter in determination of the GB structure. Nevertheless, they lead to exciting insights on what can be expected on metallic GBs at least in terms of similarity in close-packing.

Apart from being commercially important, the relative ease of manufacturing and their low beam sensitivity, sapphire and ZnO GBs have been extensively studied. The low beam sensitivity was especially important for the 1.25 MeV microscopes that were used for the early HRTEM work. The advancement in STEM imaging and atomistic simulations of GB structures has lead to a much better understanding of hcp GBs in the recent years. Table 2.2 enlists the literature in a chronological order to show the evolution of our knowledge and improved understanding of hcp GBs.

**Table 2.2** Studies on hcp grain boundary atomic structure grouped by the material and the chronological order.

Material	Grain boundary	Key results	Ref.
Ti	$\{10\bar{1}1\}$ , $\{11\bar{2}1\}$ and $\{11\bar{2}2\}$ twins	Using computer simulations, atomic structure of most frequently observed twin boundaries was studied for the first time. The translation/shuffle required to obtain the equilibrium twin structures is obtained.	[211]
Zinc	high angle CCSL GBs	Experimental evidence of dislocation structure at high angle GBs. 8 different high angle constrained CSL (CCSL) GBs are observed. The theoretical dislocation spacing is correlated with the experimental measurements.	[212]
$\alpha$ - Al <sub>2</sub> O <sub>3</sub>	$\{10\bar{1}n\}$ n = 0, 1, and 4	Static-lattice calculations of the energies and GB structures. HRTEM images are seen to compare favourably with simulated images for the first time in sapphire.	[213]
$\alpha$ - Al <sub>2</sub> O <sub>3</sub>	$\Sigma 7 [0\bar{1}11] \{1\bar{1}02\}$	Four possible unrelaxed CCSL GB structures are investigated. A DSC dislocation of pure-edge character is identified in the GB. Al-O bonds in the GB core are observed to be elongated.	[214]
ZnO bicrystals	Asymmetric [0001] $\Sigma 31$ & $\Sigma 13$	Periodic SUs are observed in the $\Sigma 31$ GB. Extensive faceting of asymmetric $\Sigma 13$ GB into symmetric $(\bar{2}7\bar{5}0)$ and $(13\bar{4}0)$ Circuit mapping was used to identify the burgers vector at the interface.	[215]

$\alpha$ - $\text{Al}_2\text{O}_3$	$\Sigma 7 [0\bar{1}11] \{1\bar{1}02\}$ 180° tilt GB	GB structure is determined such that the two oxygen terminated (01 $\bar{1}2$ ) planes are joined together. Displacement parallel to the GB is determined using simple geometry. Displacement vertical to the GB is determined by calculating net charge and bond overlap population.	[216]
GaN on sapphire	$\Sigma 7, \Sigma 19 [0001]$ STGBs	Topological analysis is carried out to measure defect content at the interface. All CSL GBs are observed to have a pure edge-like character. SUs are observed with 5/7 or -8 atomic units instead of 6 at the interface.	[156]
$\alpha - \text{Al}_2\text{O}_3$	$\Sigma 7 [0001] \{1\bar{1}02\}$	GBs with same $\Sigma$ having varying GB planes. Symmetric structure with respect to GB plane.	[217]
	$\Sigma 7 [0001] \{1\bar{1}02\}$	The asymmetric structure which includes an atomic translation along the GB. HRTEM images were consistent with the static lattice calculations.	
	$\Sigma 7 [0001] \{1\bar{1}02\}$	Asymmetric structure. Contains a large open space at the GB. Different thermal grooving behaviour within the same CSL sigma value indicates the role of the GB plane in GB energy determination.	
$\alpha$ - $\text{Al}_2\text{O}_3$	$\Sigma 7 [0001] \{2\bar{3}10\}$	Two different CSL $\Sigma$ values that have identical GB planes. Both the symmetric GBs have asymmetric SUs.	[218]
	$\Sigma 21 [0001] \{2\bar{3}10\}$	Open spaces are noted in the GB core in both the GBs.	

ZnO	$\Sigma 7$ [0001]	$\Sigma 7$ GB consists of multiple SUs that are very similar to the core structures of edge dislocations. Changing GB plane changes the arrangement of SUs from straight to zigzag.	[219]
ZnO	$\Sigma 49$ [0001]	HRTEM used to observe the GB edge-on. Combination of three dislocation-like SUs, "a", "b", and "c" appear. A straight array of a+b+c units effectively relaxes the GB strain.	[220]
ZnO	$\Sigma 7$ and $\Sigma 49$ [0001] with and without Pr doping	The undoped GBs contain SUs that have unusual coordination. I-V measurements made across GB show linear I-V characteristics, while the same across Pr doped GB shows non-linear characteristic. HAADF-STEM image shows periodic segregation of Pr by substituting Zn. Incoherent GBs show higher Pr amount and greater non-linear I-V behaviour.	[221]
Generic hcp	$(11\bar{2}1)$ twin	Ab initio calculations predict the structure of twin boundary. GB energy scales linearly with the second order elastic shear constant ( $c_44$ ).	[222]
Mg-Ti alloy	$\langle 10\bar{1}2 \rangle$ $\{10\bar{1}1\}$ twin boundary	Activation of additional slip systems, $\{10\bar{1}1\}$ $\langle \bar{1}\bar{1}23 \rangle$ , by solute (Ti) segregation to Mg GBs. Ti segregation in nanocrystalline Mg GBs	[223]



Generic hcp	STGB with $[1\bar{2}10]$ tilt axis	MD and interface defect theory are used to study the energy and characteristics of relaxed structures of STGB. All GBs are either ordered or contain a single array of GB dislocations. GB dislocations are different from the bulk dislocations. Four minimum energy coherent STGBs are identified: $(\bar{1}011)$ , $(\bar{1}012)$ , $(\bar{1}013)$ and $(\bar{2}021)$	[210]
Mg	$\{10\bar{1}1\}$ , $\{10\bar{1}2\}$ and $10\bar{1}3$ twins	Periodic solute (Gd and Zn) segregation at twin boundary plane. Segregation to GB even within solubility limit of solute to reduce strain energy.	[224]
Ti, Zr and Mg	#190 STGBs with $[11\bar{2}0]$ tilt axis	Vacancy binding energy for various STGBs is calculated using molecular static simulations. The binding energy is observed to steeply increase with increasing $c/a$ ratio. SUs are observed to significantly change with vacancy absorption.	[207]
Co	$\{10\bar{1}2\}$ twin boundaries	Structure of $10\bar{1}2$ twin boundaries characterized. Twin boundary consists of basal-prismatic interfaces. Dislocation theory based migration mechanism of twins is developed.	[225]
Mg and Ti	$\langle 1\bar{1}00 \rangle$ twin boundary	GB energy as a function of changing tilt angles is calculated using EAM potentials (MD). The difference in $c/a$ ratio between Ti and Mg results in a difference in energy of $11\bar{2}6$ TB	[226]

Mg (generic hcp)	Twin boundaries	Ab initio and MD simulations to predict twin boundary structure. The mechanical instability of glide twins against reflection twins is identified as the reason for why only reflection twins are experimentally observed.	[227]
Mg	78.9° $\langle 10\bar{1}0 \rangle$ $1\bar{2}14$ , 116.9° $\langle 10\bar{1}0 \rangle$ $1\bar{2}12$ , 145.85° $\langle 10\bar{1}0 \rangle$ $1\bar{2}11$	MD calculations prove the validity of the SUM in Mg. A sharp transition in SUs of GB is observed at a certain misorientation angle. Nanofaceting is observed at some GBs near the transition point. Between the angular range of 78.9° and 116.9° the SUM is seen to follow simple lever rule.	[228]
Zr	$\{10\bar{1}1\}$ GB plane	First principle calculations to study solute behaviour at GB. Ag, Bi, Au and Sn embrittle the GB. V, Cr, Nb, Mo, Ta and W strengthen the same GB.	[229]
ZnO	[0001] STGBs	3D-polyhedra that when projected appear as 2D-SUs in STEM imaging are defined. Arrangement of SUs changes around critical point of 32.2° which is a singular GB. A Farey diagram is used to quantitatively predict the spacing between SUs. It is observed that the SUs arrange such that they are maximally spaced from each other.	[230]

Due to the similarity in the geometry, materials with zinc-blend structure have shown SUs that appear similar due to projection. One such important material is GaN, which is commercially used in high-power high-frequency electronic devices. Defects in

such materials strongly influences their properties. Therefore, GBs in GaN were one of the earliest hexagonal materials to be studied extensively. Table 2.3 provides the CSL value for a misorientation along [0001] tilt axis for hcp crystal structure. Evidently, tilt along [0001] axis, does not depend on the  $c/a$  ratio. When GaN is grown on (0001) sapphire, it grows epitaxially but there are often growth defects that result in tilt GBs.

**Table 2.3** CSL misorientations with  $\Sigma < 50$  for grain boundaries with a [0001] rotation axis in the hexagonal system

$\Sigma$ value	Misorientation angle
7	21.79°
13	27.80°
19	13.17°
31	17.90°
37	9.43°
43	15.18°
49	16.43°

An edge dislocation present in the basal plane in a hexagonal system has a Burgers vector of  $1/3 \langle 11\bar{2}0 \rangle$ . Potin *et al.* constructed the possible atomic configurations of dislocation in a basal plane. They concluded that two possible structures can be obtained for the core, either with 8 or 4 atoms. If the dangling bond represented by 'R' is removed, it results in a 5/7 atom structure. Later, they went on to simulate the structures of high angle symmetric GBs, namely  $\Sigma$  7, 19 and 31. They revealed that the GB is made of same units arranged in periodic manner. The SUs were verified both using TEM image simulations and HRTEM [156].

Soon after, Bere *et al.* conducted a similar study on GaN by including all CSL GBs obtainable in a wurtzite (hexagonal, P6<sub>3</sub>mc) using empirical potential of Stillinger-Weber type. They observed that all the investigated tilt GBs are formed by the combination of the above mentioned 8, 4, or 5/7 SUs [232, 233]. They predicted that in other hexagonal structures, especially in pure metals, the change of bond length and bond angle would change the energy smoothly, unlike in GaN, which due to the ionic nature of bonds is more restricted in the choice of bond lengths and angles. Therefore, one might expect to see additional SUs in metallic bonds than in ionic bonded GaN. Quantifying the energy of [0001] tilt GBs in GaN, Chen *et al.* discussed that two types of interfaces should exist in the CSL GBs of wurtzite structure. The edge and the long body diagonal of the CSL unit cell result in lowest GB energy. The resulting delimiting GB structures were shown to have an energy minima, as shown in Fig. 2.14.

Moving a step ahead from the conventional 2-dimensional SUM, the 3-dimensional GB structure of ZnO was recently investigated [230]. A 24° [0001] tilt GB that is

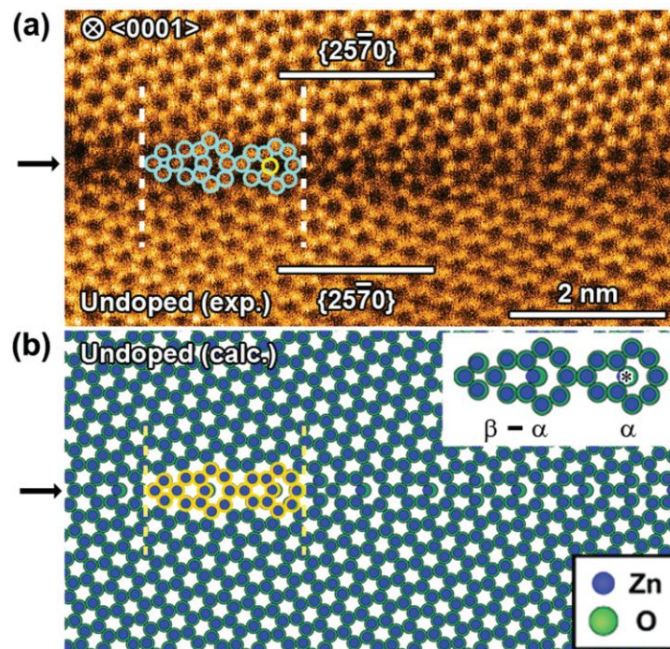


**Figure 2.13** Atomic configuration of  $\Sigma 13$  symmetric tilt GB in ZnO. a) HAADF-STEM image, b) stable structure from first-principles. Taken from [231].

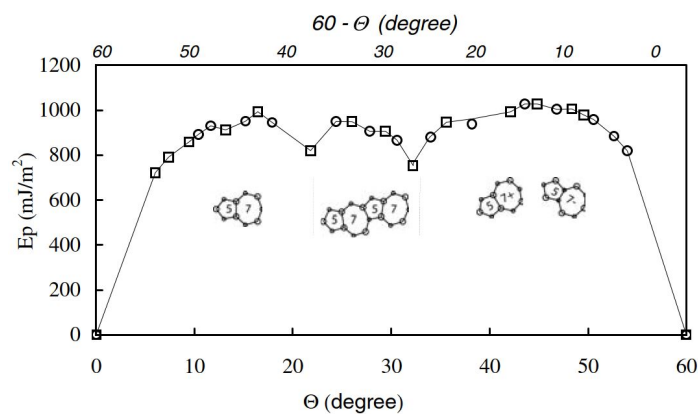


**Figure 2.14** The structural units made of 5,7- atom rings that make the  $[0001]$  wurtzite tilt GBs exhibit two pronounced minima at rotation angles corresponding to  $\Sigma 7$  and 13. Taken from [234].

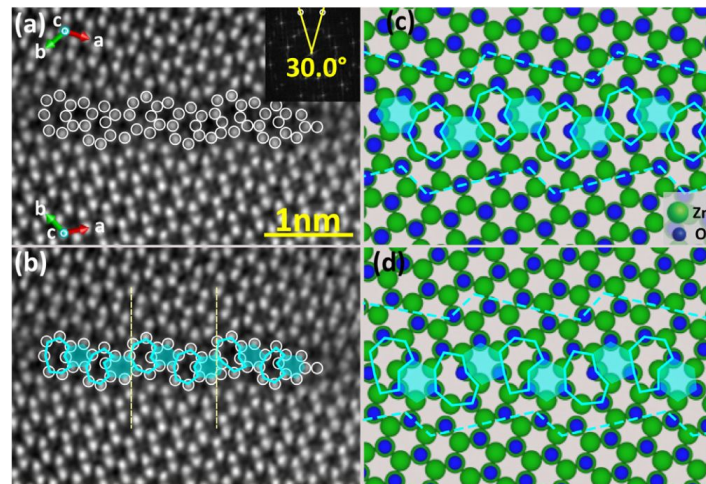


**Figure 2.15** The structural units made of 5,7- atom rings that make the [0001] wurtzite tilt GBs exhibit two pronounced minima at rotation angles corresponding to  $\Sigma 7$  and 13. Taken from [234].

$3.8^\circ$  away from the exact  $\Sigma 13$  CSL misorientation was shown to have structural units similar to the 5,7-atom units reported earlier, as seen in Fig. 2.15. The octagons and hexagons seen in the 2-dimensional projection were shown to be capped trigonal prisms and octahedra, respectively in 3-dimensions.

Striking similarities can be observed in the SUs observed in ZnO, GaN (ionic bond) and Ti (metallic bond) when comparing [232] and [230] with the present work. The same is discussed in greater detail in Section 4.3, where we observe the same 8-, 4-coordinated SUs in  $\Sigma 13$  GB in pure Ti.

## 2.5 Characterization

Materials characterization involves many techniques that are used for the determination of correlation between microstructure and properties of any material. The order of size scale when defining microstructure can vary from millimeters down to atomic scale. The properties that the microstructure is in turn associated with can be anything from mechanical properties like strength and toughness to other functional properties such as resistivity and thermal capacity. In this thesis, the foundation for microstructure determination of hcp GBs at atomic scale is established, although no specific property of the GB is measured. Linking the observed structure to GB properties is the evident next step.

### 2.5.1 X-Ray diffraction

X-Ray diffraction is one of the earliest known and widely used techniques for studying the crystal structure and microtexture of materials [235]. Following the Bragg's law, when a crystalline material having interplanar spacing of the order of wavelength of a monochromatic X-ray beam diffraction takes place at specific Bragg angles. An X-ray detector can be scanned across a range of angles to determine the position of diffracted beam. A plot of intensity of the diffracted beam against detector scanning angles can be used to determine important details of our material like the crystal structure, lattice parameters, grain size, residual stresses, texture and phase fractions in multi-phase material [236].

### 2.5.2 Thin film resistivity measurement

Surface resistivity or thin film resistivity is the material's inherent resistance against flow of electricity. With the increasing use of thin films for microelectronics, their resistivity is of fundamental interest. When a desired current is passed between two points, based on the resistivity of the material, there is a certain voltage drop. In principle, by measuring the drop in voltage, resistivity of material can be measured [237, 238]. However, when only using two contact points, the resistivity of the contact points adds in series with the resistivity of the material being measured. Therefore, about 100 years ago, four probe resistivity measurement was introduced where four instead of two contact points are used [239]. The probes can be positioned across a certain region of interest (ROI) to measure the resistivity across the contacts. The current passes through the two outer probes and a voltmeter is used to measure the potential between the two inner probes [240]. The sheet resistivity ( $\rho$ ) is given by the following equation:

$$\rho = \frac{\pi}{\ln 2} \times \frac{V}{I} \quad (2.7)$$

where  $V$  and  $I$  are the voltage and current. Conventional four-probe measurement methods for thin films involve probes that are placed few millimeters away that is comparable to the overall film dimensions. Several correction factors have been proposed to include the film thickness and the semi-infinite nature of the wafers [239, 241].

### 2.5.3 Scanning electron microscopy

A scanning electron microscope (SEM) is a versatile tool mainly used to observe the microstructure of a material at submicrometer length scales. An electron beam is

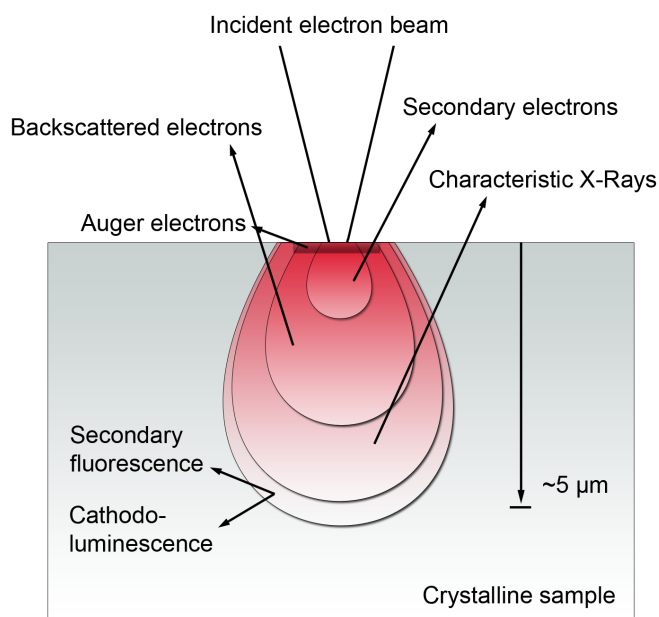


**Figure 2.16** Overview of the interaction volume of the incident electron beam with a crystalline sample in an SEM. Adapted from [242].

rastered over the sample surface and a host of detectors collect the generated signal of interest pixel by pixel. The four principle components of an SEM are the electron source, the electromagnetic lenses, a specimen chamber and various detectors.

A beam of electrons can be generated by heating a pointed tungsten needle or an  $\text{LaB}_6$  crystal such that the electrons have enough energy to escape the surface. As the generation of electrons is caused by heat, it is called a thermionic source. More recently, field emission sources (FEGs) have been developed in which a strong electrostatic field is applied in the vicinity of a tip made of tungsten wire. The quantum mechanical tunneling due to the applied electric field allows the electrons to escape the sharpened tip. Although expensive, FEGs are preferred because of their higher brightness and stability, among other advantages.

A positively charged anode accelerates the electrons towards a set of electromagnetic lenses that are used to form a fine probe. The lenses are simply coils through which variable current can be passed to control the generated magnetic field. The electrons first encounter a condenser lens whose role is to define the probe size and probe current. The beam then passes through a set of scan coils that are responsible for the x and y positioning of the probe in the plane of field of view. The objective lens can be considered to control the z position, i.e. the focal point of the electron probe. The stage containing the sample to be studied can be moved along all three axes so that the ROI lies on the focal plane the electron probe.

The interaction of an electron beam generates an array of signals that are used to

study various properties of the material. Fig. 2.16 shows the volume of interaction and the signals generated. The backscattered electrons (BSE) give a Z-contrast because heavier atoms are more likely to backscatter the incoming beam. The surface and topography information is acquired from the SE because they are generated from the very top part of the sample and the shadowed regions help to understand the topography better. Characteristic X-rays generated by various elements can be used to quantify the chemical composition of the material. SEs are captured using the Everhart-Thornley detector, which basically converts incoming electrons to photons that are guided into a photomultiplier tube to be converted back into electrons. They are finally amplified and displayed in terms of the difference in intensity between the probe positions. SEs have a low energy of  $\sim 50\text{eV}$ ; therefore, only the signal from the surface is obtained. The BSE are detected using a silicon diode detector that is placed near the pole-piece. Their energy is about the same as the incoming beam energy. When they strike the p-n junction, they generate electron-hole pairs. The number of such pairs determines the amount of current generated. Similar semiconductor-based detectors are used to count the number of x-ray photons.

### **Electron backscatter diffraction**

The electron backscatter diffraction (EBSD) is a highly used technique for the diffraction-based analysis of bulk samples. Materials that are crystalline in nature diffract the backscattered electrons. The Bragg scattering of diffracted beams result in a diffraction pattern that is characteristic of the atomic planes and their spacing from which the diffraction occurs. To capture these patterns, a phosphor coated electron detector is placed a few mm away from the sample that is held facing the detector at a  $70^\circ$  angle to the incoming beam. The interference lines obtained are called Kikuchi lines, and the pattern is called a Kikuchi pattern. The angle and spacing between the lines can be used to find the lattice parameters and the grain orientation. The pattern analysis is carried out using software like TSL-OIM, where rich dataset like grain size measurement, misorientation distribution, texture maps, pole figures and partitions based on phase distribution can be produced. Using modern day detectors, thousands of such patterns can be acquired and indexed simultaneously within few seconds. A spatial resolution of a few tens of nanometres and an angular resolution of  $< \sim 0.5^\circ$  can be routinely obtained [243]. In terms of phase analysis and lattice parameter calculation, EBSD provides better spatial resolution than XRD.



### 2.5.4 Focused ion beam

A focused ion beam (FIB) can be thought of as a combination of SEM and sputtering discussed in the previous section. A FIB consists of an ion source, an electromagnetic lens system and a stage for sample displacement. Most modern-day FIB machines are available as dual-beam equipment with both an electron and an ion beam column, making it feasible to simultaneously observe the milled region from two different viewing angles. A focused beam of ions using electromagnetic lenses can be focused at the desired position to sputter away the atoms. The binding energy of the target material, the acceleration voltage and the mass of the ions determine the sputter yield. The most widely used ion sources are argon, gallium, and xenon [244]. Due to its relatively low atomic mass, argon milling is used only for fine-scale polishing of surfaces at an acceleration voltage of 1-3 keV.  $\text{Ga}^+$  FIB is the most widely used FIB in the semiconductor industry and for the preparation of TEM / APT samples. A liquid metal ion source holds the ions (Ga) that are supplied to a sharp tungsten tip when heated. The ions are accelerated using a 5 to 30 keV potential. Higher voltages are used for coarser milling and lower voltage for fine milling and smooth surface finish. A FIB also contains a gas delivery system that is used in conjunction with the ion beam to site-specifically deposit thin protective metallic films using chemical vapor deposition methods. Organometallic gases of metals such as tungsten or platinum are released by means of an inlet capillary about 100  $\mu\text{m}$  above the sample which is adsorbed on the surface. The gas molecules decompose and accumulate when the ion beam interacts with it. The micromanipulator is another essential component of an FIB to attach and move around the sliced specimen wedges during the sample preparation. Detailed procedures for using FIB to prepare the TEM sample are well documented in [245, 246].

It is essential to take care of the milling angles and the accelerating voltage used to minimize the damaged or amorphous layer on the sample. A final thickness of upto 10 nm is achievable based on the material being milled. For metallic samples, obtaining such thin samples is often challenging because of bending at higher voltages and amorphization when milled at lower voltages for a long time. Defect density, residual stresses, and binding energy are some of the parameters that can greatly influence the final steps of fine milling to obtain ultra-thin samples for advanced microscopy analysis [247].

### 2.5.5 Transmission electron microscopy

Transmission electron microscopy is a microscopy technique where a beam of electrons interacts with a thin sample and transmits with a wealth of information about the sample. The versatility of the instrument can be understood from the fact that a TEM can be seen in perhaps every research lab that deals with the length scale lower than a micron, may it be biology and life sciences or condensed matter studies such as material science and geology. To let the electrons transmit through the sample, TEM demands special sample preparation techniques. TEM samples have to be thinned down to  $<100$  nm. This requires the use of special sample preparation techniques that have been extensively discussed in the literature [248].

A microscope is a device that transfers information from the sample to a screen or recording device. When a high energy electron beam interacts with the sample, because of its small wavelength, it interacts with the atomic potentials of crystalline materials. When the right set of objective and condenser lenses are used in combination with the specially designed aberration correctors, atomic level information can be obtained. Additionally, TEM also provides the access to information in the reciprocal space [249].

A wide array of signals are obtained when an electron beam shines on a crystalline sample. In a TEM, the majority of the electrons go through the sample without any deviation in their path or change in energy. This is called forward scattered or direct beam. Although these electrons seemingly do not carry any information, they are necessary to generate contrast. A small fraction of them incoming beam is elastically scattered to specific angles, which are given by Bragg's law. The angle depends on the energy of the electrons and the lattice spacing of the crystal and is often less than  $1^\circ$  in metals studied in a TEM. The direct and the diffracted beams can be imaged in the back-focal plane and can be used to find out the crystal structure and lattice parameters. The term coherency refers to the wave nature of the electron beam. If the waves are in phase, they are coherent; otherwise, they are incoherent. If an electron loses energy, i.e. if there is an inelastic scattering event, the beam is mostly incoherent. When the interaction is elastic, the beam is mostly coherent and becomes incoherent at larger angles [248].

Contrast is perceived when there is a change in the intensity between any two pixels of the image. There are two main contrast-forming mechanisms in a TEM, mass-thickness contrast and diffraction contrast. The mass-thickness contrast, as the name suggests, can arise due to the difference in the mass or thickness of the sample at different regions or because the two regions diffract the incoming beam differently. When the sample is imaged using only the direct beam and the diffracted beam is blocked by an aperture, it is called a bright field image. On the contrary, when the

direct beam is blocked to image using a diffracted beam, it is called a dark field image. If both the direct beam and the diffracted beam form the image phase contrast is obtained. The physics of image formation and an extensive description of all the methods used in TEM is well documented in many textbooks [248, 250].

### High-resolution transmission electron microscopy

When a plane wave interacts with the sample, it undergoes certain phase shifts. By the interference of the direct beam and the phase-shifted beam, we should be able to obtain the information about the sample that causes the phase shift. This requires that we remove the aperture on the sample plane and allow both direct and diffracted beams to form the image. However, it is physically not possible to perceive the changes in phase by imaging because the detector only registers the amplitude and the phase shift information is lost [248]. For a weak phase object, there is only a minor change in the phase of the electron beam, however the amplitude remains unaffected. The point at which the first contrast reversal occurs is called the Scherzer point resolution. By tuning the microscope to certain (de-)focus called the 'Scherzer defocus', based on the spherical aberration and the wavelength of the electron beam, the resolution can be pushed to the point resolution of the microscope.

$$d_{Sch} = c \times C_s^{1/4} \times \lambda^{3/4} \quad (2.8)$$

where  $C_s$  is the spherical aberration coefficient and  $\lambda$  is the wavelength. For a weak phase object, working in the Scherzer focus facilitates the transmission of a wide range of spatial frequencies with consistent contrast and allows for an unambiguous interpretation of the image [251]. The information limit, that is mainly defined by the chromatic aberration, is a popular criterion used to define the resolution of a microscope. It is the inverse of the maximum spatial object frequency that is linearly transmitted with sufficient intensity from the exit plane of the object to the image plane and is limited due to partial temporal coherence [252]. In an ideal microscope the point resolution must be as good as the information limit. This can now be achieved because of the development of aberration correctors. To interpret the phase contrast images, it is necessary that the user is able to simulate them by using the same aberration values, defocus, and other instrument parameters. The interference is highly sensitive to the thickness of the sample and the instrument parameters. Therefore, it is a common practice to obtain a focal-series and to also simulate the images with varying defocus to be able to interpret the contrast in HRTEM images. Further details on these techniques can be found in textbooks [253, 254].

### 2.5.6 Scanning transmission electron microscopy

A scanning transmission electron microscope (STEM) routinely allows imaging at sub-angstrom-level precision for the localisation of atomic units [255]. The majority of the work in this thesis was performed with an aberration-corrected STEM. Beyond imaging, STEM is proving to be a full laboratory in and of itself, with a plethora of conceivable signals that could be acquired simultaneously and the ability to conduct multiple in-situ experiments. A great account of the history and development of STEM can be found in [256].

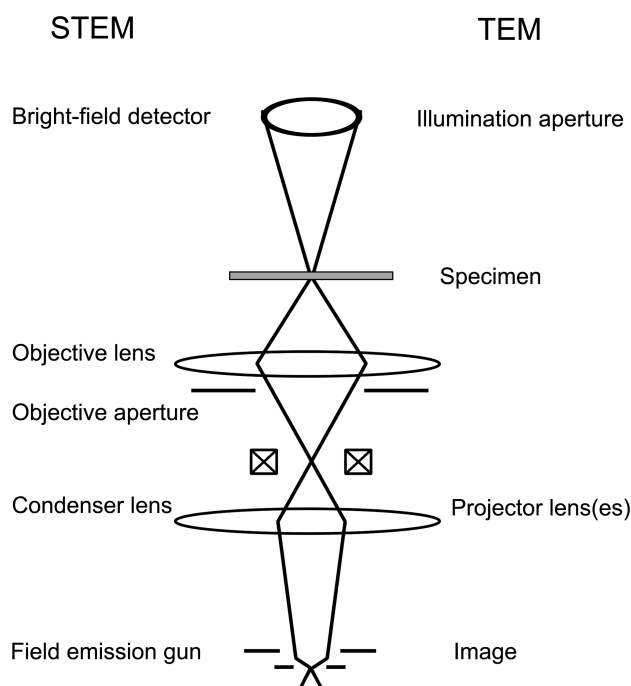


**Figure 2.17** A schematic ray diagram showing the equivalence between STEM and TEM according to the principle of reciprocity. Redrawn from [255].

Fig. 2.17 shows the principle of reciprocity in a TEM and STEM. When only elastic electrons are considered, their path is time-reversible, that means that the electron's path is the same in both directions. In other words, the electron source and the detector could be switched, and the electron path would remain the same. The TEM and STEM are basically examples of these two paths. In TEM, the plane wave interacting with the sample is magnified to the detector, whereas in STEM, the source is demagnified to make the image of a small probe on the sample. Therefore, the concepts for image formation from TEM can be translated into STEM [249]. In contrast to TEM, one advantage of STEM is that all of the crucial optics are located above the sample,

allowing for a wide range of detectors to be used beneath the sample. Incoherent imaging was theoretically expected to result in a better resolution than coherent imaging. By increasing the size of objective aperture, (HRTEM-like) phase contrast imaging can be performed by using BF-STEM detector. The BF image in STEM is the same as an HRTEM image, because they are both phase-contrast images. Furthermore, by using an annular BF detector the interference between the diffracted discs can also be captured. Therefore, the size of objective aperture determines the resolution of STEM. However, it should be remembered that the aperture is used to keep the highly aberrated rays away, and this limits the resolution [255].

As shown in Fig. 2.18, STEM often contains a range of retractable detectors are commonly used, starting from a BF detector to capture the forward scattered beam to HAADF detector to obtain Z-contrast, and other intermediate angle detectors. STEM signal strongly varies with the changing collection angle. For this, apart from using multiple detectors, the camera length and the convergence angle can be modified. More recently, pixelated detectors have been used where the entire back-focal plane is captured using individual pixels that have a very high dynamic range allowing for annular detectors of any desired range of collection angles to be made virtually once the data are acquired.

The most popular imaging method in STEM is to use an annular dark field detector. Here, the elastically scattered electrons that are incoherent at angles higher than  $\sim 75\text{mrad}$  ( $4.3^\circ$ ) are used to form the images [257]. At such high angles, the contribution of coherent part of the beam in image formation can be neglected. For a thin sample, the imaging is not dependent on the objective lens's strength, therefore the issues encountered with HRTEM that necessitate image simulation are avoided.

If we assume the interaction of an electron beam with a single scattering centre, there exists a smooth angular distribution of the elastic and inelastic scattering. However, in real crystalline materials, diffraction disturbs such uniform angular distribution and makes it not feasible to interpret the contrast. This understanding led to the realization that increasing the inner angle of an annular detector to reduce the contribution on diffraction contrast in the image formation [258]. The elastic scattering cross-section of elements increases with the increasing Z-number. Therefore, if a detector could detect the elastically scattered electrons, the obtained signal would contain the Z-number information in it. At lower angles due to the additional strong diffraction contrast, the Z-contrast cannot be interpreted. However, at higher diffraction angles, only the incoherent elastically scattered electrons contribute to the image resulting in Z-contrast. In fact, when using a high angle annular dark field (HAADF) detector, there exists a

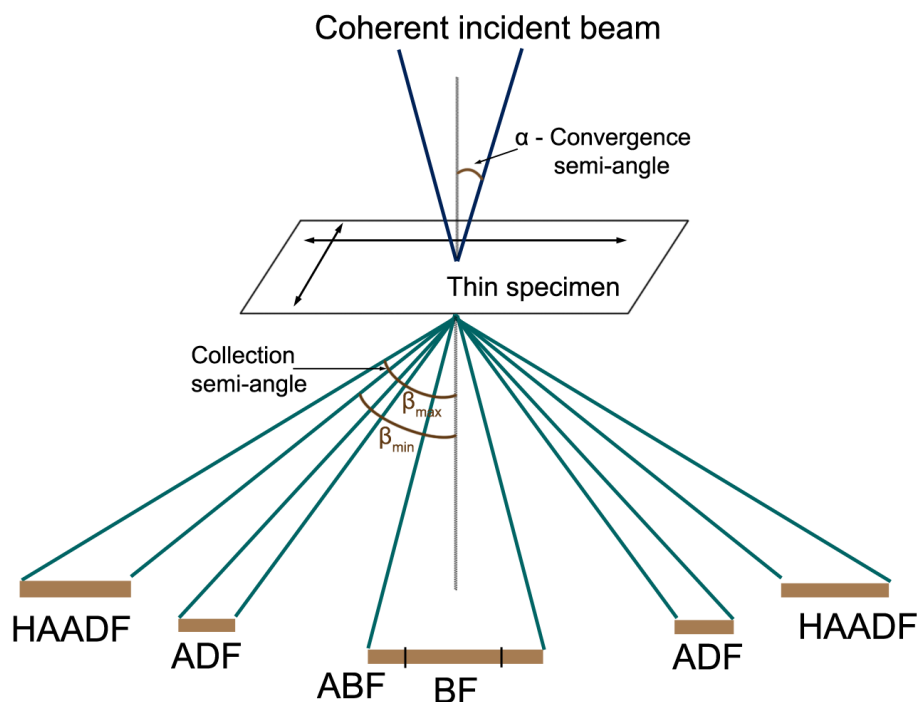


**Figure 2.18** An overview showing the relative position of high-angle annular dark field (HAADF), annular dark field (ADF), annular bright field (ABF) and bright field (BF) detectors in a STEM.

near- $Z^2$  dependence to the image contrast [258]. The  $Z^2$  dependence on atomic resolution is observed in both thick and thin specimens [259]. In reality, since the nucleus is partially shielded by the electron cloud, the exponent is between 1.6 and 1.9 (smaller than 2) [260].

### Coherent and incoherent imaging

Much of the early high-resolution work was performed using TEM. To analyse HRTEM images, we require rigorous simulations that involve knowledge of the microscope parameters and the sample. This problem is avoided in HAADF-STEM, as the image contrast can be more readily inferred. The same can be understood mathematically in the following way: Suppose that an electron plane wave interacts with the sample in a STEM. If an object is sufficiently thin, we can assume that there is only one scattering event. This is known as weak phase object approximation. The object is such a case can be represented by a transmission function. When the incoming plane wave of a unit amplitude interacts with a weak phase object, it undergoes a pure phase shift of  $\phi(R)$ .

$$\phi(R) = e^{i\sigma V(R)} \quad (2.9)$$

where  $\sigma$  is the interaction constant,  $V$  is the projected potential of the sample and  $R$  is the two dimensional position vector of the specimen. The exponential can be expanded to give

$$\phi(R) = 1 + i\sigma V(R) \quad (2.10)$$

the sum of the incident wave and the wave that is scattered by  $90^\circ$  out-of-phase. The same can also be represented in the reciprocal space by a Fourier transformation.

$$\phi(K) = \delta(0) + i\sigma V(K) \quad (2.11)$$

With the optimum choice of defocus, we can obtain:

$$\phi(K) = \delta(0) - \sigma V(K) \quad (2.12)$$

Since this is expressed in reciprocal space, we can perform a Fourier transform to switch back to the real space and obtain the image amplitude, which is given as:

$$\phi(R) = 1 - \sigma V(R) \quad (2.13)$$

Finally, by squaring the amplitude, we obtain the intensity in a bright field image.

$$I_{BF}(R) = 1 - 2\sigma V(R) \quad (2.14)$$

On the other hand, the intensity in a dark field image can be obtained by excluding the transmitted beam from the total scattering. Therefore, the dark field image intensity is given by:

$$I_{DF}(R) = [\sigma V(R)]^2 \quad (2.15)$$

Instead of weak phase object approximation, if we consider the complete equation, we can show the phase change to be:

$$\phi(K) = e^{i\sigma V(K)} \times e^{-i\chi(K)} \quad (2.16)$$

where  $\chi(K)$  is the function determining the aberrations.

$$\chi(K) = \pi(\delta f \times \lambda \times K^2 + \frac{1}{2} \times C_s \times \lambda^3 \times K^4) \quad (2.17)$$

where  $C_s$  is the spherical aberration coefficient, which is most dominant. If the defocus ( $\delta f$ ) is chosen such that there is an additional  $90^\circ$  phase shift, then the diffracted beam can interfere with the (unscattered) forward scattered beam. The Fourier transform of

the phase changes due to lens aberrations is called the probe amplitude distribution  $P(\mathbf{R})$ . Therefore,  $\text{FT}[e^{-i\chi(K)}] = P(\mathbf{R})$ . From Eq. (2.16), the intensity of the BF STEM image at any probe position  $\mathbf{R}$  is given as:

$$I_{BF}(\mathbf{R}) = |\phi(\mathbf{R}) \otimes P(\mathbf{R})|^2 \quad (2.18)$$

All throughout this derivation, we simply take a Fourier transform to switch between the real-space and reciprocal space. This is valid because the information in the back-focal plane is same as the information in the real-space when expressed in the frequency domain. The features that are closer in real space and hence more frequent and farther apart in frequency/ reciprocal space and vice versa. We can see from the Eq. (2.18) that the BF image intensity is the square of convolution, which is the reason that BF images can have a contrast reversal based on the defocus conditions.

On the other hand, theoretical calculations of DF STEM imaging show no contrast reversals in a through-focus series and no discernible influence of collection angles on the image contrast [261]. For an annular DF detector, assuming that all scattering angles are collected, we obtain the fundamental equation of incoherent imaging.

$$I(\mathbf{R}_0) = |\phi(\mathbf{R}_0)|^2 \otimes |P(\mathbf{R}_0)|^2 \quad (2.19)$$

where  $\mathbf{R}_0$  are the coordinates of the probe position on the sample. We can see that for an annular DF STEM image, the image intensity is the convolution of the intensities, and not the amplitude of phase changes due to the sample and lenses. From Eq. (2.18) and Eq. (2.19), we can deduce that the BF imaging is coherent and the DF imaging is incoherent. Further detailed discussion of the same can be found in [249].

Instead of using the weak phase object approximation, a thicker crystalline sample can be represented using a Bloch wave. A Bloch wave is a wave function for a particle having certain potential repeating periodically. The 1s Bloch state peaks near the atomic columns, while the 2s or other Bloch states peak in the middle of atomic columns. The fact that high-angle Rutherford scattering is generated only extremely close to the atomic nuclei means that the interference between different Bloch states does not influence the image intensity. For a HAADF detector it is as if only the 1s state was present in the specimen [249]. This is the key to the incoherence in ADF images [262].

Although the incoherent images are directly interpretable and change little with change in focus, simulations are needed to obtain any quantitative information. However, one of the most persistent issues with HRSTEM image simulations is that they have a threefold higher contrast than the experimental images. This is called as Stobbs



factor. To account for the interaction between the electron and phonon, frozen phonon approximation was introduced. The basic premise is based on a relatively traditional description in which each electron sees a distinct configuration of displaced atoms, and the atoms are perceived as frozen since the time of interaction between electron and object is significantly longer than the time of the atom's period of vibration [263]. However, recently the quantum excitation of phonons model has been introduced which predicts that the Z-contrast imaging is based on the inelastic scattering associated with phonon excitations, not consistent with the frozen phonon model which assumes elastic scattering from different configurations of the atoms in the specimen [264].

The spacial origin of the signal in image cannot be directly attributed to a specific region in the sample, because of the geometric beam spreading and the elastic and inelastic beam spreading as the beam travels through the specimen. Multiple atomic columns can contribute to the image signal, often referred to as 'cross-talk'. The specimen orientation, the crystal structure and the shape of incoming electron wave field can all modify the amount of 'cross-talk' making it harder to simulate [265].

### **Aberration correction**

If the electromagnetic lenses were perfect, the achievable resolution would be limited by diffraction. However, it is well-known that the lenses in an electron microscope are far from perfect. The resolving power of a (S)TEM is limited by spherical aberrations, astigmatism, coma, distortion, other higher-order geometric aberrations, and chromatic aberrations. Many authors have provided a succinct description of aberrations in an electron microscope [248, 266]. The advent of aberration correctors, and with increased stability of the electron source, a bright coherent probe of few tens of picometer diameter has been achieved, making atomic resolution in STEM imaging routine. Theoretical understanding of how aberrations affected microscopy and ways to eliminate them has existed since the 1950s. However, it took many decades of research to build them, and few key elements that led to the breakthrough of the development of aberration correctors simply being the availability of stable electronics, the development of CCD detectors, and computers to analyse the data. Rose [267] and Krivanek [268] have written a detailed account of the history of the development of aberration correctors for STEM.

A whole zoo of possible axial geometric aberrations are classified from the 0<sup>th</sup> order to the n<sup>th</sup> order. The higher the order, the more complicated is the shape of the plane wave and therefore the more difficult it is correct it. The 'tools' used to correct these complicated aberrations are just round lenses and multipoles. Dipoles and weak

quadrupoles are already part of uncorrected microscopes. In the correctors, a combination of either sextupoles or quadrupole-octupoles is used. Although a sextupole (or any multipole) working on its own cannot correct enough aberrations, a combination of them results in additional aberrations, which are then effectively used to nullify the actual aberrations. Exact details of how the real-time aberration measurement works and how the combination of multipoles are used for correction are mentioned in [268, 269].

Beyond our ability to obtain sub-angstrom level imaging, aberration correction has also improved the attainable levels of contrast for elements with low atomic numbers, like imaging oxygen in BF STEM. The increased probe current also facilitates the acquisition of electron energy loss spectra even from single atoms [270, 271]. Similarly, an increase in the probe current has also lowered the detection limits for energy dispersive X-ray spectroscopy [249].

### Energy dispersive X-ray spectroscopy

X-rays are photons having a small wavelength ( $10^{-8}$ – $10^{-12}$  m) and high-energy. X-rays are generated when an energetic beam of radiation or particles collide with a target material. The generated X-rays can be divided into two categories. a) White radiation/ 'Bremsstrahlung', b) Characteristic X-rays [272]. The white radiation is emitted due to the rapid deceleration of the incoming beam when interacting with the target. The loss of kinetic energy is converted into radiation and leads to a continuous spectrum. The X-rays of greater interest to us are the characteristic X-ray peaks that when emitted by an element can be used to chemically characterize materials. Characteristic X-rays are generated in a two step process. First, an electron from the inner shells of an atom is removed upon collision with an incoming electron. Second, an outer electron loses energy to fill the inner shell. The difference between the higher and the lower energy level is the energy of the emitted X-ray. Depending on the material, such an X-ray has a characteristic energy value and is commonly used for analytical microscopy. The nomenclature of the characteristic X-rays depend on which shell the X-ray is emitted from. The innermost shell is called K, the second innermost L, and so on. The shell that fills the generated vacancy is shown in Greek letters. If the electron transitions from L to K, the X-ray is called K- $\alpha$ , the transition from M to K is called K- $\beta$  and so on [248].

The interaction of electron probe with a TEM sample also generates X-rays. Silicon drift detectors (SDDs) are used to directly detect the X-rays with a short dead time, low noise, and without the liquid N<sub>2</sub> cooling required for the old Si(Li) detectors. Details on the working principle and the latest developments in SDDs are discussed

in [248, 266, 273]. The strong interaction and inelastic scattering can lead to sample getting damaged. Therefore, it is in our best interest to increase the collection efficiency and reduce the acquisition time. Therefore, an X-ray detector is placed in the close vicinity of the sample (next to the pole piece) to maximize the collection of X-rays. The collection efficiency is best represented by using the solid angle ( $\Omega$ ). In an ideal but impossible case, the entire sample would be surrounded by the detector, giving 100% collection efficiency ( $4\pi$  sr). Obviously, we need a finite volume for the incoming electron beam, for the pole pieces, and the shadow region of the sample holder. In recent years, the solid angle of the X-ray detectors has risen to nearly 4.5 Sr with race track-like detectors, up from 0.2 Sr with a single detector [274]. The high probe currents provided by FEG sources have also helped in reducing the acquisition time. However, because of the lower angular distribution, higher sensitivity for the light elements, and depth of other information, electron energy loss spectroscopy (EELS) is many times the preferred analytical microscopy choice.

The spacial resolution of X-ray analysis is mainly limited by the incident probe dimension and the interaction volume [275]. The probe size is mainly determined by the probe diameter at the source and the aberrations. Aberration correctors combined with cold-FEGs have therefore allowed for much improved spacial resolution in X-ray analysis. The interaction volume is determined by the thickness of the sample and the orientation. If the sample is oriented in a low-index zone axis, due to the channelling conditions, the beam does not spread. However, away from the zone axis, the interaction volume steeply rises for increasing sample thickness [276]. Examining the GB segregation of Zr in Ni crystal, spatial resolution of 0.4-0.6 nm has been reported [277]. However, quantification of composition was noted to be challenging due to the abnormal X-ray emission under channeling conditions. To process the large data sets, multivariate statistical analysis like principal component analysis (PCA) is becoming increasingly popular. PCA involves finding out the minimum number of variables needed to describe the data to reduce the dimensionality. This allows to highlight regions having large deviation from the average, such as segregation to GBs [278].



## Chapter 3

# Experimental Details

### 3.1 Thin film depositions

#### e-beam deposition

Ti pellets (99.995%, 1/4" *dia.*) were purchased from Kurt J. Lesker Company to be used as the target. The films were deposited in a BesTeck PVD cluster (Marolles-en-Hurepoix, France) on NaCl (100), SiN<sub>x</sub> on silicon (100) and sapphire C-plane (0002), C-plane with a 2° miscut along [11 $\bar{2}$ 0], sapphire A-plane (11 $\bar{2}$ 0) and R-plane (1 $\bar{1}$ 02) substrates. SiN<sub>x</sub> and sapphire substrates were obtained from Siegert Wafer GmbH. Amorphous SiN<sub>x</sub> is a typical diffusion barrier in microelectronic devices for seed and metallization layers, and thus the growth and microstructure evolution of Ti thin films is of basic interest [279]. In the SiN<sub>x</sub> substrate, the 50 nm nitride layer on the Si (100) substrate acts as a diffusion barrier and prevents the reaction of Si with Ti at higher temperatures. The SiN<sub>x</sub> substrate was heated to 500°C for 30 min before the deposition to clear off adsorbates and improve film adhesion. The substrate was then cooled down to 200°C for deposition. The NaCl substrate was cleaved in air right before the deposition to obtain clean (100) surface planes. Sapphire wafers were one side epi-polished having a surface roughness of  $\leq 0.3$  nm. These substrates were used in the as-received state with no additional surface treatments required. The deposition chamber was pumped down to  $2 \times 10^{-8}$  mbar for all the depositions. The substrate to target distance was  $\sim 250$  mm. The e-beam current was tuned to the values ranging from 50 to 150 mA, which was calibrated using a quartz microbalance and constantly monitored during the deposition. To double-check the calibration, the effective deposition rate was calculated post-deposition using film thickness and deposition duration.

## Direct current magnetron sputtering

Thin films of Ti were deposited onto  $10 \times 10 \text{ mm}^2$  SrTiO<sub>3</sub> (001) substrates (Crystal GmbH, Germany) using pulsed magnetron sputtering in a commercial deposition system (Ceme Con AG CC 800-9). A rectangular  $500 \times 88 \times 10 \text{ mm}^3$  Ti target of above 99 wt.% nominal purity (grade 2) with 0.2 wt.% Fe (0.17 at.%), 0.18 wt.% O (0.54 at.%) and 0.1 wt.% C (0.54 at.%) as a major impurity was positioned at a distance of 10 cm to the substrate holder. The base pressure was  $2.2 \times 10^{-6}$  mbar and increased to  $3 \times 10^{-6}$  mbar after heating the substrate to 600°C using radiation heaters. During deposition, an Ar flow rate was set to 200 sccm leading to a working pressure of approximately  $3.8 \times 10^{-4}$  mbar. A Melec SIPP2000USB-16-500-5 power supply was used and the substrates were at floating potential. Four different deposition conditions are discussed in the following article. The first film was deposited using direct current magnetron sputtering (dcMS) with 250 W power for 2.5 h where a deposition rate of 1.33 Å/s was obtained. The pulsing unit was not used in this deposition.

## Pulsed magnetron sputtering

For the subsequent three films, pulsed magnetron sputtering was used. In pulsed magnetron sputtering, the conventional sputtering source is used in a pulsing mode with a predetermined pulse duration ranging from 1  $\mu\text{s}$  to 1 s to increase the current density. This additional degree of freedom to adjust the pulse duration can be used to tailor desired microstructures [280, 281]. The target voltage and current variation during a single pulse is shown in Fig. 3.1.

The time average power was set to 1500 W with a pulse duration of  $t_{on}/t_{off}$  of 200/1800  $\mu\text{s}$ . This led to the peak current ( $I_{ion}$ ) of 40 A resulting in a dense film and a peak target power density of 46 W cm<sup>-2</sup>. The three films were grown under identical conditions by keeping all the film deposition parameters unchanged but changing the post-deposition annealing duration between 2h, 4h and 8h at 600°C to investigate its influence on the film microstructure, texture and grain size. The annealing was performed immediately post turning off the plasma without breaking the vacuum because Ti is known to be highly prone to oxidation. With a deposition rate of about 8.3 Å/s, a film thickness of 1.5  $\mu\text{m}$  was obtained in  $\sim 30$  min. The venting temperature was always  $< 70^\circ$  to reduce surface oxidation [282].

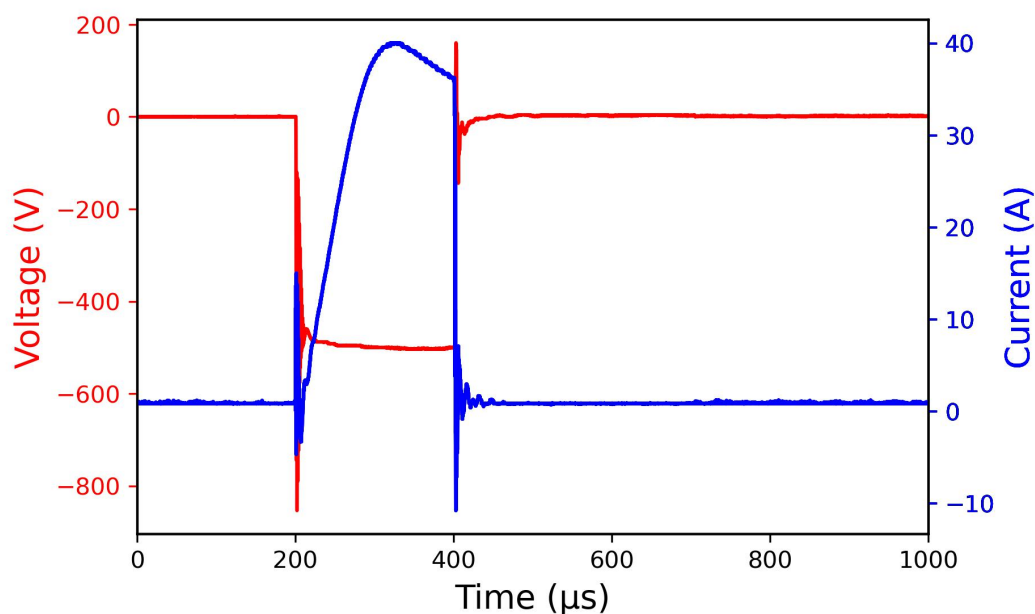


**Figure 3.1** Evolution of the target voltage and current during a single cycle of pulsed magnetron sputtering. A strong voltage overshoot is observed during ignition followed by a steady state of voltage for 200  $\mu\text{s}$  resulting in a peak target power of 20 kW and peak target power density of 46  $\text{W cm}^{-2}$ . The pulse period was 2 ms.

## 3.2 Material characterization

At the heart of material science and is the structure-property correlation of materials. This thesis lays specific emphasis on the structure determination of hcp GBs. This section provides a brief overview of the parameters employed when using the various characterisation tools based on the length scale to be probed. The preliminary investigation was carried out using a light optical microscope to check for any cracks/ defects on the surface. Subsequently, orientation of all grains was mapped using EBSD in an SEM. The GBs of interest were site-specially lifted-out using  $\text{Ga}^+$  FIB and thinned to electron transparency. Aberration corrected TEM and STEM were thereby used for the advanced characterization.

### X-ray diffraction

Before applying techniques based on electron microscopy for a more thorough examination, XRD was employed to take a broad sampling of the microstructure. XRD was primarily employed for texture analysis and phase analysis. A Huber 4 circle goniometer-equipped Seifert ID3003 diffractometer was utilized to conduct XRD to determine the overall film microstructure. Two sources of X-rays were used,  $\text{Cu-K}\alpha$  with a wavelength of 1.54 Å and  $\text{Co-K}\alpha$  with a wavelength of 1.78 Å. The purity of the

films was checked, and the macro-texture was measured, using a scintillation detector. XRD was performed for a  $2\theta$  range of 30 to 90° with a point focused beam of  $1 \times 3$  mm in diameter. Grazing incidence XRD (GIXRD) was used with a 1° incidence angle to avoid diffraction from the single crystal substrates.

## SEM and EBSD

SEM imaging and EBSD is extensively used throughout this thesis. All the SEM experiments were performed on Thermo Fischer Scientific Scios 2 HiVac which is a dual beam instrument with an electron gun and an Ar-ion beam. The SEM chamber is sufficiently large that multiple detectors including EBSD and EDS can be inserted in-situ based on the sample dimensions. SEM imaging of the surface of the thin films was performed using an e-beam of 0.5–7 nA current and 5–30kV potential to get a coarse outlook of the grain size, grain distribution and film surface roughness. A working distance of 4 mm was used for imaging.

For EBSD measurements, the angle between the sample and the detector was held at 70° by tilting the sample stage appropriately. The distance between the sample and the pole piece was  $\sim 14$  mm which could be adjusted such that the pattern center of the EBSD signal was positioned at roughly the center of the detector. The beam current and voltage were chosen based on the thickness of the film. A high voltage results in a larger interaction volume. Therefore, to avoid any contribution to the patterns from the substrate it was necessary to lower the voltage such that the film is thicker than the interaction volume. For a 200 nm thick Ti film grown on Si and NaCl substrate, 20 kV potential was utilized. For the 1.5  $\mu\text{m}$  thick Ti films on  $\text{SrTiO}_3$ , even 30 kV could be employed, but to generate a fine scan and small step size, 20 kV was used also for the thicker films. Beam current of 13 nA resulted in patterns with very high contrast and high signal to noise ratio. To resolve the patterns better, a background correction routine was followed. This involved capturing multiple frames of EBSD patterns at a low-magnification and averaging them out such that sufficient patterns are acquired at once to obtain the background. This background is subtracted from every acquired pattern followed by intensity normalisation to obtain better contrast and facilitate the automatic detection of Kikuchi bands for more accurate pattern indexing. In case of single crystalline films, there is evidently no need to capture any background as the entire film surface is oriented in the same fashion. To obtain OR between the film and the substrate, it is essential to take a note of the scanning direction when setting up the experiment, unless some bare substrate is available (for example, by scratching



on the surface). Typically the low-index direction in any substrate is marked with a straight edge and scanning along the edge aids the OR determination.

### Grain boundary plane determination

As the thesis mainly concerns with GBs and their structures, it is necessary to identify all the GB parameters. In this section, we shortly recollect the method for finding out the GB planes from the 2D projected images of the GBs. 3D-EBSD using FIB has been used in the past to determine all the GB parameters, but it is a destructive technique [283], and therefore the GB cannot be analyzed any further. Other methods include using a stereographical technique wherein the 2D projected views of a large number of GBs obtained using large-area EBSD scans are statistically analyzed. However, such a method is not suitable for a specific GB but can only give an averaged out information [284]. A trick to avoid the projection problem is to use GBs whose plane normals lie on the surface of the plane. In other words, if all the grains grow only normal to the surface, all GB normals lie on the surface. Therefore, just by observing the GB projection on the surface plane, we can identify all the GB plane indices. We only need the orientation of the grain to index the GB plane after confirming that the GBs are vertical from the cross-section view. By drawing the tangential vector at the GB plane of interest, the normal of the vector can be traced on the pole figure. Because the GB plane is known to be vertical, the pole that lies on the outermost edge of the pole figure is the GB plane index. The direction of the pole of any plane in the reciprocal space is same as in a pole figure, therefore the FFT (reciprocal space) of the high-resolution images can be used for the GB plane indexing in a dedicated STEM. In a TEM, a diffraction pattern can be used for the same. Using this with a combination of topological theory method described in Section 4.2.3, all the GB planes in Section 4.3 are identified.

### Focused ion beam

As already mentioned above, the dual-beam SEM-FIB machine was used to prepare samples required for TEM investigation. To find out the ORs between various films and their respective substrates, conventional FIB lift-outs were performed. The conventional procedure is a well-established technique and has been reported in detail [245]. On the other hand, in-plane lift-out technique was deployed, the steps of which have been pictorially elucidated in Fig. 3.2. The change of beam current and voltages for various stages of sample preparation have been mention in Table 3.1. The beam

current was gradually reduced in several steps starting from 1 nA at 30 kV for coarse milling to eventually 27 pA at 5 kV for final polishing to obtain a thickness of <100 nm.

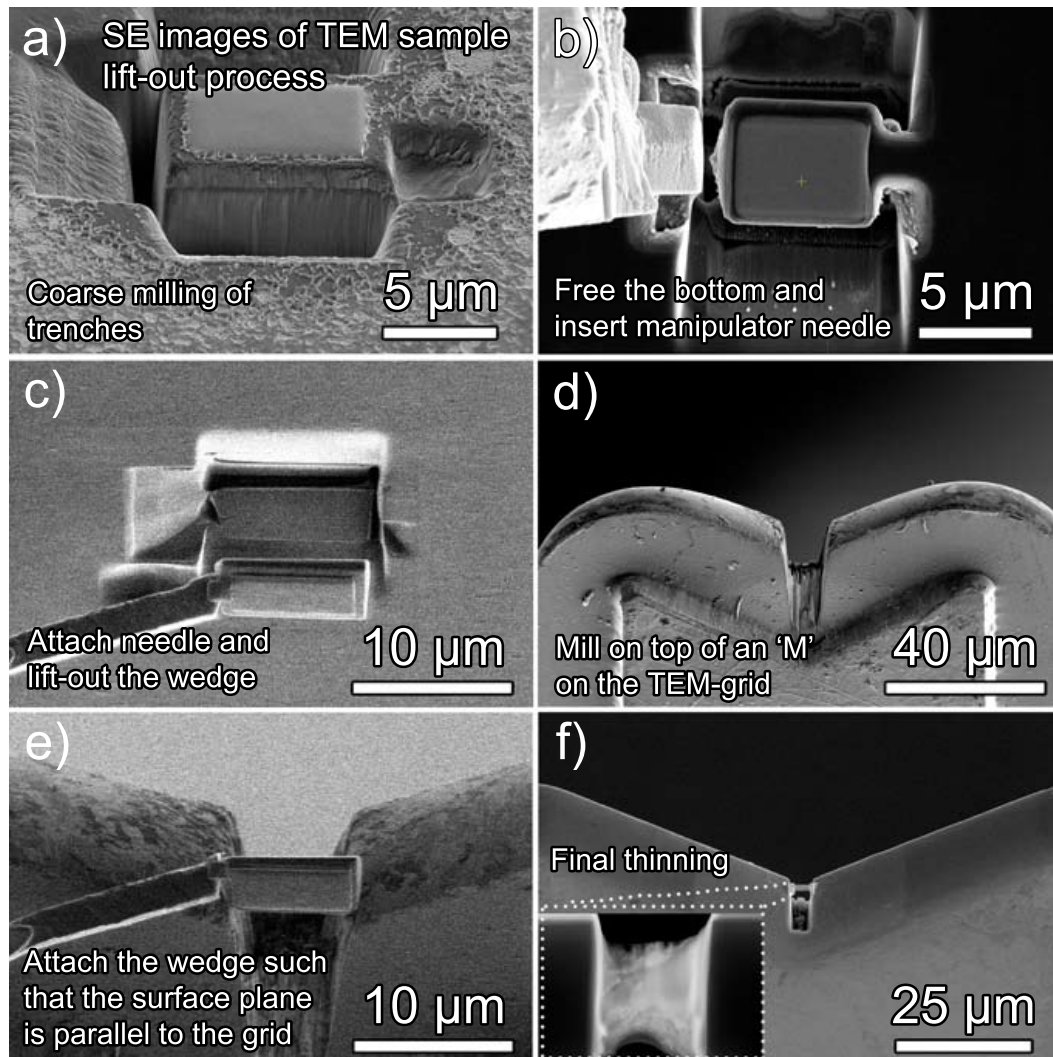


**Figure 3.2** The stages for preparing a plane-view sample using FIB are presented in chronological sequence.

## Scanning transmission electron microscope

In Section 4.2, the BF/DF TEM imaging and diffraction pattern imaging was performed in an FEI Titan Themis 80–300 (Thermo Fischer Scientific) TEM at an acceleration voltage of 300 keV. Selected area diffraction images were obtained by inserting a  $\sim 10 \mu\text{m}$  aperture. The HRTEM imaging was performed under negative  $C_s$  ( $-10 \mu\text{m}$ ) conditions. For STEM imaging and analytical experiments, a probe corrected STEM, Titan Themis 80–300 (Thermo Fischer Scientific), was used at an acceleration voltage of 300 kV. The semi-convergence angle of 23.8 mrad resulted in the collection angles

Purpose	Current	Voltage
Pt deposition	0.5 nA	30 kV
Coarse milling of trenches	13 nA	30 kV
Coarse thinning		
> 800 nm	1 nA	30 kV
> 400 nm	0.5 nA	30 kV
> 200 nm	0.1 nA	30 kV
Fine thinning		
> 150 nm	50 pA	30 kV
> 100 nm	48 pA	5 kV
Polishing	27 pA	5 kV

**Table 3.1** FIB parameters used for STEM sample preparation to obtain samples of the thickness of <100 nm.

of 78-200 mrad and 38-77 mrad for the high-angle annular dark field (HAADF) and the annular dark field (ADF) detectors, respectively, with a camera length of 100 mm. To collect lower angular range on HAADF detector, the camera length was increased upto 195 mrad or higher. By inserting a smaller condenser aperture, the convergence angle can be lowered to 17 mrad, which results in a lower spatial resolution albeit a more coherent and less aberrated beam. Due to the higher inelastic cross-section and lower beam-damage, high-tension of 120 kV was used for EDS measurements. Thermo Scientific ChemiSTEM Technology using four in-column Super-X detectors was used with a beam current of  $\sim 50$  pA for the EDS analysis. These numbers are only an indication of the acquisition parameters generally employed. The actual parameters for each image are modified based on the sample thickness, the dimensions of the region of interest, and other sample characteristics such as its beam sensitivity and cannot be summarised at once. Therefore, the important parameters have been stated alongside the figures in the following chapters, whenever deemed essential. After acquiring many frames at a rapid scan rate, drift-corrected frame integration (DCFI) was used for image acquisition using Thermo Scientific Velox software (version 2.8). Because it increases the signal-to-noise ratio and lowers scan noise, this is favoured over a single slow scan with a long acquisition period.

### Atom probe tomography

Laser-pulsed atom probe tomography (APT) was performed in a LEAP<sup>TM</sup> 5108XR (CAMECA) at a repetition rate of 200 kHz, a specimen temperature of about 50 K, a pressure lower than  $1 \times 10^{-10}$  Torr ( $1.33 \times 10^{-8}$  Pa) and a laser pulse energy of 20 pJ.

The evaporation rate of the specimen was 5 atoms per 1000 pulses. Datasets were reconstructed and analyzed with the AP Suite 6.1 software based on the voltage curves.

Using the results from APT, the interfacial excess was experimentally determined by selecting a region of interest (ROI) across the interface where the solute is segregated and plotting the so-called, *ladder diagram*. A *ladder diagram* is established by taking the total number of atoms in the ordinate and the integral of solute atoms in the abscissa. A linear fit within the concentration profile of the two grains can be extrapolated to the Gibbs dividing surface (GB surface) to find the solute content in both the grains,  $N_a$  and  $N_b$ . Using this, the Gibbsian interfacial excess is calculated as:

$$\Gamma_{excess} = \frac{N_b - N_a}{(\text{Detection efficiency} \times \text{Area of ROI})} \quad (3.1)$$

Additional details are described in [285]. The detection efficiency was 0.52.

### 3.3 Software

Apart from the software already mentioned with the instruments, there are few additional software that were used mainly for data analysis. XRD data was analysed using a home-built Matlab package. TSL-OIM was used for all EBSD data reconstruction and analysis. ImageJ was used for some quick image analysis [286]. Few figures were made on Adobe Photoshop (CS 5.1). Several python packages which mainly include 'matplotlib' [287] and 'hyperspy' [288] were used for making most of the figures and for analysis of STEM data. An effort was put to encourage the use of open source software and FAIR data practice during the course of this work.

## Chapter 4

# Results

### 4.1 Ti thin film deposition using e-beam evaporation

This section is based on:

V. Devulapalli, H. Bishara, M. Ghidelli, G. Dehm, and C. H. Liebscher, *Influence of substrates and e-beam evaporation parameters on the microstructure of nanocrystalline and epitaxially grown Ti thin films*, *Applied Surface Science* vol. 562, pp. 150194, 2021

In the initial part of this work, we deposited Ti thin films on NaCl, silicon nitride ( $\text{SiN}_x$ ) on Si (100), and sapphire substrates using e-beam evaporation. The  $T_{dep}$  was varied from RT to 400°C and the growth rate was altered between 0.25 Å/s to 2.5 Å/s. The film thicknesses were on the order of 100–300 nm. The microstructure and orientation relationship (OR) between the film and substrate were studied using electron backscatter diffraction (EBSD) and transmission electron microscopy (TEM). The first section presents the textured nanocrystalline films obtained on  $\text{SiN}_x$  and NaCl substrates, followed by details of single-crystalline films obtained on sapphire. The role of the substrate on the resulting microstructures and ORs is discussed. Electrical resistivity measurements indicated a limited change of resistivity within the SC films based on their thickness but a steep increase in the nanocrystalline film.

#### 4.1.1 e-beam deposition parameters

The parameters tabulated in Table 4.1 were used for deposition of fourteen Ti thin films using e-beam evaporation. A systematic change in the deposition rate, substrate

temperature and film thickness was performed to find the influence of each of the parameter on thin film growth.

### 4.1.2 Deposition on $\text{SiN}_x$ and NaCl

At a deposition rate of  $2.5 \text{ \AA/s}$ , a 75 nm thick Ti film was deposited on  $\text{SiN}_x$  substrate heated to  $200^\circ\text{C}$ . As seen in Fig. 4.1 using LOM, a film with silver-lustre, smooth surface and with no visible cracks or porosity was obtained.

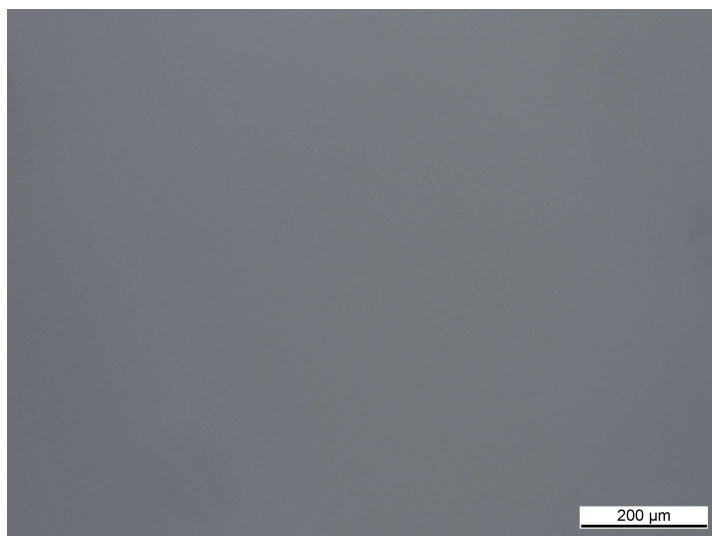


**Figure 4.1** Light optical microscope image of Ti film deposited on  $\text{SiN}_x$  substrate at  $200^\circ\text{C}$  at a deposition rate of  $2.5 \text{ \AA/s}$  (sample #Si1) exhibiting crack and porosity free surface

The polycrystalline nature of the film is revealed by the presence of all diffraction planes in the GIXRD data shown in red in Fig. 4.2. From the full width at half maximum (FWHM) of the most intense Ti peak and using the Scherrer equation [289], the average crystallite size was estimated to be 20 to 30 nm along the surface normal direction. The peaks were symmetrical with the  $2\theta$  peak positions coinciding with that of bulk  $\alpha$ -Ti [39], which indicates that global residual stresses in the film are negligible. However, a preferred  $(10\bar{1}0)$  texture was observed.

To explain the observed texture, the total free energy of a thin film can be calculated by the sum of the surface and strain energy [290] which the system tries to minimize during deposition. The surface energy is determined by the coordination number or atomic density of the respective lattice planes. In Ti, the  $(0002)$  plane has the lowest surface energy ( $2.8 \text{ J/m}^2$ ), followed by  $(10\bar{1}0)$  and  $(10\bar{1}1)$  ( $3.7 \text{ J/m}^2$ ). Detailed thermodynamic calculations of the surface energy using their planar densities have been reported earlier [116, 122]. The strain energy, on the other hand, is defined by the

**Table 4.1** List of deposited films using e-beam deposition with their deposition parameters.

Sample No.	Substrate	Deposition temperature (°C)	Thickness (nm)	Rate (Å/s)	Microstructure
Si1	SiN <sub>x</sub> (100) (50 nm)	200°C	75	2.5	NC
N1	NaCl (100)	RT	90	0.25	NC
N2	NaCl (100)	RT	90	0.8	NC
N3	NaCl (100)	200°C	75	2.5	NC
S1	Sapphire – C-plane (0001)	RT	200	0.5	SC
S2*	Sapphire – C-plane (0001)	300°C	200	0.7	SC
S3	Sapphire – C-plane (0001)	RT	90	2.5	SC
S4	Sapphire – C-2° miscut	RT	90	2.5	NC
S5	Sapphire – A-plane (11 $\bar{2}$ 0)	RT	90	2.5	NC
S6	Sapphire – R-plane (1 $\bar{1}$ 02)	RT	90	2.5	NC
S7	Sapphire – C-plane (0001)	200°C	300	2.5	SC
S8	Sapphire – C-2° miscut	200°C	300	2.5	SC
S9	Sapphire – A-plane (11 $\bar{2}$ 0)	200°C	300	2.5	SC
S10	Sapphire – R-plane (1 $\bar{1}$ 02)	200°C	300	2.5	NC
S11	Sapphire – C-plane (0001)	400°C	300	2.5	SC
S12	Sapphire – C-2° miscut	400°C	300	2.5	SC
S13	Sapphire – A-plane (11 $\bar{2}$ 0)	400°C	300	2.5	SC
S14	Sapphire – R-plane (1 $\bar{1}$ 02)	400°C	300	2.5	SC

film's strain and the anisotropy of elastic modulus [122]. The elastic anisotropy of Ti results in a 30% lower elastic modulus for the  $[10\bar{1}0]$  than the  $[0002]$  direction [122]. As a result, a competing growth between  $(10\bar{1}0)$ ,  $(10\bar{1}1)$  and  $(0002)$  planes is observed, resulting in the film's overall free energy being minimized [99]. The lower strain energy of the  $(10\bar{1}0)$  orientation seems to be responsible for the observed texture in the film grown on  $\text{SiN}_x$ .

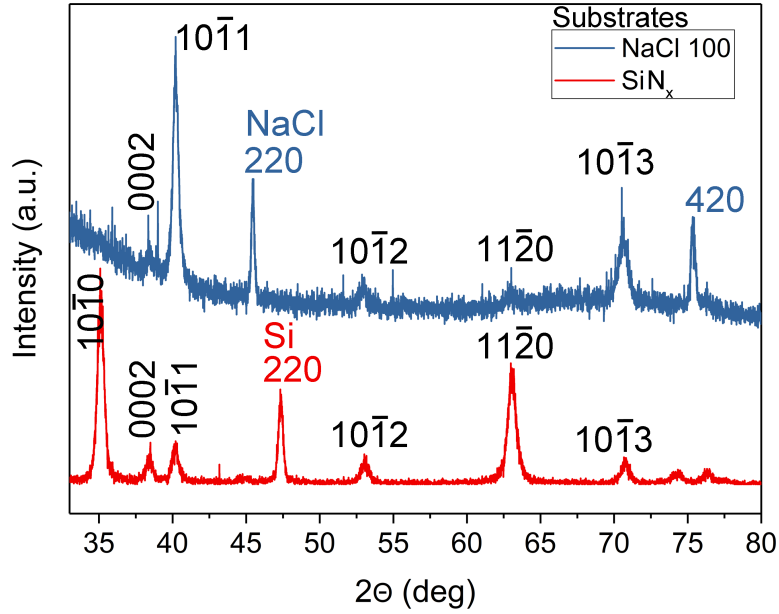


**Figure 4.2** Grazing-Incidence XRD (Cu-K $\alpha$  source) of a 75 nm thick Ti thin film deposited at 200°C on  $\text{SiN}_x$  (100) (sample #Si1) and NaCl (100) (sample #N3). Both films exhibit a polycrystalline microstructure. The film deposited on  $\text{SiN}_x$  shows a strong  $(10\bar{1}0)$  texture; the film grown on NaCl a  $(10\bar{1}1)$  texture.

The film deposited on NaCl (100) under the same conditions ( $T_{dep} = 200^\circ\text{C}$ , Rate = 2.5 Å/s, thickness = 75 nm), was observed using LOM to severely buckle, indicating large residual compressive stresses in the film. The thermal expansion coefficient of NaCl is an order of magnitude higher than Ti [291], which promotes the evolution of large compressive stresses in the film upon cooling from  $T_{dep}$  to RT leading to buckling. The GIXRD pattern shown in Fig. 4.2 confirms the polycrystalline nature of the film albeit with a  $(10\bar{1}1)$  texture. The revealed texture matches well with that observed by Campbell *et al.* [115]. This can be explained by the relatively low surface energy of the  $(10\bar{1}1)$  plane, as discussed above, making it one of the favoured surface normal planes. In addition, the  $(10\bar{1}1)$  orientation leads to lower lattice misfit than  $(0002)$  orientation. NaCl has a lattice constant of 5.64 Å, and the Ti  $(10\bar{1}1)$  plane has a cell size of  $2.95 \times 10.66 \text{ \AA}^2$ . Simply based on the geometry, the misfit between the film and



substrate can be calculated by superimposing the Ti  $(10\bar{1}1)$  plane on the NaCl  $(100)$  plane. The OR leading to the lowest misfit can hence be calculated as:

$$\delta = \left(1 - \frac{d_f}{d_s}\right) \quad (4.1)$$

where  $d_s$  is the lattice spacing of the substrate,  $d_f$  the lattice spacing of the film plane. The lowest misfit of 5.49 % is achieved for  $(10\bar{1}1)_{Ti} \parallel (001)_{NaCl}$  when using the domain matching epitaxy (DME) [292] with a 1/2 domain matching between Ti and NaCl. This describes the  $(10\bar{1}1)$  texture that is observed.

In Fig. 4.3a, the cross-sectional bright-field TEM (BF-TEM) image of the film grown on  $\text{SiN}_x$  substrate confirms the nanocrystalline microstructure and the absence of any chemical reaction or diffusion between the film and the substrate. The grain size of  $20 \pm 5$  nm is in the same range as estimated from the XRD data in the Fig. 4.2. The corresponding diffraction pattern shown in Fig. 4.3b also verifies the film's nanocrystallinity and hcp crystal structure.

Furthermore, for all films grown on NaCl, TEM was used to examine the nanocrystalline grain structure and to determine the impact of deposition rate and  $T_{dep}$  on the film microstructure. Fig. 4.3c shows a representative plane view BF-TEM image of sample #N1 (nanocrystalline film on NaCl at RT; deposition rate =  $0.25 \text{ \AA/s}$ ). The grain size was measured by the line intercept method [293] to be  $\sim 54 \pm 13$  nm. The film adopts the  $\alpha$ -Ti (hcp) structure as verified from the diffraction rings in Fig. 4.3d. Although the film produced ring patterns, a preferred  $(10\bar{1}1)$  texture is observed, which is identical to what the XRD revealed above. The surface diffusivity of condensing Ti atoms on the substrate surface is considerably lower at RT compared to elevated temperatures. According to the structural zone model, the lack of sufficient thermal energy to activate surface diffusion of adatoms results in the formation of nanocrystalline grains at RT [111].

The BF-TEM images shown in Fig. 4.4a and Fig. 4.4c are taken from sample #N2 on NaCl  $(100)$  at RT; deposition rate =  $0.8 \text{ \AA/s}$  and sample #N3 on NaCl  $(100)$  at  $200^\circ\text{C}$ ; deposition rate =  $2.5 \text{ \AA/s}$  respectively. The average grain size of both films was determined to be  $\sim 31 \pm 10$  and  $\sim 53 \pm 18$  nm, as shown in Table 4.2. At RT, The grain size decreases from  $54 \pm 13$  down to  $31 \pm 10$  nm respectively for #N1 and #N2, with increasing deposition rate. The smaller grain size is due to the increase in nucleation rate. The increased nucleation events are a direct consequence of the lower mean

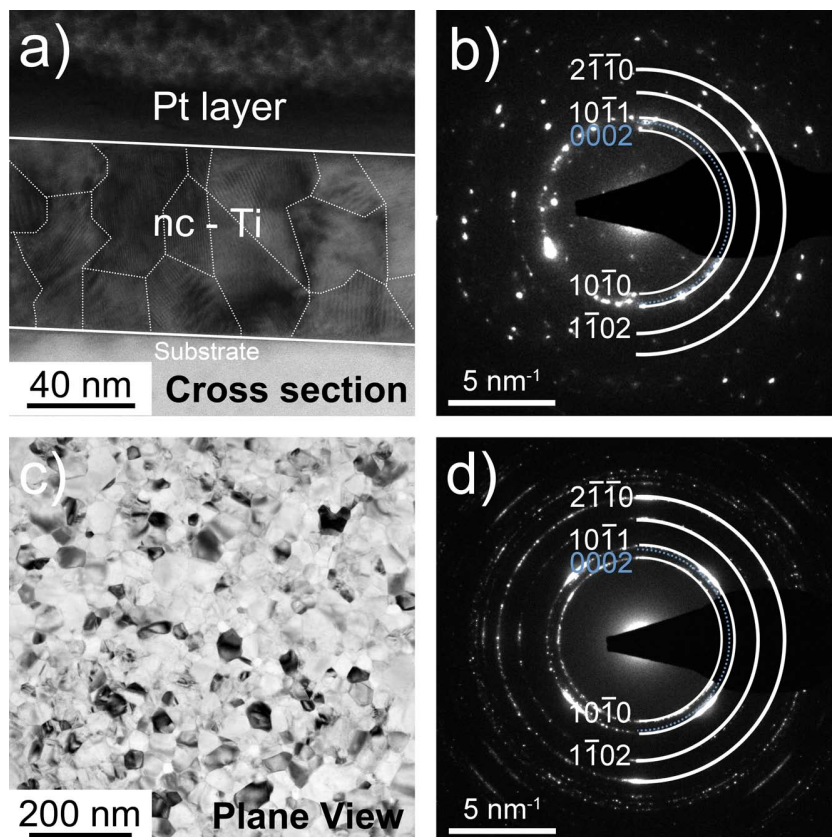


**Figure 4.3** TEM bright field image showing the microstructure of the Ti thin film deposited a) at  $200^\circ \text{C}$  on  $\text{SiN}_x$  substrate (cross section, sample #Si1) and c) at RT on NaCl (100) substrate (plane view, sample #N1), with respective selected area diffraction patterns in b) and d) verifying the nanocrystalline hcp  $\alpha$ -Ti structure.

free path due to the higher flux of sputtered species (atoms or small clusters) at higher deposition rates [294, 295]. Moreover, since these depositions were performed at RT, surface diffusion is severely limited. On the other hand, for sample #N3 (Fig. 4.4c), the deposition was carried out at 200°C resulting in a higher surface diffusivity and leading to larger grain size. Assuming that the cleaved NaCl substrate surface played an identical role in the film growth in all cases, the observations indicate that lowering the deposition rate at RT and increasing the deposition rate at higher temperatures leads to an increase in grain size for NaCl (100) substrate.

**Table 4.2** Grain size distribution of Ti thin films deposited on NaCl (100) by varying substrate temperature and deposition rate

Film	$T_{dep}$ (°C)	Rate (Å/s)	Grain size (nm)
Si1	200°C	2.5	$20 \pm 5$
N1	RT	0.2	$54 \pm 13$
N2	RT	0.8	$31 \pm 10$
N3	200°C	2.5	$53 \pm 18$

The corresponding SADPs shown in Fig. 4.4b and Fig. 4.4d confirm the nanocrystalline nature of the films. The intensity of diffraction spots is restricted to only certain orientations going from film #N1 to #N3 as seen in Fig. 4.3d, Fig. 4.4b and Fig. 4.4d, respectively. Hence, an increasing degree of (10 $\bar{1}$ 1) texture is observed on increasing both deposition rate and  $T_{dep}$ .

It is known that water is adsorbed on the surface of alkali halides such as NaCl [296]. Based on the humidity of the environment the (100) surface of NaCl is most likely covered with 0.5 mono-layer of water at RT [297]. Thus, the surface partly resembles an amorphous state. For amorphous substrates, the surface energy  $\gamma_i$  is not expected to change with the in-plane rotation. This results in an equal probability of grains with all possible in-plane rotations to grow [298]. Since the substrate was cleaved in air in our experiments, we can conclude that water is physisorbed on its surface and the polycrystalline film deposited on NaCl at RT should exhibit all in-plane rotations. However, the minimization of surface and interface energy during the pre-coalescence stage of the film growth plays a major role in deciding the texture of the film [298]. Hence, a weak (10 $\bar{1}$ 1) texture is observed in Fig. 4.3d. In film #N2, the increased deposition rate leads to preferred growth of low energy planes promoting the (10 $\bar{1}$ 1) texture. Once the deposition temperature is raised, the physisorbed water layer evaporates from the NaCl surface. Hence, in film #N3, where the substrate was heated to 200°C during deposition, the surface anisotropy of NaCl comes into play leading to

a much stronger  $(10\bar{1}1)$  texture. This exhibits the control in microstructure that is made available by alteration of the deposition parameters. All the four films discussed in the preceding section are nanocrystalline. As a result, these findings pave the way for better-informed deposition of nanocrystalline Ti, which is known for its exciting properties such as high strength and corrosion resistance [299].

### 4.1.3 Deposition on sapphire substrate

Apart from the commercial importance due to its atomically flat and chemically inert surface, sapphire represents an excellent template for understanding the influence of substrate on thin film growth. As shown in the Fig. 4.5a, the GIXRD patterns of Ti deposited on C-plane sapphire (0001) at RT resulted in a (0002) peak. The film grew as a SC, which means that there was only one orientation present across the entire two-inch wafer. The (0002) plane grows parallel to the *c*-axis of the substrate to minimize the surface energy. Although there is a large misfit of 7.5% between Ti and C-plane sapphire, an apparent six-fold symmetry of the oxygen-terminated sapphire surface allows the first monolayer of Ti to conform to the oxygen sub-lattice. This reduces the mismatch and allows for epitaxial growth [300].

Ti films were also deposited at RT on other configurations and orientations of sapphire like C-plane with a  $2^\circ$  miscut ( $C_{2mis}$ ) along the  $[11\bar{2}0]$  direction, the A-plane  $(10\bar{1}0)$  and the R-plane  $(1\bar{1}02)$ . The GIXRD patterns of these films led to multiple diffraction peaks, indicating the growth of polycrystalline films. The varying degree of texture based on the substrate orientation can be seen in Fig. 4.5b.

The sapphire substrate surface with a miscut is not atomically flat unless annealed [301]. Hence, the defects on the substrate surface lead to films having no preferential orientation during nucleation. The limited adatom mobility at RT promotes poly-/nanocrystalline film. Hence, a  $2^\circ$  miscut was seen to be sufficient to modify film growth from SC to poly-/nanocrystalline as has been reported in several other materials grown on sapphire [301, 302]. However, a (0002) texture is observed in all three cases similar to the C-plane substrate which can be explained by its low surface energy.

Further batches of depositions using the same set of sapphire substrates were performed at higher deposition temperatures to study the influence of  $T_{dep}$  on film microstructure. The deposition on C-plane sapphire,  $C_{2mis}$  and A-plane at  $200^\circ\text{C}$  (samples

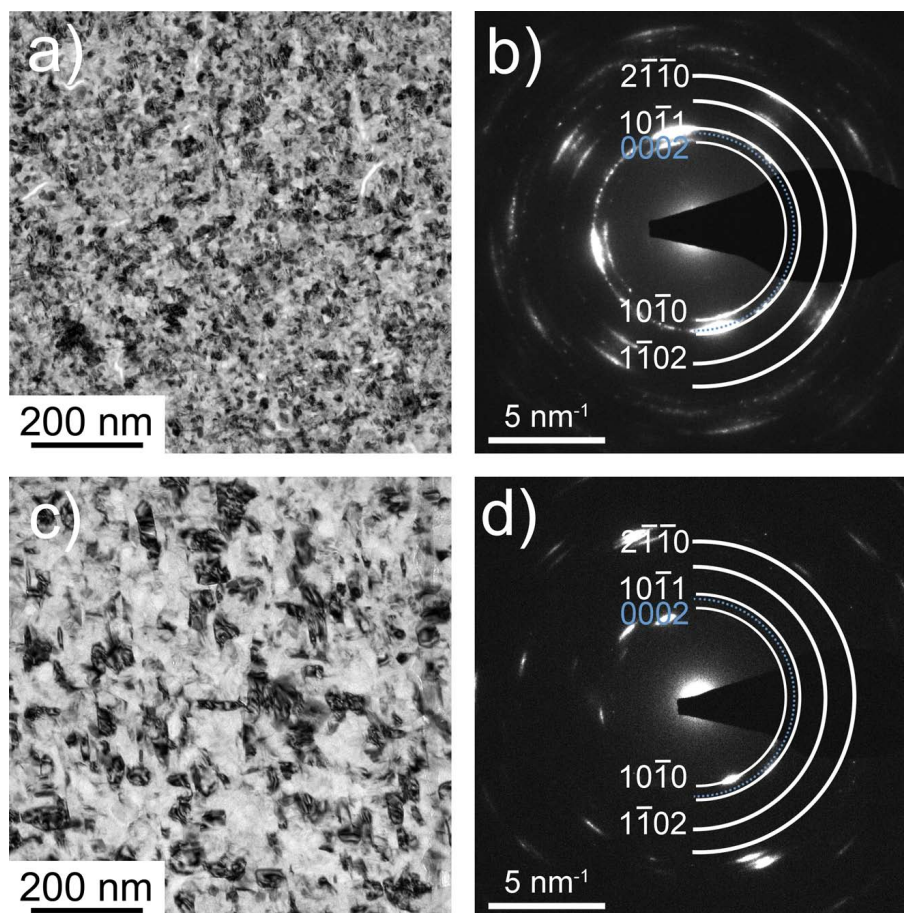


**Figure 4.4** Plane view TEM bright field image of a Ti thin film deposited at a) 0.8 Å/s at RT (#N2) and b) 2.5 Å/s at 200°C on NaCl(100) (#N3). The corresponding selected area diffraction patterns are shown in c) and d), respectively, both exhibiting a strong (10 $\bar{1}$ 1) texture.

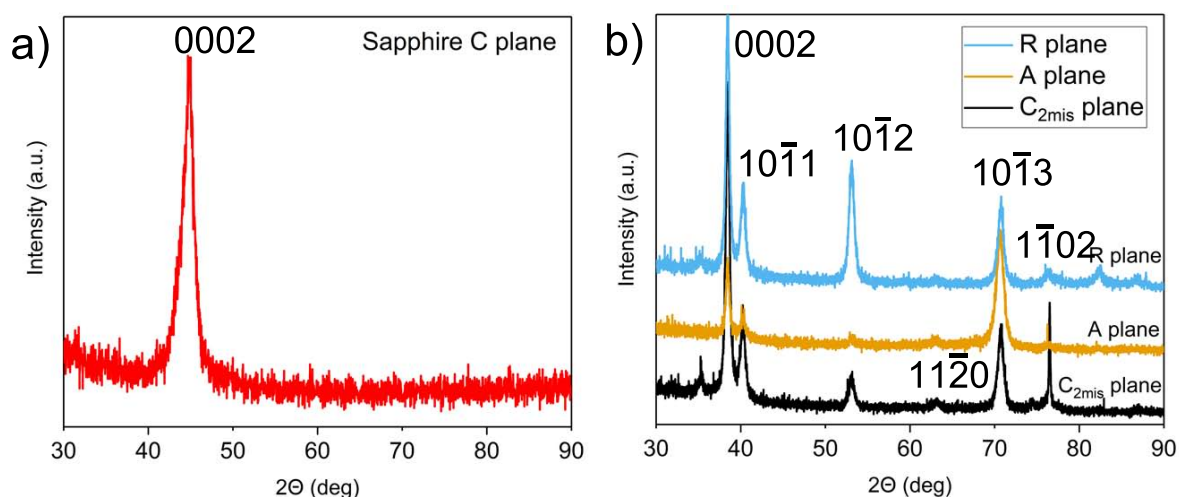


**Figure 4.5** Grazing-Incidence XRD of 90 nm thick Ti thin films deposited at RT on a) C-plane sapphire with only the (0002) peak present (Co-K $\alpha$  source), b) C-plane with a 2° miscut ( $C_{2mis}$ ), A-plane and R-plane sapphire displaying multiple diffraction peaks (Cu-K $\alpha$  source)

#S7, #S8 and #S9) resulted in highly epitaxial single-crystalline films. They were deposited after holding the substrates at  $T_{dep}$  for  $\sim 1$  h to ensure uniform temperature. The holding period results in desorption of water and any organic/ volatile impurities from the substrate surface. An epi-polished sapphire substrate surface is known to exhibit surface steps [303]. Additionally, the increase of  $T_{dep}$  results in an increased surface diffusion of adatoms. The islands which nucleate on the atomic steps in the  $C_{2mis}$  substrate are hence expected to have fixed orientation relationship with surface steps and better inter-connections between neighboring grains at higher  $T_{dep}$ , which leads to a single dominant orientation [301]. A similar effect is observed in A-plane sapphire which leads to the ease of SC film formation. However, the film remained polycrystalline for the R-plane sapphire substrate at  $200^\circ\text{C}$ .

There are three ways epitaxial films deposited on sapphire substrates can grow. When the bond between the adatom and the substrate is strong, a layer-by-layer deposition called Frank-van der Merwe (FM) mode can occur [304]. The Volmer-Weber (VW) growth mode is caused by a stronger bond between the adatoms, resulting in their three-dimensional clusters to coalesce and form a continuous film. A combination of the two modes, where clusters form on top of a few monolayers is termed Stran-ski-Krastanov (SK) growth mode. The dominant growth mode is determined by the rivalry between the bare substrate's surface energy ( $\gamma_{sv}$ ), the interface energy between the substrate-film ( $\gamma_{sf}$ ), and between the film-vapor ( $\gamma_{fv}$ ). A large misfit system like in the above films leads to a high  $\gamma_{sf}$  value, which results in a significantly lower barrier to nucleate clusters, favouring the VW growth mode. As a result of the formation of several tiny nuclei at RT, a nanocrystalline film was found in all but one of the cases. The only exception was C-plane sapphire, which was SC as previously discussed.

To verify the observations and to explain the anomalous behaviour of R-plane sapphire, the substrate temperature was further increased to  $400^\circ\text{C}$ . This leads to a further increased mobility of adatoms resulting in SC film formation on all the sapphire substrate orientations (samples #S11, #S12, #S13 and #S14). EBSD scans of the film surfaces revealed no change in orientation. The scans were observed in both transverse and planar viewing direction using TSL-OIM software to confirm the absence of grain boundaries even with a  $1^\circ$  angular deviation. The film deposited on C-plane (not shown),  $C_{2mis}$  and A-plane all demonstrated the same preferred  $(0002)_{Ti}$  orientation as shown in Fig. 4.6 a and b. The orientation of the film on C-plane and  $C_{2mis}$  can be explained in the same way as in the previous two cases. A-plane sapphire has a two-fold symmetry with  $[0001]$  perpendicular to  $[1\bar{1}00]$  results in a super-cell of 12.99

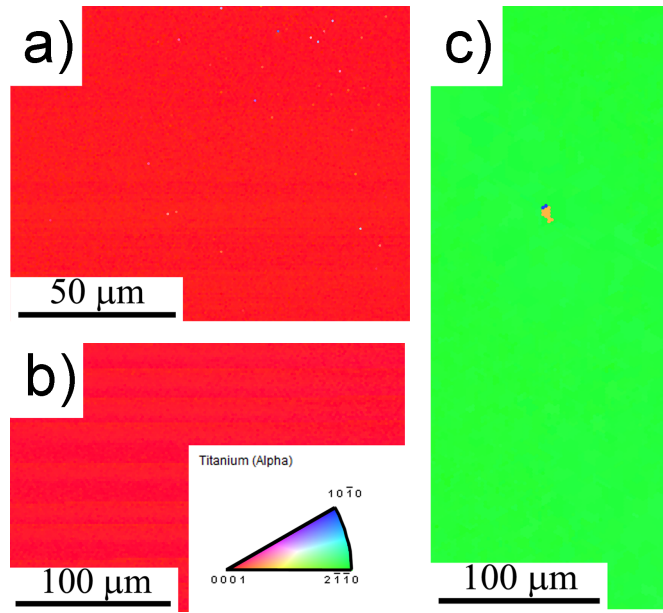


**Figure 4.6** Inverse pole figure (IPF) obtained from EBSD of Ti thin films deposited at 400°C on (a)  $C_{2mis}$ -plane (b) A-plane and (c) R-plane sapphire at low magnification to display uniform orientation over the entire wafer.

$\text{\AA} \times 8.22 \text{\AA}$ . When depositing Ti on this plane at sufficiently high temperature (here 200°C), the favoured out-of-plane OR is observed to be  $(0002)_{Ti} \parallel (\bar{1}\bar{1}20)_{Sapphire}$  [305]. However a 30° in-plane rotation separates the two ORs. The  $\langle 10\bar{1}0 \rangle_{Ti} \parallel \langle 1\bar{1}00 \rangle_{Sapphire}$  results in 18.01% and 7.6% misfit in [0001] and [10 $\bar{1}$ 0] directions respectively, whereas, in the same directions  $\langle 11\bar{2}0 \rangle_{Ti} \parallel \langle 1\bar{1}00 \rangle_{Sapphire}$  results in a misfit of 9.16% and 24.33%, respectively. Due to the relatively lower misfit, the former is observed here. The SC film on R-plane sapphire exhibited a  $(2\bar{1}\bar{1}0)_{Ti}$  surface plane normal, which is reported here for the first time.

Unless the in-plane orientation of the underlying substrate is known, observing the film surface using EBSD is insufficient to find the OR. Hence, high resolution-TEM (HRTEM) of the interface viewed in cross-section was used to observe the OR between the SC film and the C-plane sapphire substrate in the sample #S3 (deposited using e-beam evaporation at RT). As shown in Fig. 4.7, accommodating a 7.58% misfit [11], the film was found to have  $(0002)_{Ti} \parallel (0006)_{Sapphire}$ ,  $\langle 11\bar{2}0 \rangle_{Ti} \parallel \langle 03\bar{3}0 \rangle_{Sapphire}$  OR in agreement with [105]. Sup. Fig. 3 shows the sample #S2 deposited with Ar-ion sputtering at 200°C exhibits the same OR. This demonstrates that the OR between Ti and sapphire C-plane is independent of the deposition method.

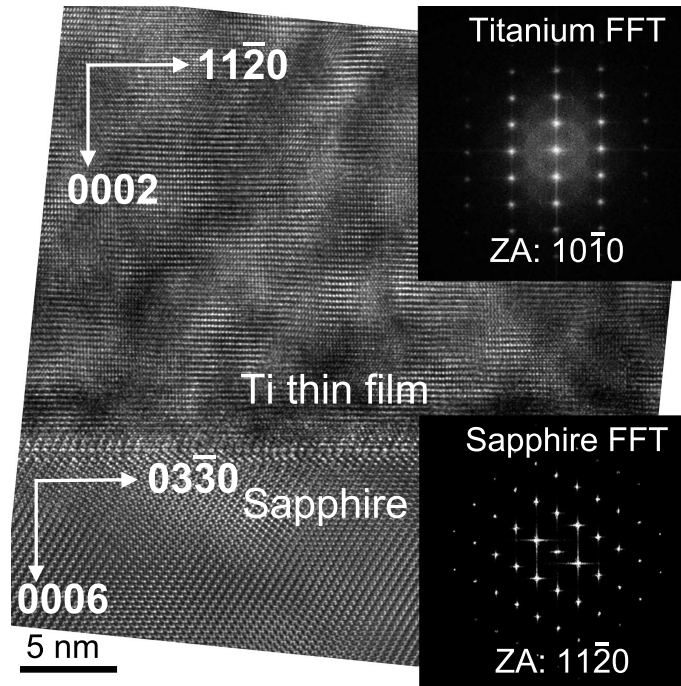


**Figure 4.7** HRTEM image of cross-section of Ti thin film deposited on C-plane sapphire shows a 90 nm thick Ti film deposited using e-beam evaporation at RT (sample #S3) observed in  $[11\bar{2}0]$  zone axis orientation of the sapphire substrate. The insets show fast Fourier transforms (FFTs) of the film and substrate, respectively, which are used to determine the ORs

#### 4.1.4 Resistivity measurements

Ti thin films can be used in micro-electronic miniaturised circuits, electrical contacts and sputter ion pumps. These applications require a control of the electrical resistivity of the thin films. Based on the thickness, deposition parameters, chemical purity of the target and microstructure of the film, the resistivity values can largely vary [306]. As shown in Fig. 4.8, for the films deposited on C-plane sapphire, the thinnest (90 nm) film (sample #S3), shows a higher resistivity equal to  $\sim 70 \mu \Omega \text{ cm}$ . This increased resistivity is attributed to surface scattering. For the 300 nm thick SC films (samples #S7 and #S11) resistivity remains uniform at  $\sim 60 \mu \Omega \text{ cm}$ , which is slightly higher than the pure Ti bulk single crystal values equal to ( $\sim 40 \mu \Omega \text{ cm}$ ) [103, 307] which is also attributed to surface scattering. The values measured here are in agreement with other epitaxial Ti films [103], and are much lower than the polycrystalline films reported in literature [129, 307, 308]. Apart from the surfaces, grain boundaries can also act as scattering centers. Resulting from increased scattering from grain boundaries, the nanocrystalline film grown on sapphire A-plane at RT (sample #S5) exhibited a much higher resistivity of  $\sim 95 \mu \Omega \text{ cm}$ , while the SC thicker films on A-plane sapphire show the same trend as seen for C-plane. As suggested by Bel'skaya *et al.* [309], the resistivity values of thin films can also be used as a measure of the impurity content,



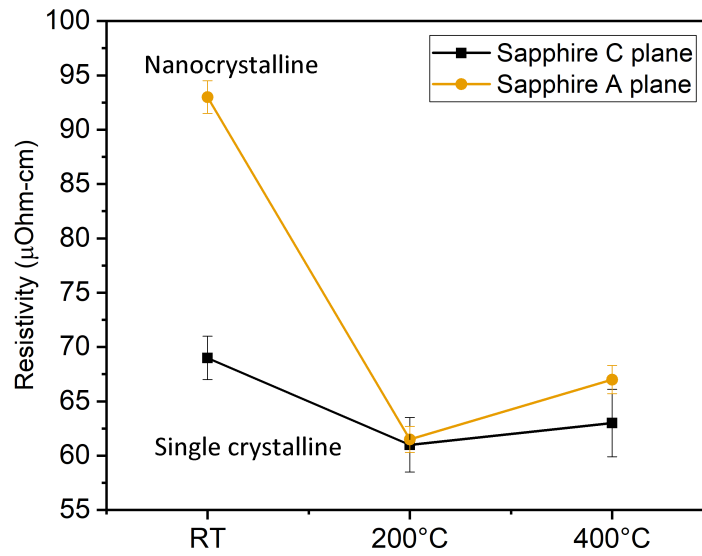


**Figure 4.8** Resistivity values of films grown on C-plane sapphire and A-plane at varying  $T_{dep}$ . The nanocrystalline film shows higher resistivity of  $\sim 95 \mu \Omega \text{ cm}$  while all SC films show resistivity of  $\sim 60 \mu \Omega \text{ cm}$

given the deposition conditions are same. Hence, the resistivity of  $\sim 60 \mu \Omega \text{ cm}$  in the SC films indicates that impurities play a minor role on resistivity.

## 4.2 Microstructure, grain boundary faceting and anisotropic Fe-segregation

This section is based on:

V. Devulapalli, M. Hans, T. S. Prithiv, J. M. Schneider, G. Dehm, and C. H. Liebscher, *Microstructure, grain boundary evolution and anisotropic Fe segregation in (0001) textured Ti thin films*, *Acta Materialia* 238 (2022), 118180

Systematic study of the influence of GB character on material properties requires a template-based approach to obtain desired GBs. For many metals, bicrystalline samples with predefined GB parameters have been grown using the vertical Bridgman technique for specific GB property studies [310]. However, in Ti, the hcp-bcc allotropic transition makes it impossible to fabricate bicrystals to form a specific GB. Therefore, a novel thin film deposition route to obtain bicrystalline Ti has been established here. A bicrystalline thin film here is referred to as a film that only contains a certain misorientation of the crystals, although multiple grains can be present in the same film. Such thin films with multiple grains but only two orientations of them being present have been consistently classified as bicrystalline in literature, mostly reported in cubic metals like Al on Si(100) substrate and Au on Ge(001) substrate [105, 311–315]. To deposit such films, a thorough understanding of the impact of various deposition parameters on the microstructure of the film is required. In physical vapour deposition, the degree of ionisation of the plasma particles determines the ion flux towards the growing film [316, 317]. A high ion fraction in a discharge is achieved by promoting the electron impact ionization which is achieved by using plasma of high electron density and higher temperature. Such a plasma is formed by using a pulsing unit at the target. Textured Ti films with (0002) out-of-plane orientation were recently reported using a similar deposition route [121].

In this work, firstly a template-based approach to obtain  $\Sigma 13$  GBs in thin films of Ti on SrTiO<sub>3</sub> substrate is established. Pulsed magnetron sputtering using a commercially pure Ti target with trace Fe impurities is used to obtain a bicrystalline thin film with columnar grains. Subsequently, EBSD in a SEM is used to characterize the thin film microstructure. The GBs contained in the thin film are analyzed in detail using a STEM and are observed to be faceted into symmetric and asymmetric segments. Using

high resolution EDS analysis, the segregation of Fe to these topographically complex GBs is explored.

### 4.2.1 Evolution of thin film microstructure and grain boundaries

The Ti film deposited on SrTiO<sub>3</sub> (001) at 600°C using dcMS is characterized by SEM and EBSD as shown in Fig. 4.9. Following the deposition, the film was post-annealed at 600°C for 2 h in the deposition chamber. The SE image in Fig. 4.9 a) reveals a rough surface and small grains. Fig. 4.9 b) shows the crystallographic orientation map based on the [0001] IPF obtained using EBSD. The grain size is measured to be ~500 nm using the line intercept method [318]. To visualize the change in misorientations, a black line is highlighted inside the orientation map in Fig. 4.9 b). The misorientation between every point on the line and the first point (origin) on the line is displayed as a misorientation profile chart. In the profile, a range of varying orientations is observed in Fig. 4.9 c). Using the [10 $\bar{1}$ 0] pole figure in Fig. 4.9 d), two dominant textures are observed. First, a strong (10 $\bar{1}$ 1) fiber texture is seen revealing the presence of all possible in-plane rotations. These grains are highlighted in purple in both the orientation map and the pole figure. Second, a (0002) texture is observed with only two in-plane grain rotations, with each orientation highlighted in red and blue in the pole figure. The pole figure comprises a single point per grain that is weighted by grain size; thus, the distribution of both orientations can be seen to be approximately equal. It is known that the (0002) plane has the lowest surface energy in Ti due to the highest atomic density and (10 $\bar{1}$ 1) has the least strain energy due to the lowest elastic modulus [122]. Hence, the two orientations seem to compete and both are observed by EBSD in the film deposited by dcMS.

To understand the influence of higher ionization of the plasma and increased adatom mobility on the film microstructure, pulsed magnetron sputtering was subsequently used to deposit three additional films of Ti. The depositions were performed at 600°C and post-annealed at the same temperature for 2 h, 4 h and 8 h. A larger grain size (see Table 4.3) is seen for the film deposited by pulsed magnetron sputtering compared to the film deposited using dcMS. Likewise, for the film annealed for 4 h, a much smoother surface and larger grain size is observed, as seen in Fig. 4.10.

In Fig. 4.10 b), the orientation map obtained from EBSD confirms that almost all of the grains have a [0001] surface plane normal. The pole figure shown in the inset

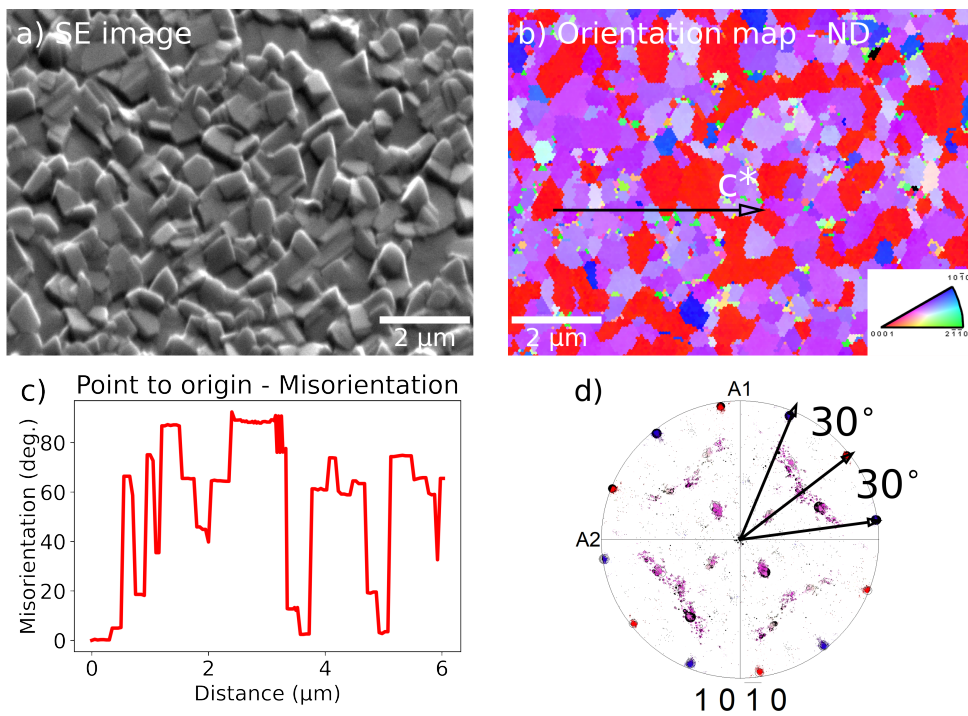


**Figure 4.9** Ti film deposited using DC Sputtering with 250 W power on SrTiO<sub>3</sub> at 600°C and post annealed at 600°C for 2 h. a) SE image showing rough surface and small grain size. b) Inverse pole figure (IPF) map obtained from electron backscatter diffraction (EBSD) revealing the two dominant surface plane orientations to be  $\{10\bar{1}1\}$  and (0002). The arrow highlights the points along which a point-to-origin misorientation profile chart is plotted in (c). d) Pole figure confirming the dominance of two surface plane orientations with a fiber texture of  $\{10\bar{1}1\}$  planes and only two in-plane rotations of (0002) planes.

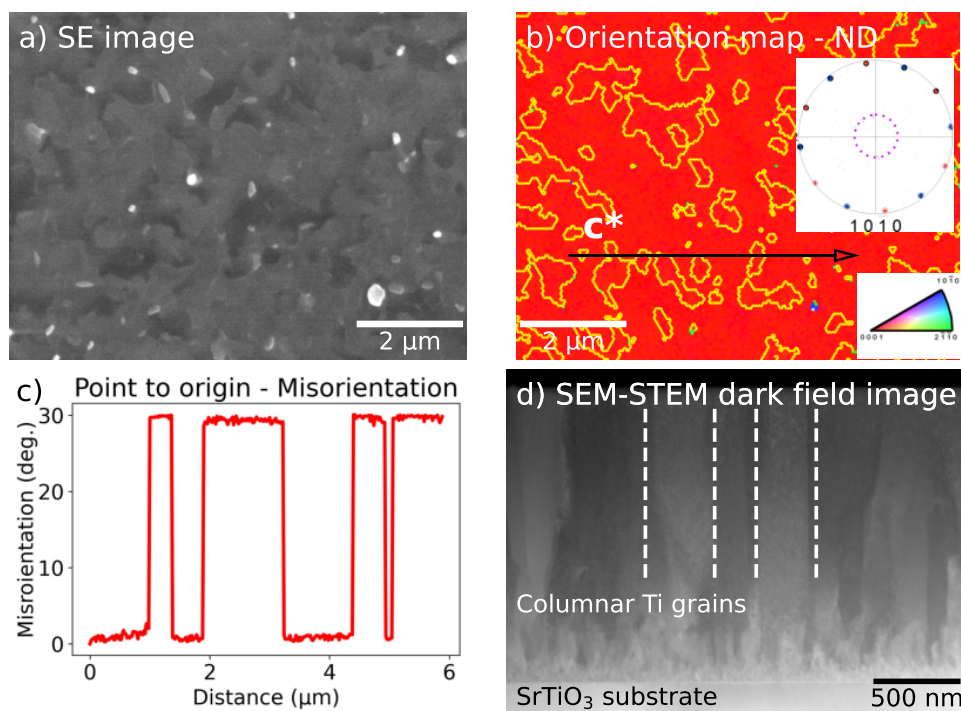


**Figure 4.10** a) SE image of Ti film deposited on SrTiO<sub>3</sub> at 600°C using pulsed magnetron sputtering with a pulse duration of 200 μs and 1500 W power followed by post annealed at 600°C for 4 h showing smoother surface and relatively larger grain size. b) Inverse pole figure (IPF) map obtained from EBSD with Σ13 grain boundaries highlighted in yellow. The arrow highlights the points along which a point-to-origin misorientation profile chart is plotted in (c). Upper right inset is the pole figure obtained from IPF confirming the ~ 30 ° misorientation corresponding to Σ13 [0001] grain boundaries with the orientations highlighted in blue and red, respectively. A dashed purple circle highlights the presence of trace {10 $\bar{1}$ 1} orientated grains. d) A dark field SEM-STEM image of the cross-section of the film revealing columnar grain growth.

is obtained from the same data set. It confirms the  $30^\circ$  misorientation corresponding to  $\Sigma 13$  [0001] GBs. The orientation is determined using 2-dimensional Hough transformation that has an error of  $<0.7^\circ$ . The Brandon criteria determines the amount of deviation ( $\delta\theta$ ) from a misorientation that may be tolerated by addition of secondary dislocations/ defects at the GB while maintaining a particular CSL value [137]:  $\delta\theta = 15^\circ \times \Sigma^{-1/2}$ . For a  $\Sigma 13$  GB one obtains  $\delta\theta = 4.16$ . The exact  $\Sigma 13$  misorientation around the [0001] tilt axis is  $28.8^\circ$ . Therefore, all the GBs in the present film fall very well within the accepted deviation of  $\Sigma 13$  CSL GB. For better statistics, we show a large scan area of  $40 \times 50 \mu\text{m}$  in Fig. 4.11 which illustrates that we have only  $\Sigma 13$  GBs all over the film.

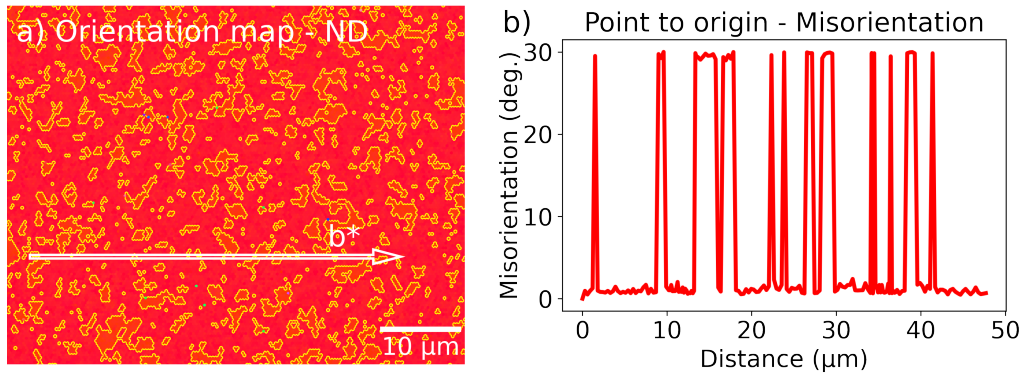


**Figure 4.11** a) Orientation map of Ti thin film deposited on  $\text{SrTiO}_3$  at  $600^\circ$  and annealed at  $600^\circ$  for 8 h. A large area ( $\sim 50 \mu\text{m} \times 40 \mu\text{m}$ ) was scanned using EBSD for better statistical analysis showing the  $\Sigma 13$  GBs highlighted in yellow. b) Point-to-origin misorientation plot from the region marked with an arrow in a). All the grains can be seen to belong to only two orientations.

Furthermore, as previously observed, all of the grains with (0002) surface plane normal have either of the two orientations shown in the pole figure, which are denoted by red and blue. A purple dashed-circle is drawn in the inset of Fig. 4.10 b) that marks the additional reflections at  $\sim 25^\circ$  away from the center. As every reflection in the pole figure is weighted by the grain size, these additional reflections correspond to small grains of other orientations. They account for less than 2 area % of the total scan area. As a result, we follow the definition used in the literature to term these films as bicrystalline. This is supported by the presence of only two alternating orientations in a representative misorientation profile chart in Fig. 4.10 c). The high peak current of 40 A during pulsed magnetron sputtering in contrast to 5 A during dcMS is responsible for the shift of surface plane orientation from  $(10\bar{1}1)$  and (0002) in the dcMS film to all the grains being only (0002) oriented in the pulsed magnetron sputtered film. A cross-section FIB lamella was prepared to resolve the microstructure of the film in growth

direction. The majority of the grains were found to be columnar as seen in Fig. 4.10 d). Additionally, many nanocrystalline grains are observed at the film-substrate interface. Further details of this interfacial layer are discussed in the following section where a similar distribution of fine columnar grains at the interface is observed for the film annealed for 8 h at 600°C.

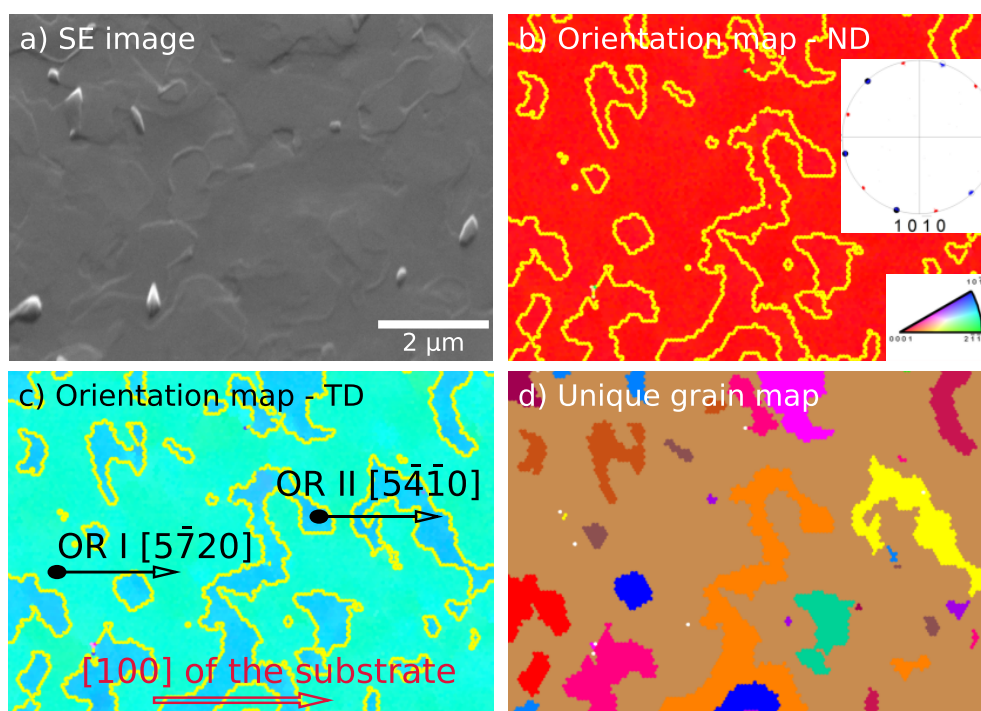


**Figure 4.12** Ti deposited on SrTiO<sub>3</sub> at 600°C and post annealed at 600°C for 8 h a) SE image showing traces of grain boundaries. b) Inverse pole figure (IPF) map in the normal direction (ND) showing all grains in (0002) out of plane orientation. In the upper right inset is the pole figure obtained from IPF confirming the  $\sim 30^\circ$  misorientation corresponding to  $\Sigma 13$  [0001] grain boundaries. c) IPF map in the transverse direction (TD) with  $\Sigma 13$  grain boundaries highlighted in yellow. The two arrow marks point the crystal directions in the OR I and OR II grains parallel to [100] of the substrate. d) Unique grain map confirms that OR I is a single grain that is spread all over the substrate. All the other grains belong to OR II. All subfigures share the same scale bar as (a).

When the post annealing time is extended to 8 h, the film surface remains smooth and a further increase in grain size to  $3.76 \pm 2.4 \mu\text{m}$  is measured using EBSD, as seen in Fig. 4.12. The increase in grain size with respect to the annealing duration is tabulated in Table 4.3. It is generally considered that grain growth in thin films is arrested when the grain size is about one to two times the film thickness [319]. The driving force for grains to grow 2-dimensionally is much smaller than 3-dimensional growth. As seen from the EBSD results in Fig. 4.12, the GBs are meandering through the film, resulting in a low radius of curvature. This leads to capillary forces driving the GBs

to straighten and migrate towards their centre of curvature. This causes both grain growth and shrinkage in different sections of the grain. Similar phenomenon has been observed in the bicrystalline films of Au [312]. In a bicrystalline film there are no triple junctions which potentially act as pinning points against grain growth. The increase in the grain size as a function of annealing duration can also be noted by measuring the length of GB per unit area of the film. As seen in Table 4.3, for an area of  $25 \mu\text{m} \times 20 \mu\text{m}$ , the length of  $\Sigma 13$  GB reduces from 1.38mm to  $895 \mu\text{m}$  to  $525 \mu\text{m}$  as a function of increasing annealing duration.

EBSD also verifies that the film continues to show the same mazed bicrystalline microstructure as observed previously. When comparing the films annealed for 4 h and 8 h, the isolated grains of other orientations are seemingly overgrown by the larger grains having (0002) orientation in the 8 h sample. The pole figure in Fig. 4.12 b) shows the presence of only (0002) out-of-plane orientations. The full width at half maximum (FWHM) for the poles of both the grains in the pole figure is less than  $1^\circ$ . After 8 h of annealing, no fringe orientations are observed. According to the Brandon criterion, all the grains have a  $\Sigma 13$  misorientation. Additionally, SADPs acquired from three different TEM-lamellae prepared from the same film revealed an exclusive bicrystalline diffraction pattern even at low magnification as seen in Fig. 4.14. The bright field (BF) images with marked GBs in Fig. 4.14 a), b) and c) reveal that we obtain diffraction information from multiple grains at once. The SADPs in Fig. 4.14 d), e) and f) show that all grains have exactly  $30^\circ$  misorientation. This proves that apart from the OR I and OR II grains, there are no grains present with any other orientation.

Furthermore, by keeping the substrate's [100] direction parallel to scan direction, we were able to determine the orientation relationship between the film and the substrate. All the grains can be primarily attributed to only two orientations. One grain is continuous and extends all over the substrate. This orientation is here on wards referred to as 'OR I'. The other orientation, 'OR II', is present as small islands surrounded by the large OR I grain. As seen in Fig. 4.12 c), the out-of-plane direction in the entire film is (002). To establish the complete orientation relationship of both grains, the direction of the grain that is parallel to [100] of the substrate is found from the EBSD data shown in Fig. 4.12 c). Using this we can determine the following orientation relationship:

$$\begin{aligned} \text{OR I: } & (0002)_{Ti} \parallel (001)_{SrTiO_3}, [5\bar{7}20]_{Ti} \parallel [100]_{SrTiO_3} \\ \text{OR II: } & (0002)_{Ti} \parallel (001)_{SrTiO_3}, [5\bar{4}\bar{1}0]_{Ti} \parallel [100]_{SrTiO_3} \end{aligned}$$



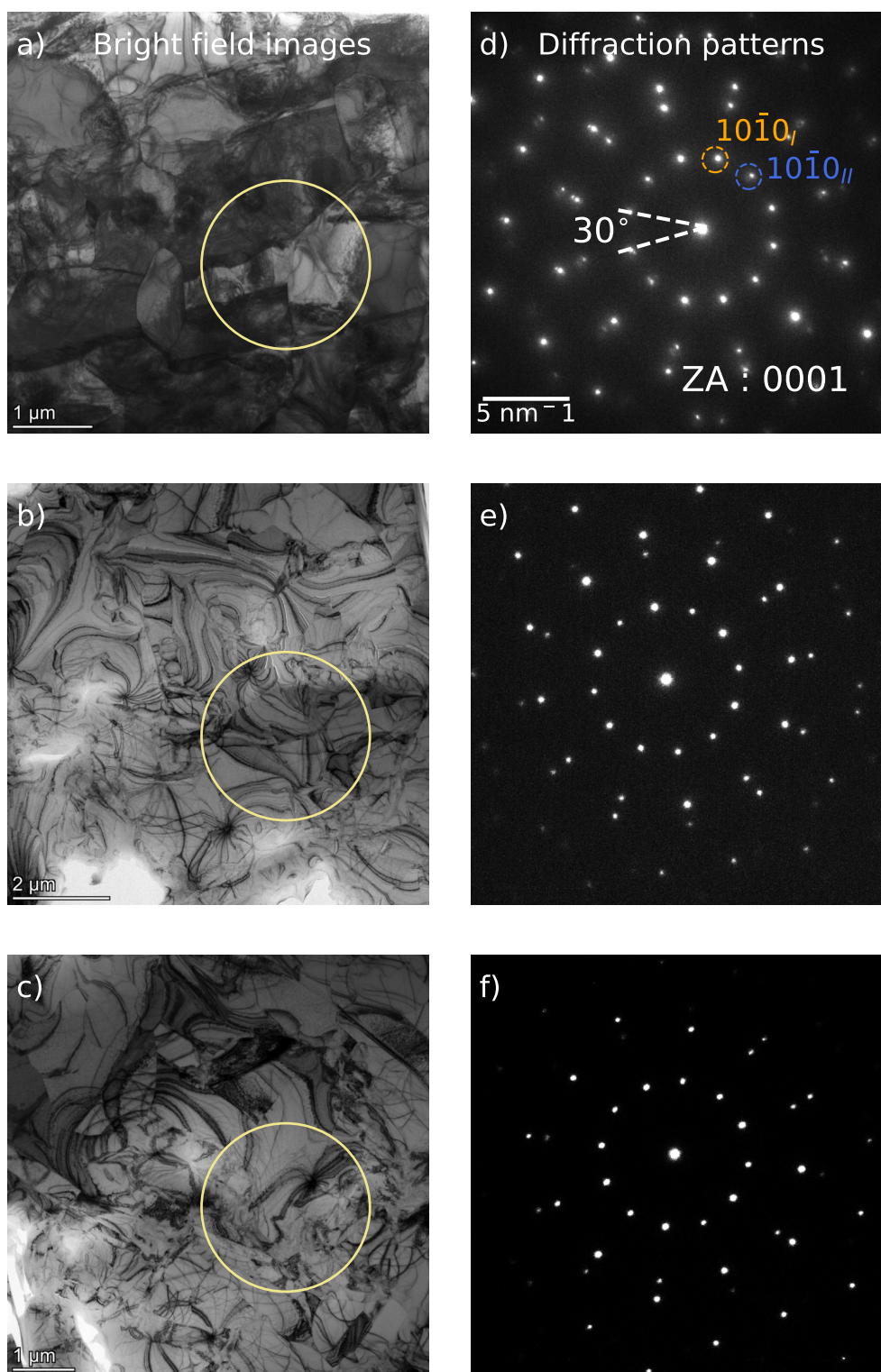


**Figure 4.13** a), b) and c) Bright field TEM micrographs acquired at low magnification from three different lamellae lifted out from the Ti thin film deposited on  $\text{SrTiO}_3$  at  $600^\circ\text{C}$  and annealed at  $600^\circ\text{C}$  for 8h. The selected area apertures used to capture the SADPs are marked in yellow circles. d), e) and f) The corresponding  $[0001]$  zone axis SADPs confirm the  $30^\circ$   $[0001]$  misorientation.

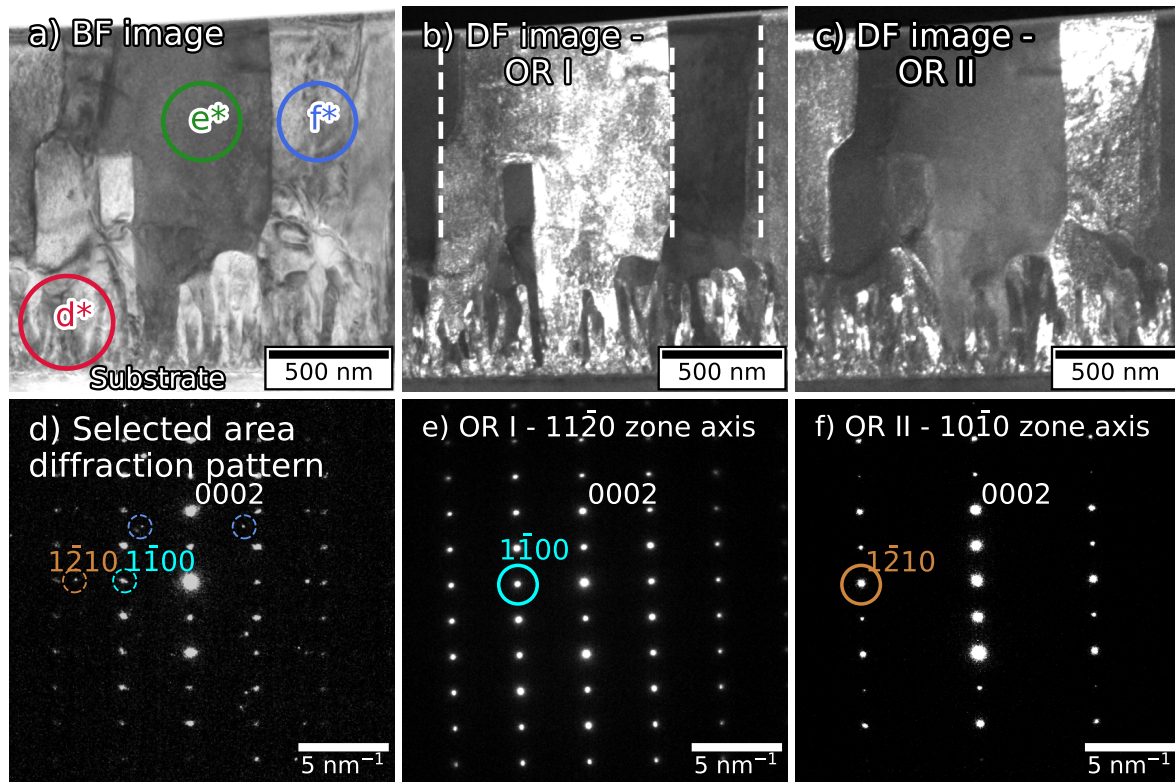


**Figure 4.14** Ti thin film deposited on SrTiO<sub>3</sub> at 600°C and annealed at 600°C for 8h a) Bright field (BF) TEM micrograph of the cross-section showing columnar grains and vertical GBs. The red, green and blue coloured circles schematically indicate the aperture locations used to acquire the selected area diffraction patterns (SADPs) seen in d), e) and f), respectively. b) Dark field (DF) TEM micrograph acquired using the  $1\bar{1}00$  reflection in e). c) Dark field TEM micrographs acquired using the  $\{1\bar{2}10\}$  reflection in f). d) SADP acquired from the smaller columnar grains at the interface of the substrate and the film. The blue dotted circles highlight the additional reflections seen only in the interface region. e), f) Diffraction patterns acquired from the two grains corresponding to OR I and OR II, respectively. The cyan and brown circle represent the diffraction spots used to acquire the dark field micrographs.

The unique grain map shown in Fig. 4.12 d) shows that OR II is embedded in OR I. The novelty of the pulsed magnetron sputtered films is that they are not only bicrystalline, but the majority of the grains are columnar leading to a strongly textured film microstructure. We examined a cross-section TEM lamella to observe the microstructure of the film in the growth direction. As shown in Fig. 4.14, BF/DF TEM imaging was used to further investigate the evolution of the grain structure in growth direction. From the BF TEM image shown in Fig. 4.14 a) it becomes apparent that nanoscale columnar grains are present near the film-substrate interface, which then transition into large near micron-sized grains at a distance of  $\sim 300$  nm from the substrate. We acquired SADPs from two columnar grains with schematic locations of the apertures as indicated by green and blue circle in Fig. 4.14 a). The SADP in Fig. 4.14 e) is in  $[10\bar{1}0]$  zone axis and the SADP in Fig. 4.14 f) is in  $[11\bar{2}0]$  zone axis. Both of these SADPs were acquired without stage tilt between them and the two zone axes are  $30^\circ$  apart which is in agreement with the orientation relationship observed using EBSD. Subsequently, dark field images shown in Fig. 4.14 b) and c) were acquired from the two OR using the highlighted diffraction spots in Fig. 4.14 e) and f). The SADP acquired from the columnar nanograins (d\* in Fig. 4.14 a)) shows that it is mostly a sum of the diffraction patterns shown in Fig. 4.14 b) and c). This indicates that most of the small columnar grains also adopt either OR I or OR II orientation. The additional reflections marked in blue in Fig. 4.14 d) are stemming from a few in-plane rotated grains which exist only close to the film-substrate interface. To the best of our knowledge, this is the first report of a bicrystalline Ti thin film which is particularly interesting due to the challenges involved in producing a bulk Ti bicrystal.

Additionally, as seen in Fig. 4.15, STEM-EDS elemental mapping at the film-substrate interface was used to verify that within the detectable limits of STEM-EDS, no elemental segregation or intermixing of the film and substrate occurred. Therefore, we presume that interface have an influence on the observed columnar grain growth and orientation relationships. Ti and Sr were the major elements recorded in the EDS spectrum. Additionally, stray signals are obtained from the Cu TEM lift-out grid and Fe pole piece. A coherent bremsstrahlung peak is observed as the mapping was performed in zone-axis.

### 4.2.2 Grain size and grain growth measurement

A larger in-plane grain size is seen for the films deposited by pulsed magnetron sputtering compared to the film deposited using dcMS. However, due to the maze-like microstructure of the pulsed magnetron sputtered films, the grain size distribution

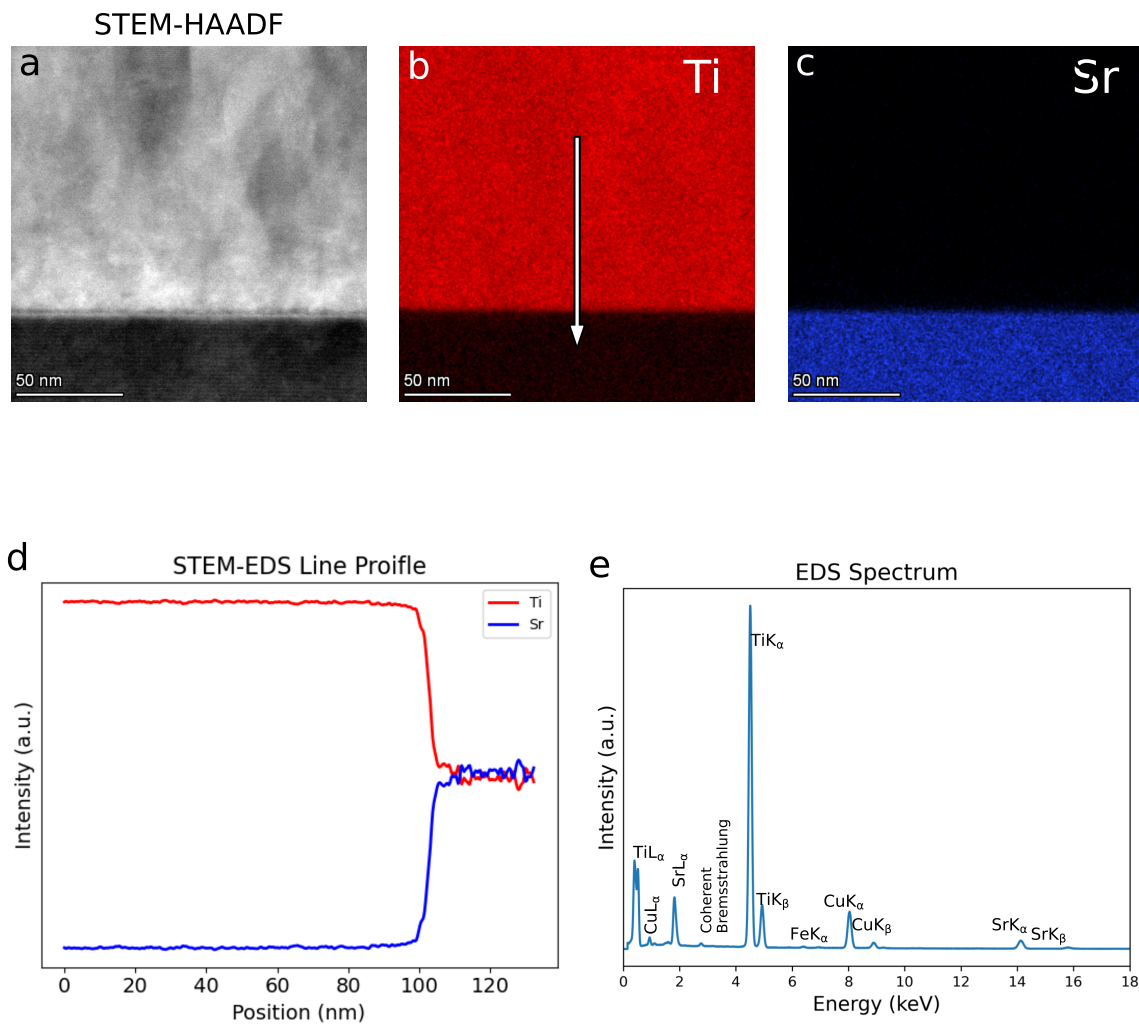


**Figure 4.15** a) HAADF image of the Ti-SrTiO<sub>3</sub> film-substrate interface. b), c) STEM-EDS area mapping showing Ti and Sr distribution. d) Line profile of Ti and Sr concentration across the interface. e) The sum of STEM-EDS spectra obtained from 512\*512 pixels from the film-substrate interface seen in the HAADF image.

data has to be generated separately for OR I and OR II grains. The OR I grain is essentially one large continuous grain extending over the entire substrate, therefore, the line interception method (in the TSL OIM software) was used to measure the average width of the grain. In this method, several horizontal lines were drawn across the EBSD scan area to measure the mean intercept length (width) of the OR I grain. For the OR II grains, the equivalent circle diameter was calculated using the grain area.

The increase in width of the OR I grain as a function of annealing duration is given in Table 4.3. The width remains almost the same within the error limit between the 2 h and 4 h annealed films, however, it largely increases for the 8 h annealed film. Similarly, a decrease in the grain size of OR II from 2 h to 8 h is observed, due to the shrinkage of the island grains. A net increase in the grain size as a function of annealing duration can be noted by measuring the length of GB for a given area of the film. As seen in Table 4.3, for an area of  $25 \mu\text{m} \times 20 \mu\text{m}$ , the length of  $\Sigma 13$  GB reduces from 1.38 mm to 895  $\mu\text{m}$  to 525  $\mu\text{m}$  for 2 h, 4 h and 8 h film, respectively. It is generally considered that grain growth in thin films is arrested when the grain size is about one to two times the film thickness [319]. The driving force for grains to grow 2-dimensionally is much smaller than 3-dimensional growth. As seen from the EBSD results in Fig. 4.12, the GBs are meandering through the film, resulting in a low mean radius of curvature. This exerts a capillary force on the GBs to straighten them which promotes their migration towards their centre of curvature. This causes both grain growth and shrinkage in different sections of the grain. Similar phenomena have been observed in bicrystalline Au films [312].

**Table 4.3** Deposition conditions, OR I/ OR II grain size and  $\Sigma 13$  GB length of the pulsed magnetron sputtered films.

Annealing temperature & time	OR I grain (intercept length- $\mu\text{m}$ )	OR II grain (diameter- $\mu\text{m}$ )	GB length
600°C & 2 h	$0.68 \pm 0.55$	$5.10 \pm 2.74$	1.38 mm
600°C & 4 h	$0.60 \pm 0.68$	$1.96 \pm 1.18$	895 $\mu\text{m}$
600°C & 8 h	$2.81 \pm 2.53$	$1.75 \pm 0.84$	525 $\mu\text{m}$

Additionally, using the TSL-OIM software, a partition of OR I and OR II orientation is created from the acquired EBSD data for all three films deposited using pulsed magnetron sputtering. The OR II oriented grains are highlighted in blue in Fig. 4.16 a), b) and c) for 2 h, 4 h and 8 h of annealing, respectively. As a function of annealing time, the OR I orientation grows at the expense of OR II orientation resulting in an increase in the single crystallinity percentage, as shown in Fig. 4.16 d).

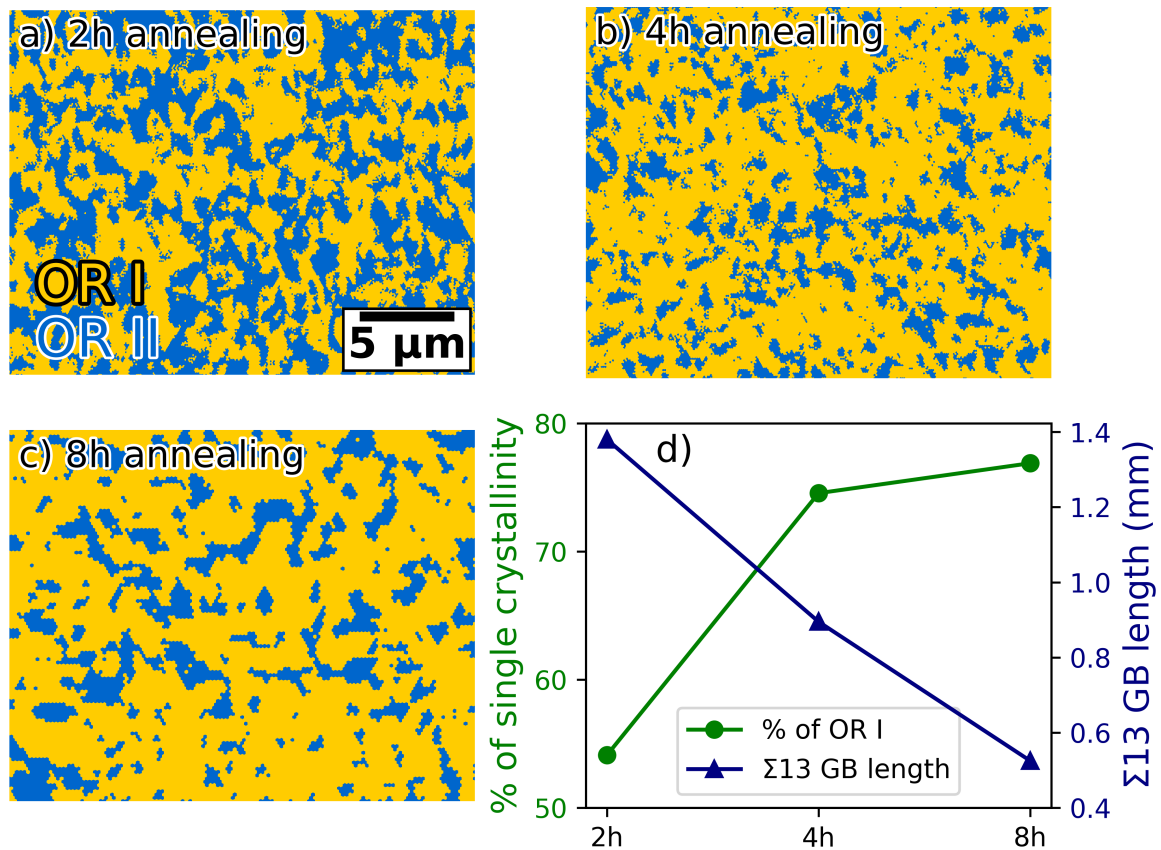


**Figure 4.16** a), b) and c) show EBSD images of pulse magnetron sputtered films deposited at 600°C and annealed at 600°C for 2h, 4h and 8h, respectively, partitioned into OR I (yellow) and OR II (blue) grains. d) The increasing area fraction of OR I grain and the decreasing length of GB per unit area are plotted with respect to annealing duration demonstrating grain growth and increasing % of single crystallinity.

### 4.2.3 Coincident site lattice and GB planes

Before discussing the results further, we briefly describe the key concepts utilised to analyse the GB structure at atomic scale. A dichromatic pattern is an essential tool to analyse GBs. Its use for interface analysis was introduced by Pond and Bollmann [151]. Dichromatic pattern is created by assigning two colours to the two lattices on either side of the GB and extending the lattices to the other side of the GB.

Due to the six fold symmetry of the basal plane in hcp crystal structure, GBs with misorientation of  $\theta$  and  $60^\circ - \theta$  are equivalent. The  $\Sigma 13$  CSL can be obtained by both  $27.8^\circ$  and  $32.2^\circ$  misorientation of both grains around the common  $[0001]$  tilt axis. There are two possible symmetric GB variants in the  $\Sigma 13$   $[0001]$  misorientation that are only  $2.2^\circ$  apart. Therefore, plane trace analysis may not be sufficient to unambiguously identify them.

Fig. 4.17 shows a dichromatic pattern obtained by a  $27.8^\circ$  tilt along  $[0001]$  resulting in a  $\Sigma 13$  CSL relationship. The two interpenetrating lattices, ' $\lambda$ ' and ' $\mu$ ', are depicted in red and blue colour, respectively. Such a dichromatic pattern can be used to evaluate the possible GB habit planes. To index the planes passing through the CSL points, we identify the  $\Sigma 13$  CSL unit cell. The 'PQRS' is a CSL unit cell whose four sides and the shorter body diagonal are symmetrically equivalent. The longer diagonal, QS is the second symmetric variant. It makes  $30^\circ$  angle to the first symmetric variant. To index the GB plane vectors (and their subsequent GB normals), first we map the path from one CSL point to the other CSL point by moving along either of the lattices. Next, we add the constituting lattice vectors to index the planes.

The direction RS in  $\lambda$  (red) grain:

$$\begin{aligned} RS &= RR' + R'S \\ &= [1\bar{1}00] + 4[01\bar{1}0] \\ &= [13\bar{4}0] \end{aligned} \quad (4.2)$$

The GB plane (perpendicular to RS) is  $(7\bar{5}\bar{2}0)$ .

The direction QS in  $\lambda$  (red) grain:

$$\begin{aligned} QS &= QQ' + Q'S \\ &= 2[01\bar{1}0] + 5[10\bar{1}0] \\ &= [52\bar{7}0] \end{aligned} \quad (4.3)$$

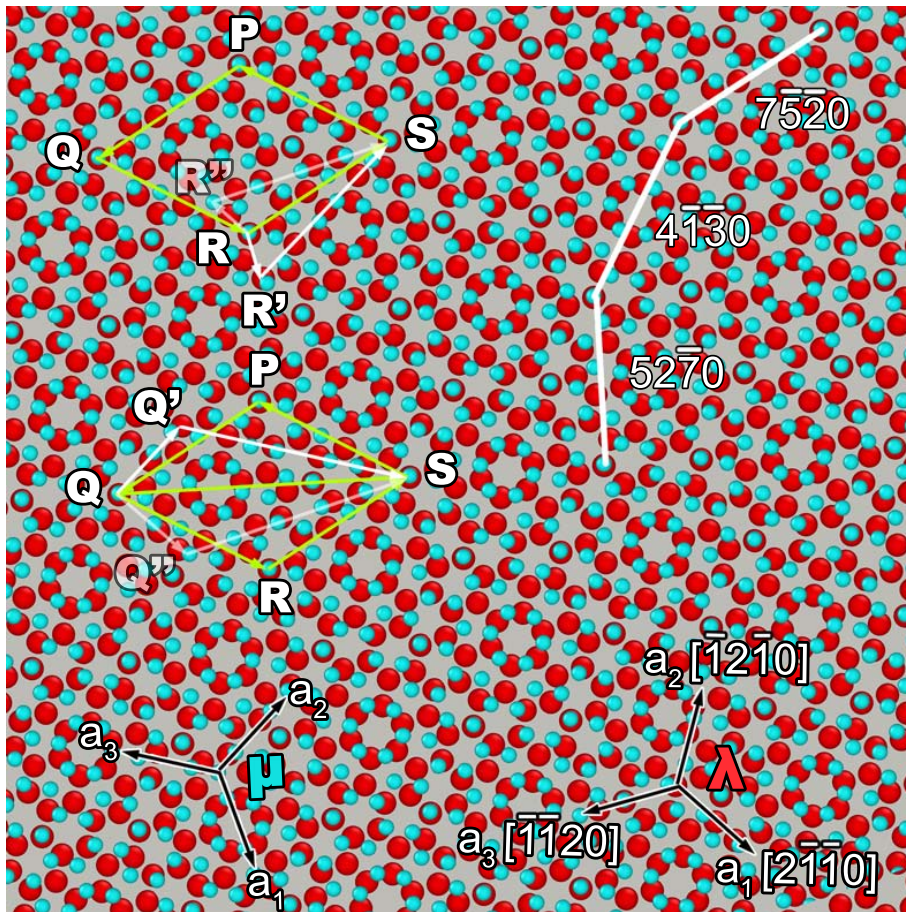


**Figure 4.17** A  $\Sigma 13$  dichromatic pattern is constructed using two grains,  $\mu$  (cyan) and  $\lambda$  (red). The CSL unit cell (PQRS) is marked. The shorter and longer diagonals are the GB planes  $\{7\bar{5}20\}$  and  $\{4\bar{3}\bar{1}0\}$ , respectively. The circuit used to index the GB planes is marked in white.



The GB plane (perpendicular to QS) is  $(3\bar{4}10)$ .

Since they are symmetric GBs, the same GB indices can also be obtained by mapping the  $\mu$  grain.

$$\begin{aligned} RS &= RR'' + R''S \\ &= [\bar{1}010] + 4[01\bar{1}0] \\ &= [\bar{1}4\bar{3}0] \end{aligned} \quad (4.4)$$

The GB plane (perpendicular to RS) is  $(7\bar{2}\bar{5}0)$ .

$$\begin{aligned} QS &= QQ'' + Q''S \\ &= 2[10\bar{1}0] + 5[01\bar{1}0] \\ &= [25\bar{7}0] \end{aligned} \quad (4.5)$$

The GB plane (perpendicular to QS) is  $(4\bar{3}\bar{1}0)$ .

The misorientation is verified by noting that the angle between  $(7\bar{5}\bar{2}0)$  and  $(7\bar{2}\bar{5}0)$  is  $27.8^\circ$ . Additionally, it can also be observed that the angle between any two adjacent GB planes (facets),  $(7\bar{2}\bar{5}0)$  and  $(4\bar{3}\bar{1}0)$  is  $30^\circ$ .

When considering the  $32.2^\circ$  GB:

For the  $\mu$  (green) grain:

$$\begin{aligned} RS &= RR' + R'S \\ &= [\bar{1}100] + 4[10\bar{1}0]RS = RR' + R'S \\ &= [31\bar{4}0] \end{aligned} \quad (4.6)$$

The GB plane (perpendicular to RS) for the  $\mu$  (green) grain is  $(7\bar{5}\bar{2}0)$ .

For the  $\lambda$  (red) grain, the GB plane can be similarly found to be:

$$\begin{aligned} RS &= RR'' + R''S \\ &= [1\bar{1}00] + 4[01\bar{1}0] \\ &= [13\bar{4}0] \end{aligned} \quad (4.7)$$

The GB plane (perpendicular to RS) for the  $\lambda$  grain is  $(5\bar{7}20)$ .

The misorientation is verified by noting that the angle between  $(5\bar{7}20)$  and  $(7\bar{5}\bar{2}0)$

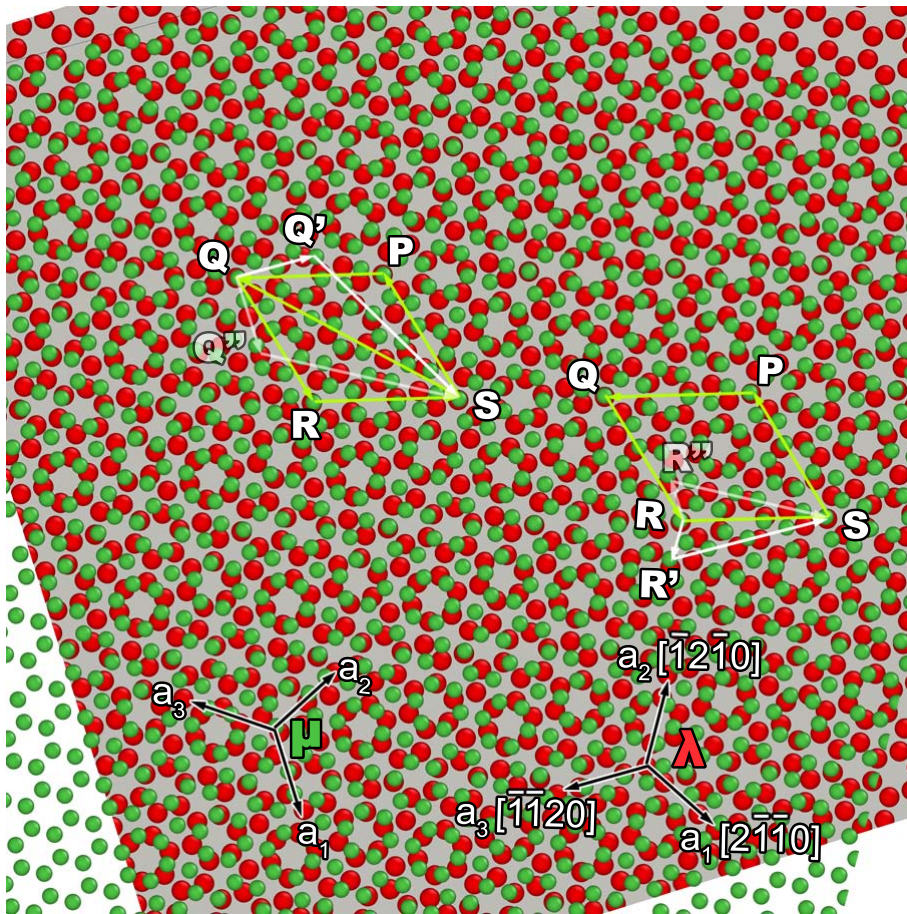


**Figure 4.18** A  $\Sigma_{13}$  dichromatic pattern is constructed by rotating the two basal planes by  $32.2^\circ$  instead of  $28.8^\circ$  as observed in the previous case. The CSL unit cell (PQRS) is marked. The shorter and longer diagonals are the GB planes  $\{7\bar{5}20\}$  and  $\{4\bar{3}10\}$ , respectively.

is  $32.2^\circ$ .

The direction QS for lambda (red) grain is given by:

$$\begin{aligned} QS &= QQ' + Q'S \\ &= 2[1\bar{1}00] + 5[10\bar{1}0] \\ &= [7\bar{2}\bar{5}0] \end{aligned} \quad (4.8)$$

The GB plane (perpendicular to RS) for lambda grain is  $(1\bar{4}30)$ .

The direction QS for the mu (teal) grain is:

$$\begin{aligned} QS &= QQ'' + Q''S \\ &= 2[01\bar{1}0] + 5[10\bar{1}0] \\ &= [52\bar{7}0] \end{aligned} \quad (4.9)$$

The GB plane (perpendicular to RS) is  $(3\bar{4}10)$ . The misorientation is verified by noting that the angle between  $(1\bar{4}30)$  and  $(3\bar{4}10)$  is  $32.2^\circ$ .

#### 4.2.4 Grain boundary faceting

The  $\Sigma 13$  GBs in Fig. 4.10 b) and Fig. 4.12 c) are observed to be continuously curved and to form a mazed bicrystalline microstructure. Such GB curvature is often accommodated by faceting if the inclinational dependence of the grain boundary energies is anisotropic [78, 320]. Upon investigation at a higher magnification, the GBs are observed to be faceted, as seen in Fig. 4.19 a). The plane normal of each facet plane is  $30^\circ$  apart from each other. A fast Fourier transform (FFT) of the HAADF-STEM image in Fig. 4.19 a) can be used to index the GB planes. Because the GBs are all edge-on, as previously demonstrated in Fig. 4.12 b), the GB planes can be indexed by simply locating the intersection of the GB plane normals to the great-circle in the (0001) stereographic projection of Ti. However, a more precise method of GB plane indexing is demonstrated in detail in Fig. 4.17 and Fig. 4.18. Using this method, the GB facets are indexed to be  $\{\bar{7}520\}$  and  $\{\bar{4}310\}$  symmetric planes. From the FFT it is also apparent that  $\{\bar{7}520\}$  and  $\{\bar{4}310\}$  are the only conceivable symmetric GB plane families in  $\Sigma 13$  [0001] hcp GBs. GB planes with any other Miller indices would be asymmetric. A preference for the symmetric GB planes is readily apparent.

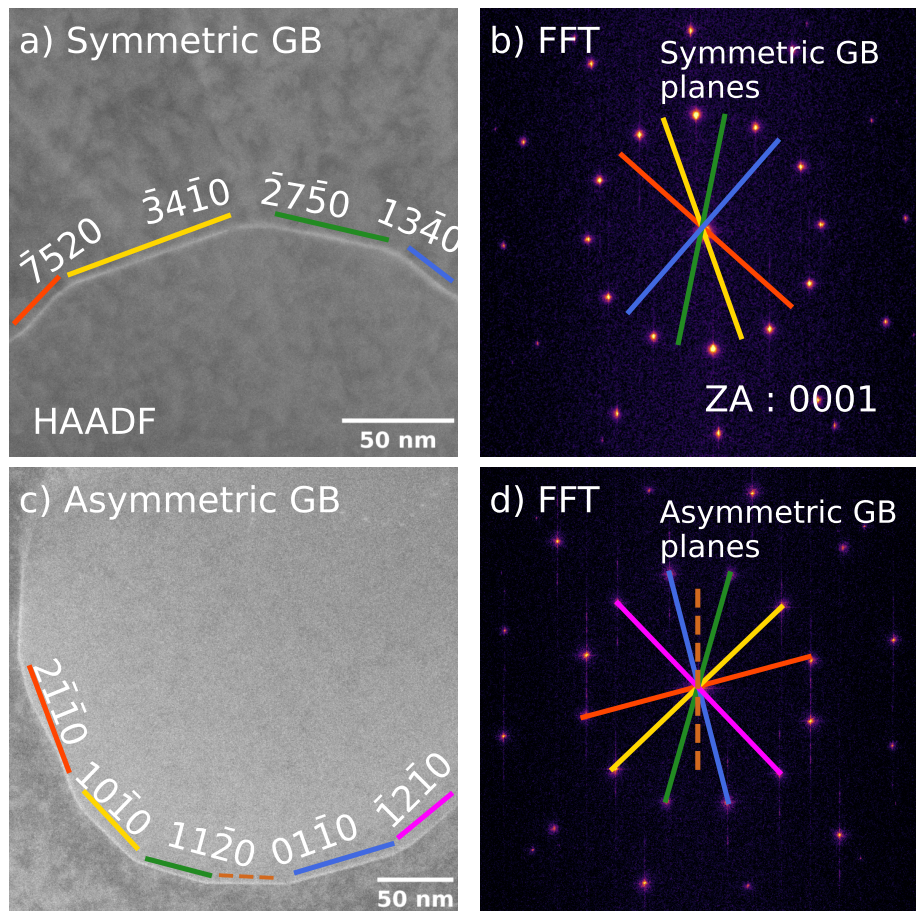


**Figure 4.19** a) HAADF-STEM image of  $\Sigma 13$  [0001] Ti GB in the pulse magnetron sputtered film deposited at 600°C and post-annealed at 600°C for 8 h showing a faceted GB with symmetric GB facets. Each GB plane is represented by a different colour. b) Fast Fourier transform (FFT) of the HAADF-STEM image in a). c) HAADF-STEM image of from a different region showing asymmetric GB facets. d) FFT from the HAADF-STEM image shown in c). The dashed brown line is a symmetric facet present between the two asymmetric facets.

In another instance, as seen in Fig. 4.19 c), although the GB facet normals are still  $30^\circ$  apart, the planes were indexed to be low-index asymmetric  $\{10\bar{1}0\} // \{2\bar{1}\bar{1}0\}$  planes. The diffraction pattern shown in Fig. 4.19 d) confirms the asymmetry of the facets. According to the authors' observations, out of over  $\sim 200 \mu\text{m}$  of GB less than  $\sim 30 \mu\text{m}$  of the GB is asymmetric, which corresponds to less than  $\sim 15\%$  of the GB being asymmetric.

It must be made clear that the contrast in the GB comes from diffraction. The change in the GB contrast with the changing collection angles of the HAADF-STEM images is shown in Fig. 4.20. Even at a HAADF collection angles of 78-200 mrad, diffraction contrast can still contribute to the image. The observed diffraction contrast stems from strain fields at the GB or local sample thickness variations. This becomes very evident when using a low-angle annular dark field (LAADF) detector for imaging. As seen in the Fig. 4.20, the GB can be seen to be very bright in LAADF-STEM compared to the HAADF-STEM image.

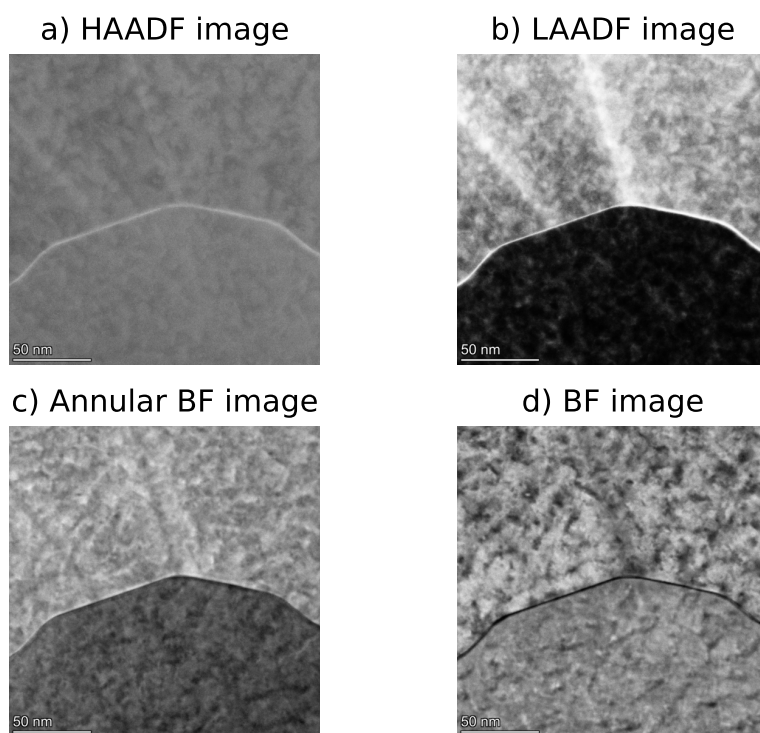


**Figure 4.20** High angle annular dark field (HAADF), low angle annular dark field (LAADF), annular bright field (ABF) and bright field (BF) images of the  $\Sigma 13$  GB captured simultaneously showing the variation in GB contrast with the change of collection angle.

#### 4.2.5 Anisotropic Fe segregation in symmetric GB facets

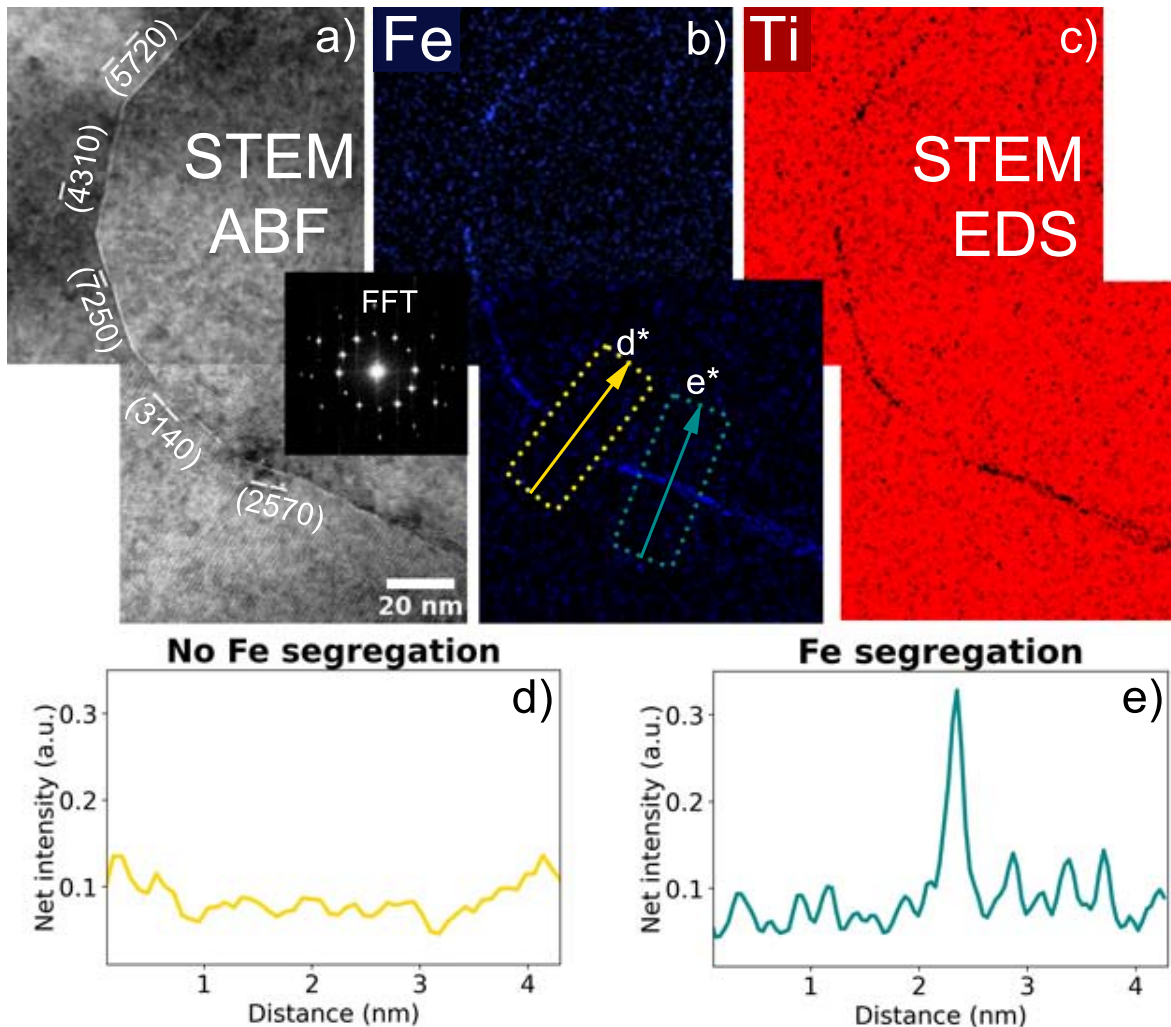


**Figure 4.21** a) STEM annular-BF image showing GB facets with symmetric  $\{\bar{7}520\}$  GB planes. EDS reveals segregation of b) Fe in alternate GB facet, c) depletion of Ti in the Fe rich region. The Fe rich GBs are found to be planes with lower CSL density. d), e) Net-intensity line profile across the two symmetric facets revealing a strong segregation of Fe in only the  $(\bar{2}570)$  facet.

Fe was present as an impurity in the sputtering target therefore it is of interest to examine where it is present in the deposited films. In the film deposited using pulse magnetron sputtering and post-annealing for 8h at  $600^\circ$ , the  $\Sigma 13$   $[0001]$  Ti GB is seen to be composed of  $\{\bar{7}520\}$  symmetric GB facets, as shown in Fig. 4.21 a). The facets are similar to the GB faceting discussed in Fig. 4.19. The elemental distribution map of Fe, acquired using STEM-EDS at 300 kV, reveals a preferential segregation of Fe to every alternate symmetric facet. However, we do not see a change in the contrast between neighbouring GB facets in the HAADF-STEM images in Fig. 4.19. This is because the contrast from GBs observed at lower resolution represents a superposition

of various effects stemming from strain contrast due to the presence of GB defects, local sample thickness and compositional variations. The Fe present in the GB facets is not high enough to produce a clear HAADF signal under these observation conditions. For completeness, the change in GB contrast with decreasing collection angles of the annular STEM detectors is shown in Fig. 4.20.

In Fig. 4.21, Fe segregation is observed at  $(\bar{5}7\bar{2}0)$ ,  $(\bar{7}250)$ , and  $(\bar{2}\bar{5}70)$  facets, but Fe is not detected at  $(\bar{4}310)$  and  $(\bar{3}\bar{1}40)$  facets. The counts of the Fe signal in the EDS spectrum are integrated along the highlighted arrow over the marked region as seen in Fig. 4.21 b). Fig. 4.21 d) and Fig. 4.21 e) show line profiles across the corresponding facets to clearly illustrate the segregation of Fe at the  $(\bar{2}\bar{5}70)$  GB plane and the absence of Fe-segregation in the  $(\bar{3}\bar{1}40)$  facet. The FWHM of the spacial distribution of Fe in Fig. 4.21 e) is  $\sim 0.15$  nm confirming the segregation of Fe is limited to the GB.

To quantify the amount of segregation APT was used. Firstly, the GB facet containing Fe was targeted to be lifted-out using the conventional FIB sample preparation technique and field evaporated in laser-mode. After the reconstruction of data using AP Suite, the atom distribution maps of Ti and O are obtained, as shown in Fig. 4.22 a). Both of them are seen to be distributed uniformly in both the grains and the GB region. Fe is seen in Fig. 4.22 b), c) and d) to distinctly segregate to the GB. To delineate the Fe GB segregation, a 0.5 at% Fe isoconcentration surface is plotted in Fig. 4.22 b) and as seen in Fig. 4.22 d), the GB is edge-on. A cylinder of 30 nm diameter and 50 nm length is highlighted as the selected region of interest (ROI). Although the GB extends over the entire cross-section of the APT tip, Fe is seen enriched at only a fraction of the GB area. The composition along the ROI in both Fig. 4.22 b) and Fig. 4.22 c) are plotted in Fig. 4.22 e) and Fig. 4.22 f), respectively. Negligible Fe segregation is observed in Fig. 4.22 e) whereas significant Fe segregation of up to  $\sim 0.5$  at.% is observed in Fig. 4.22 f). The Fe segregation is distributed to a width of  $\sim 8$  nm (FWHM  $< 4$  nm). The segregation width is significantly larger than the expected GB width due to the artefacts from field evaporation and aberrations in the trajectory of ions [321]. Nevertheless, this apparent increase of GB width is inconsequential for a homo-phase boundary as the concentration on both sides of the Gibbsian dividing surface can be considered to be identical. Although not highlighted in Fig. 4.22 b), c) and d) for clarity, three ROIs of the same dimensions were taken for better statistics.

As seen in Fig. 4.22 g), plotting the number of Fe atoms against the total number of atoms of all elements in the region of interest allows us to measure the number of

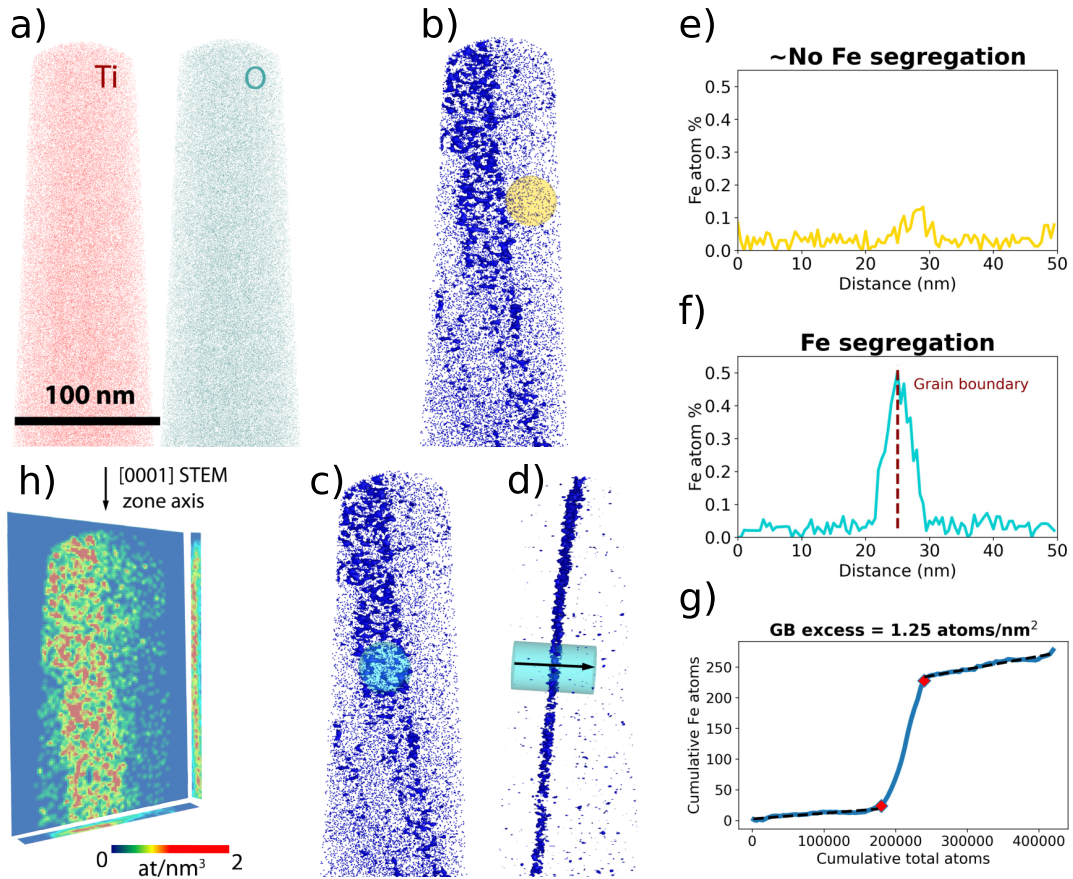


**Figure 4.22** a) Reconstruction point cloud from atom probe tomography (APT) showing Ti and O atoms marked in red and green, respectively. No enrichment or depletion of either of the elements is observed at the GB. b) Isocomposition surface of 0.5 at.% Fe delineates the GB and demonstrates the segregation limited to a fraction of the GB area present in the tip. The region of interest (ROI) used for composition analysis through the GB segment having no Fe segregation is highlighted (in gold). c), d) ROI passing through the Fe-enriched GB region is depicted in both front and side view, respectively (in teal). e), f) The composition profile of Fe plotted against the length of the highlighted ROI exhibits ~no Fe segregation and Fe-segregation, respectively. The Fe-segregation is limited to GB width and also limited to only a fraction of the GB. g) The ladder diagram shows GB segregation of Fe with equally low solubility in the grain interior on both sides of the interface; the Gibbsian GB excess is calculated as explained in [285]. h) The in-plane atomic density distribution of Fe at the GB plane.



GB excess Fe atoms per unit area of the interface,  $N_{Fe}$ . Using the equation Eq. (3.1),  $\Gamma_{Fe}$  is found to be  $1.25 \pm 0.1$  atoms/nm<sup>2</sup>. Since the  $\{\bar{7}250\}$  GB has  $\sim 8-10$  at/nm<sup>2</sup> (ambiguity arises because of the dependence of planar-atomic-density on the width of a high-index GB plane), the amount of segregation can also be described as  $\sim 0.2$  monolayers, assuming that the Fe segregation is limited to the GB plane. The relationship between misorientation and GB excess property measured using APT has been discussed in cubic materials [6, 322], however no report for hcp metals was found in the literature. To emphasize that the segregation of Fe is limited to the GB plane, and to show its distribution, an areal density plot of Fe in the GB plane is shown in Fig. 4.22 h).

## 4.2.6 Discussion

### Thin film deposition and texture evolution

Physical vapor deposition, which includes both DC sputtering and pulsed magnetron sputtering, is a plasma-based thin film deposition technique. In this technique, the inert gas ions (usually Ar) are accelerated towards the target material (cathode) and the sputtered atoms are allowed to condense on the substrate to form a thin film. The degree of ionisation of the plasma particles determines the ion flux towards the growing film [316]. In DC sputtering penning ionisation is the main ionisation mechanism. The ion-flux during the deposition can have a significant impact on the film microstructure. A high ion fraction in a discharge is achieved by promoting the electron impact ionization which is achieved by using plasma of high electron density and higher temperature. Such a plasma is formed by using a pulsing unit at the target. The electron density in the plasma varies from  $10^{14} - 10^{16}$  m<sup>-3</sup> in DC sputtering to  $10^{18}$  m<sup>-3</sup> when using the sputtering source in a pulsing mode. During deposition using pulsing mode, the frequency of the power applied to the sputtering source is defined by 'duty cycle' which is the ratio,  $t_{ON} / (t_{ON} + t_{OFF})$ . Typically, a duty cycle of up to  $<5\%$  can be termed as high power pulsed magnetron sputtering (HPPMS), while a duty cycle  $>5\%$  is called pulsed magnetron sputtering [323]. Here a duty cycle of  $10\%$  was deployed, so the method is termed as pulsed magnetron sputtering throughout the paper. Low ionisation of the plasma generally leads to a high number of defects and poor adhesion between the film and the substrate whereas high ionisation of the plasma leads to a dense film, good adhesion and lower residual stresses [280].

In a plasma with a large degree of ionization, the ion flux to the substrate is larger

than for discharges with a low degree of ionization [281]. The magnitude of ion current affects the morphology evolution which is evident when comparing the SE image of the film deposited by dcMS in Fig. 4.9 a) and the SE image of the film deposited by pulsed magnetron sputtering in Fig. 4.10 a). The incoming sputtered atoms from the target when adsorbed on the substrate surface are called adatoms. Due to the dense plasma in pulsed magnetron sputtering, adatom mobility to low surface energy sites with high coordination is promoted. Enhanced surface diffusion eliminates the voids and surface mounds and consequently reduces the surface roughness of the grown films. It also leads to a smoother surface finish [324]. Increase in surface smoothness and density of films on using higher duty cycles have been reported earlier in  $\text{TiO}_x$  [316].

Additionally, the lowest surface energy plane, (0002), dominated over the lowest strain energy plane,  $\{10\bar{1}1\}$ . The high flux of ions due to pulsing leads to the increased momentum transfer between the plasma and the condensed metal atoms. Such a high flux increases the mobility of surface adatoms and accommodates them on planes of the lowest surface energy. This determined the out-of-plane surface orientation. A similar change in texture evolution in changing the deposition method from dcMS to pulsed magnetron sputtering favouring the high atomic density surface planes has also been reported in other materials [323, 325, 326]. The two in-plane orientation relationships were found using the EBSD data in Fig. 4.12. The misfit ( $\delta$ ) can be calculated using  $\delta = (1 - \frac{d_f}{d_s})$ , where  $d_f$  and  $d_s$  are the film and substrate lattice spacing. The lattice parameter for cubic  $\text{SrTiO}_3$  is  $a=3.9 \text{ \AA}$ .  $d_{5\bar{7}20}$  and  $d_{\bar{5}410}$  are  $0.409 \text{ \AA}$  and  $0.577 \text{ \AA}$ , respectively. Using the domain matching epitaxy (DME) paradigm [292, 327], we can calculate the misfit strain for OR I in the two in-plane directions to be 4.8% and 3.5%. Because the film has hexagonal symmetry and the substrate has cubic, there are two misfit values. For the other orientation, the misfit strain is 3.5% and 4.8%. The misfit strain is the same for the other orientation, however it is merely swapped because the two orientations are  $30^\circ$  in-plane rotations of each other. The theoretical misfit calculation and the experimentally observed ORs seem to match well. But on a microscopic scale, the residual stresses, the distribution of misfit dislocations in Ti, the surface plane termination of the  $\text{SrTiO}_3$ , surface irregularities and the adsorption on the substrate surface are some of the other factors that can determine the OR. The influence of these parameters on OR determination would require further detailed analysis of the interface.

All pulsed magnetron sputtered films were observed to have columnar grains. This can be explained using the structure zone model (SZM). The SZM is commonly used

to determine the dependence of film microstructure on the discharge pressure, and the homologous temperature [328]. The film microstructure according to this model is categorized into four zones, namely Zone 1, Zone T, Zone 2, and Zone 3 based on the substrate temperature during deposition. Zone T has limited surface diffusion and grain boundary mobility. This leads to 'V' shaped columnar grains where the grains with lower surface energy compete with other orientations during grain growth. In the zone II, due to increased surface diffusion, the preferred orientations nucleate at the substrate surface and grow as columnar grains. This leads to near vertical GBs [329]. Detailed discussion on the model can be found in [329]. In the present film, the deposition temperature of 600°C lies in the early zone II ( $T_s / T_m \sim 0.45$ ;  $T_s$ : deposition T,  $T_m$ : melting point of target). As expected using SZM, the cross-section of the film reveals a combination of zone II and zone T in Fig. 4.14. The dark field micrographs reveal that most of the smaller grains at the interface belong to either OR I or OR II, an event of mere probability, because both the orientations lead to same misfit. Apart from the EBSD, the misorientation between the grains is also verified from the diffraction patterns obtained from the cross-section. All the columnar grains are observed to be either in  $[10\bar{1}0]$  or  $[11\bar{2}0]$  zone axis, which verifies a 30° in-plane rotation. The most important consequence of this is that all the GBs can be identified as  $\Sigma 13$ . These textured films are of great interest, for example in microelectronics for applications such as diffusion barriers in integrated circuits [119]. The low surface energy of the bicrystalline texture films can also improve the corrosion resistance of the coatings. One could also speculate that by using the films of right orientation, the wear resistance or mechanical properties of the thin-film could be enhanced.

Due to the mazed bicrystalline microstructure, the GB plane changes continuously but the GB is characterized by the same disorientation. High-resolution STEM imaging was used to identify the GB planes because even a detailed EBSD scan with a step size of <10 nm is not sufficient to index such finely faceted/rounded GBs.

### Grain boundary faceting

Faceting is the dissociation of a GB into segments with different GB plane inclination but the same overall misorientation. It principally occurs to reduce the overall GB energy. The total energy of a faceted GB is the sum of the energy of individual GB segments and their interaction energy at the facet junctions. As faceting leads to an increase in GB plane area, the facets must have lower energy than the parent GB for faceting to occur. Although GB faceting has been widely reported in many cubic metals [330–332], to the best of the authors' knowledge, no experimental evidence of GB

faceting has been reported for Ti. Here, we show that the GB plane which would otherwise be asymmetric due to its continuous curvature, dissociates into distinct facets.

Since all grains are columnar, it is evident that all the GBs in a basal-plane textured film are prismatic in nature. Moreover, there is a competition between the low index asymmetric prismatic  $\{10\bar{1}0\} // \{2\bar{1}\bar{1}0\}$  GB planes and the symmetric prismatic  $\{\bar{7}520\}$  and  $\{\bar{4}310\}$  GB planes. The prismatic planes have been shown to be the preferred GB facet plane in other hcp materials [333, 334]. A 3D-EBSD study on bulk-Ti reported a large fraction of grains with misorientation  $\leq 30^\circ$  having prismatic GB planes with a preference for  $\{\bar{7}520\}$  [334]. Therefore, not only are the  $\{\bar{7}520\}$  GBs preponderant in thin films, but they are also frequently observed in the bulk commercially pure Ti. Also, prismatic planes are preferred in the  $\beta \rightarrow \alpha$  martensitic phase transformation in Ti [335]. The  $\{\bar{7}520\}$  prismatic planes are also predominant in  $\Sigma 13$  [0001] GBs in Mg [336]. Using atomistic calculations, Ostapovets et al. were able to show that the minima of [0001] tilt GB energy corresponds to  $\{\bar{7}520\}$  [336]. Although, similar GB energy calculations via MD simulation for Ti [0001] tilt-GBs are missing, it is expected that Ti could follow a similar trend as in Mg. Therefore, the observed GB faceting in Fig. 4.19 a) and Fig. 4.21 a) into  $\{\bar{7}520\}$  and  $\{\bar{4}310\}$  symmetric segments can be considered to be a result of the GB energy-minimization in hcp materials.

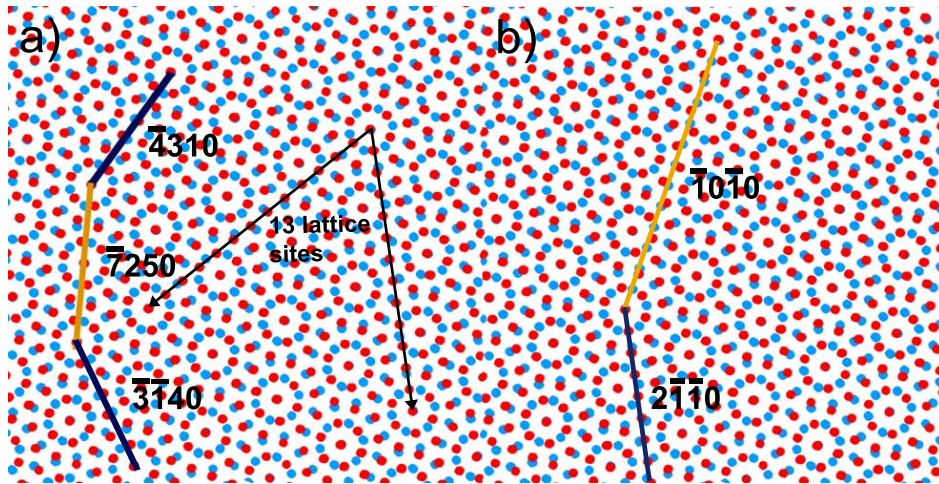


**Figure 4.23** Schematic of  $\Sigma 13$  GB with planes a)  $\{\bar{7}520\}$  and  $\{\bar{5}7\bar{2}0\}$  consisting of highest and second highest planar coincident site density (PCSD), respectively leading to reduction of GB energy. b)  $\{2\bar{1}\bar{1}0\}$  and  $\{10\bar{1}0\}$  have a lower PCSD but higher effective d-spacing ( $d_{eff}$ ) leading to the second most frequently observed GB facet plane.

To develop a thermodynamic understanding of the GB plane selection during faceting and anisotropic segregation of Fe observed in Fig. 4.21, it is necessary to reveal the atomic structure and the local energetics of the particular GB. The atomic structure

investigation is beyond the scope of the present study but a simple approach to rationalize the observations can be used. The CSL model is the most widely applied tool for classifying GBs. It distinguishes grain misorientations that place a large fraction of the lattice sites of the two grains in coincidence from the remaining 'general' misorientations. The sigma value represents the inverse of the number of the coinciding sites. If the GB plane passes through the coinciding points, then such a GB plane can have low energy. The term, 'planar coincident site density' (PCSD) is used to quantify the density of CSL sites on the GB plane. In a SrTiO<sub>3</sub>  $\Sigma 3$  (111) twist boundary, the high PCSD was held responsible for the observed GB plane [337]. To illustrate the role of PCSD in GB plane selection, a dichromatic pattern of hcp (0001) is drawn in Fig. 4.23. The  $(\bar{7}520)$  symmetric plane that is highlighted in 'gold' has the highest PCSD,  $\Gamma = 0.43$ , in  $\Sigma 13$  [0001] hcp GBs. This is followed by the  $(\bar{3}4\bar{1}0)$  plane highlighted in 'dark-blue' which has a  $\Gamma = 0.33$ .

Additionally, when considering the prismatic plane with the smallest Miller indices,  $\{2\bar{1}\bar{1}0\}$  and  $\{10\bar{1}0\}$  can be seen to have a much lower PCSD in Fig. 4.23 b). However, the selection of GB planes cannot be entirely described by PCSD. In several cubic materials, no dependence of GB plane selection on PCSD is seen [337]. In brass and nickel, a systematic GB plane analysis demonstrated that the dependence of interplanar spacing of the GB planes,  $d_{eff}$ , is the more critical criterion than PCSD in the selection of the GB planes [338]. For a symmetric GB, the  $d_{eff}$  is same as the d-spacing of the GB plane, while for an asymmetric GB, the  $d_{eff}$  is given by:

$$d_{eff} = \frac{(d_1 + d_2)}{2} \quad (4.10)$$

where  $d_1$  and  $d_2$  are the d-spacing of the GB planes for each grain. The  $d_{eff}$  is a means to generalize the d-spacing criterion for the asymmetric boundaries [339]. The energy of an unrelaxed boundary increases as the d-spacing decreases, because the atoms with the shortest d-spacing contribute the most to the boundary energy. Consequently, low-index GB planes due to their larger d-spacing are preferred [340]. In terms of probability, there are many possible asymmetric GBs and limited symmetric GBs. However, once the low-index plane for one grain is fixed, the index of the other plane is constrained by the misorientation. As a result, most asymmetric GBs have a low  $d_{eff}$  and are hence unfavorable. This is why symmetric GB planes appear more frequently than random distribution.

For the  $\Sigma 13$  GB, the two symmetric GB planes  $\{\bar{4}310\}$  and  $\{\bar{7}520\}$  have a d-spacing of 0.709 Å and 0.409 Å, respectively. The d-spacing of GBs with  $\{10\bar{1}0\}$  and  $\{2\bar{1}\bar{1}0\}$

habit planes is larger with  $2.55 \text{ \AA}$  and  $1.475 \text{ \AA}$ , respectively. However, they typically form asymmetric GB variants with  $\{10\bar{1}0\} // \{15\bar{7}\bar{8}0\}$  habit planes leading to a smaller  $d_{eff}$  of  $1.421 \text{ \AA}$ . Despite the fact that the asymmetric GBs exhibit a larger  $d_{eff}$  than the symmetric GBs, GBs with  $\{\bar{7}520\}$  and  $\{\bar{4}310\}$  habit planes are observed more frequently in the present study, but also in Mg and Ti-64 alloys [334, 336]. This confirms that other than the PCSD and d-spacing, the atomic structure of the GBs and their related excess thermodynamic properties influence the GB plane selection. It is well established that GBs act as a 'phase' in themselves and have an atomic structure that is distinct from the two abutting grains [8, 341]. In all of existing literature that discusses the rules for selection of the GB [337, 338, 340], the atomic structure of GB has never been taken into consideration. However, the structure of the GB can play a major role in determining its thermodynamic properties. The structure of the GB would also determine its ability to accommodate defects, equilibrium solute segregation and their influence on the GB energy. Therefore, although a combination of PCSD and  $d_{eff}$  can be used to argue the stability of certain GB planes, further investigation of the atomic structure of the  $\{\bar{7}520\}$  is needed to establish the reason for stability of the high-index symmetric GB plane over the low-index asymmetric plane, which is an ongoing work.

### Grain boundary segregation

Solute segregation at GBs is known to largely influence the mechanical behaviour of metals either negatively, such as by embrittlement, or positively, by pinning the GBs and thus restricting grain growth, thereby strengthening it [342–344]. Solute segregation can also lead to faceting of the GB [345, 346].

Following the Gibbs adsorption isotherm, the earliest model of GB segregation was given by McLean [347]. It was built on the theory of surface adsorption by Langmuir [348]. The Langmuir-McLean isotherm describes that increasing the concentration of solute in the grain or lowering the temperature leads to higher solute concentration in the GB for a dilute binary system. This is a highly simplified model and does not differentiate between any two sites at the interface, nor does it consider the interaction between the solute atoms. Fowler and Guggenheim treated GBs as a regular solution by introducing an additional parameter,  $\omega$ , to describe the interaction between the solute species. In many dilute systems, such as B in Fe-40%Al [349] and P, S, Sn in Fe [350], Fowler and Guggenheim isotherm has been used to describe the segregation behaviour. However, besides the model being valid in a limited concentration range, it

also does not consider the GB parameters. Numerous statistical thermodynamic models have been proposed by Wynblatt and Ku [351], Seah [352], BFS [353] and others to calculate the enthalpy and entropy of segregation by, for example, calculating the difference in heat of formation with and without solute at the GB. These models can calculate the thermodynamic functions accurately, given the atomic structure of the GB is known. Similarly, several phase field models have been used to define GBs as the spatial variations in an otherwise continuous atomic density field. These approaches require assumptions of GB parameters such as GB site coordination [354] or GB density [355]. Such calculations for a specific GB require the knowledge of its atomic structure and available sites for solute segregation. The knowledge of atomic structure of hcp GBs is severely limited. Films deposited in the present study paves the way for study of GB atomic structure which is essential for all thermodynamic GB property calculations.

The segregation of Fe in Ti is a known phenomenon. Random high angle GBs in Ti have been shown to be stabilized by the segregation of Fe in the substitutional sites [47]. Fe segregation has also been reported in commercial Ti alloys with no analysis of the influence of GB type on the segregation behaviour [356, 357]. In the present study, Fe was observed to segregate preferentially in selected symmetric facets in  $\Sigma 13$  (0001) Ti GB, as seen in Fig. 4.21. All the symmetric facets were a priori expected to show isotropic behaviour as they belong to the same family of planes and are bound by the same two grains. The observed peculiar anisotropy is to a first approximation rationalized using the PCSD. The GB planes  $(\bar{7}520)$  and  $(\bar{5}270)$  have a higher PCSD and are seen to have lean or no segregation whereas, the GB planes  $(\bar{5}7\bar{2}0)$ ,  $(\bar{7}250)$ , and  $(\bar{2}570)$  have a lower PCSD and have much higher Fe segregation. Clearly, a lower PCSD seems to favour Fe solute segregation in Ti.

Beyond characterizing the GB plane, it is of great interest to quantify the amount of segregation. Such studies began in the early 1980s using surface analysis techniques like Auger electron spectroscopy (AES) and secondary ion mass spectroscopy (SIMS) of fracture surfaces [349, 358–360]. With the manifold advancement of the analytical power of STEM, EDS and electron energy loss spectroscopy (EELS) are now regularly used to quantify the lean segregation of even less than 0.01 monolayer at the GB [184, 361, 362]. More recently, state-of-the-art STEM techniques and atom probe tomography have been utilized in a correlative fashion to obtain spatial and chemical information from the same region down to almost atomic scale [6, 322, 363–366]. A similar approach was used here to site specifically lift-out a symmetric GB and quantify the Fe segregation as seen in Fig. 4.22. Although, the EDS clearly shows Fe segregation

and partitioning to different GB segments, it needs however long counting times and thus may cause redistribution of Fe like seen in other metallic systems [7]. Therefore, APT is used for the quantification of solute concentration. Additionally, the distribution of concentration in the third-dimension cannot be obtained in the STEM-EDS. It also helps to find any additional scarce impurity present in the material. From the atom distribution in Fig. 4.22, a uniform distribution of Ti and O is confirmed. Although the concentration of O is high,  $\sim 28\text{at.}\%$ , it is measured to be uniformly distributed over the entire tip volume. The high O content in the film is due to the high solubility limit (32 at.%) of O in Ti [367, 368]. Because the deposition chamber had a vacuum of only  $2.2 \times 10^{-6}$  mbar, and Ti is widely used as a getter for O, the film is expected to have a high dissolved O content. However, no oxides or other secondary phases are detected. Most importantly, the distribution of O is not altered at the GB and can therefore be assumed to not have an influence on the Fe segregation.

Although the GB plane cannot be found from the APT data, we know that the film has mostly  $\Sigma 13$  GBs, with only two possible GB planes. As discussed earlier, the symmetric  $\{\bar{7}250\}$  and  $\{\bar{4}310\}$  GB is present  $\sim 20$  times more often than the  $(10\bar{1}0)$  /  $(11\bar{2}0)$  asymmetric variant, therefore we assume the captured GB to be a symmetric GB. Furthermore, the Fe distribution is restricted to  $\sim 40\text{-}50$  nm, which is about the same as the length of symmetric facet. Combining the results of STEM and APT, it is likely that we captured two of the symmetric GB facets, for example,  $\{\bar{2}\bar{5}70\}$  and  $\{\bar{3}\bar{1}40\}$  within our atom probe tip. While the former has a rich and uniform Fe distribution, the latter is lean in Fe. The area density distribution map in Fig. 4.22 h) distinctly shows that Fe is uniformly distributed in an area corresponding to one GB segment. The decrease in the density of the Fe in the right part of the GB can be attributed to the commencement of the adjacent facet that is lean in Fe. A striking similarity suggesting the Fe-segregation restricted to symmetric GB segment can be seen in both Fig. 4.21 d), e) and Fig. 4.22 e), f).

The subsequent measurement of interfacial excess using a 'ladder diagram' gave a  $\Gamma_{Fe}$  of  $1.25 \text{ at/nm}^2$  or 0.2 monolayer. The  $\text{GB}_{\text{excess}}$  measurement has been used as a method to scrutinize phase formation in the GBs [369]. 0.2 monolayer corresponds to one in every five atoms at the GB plane being Fe. Assuming that all Fe atoms are restricted to the GB plane, the stoichiometry corresponds to a  $\text{Ti}_{0.8}\text{Fe}_{0.2}$  intermetallic BCC phase [370]. With the spatial resolution of APT, there is no way to ascertain if the present observation is GB segregation (either by strain or chemically induced by



bonding/charge transfer) or a GB phase transformation. Based on the local arrangement and bonding of Fe, its influence on the material properties could largely vary. This necessitates the requirement of additional experiments using STEM to discern the atomic structure of the GB with and without Fe, which is an ongoing work. Moreover, the measurement of GB excess properties for all other frequently observed GBs will pave way for GB phase diagrams and GB engineering in the future.

## 4.3 STEM investigation of atomic-scale structural transitions in Ti grain boundaries

This section is based on:

V. Devulapalli, M. Hans, J. M. Schneider, G. Dehm, and C. H. Liebscher, *Influence of Fe segregation on atomic structure of  $\Sigma 13$  [0001] grain boundary in Ti*,

*Manuscript prepared, yet to be submitted*

In this chapter, HRSTEM is used to reveal the atomic structure of GBs present in the Ti thin films that were discussed in the previous chapter. After analysing the GB facets at the atomic scale, we found that the symmetric GBs that are free of any solute content are constituted of periodic structural units. The defect content of the structural units is found using the topological theory. When a small amount of Fe is introduced to the same GB, the GB structure gets completely modified. The Fe-containing atomic columns in the new structural units are encircled by a cage-like Ti structure. EDS is used to verify that the bright atomic columns in HAADF-STEM imaging correspond to Fe. Asymmetric GBs with same misorientation are observed to have similar cage-like structural units with varied Fe-column spacing. Kinks in the GB are observed to lead to a clustering of the cages. Overall, the structural unit model is established for the first time for Ti and a structural transformations of the GB are seen due to segregation.

### 4.3.1 Thin film characterization

The GBs that are discussed in the following section were all obtained from the thin films that were discussed in the previous section. A commercially pure Ti target (with 0.2 wt. % Fe impurity) was used to deposit a Ti thin film on (100) orientated SrTiO<sub>3</sub> substrate by using pulsed magnetron sputtering. The deposition and the post-annealing was carried out at the same temperature of 600°C for 8 h.

As seen in Fig. 4.24, the combination of orientation map, pole figure and unique grain map reveal a bicrystalline microstructure consisting of two ORs. All the identified GBs can be attributed to  $\Sigma 13$  [0001], as discussed in Section 4.2.

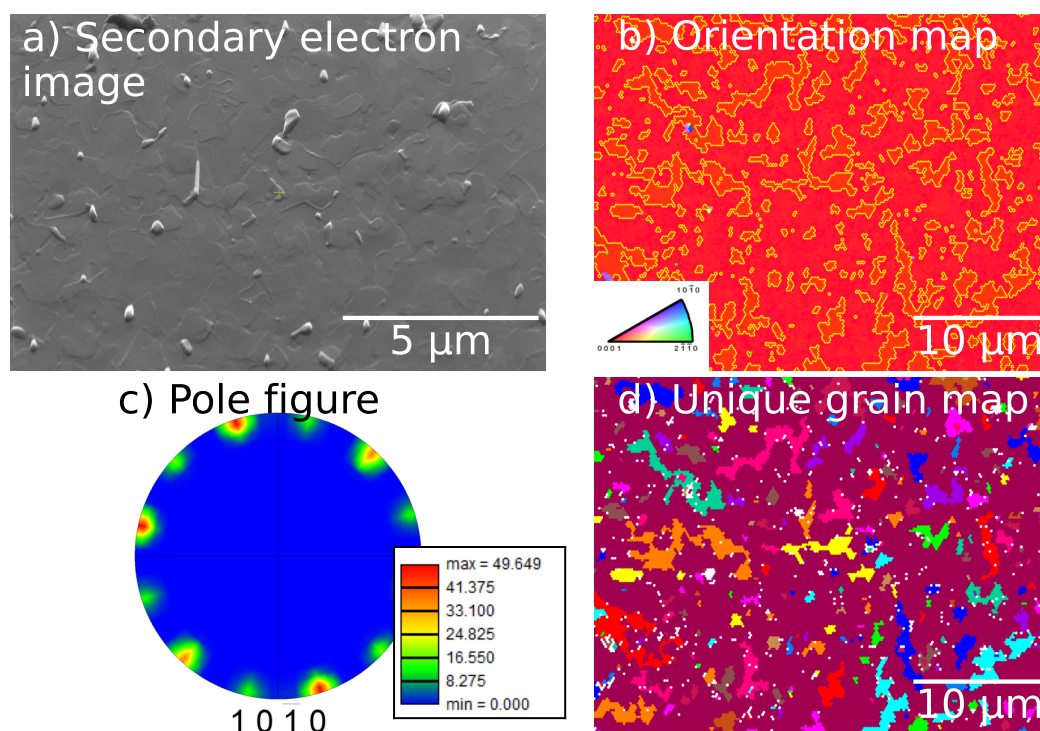


**Figure 4.24** Ti thin film deposited on SrTiO<sub>3</sub> at 600°C. a) SE image shows a smooth surface finish and little contrast between the grains. b) Orientation map obtained using the EBSD shows the two highly dominant out-of-plane orientations. c) 10 $\bar{1}0$  pole figure generated from the same EBSD data shows only two dominant in-plane rotations. d) The combination of unique grain map and orientation map shows that one of the orientation relationships is a single grain that extended all over the substrate, while all the other fragmented smaller grains belong to the second orientation relationship.

### 4.3.2 Structural unit model for 'clean', symmetric $\Sigma 13$ GB

The GBs are further investigated in greater detail using aberration corrected STEM imaging. As shown in Fig. 4.19, TEM investigation revealed that GB facets could be indexed as symmetric  $\{\bar{7}520\}$  and  $\{13\bar{4}0\}$  or asymmetric  $\{11\bar{2}0\} // \{10\bar{1}0\}$  planes. First, we investigate the symmetric GBs at atomic scale. Fig. 4.25 shows a symmetric  $\Sigma 13$   $[0001] \{\bar{7}520\}$  GB. The HAADF-STEM image was acquired with a beam convergence angle of 17 mrad and HAADF collection angle of 78-200 mrad at 5.1 Mx magnification. 40 frames of 512 \* 512 pixels are integrated using DCFI function in Thermo Scientific Velox<sup>TM</sup> software. Although faster scan results in more noise per frame, averaging multiple frames reduces it. Higher dwell time causes the beam profile to grow larger, thereby increasing the diffusion and accentuating the beam damage [371]. Therefore, with a faster beam raster, we lower the 'beam influence' to reduce the beam damage. lower beam damage. The raw integrated HAADF-STEM image is shown in the background. In the foreground is the Fourier-filtered image that allows

for easier peak detection and structure analysis.

Fig. 4.25 reveals that the atoms in the GB region are locally rearranged. The local rearranging of atomic columns at the GB region takes place in such a way that repeated polygons with specific lengths and angles are formed in the 2-dimensional projected view. These polygons are termed as structural units [5, 372]. In contrast to the hexagonal lattice seen inside the grains, the coordination of the atomic columns at the GBs differ. The structural units, named A, B, and C, for convenience, are found to constitute the entire GB in a periodic fashion. Using this notation, the GB can be represented as  $\dots ABCABC\dots$ . The inset shows a magnified region of the GB for clarity. The FFT in the bottom-left inset can be used to index the GB plane and to verify the symmetric nature of the GB.

Table 2.3 (43) shows the exact misorientation values along the  $[0001]$  axis to form exact-CSL GBs. The GB in Fig. 4.25 has a misorientation of  $30^\circ$ . Due to a  $2.2^\circ$  deviation between the exact  $\Sigma 13$  misorientation and the experimentally observed GB, we observe secondary defects in the GB. The  $\text{'ABCABC'}$  repeating pattern is broken at certain positions and replaced by a stacking fault-like defect consisting of  $\text{'AC'}$ ,  $\text{'AB'}$  or  $\text{'BC'}$  instead of  $\text{'ABC'}$ . This is expected because GBs are known to act as sinks for defects. Therefore, any deviation from the ideal CSL misorientation is compensated by defects. However, it is possible to pick a defect free region to further investigate the GB structure.

Firstly, we investigate the projected defect content of a single  $\text{'ABC'}$  GB structural unit. To perform this we utilize the GB circuit mapping, introduced by Pond *et al.* [151], to measure the defect content of structural units in several GBs [156, 215, 373]. The topological theory used here is briefly introduced in Section 2.4.2.

### Defect content of the experimentally observed structural units

In hcp system, the rotation along  $[0001]$  axis can be represented as:

$$R = \begin{bmatrix} \cos\theta & -\sin\theta & 0 & 0 \\ \sin\theta & \cos\theta & 0 & 0 \\ 0 & 0 & 1 & 0 \\ 0 & 0 & 0 & 1 \end{bmatrix} \quad (4.11)$$

For two grains in an hcp system,  $\lambda$  and  $\mu$ , a vector in the  $\lambda$  reference frame can be translated to  $\mu$  reference frame by using a transformation matrix  $\mathbf{P}$  that is derived using the R matrix. The transformation matrix P for a  $\Sigma 13$   $[0001]$  can be calculated

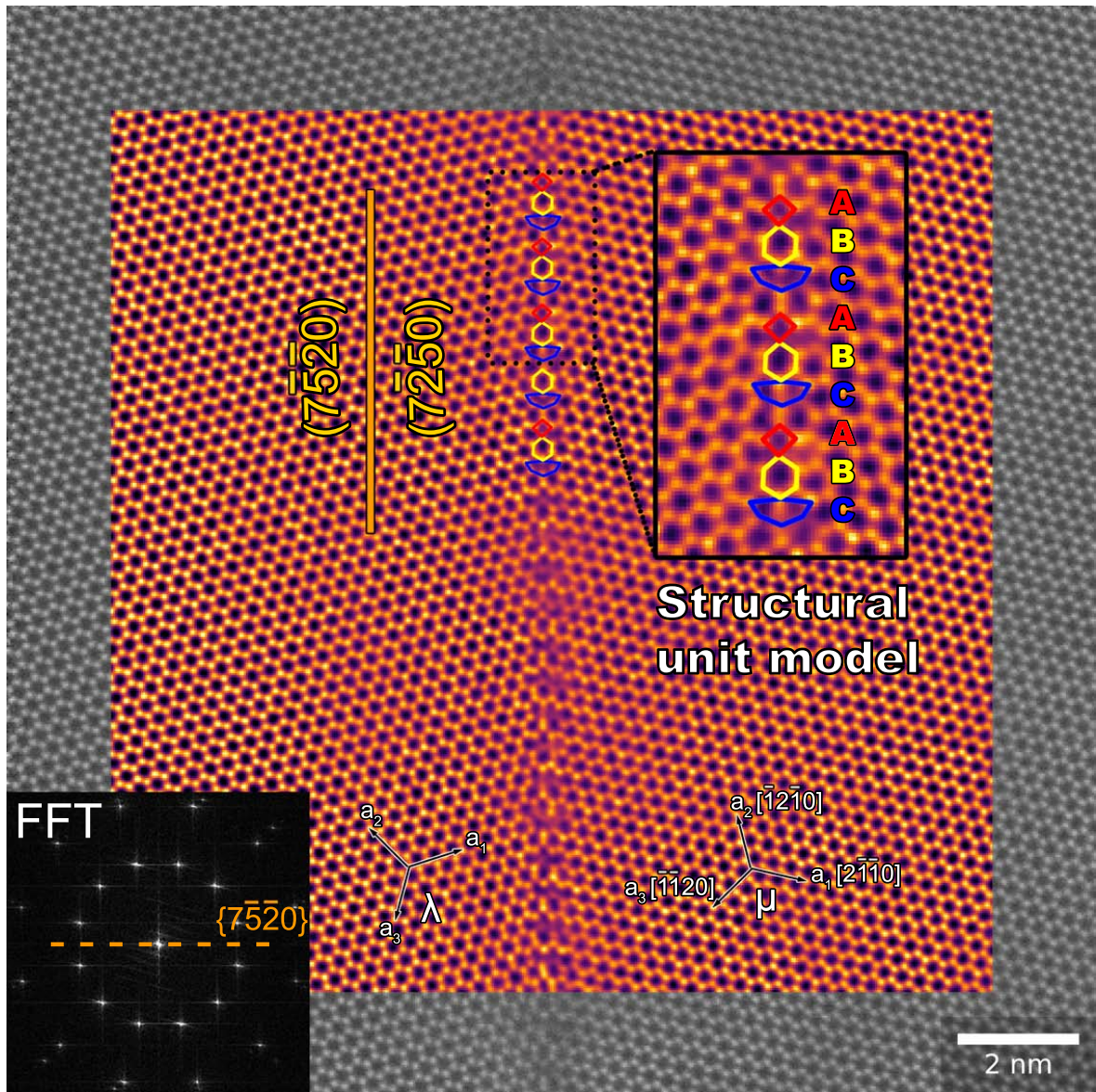


**Figure 4.25** Symmetric  $\Sigma_{13}$  [0001]  $\{7\bar{5}20\}$  GB in Ti imaged using HAADF-STEM demonstrates periodic arrangement of structural units ('ABC'). The FFT in the inset shows the  $30^\circ$  misorientation that is  $2.2^\circ$  away from the exact  $\Sigma_{13}$  misorientation.

to be: [215]

$$P_{13} = \frac{1}{39} \begin{bmatrix} 35 & -10 & 14 & 0 \\ 14 & 35 & -10 & 0 \\ -10 & 14 & 35 & 0 \\ 0 & 0 & 0 & 35 \end{bmatrix} \quad (4.12)$$

Additional details on obtaining the transformation matrix can be found in [154, 374–376]. The complete transformation relationship between the two grains is given by  $(\mathbf{P}, \mathbf{p})$  where  $\mathbf{p}$  is the rigid body translation. For the convenience we choose the

starting point of the circuit to be a coincident point such that  $\mathbf{p} = 0$ . Using the translation vectors and  $\mathbf{P}$ , the projected defect content of the circuit can be written as [154]:

$$\vec{b} = t(\mu) - P \times t(\lambda) \quad (4.13)$$

where  $\vec{b}$  is the Burgers vector of the defect at the interface.

Fig. 4.26 shows the magnified HAADF-STEM image of the 'clean'  $\Sigma 13 \{\bar{7}520\}$  structural units that were previously discussed in Fig. 4.25. As shown in Fig. 4.26 a), the period of the GB can be defined as the translation of  $a_1 + 4a_3$  in the  $\mu$  grain or a translation of  $a_1 + 4a_2$  in the  $\lambda$  grain. Such a translation moves the observer from one coincident site to another coincident site in the grain boundary. Next, we map the same translation in the undistorted reference lattice as shown in Fig. 4.26 b). The projected primary dislocation content of the GB can be found by mapping the GB circuit to either of the  $\mu$  or  $\lambda$  grain. The projected secondary defect content is determined when the GB circuit is mapped to the dichromatic pattern instead [215].

In Fig. 4.26 b), the SXF circuit from the experimental image is mapped once to the dichromatic pattern and once to  $\mu$  grain. The S and F in the dichromatic pattern are seen to coincide, which means that there are no secondary dislocations (sometimes referred to as disconnections) present at the selected region of the GB. When the circuit in the  $\lambda$  grain is rotated by the rotation matrix  $\mathbf{P}$ , the circuit is equivalent to being mapped on only the  $\mu$  grain. We can see that  $F' \rightarrow S = -2a_1$ . The same can also be calculated by using Eq. (4.13). From Fig. 4.26 and Fig. 4.27:

$$\begin{aligned} \vec{b} &= t(\mu) - Pt(\lambda) \\ &= ((-2a_1) + 4a_3 + 3a_1) - P(3a'_1 + 4a'_2 + (-2a'_1)) \\ &= ((-2a_1) + 4a_3 + 3a_1) - (3a_1 + 4a_2 + (-2a_1)) \\ &= 2a_1 + 4a_2 + 4a_3 \\ &= 2a_1 + 4(-a_1) \\ &= -2a_1 \\ \vec{b} &= \frac{-2}{3}[11\bar{2}0] \end{aligned}$$

Only when the reference frames for the two translation vectors,  $t(\lambda)$  and  $t(\mu)$ , are aligned, any vector operation can be performed on them. Therefore, we multiply  $t(\lambda)$  with  $\mathbf{P}$  to rotate it by  $27.8^\circ$  such that  $a'$  aligns with  $a$ . The same equation is also illustrated in Fig. 4.27. From this figure we can again see that the periodically

repeating structural unit, 'ABC', has a projected defect content of  $-2a$  or  $-2/3[11\bar{2}0]$  which is equivalent to two edge dislocations on the basal plane.

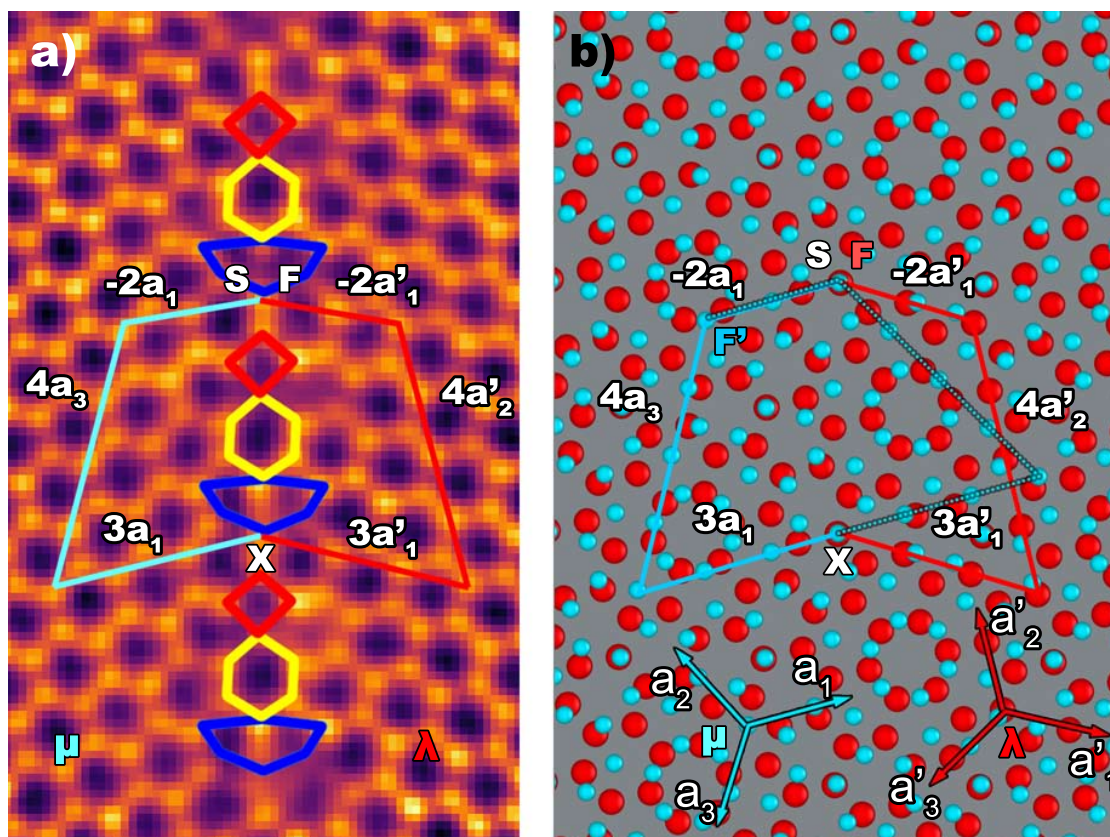


**Figure 4.26** a) Symmetric  $\Sigma 13$   $[0001] \{7\bar{5}20\}$  GB in Ti imaged using HAADF-STEM demonstrates periodic arrangement of structural units ('ABC'). The Burgers circuit is drawn connecting the two periodic atomic positions. b) The same circuit is retraced on a dichromatic pattern.

### 4.3.3 GB structural transition due to segregation

Fe segregation to the above discussed  $\Sigma 13$  GBs has already been discussed on a macroscopic scale in Section 4.2 [377]. It was shown that Fe preferentially segregates to certain GBs segments over others. The mechanism behind the preferential and anisotropic segregation was estimated to be a combination of interplanar spacing of GB planes and the planar coincidence site density (PCSD). However, only an atomic resolution investigation of the segregated GB region can provide a direct understanding of the mechanism behind segregation.

Fig. 4.28 shows a  $\Sigma 13$   $[0001] \{25\bar{7}0\}$  symmetric GB that is decorated with Fe. Few distinct features can be readily noted from the HAADF-STEM image. First, because

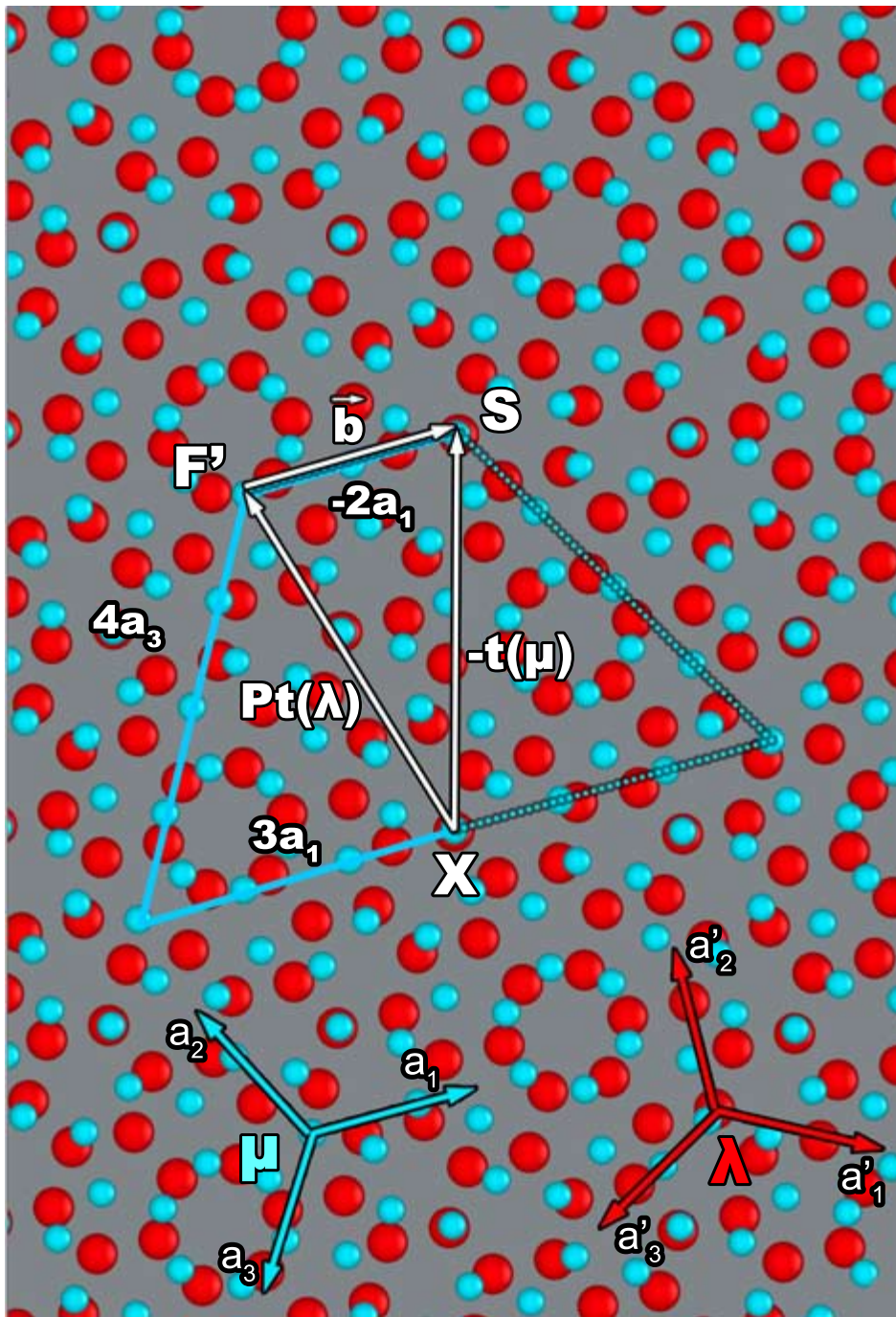


**Figure 4.27** The dichromatic pattern seen in Fig. 4.26 (b) is used to draw the vectors that represent the equivalents of mapped GB circuits to subsequently calculate the projected primary and secondary defect content of the  $\Sigma 13$  [0001] GB SUs.

the contrast in a HAADF image roughly corresponds to  $\sim Z^2$ , the brighter atomic column is rich in a relatively heavier element. A Fourier-filtered image is shown in the foreground with enhanced contrast to locate the peak positions with greater accuracy. Atomically resolved EDS discussed later shows the bright atomic column to be Fe.



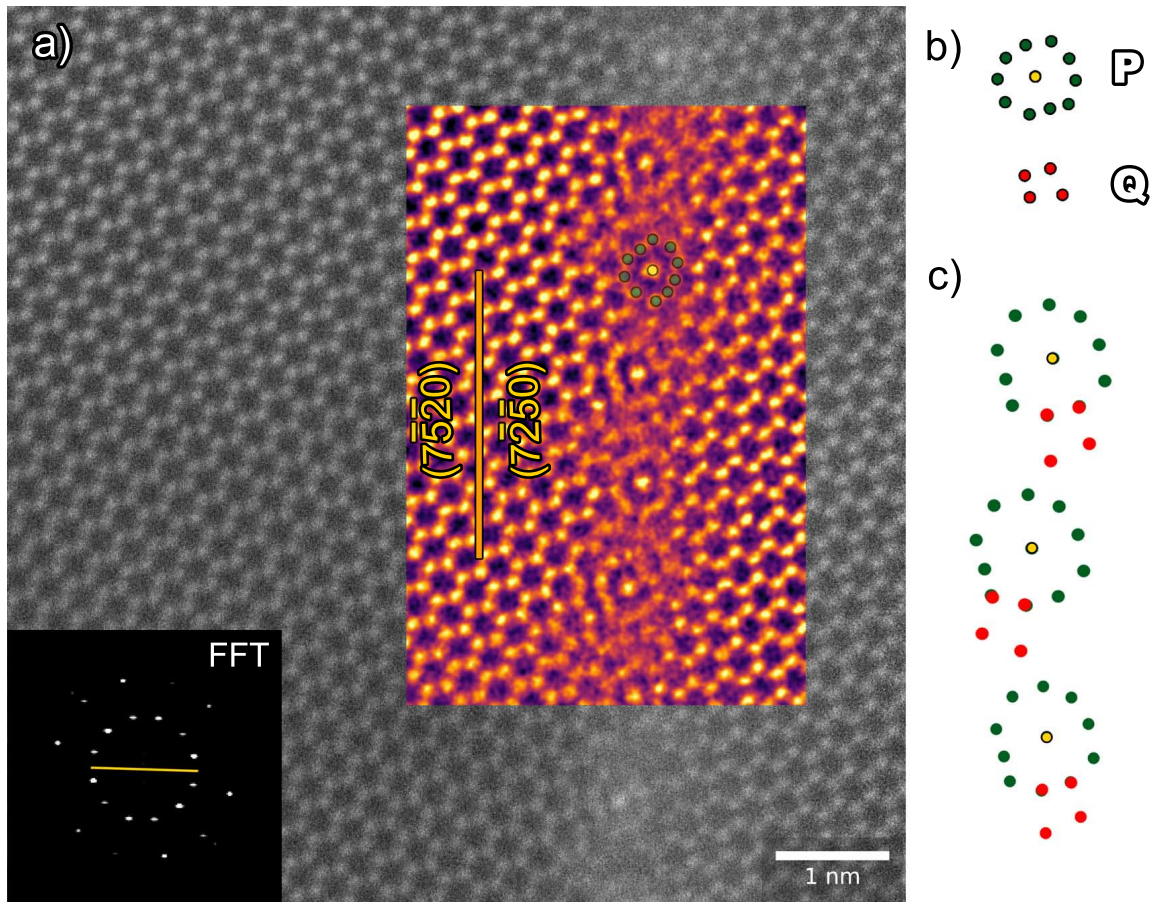
Next, the Fe atomic columns are observed to be equally spaced with 0.9 nm spacing between every two Fe columns. This is same as the spacing between any two repeating 'ABC' structural units discussed in the clean-GB. In an unrelaxed, undistorted  $\Sigma 13 \{25\bar{7}0\}$  symmetric GB, as seen in Fig. 4.26, the CSL sites are also spaced  $\sim 0.9$  nm apart. This indicates that Fe-segregation is favoured at the CSL sites. Such a periodic segregation of solute at the GB has also been shown in Mg, where Gd and Zn were shown to segregate in fully coherent twin boundaries using HAADF-STEM imaging [224].

Fig. 4.28 b) and c) show that the symmetric GB with Fe segregation also follows the SUM. Two repeating structural units, 'P' and 'Q' are identified at the GB. Because the spacing between two 'ABC' units is same as the spacing between two 'PQ' units, it is likely that 'ABC' transforms to 'PQ' upon segregation. To the best of our knowledge, this is the first observation of a segregation induced GB structural transition in hcp metals. A 3-dimensional understanding of the structural transition requires further theoretical analysis.

### Change of GB Fe concentration

In another symmetric  $\Sigma 13 [0001] \{\bar{7}520\}$  GB having a relatively higher number of bright Fe-rich columns per unit length (probably because of higher concentration of Fe), the 'P' units were seen grouped together in a periodic manner. Fig. 4.29 shows four 'P' units that are grouped together in the form of clusters, referred to as '4P' which is followed by two 'R' units. This observation suggests the high stability of 'P' unit in the presence of Fe in the GB. Another important question that cannot be answered with the available data is the difference in the Fe-concentration between Fig. 4.28 and Fig. 4.29. It was recently noted by Frolov *et al.* in Cu-Ag system, that the net solute concentration at the GB is lower in a bilayer than in a monolayer. This is counter-intuitive to what is apparent from the 2D projection [378]. Therefore, in the present case, the observed change in the GB structure cannot be directly correlated to an increase or decrease in the Fe concentration.

Several GB solute segregation models have been developed by McLean [347], Hondros and Seah [379], and Wynblatt and Chatain [351]. The Lanmguir-McLean model adapted the use of Lanmguir adsorption model from surfaces to interfaces [347]. The model from Hondros and Seah applies the modification introduced by the Fowler-Guggenheim model to interfaces [379]. The common element in these models is that they do not consider the atomic structure of the GB. Essentially any GB is expected to have certain preferential sites for solute segregation which is independent of its atomic structure.



**Figure 4.28** a) Symmetric  $\Sigma 13$  [0001]  $\{\bar{7}520\}$  GB in Ti imaged using HAADF-STEM demonstrates periodic Fe segregation that are uniformly spaced apart. b), c) The structural rearrangement caused by Fe segregation is observed to follow the SUM, with repeating 'PQ' units. The atomic column rich in Fe is highlighted in yellow.

From Fig. 4.28 and Fig. 4.29, it is clearly evident that a change in solute content can be accommodated by changing the atomic structure. This means that all the GB segregation models are only an approximation at their best, when the atomic structure of the GB is not considered in the model.

What exactly a GB phase transition is seems to be widely disputed in the literature. Solute addition leading to the so-called GB complexion transitions have been recently frequently reported. Addition of Au in Si was shown to transform a 'clean' GB to a bi-layer GB [380]. Similarly, distinct GB phases were reported in  $\text{WO}_3$  and CuO doped  $\text{TiO}_2$  bicrystal [187]. However, they are not actual structural changes within the GB. Hence care must be used when defining what constitutes GB phases or *complexions*.

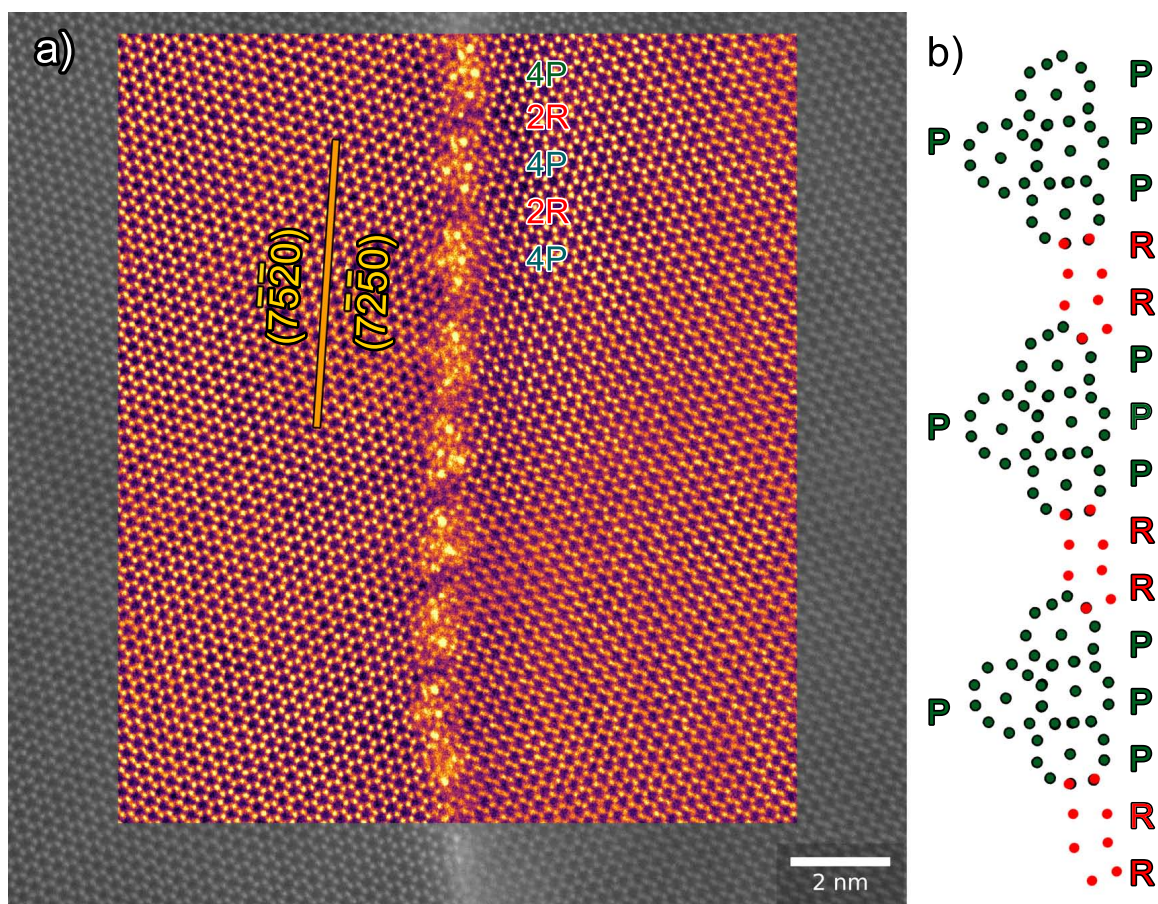


**Figure 4.29** Symmetric  $\Sigma_{13}$  [0001]  $\{7\bar{5}20\}$  GB with greater Fe-rich columns per unit GB length than Fig. 4.28 demonstrates periodicity in clustering of the 'PR' units to form '4P-2R' units.

#### 4.3.4 Atomic structure of Fe-segregated asymmetric GBs

As asymmetric GBs have higher energy than the symmetric GBs, it is expected that solute would preferentially segregate in such GBs. The same is observed for the  $\Sigma_{13}$  GBs. As seen in Fig. 4.30, Fe is segregated to the GB. As marked in the figure, the overall GB in a macroscopic sense would appear to be  $\Sigma_{13}$   $10\bar{1}0/11\bar{2}0$ . However, when observed at the atomic scale, the  $[11\bar{2}0]$  GB is found to be clearly faceted into two neighbouring symmetric GBs,  $\{5\bar{7}20\}$  and  $\{4\bar{3}10\}$ . The same can also be observed from the FFT present in the inset. As discussed earlier, the GB planes can be indexed by overlaying the GB plane normals on the FFT. Each facet was observed to be only  $\sim 2-3$  nm long. The symmetric  $\{7\bar{5}20\}$  facet was observed to show the same 0.9 nm spacing between the Fe columns. While the  $\{4\bar{3}10\}$  symmetric segments are seen to be lean in Fe.

In another instance, a rather continuously curved GB is observed. As shown in

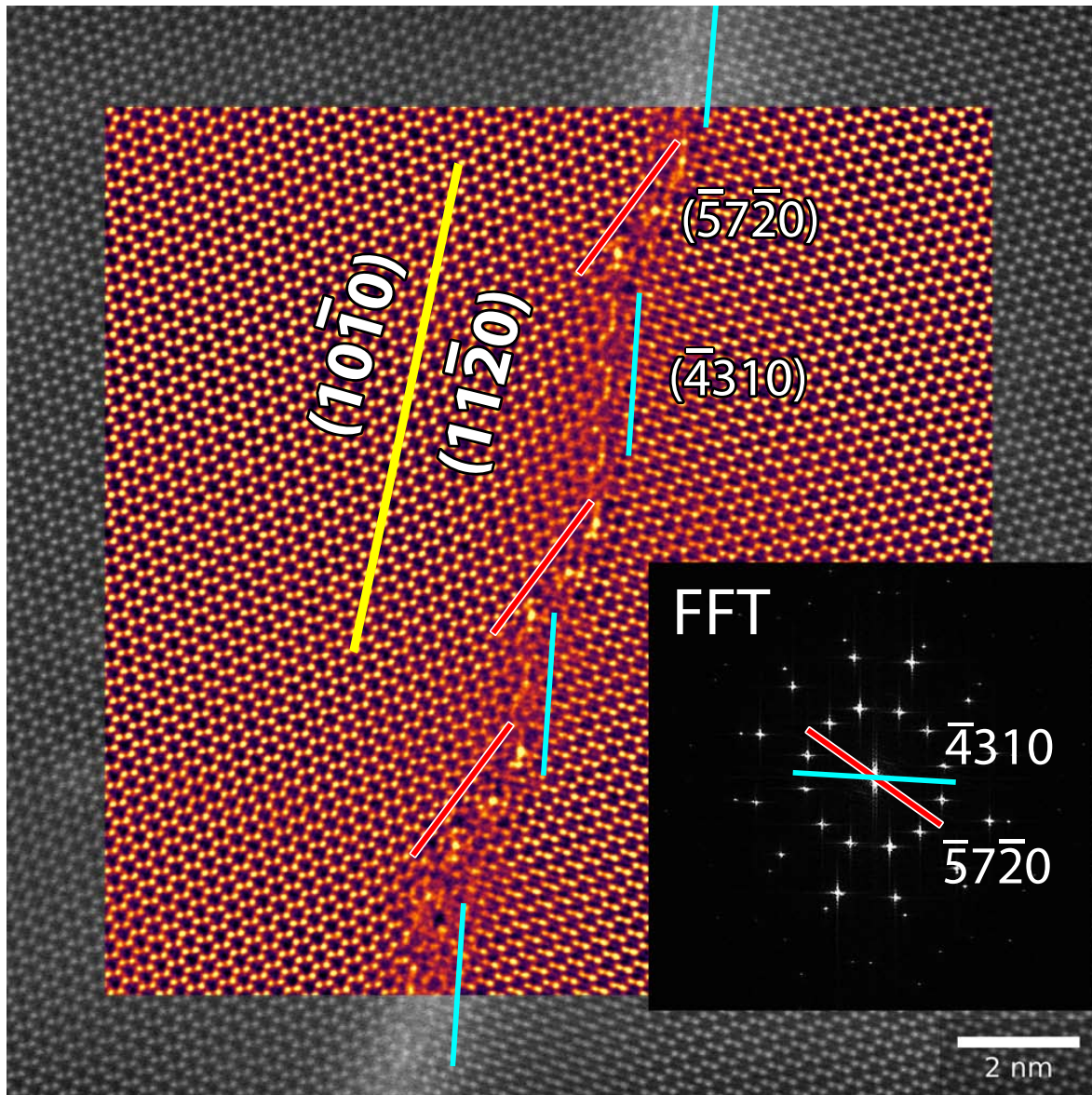


**Figure 4.30** Asymmetric  $\Sigma 13$   $[0001]$   $\{10\bar{1}0\}$  GB in Ti imaged using HAADF-STEM demonstrates GB faceting at atomic scale into the two symmetric variants,  $\{5\bar{7}20\}$  and  $\{4\bar{3}10\}$ .

Fig. 4.31, the asymmetry of the GB was seen to lead to an increased spacing between the Fe columns. Instead of the 0.9 nm spacing in a symmetric GB, Fe rich columns with a Ti-rich cage around them were spaced 2.1 nm apart. Additionally, following the SUM, the GB seems to be composed of both the 'ABC' and the 'PQ' units. The 'ABC' units as seen in detail in the Fig. 4.31 inset are placed between two Fe-rich cages. The 'C' unit in the 'ABC' structure appears slightly deformed compared to the 'clean' GB to accommodate an additional Fe-rich column in its center. On the other hand, the 'PQ' unit made of bright Fe-rich columns appear similar in both the symmetric and asymmetric GBs.

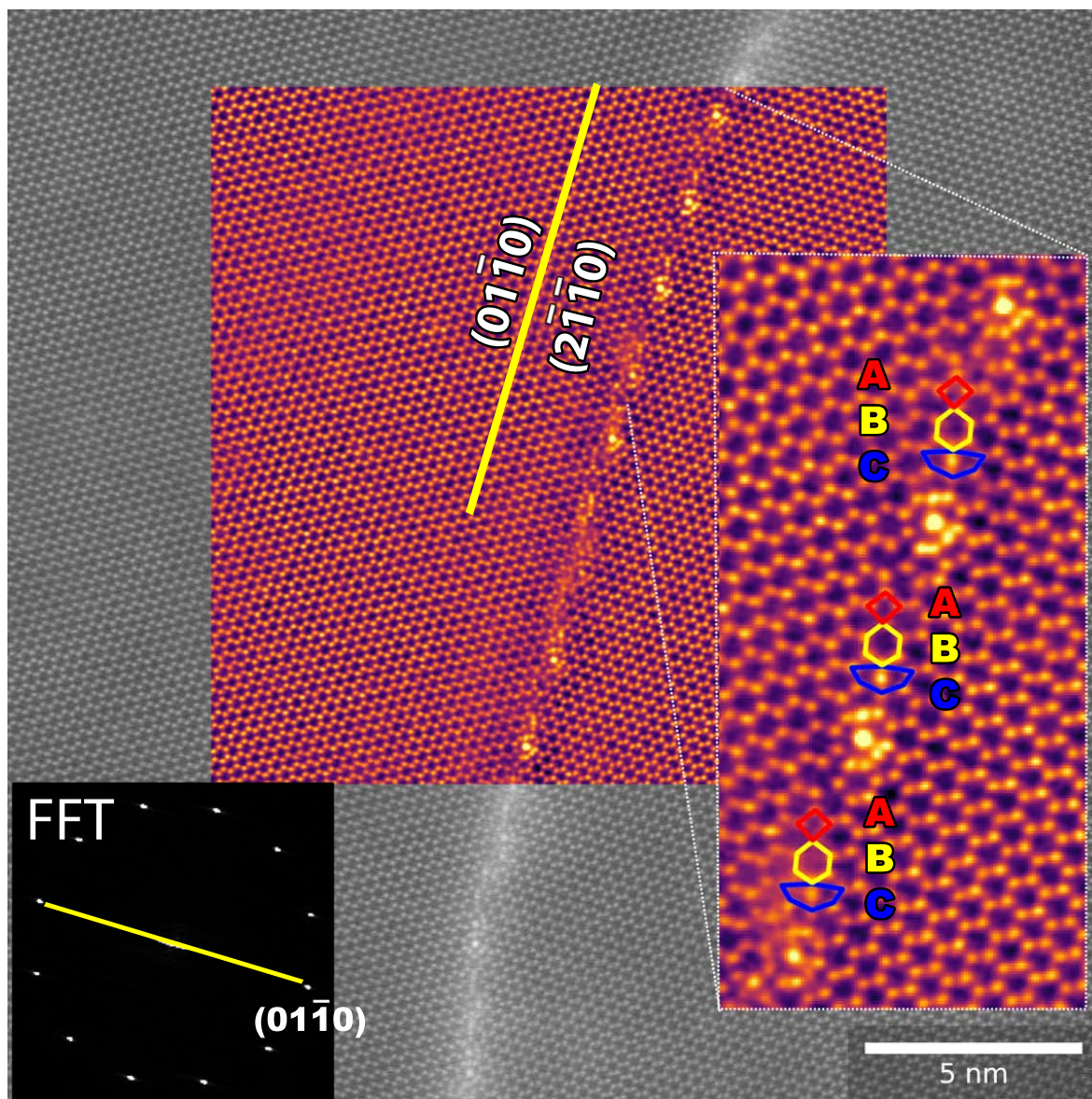


**Figure 4.31** Asymmetric  $\Sigma 13$   $[0001] \{10\bar{1}0\}$  GB in Ti imaged using HAADF-STEM shows Fe-rich columns spaced farther apart than in symmetric GB. 'ABC' units also present periodically at the GB were seen to have an additional bright Fe-rich column within the 'C' unit.

The GB circuit mapping that was deployed to measure the defect content in the segregation-free GB is not easy to implement in case of the segregated units because of the absence of a symmetrical undeformed region. The circuit mapping requires the circuit to be drawn in the grain which is in-principle not affected by the influence of elastic strain-field of the GB. While such a circuit was possible on the 'clean' GB, no such symmetrical sites were found on the segregated GBs across which the GB circuit could transverse from one grain to the other.

### 4.3.5 Dislocation on hcp basal plane

Fig. 4.32 shows two dislocations spaced 6 nm apart from each other. A Burgers circuit is drawn around them to find out the magnitude of the Burgers vector.  $\vec{b} = 1/3 [11\bar{2}0]$  for both of them. The Burgers circuit is drawn in blue and the projected Burgers vector is marked with a green arrow. It is notable that the core of the edge dislocation has a bright contrast signalling towards segregation of Fe to the dislocation core. Also, the bright column at the core appears to be surrounded by a cage, similar to the ones observed at the GB. From the contrast, we assume that Fe is located at the core and the surrounding cage is Fe-lean. The strain field around the dislocation combined with the slightly misaligned dislocation core with the zone-axis results in a blurry contrast in the immediate vicinity of the dislocation. Therefore, it was not possible to identify the exact number of Ti columns around the bright Fe-column. However, it appears that the overall structure of the dislocation core is tending towards the same 'cage-like' structure observed at the GB.

### 4.3.6 Near-atomically resolved energy dispersive spectrometry

Fig. 4.33 a) shows the HAADF-STEM image of a symmetric  $\Sigma 13 [0001] \{\bar{7}520\}$  GB. As discussed previously, the GB region has bright Fe-rich columns with Fe-lean Ti-rich atomic columns around it. The Fe decorates the GB in a symmetric manner with all Fe-rich columns equally spaced from each other. Fig. 4.33 b) shows 380 frames of EDS data collected at 120 kV. The Fe-area map reveals that the bright regions in the HAADF image are directly correlated with the Fe-rich regions in the EDS data. A line-profile along the GB length is also overlaid on the EDS data. It shows periodic enrichment of Fe at the GB.

The EDS data was collected at 120 kV as lower kV increases the inelastic cross-section and also reduces the beam damage to the sample. The Fe-rich cages throughout the study were seen to be highly unstable under 300 kV beam. In order to obtain sufficient EDS information from the same atomic column without displacing the atoms, it was necessary to use lower kV.

### 4.3.7 Discussion

#### Structural units and their defect content

A detailed discussion on the SUM is presented in Chapter 2. In summary, first proposed by Vitek et al. [5], several theoretical and experimental studies have verified it

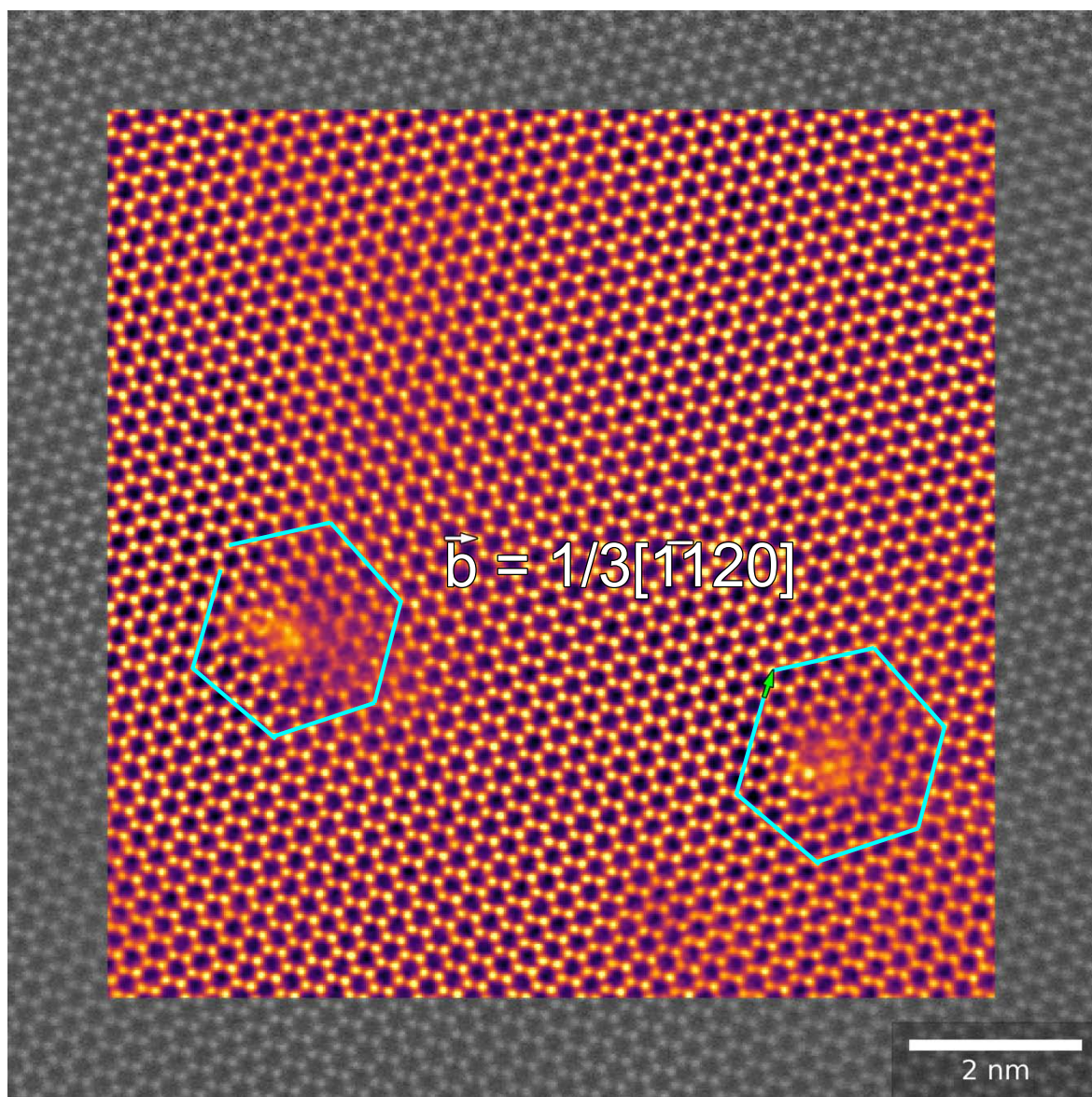


**Figure 4.32** Two edge dislocations with Burgers vector,  $b = 1/3 [11\bar{2}0]$  are observed to have bright contrast indicating Fe segregation. The dislocation core appears to have a 'cage-like' structure with Fe trapped in the core.

[177, 180, 208, 320, 381–383]. For high angle GBs, starting from an infinite dislocation model, Sutton *et al.* converged to the SUM [166, 384]. The central concept is that the GBs are made of periodic structural units that minimize its energy. GBs of certain orientations were termed as preferred GBs. Other GBs that lie in between two preferred GBs are expected to be made of a combination of the two favoured units. The main flaw in this generally recognized hypothesis is the lack of knowledge regarding the number of favored GBs.

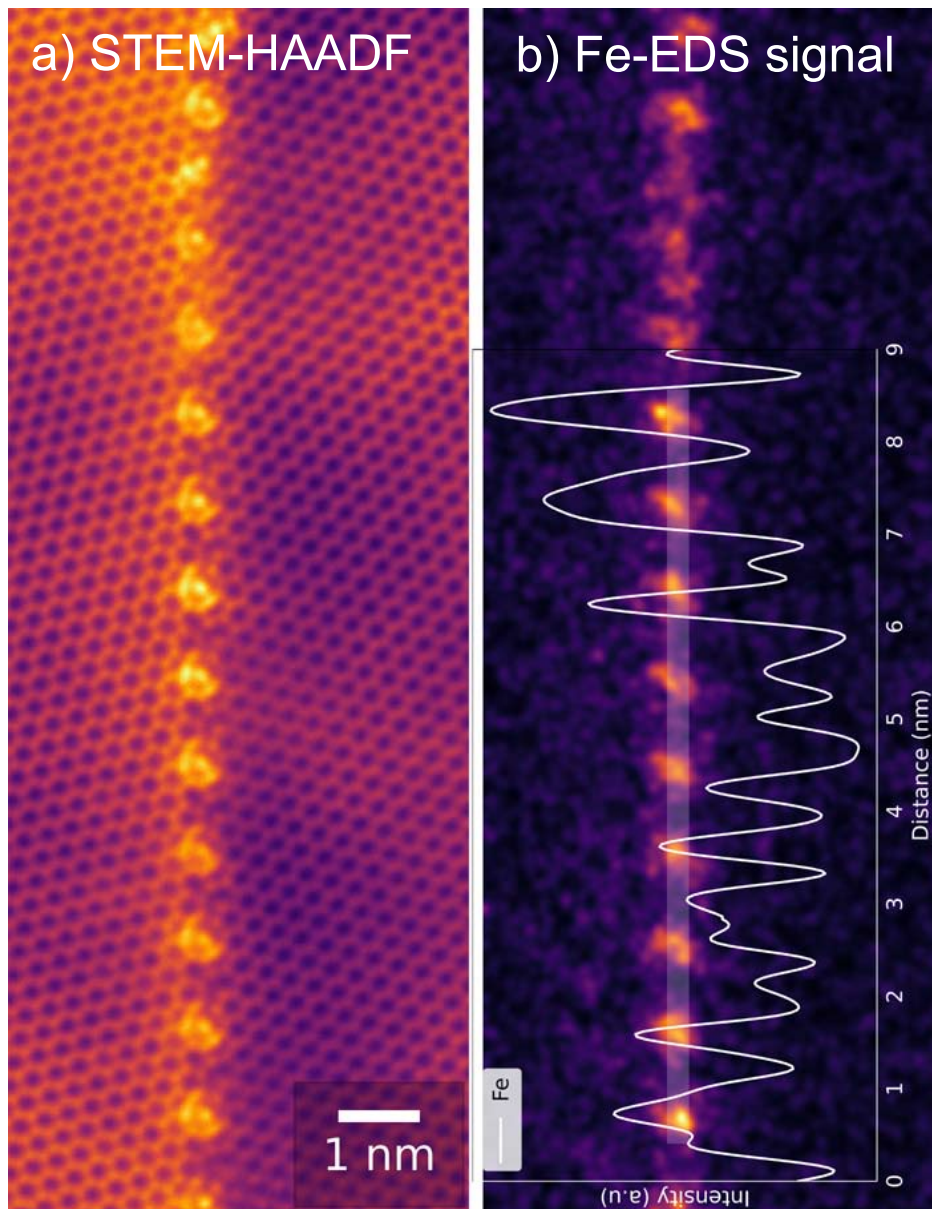


**Figure 4.33** a) HAADF-STEM signal acquired during the EDS scan at 120 kV for a symmetric  $\Sigma 13$  [0001]  $\{7\bar{5}20\}$  GB in Ti. b) The bright atomic columns in HAADF are verified to be Fe using STEM-EDS. The line-integral along the GB length depicts the Fe-K counts obtained from the EDS spectrum.

While most of the work validating SUM has been performed on fcc and bcc materials, substantial work has also been performed on ceramics having wurtzite structure whose symmetry is similar to hcp. In the present work, an uncanny resemblance was observed between the structural units imaged in both the crystal structures. [0001] tilt GBs in GaN and ZnO have been extensively studied due to their commercial importance. Using both atomic simulations and HRTEM, it was shown that all the favoured structures in [0001] tilt GBs in GaN are made of different cores of  $1/3[11\bar{2}0]$  edge



dislocations [234, 385]. The cores of edge dislocation were experimentally imaged in ZnO to have very similar structures to the 'ABC' units observed in the present study.  $\Sigma 7$  GB was shown to have a period '..BCBC..' [221], while  $\Sigma 13$  was shown to have GB period of '..ABCBCABCBC..'. Therefore, for the [0001] tilt GBs, the observed structural units in the present study match very well with the observations made on ZnO and GaN [230]. The addition of Fe to the symmetric GB resulted in a structural transition from 'ABC' to 'PQ' units. Remarkably, a similar transition was also observed in a  $\Sigma 13$  [0001] GB in ZnO when doped with Bi. Of the two probable structures that were theoretically calculated, the structure that appears like the 'P' unit of the present study was shown to be energetically favourable [386]. This indicates that the GB structure is largely governed by the geometry/crystal structure and is expected to contain symmetrical structural units for all hcp materials.

Further, using dichromatic pattern and the tools provided by bicrystallography [150], the defect content of the structural units were evaluated. A detailed review of the method can be found in [153, 387]. Defect contents of a host of GaN [0001] tilt GBs calculated using topological theory, showed that all the structural units were made of pure-edge dislocations [156]. Fig. 4.27 shows a similar circuit revealing the defect content of a single structural unit of  $\Sigma 13$  GB in Ti to be  $-2a$  or  $-2/3[11\bar{2}0]$ . This matches well with the results of Li *et al.* on GaN and ZnO [388].

The defect content of a  $\Sigma 13$  GB was also investigated in ZnO [215]. However, the GB was  $0.7^\circ$  away from the ideal  $\Sigma 13$  misorientation. This lead to secondary defects at the GB that were found to be unit Displacement shift complete (DSC) vectors. DSC lattice is a fine mesh along which either lattice can be displaced while still maintaining the CSL relation. In other words, it is the lattice that contains every point of both the lattices. The DSC lattice is created with an  $n$  times smaller mesh than the  $\Sigma n$ -CSL unit cell. This method has also been used to find out the secondary defect content/disconnections in Mg [153]. Using the same procedure in the present work, the secondary defect content in Fig. 4.26 was found to be 0.

### Grain boundary phase transitions due to segregation

Since Hart proposed two-dimensional phase transition of GBs [389], many GB phase transitions triggered by solute segregation have been reported. Au segregation to Fe GBs was shown to change the dislocation arrangement in the LAGBs [390]. In high angle GBs, phase transitions were mostly attributed to experimentally measurable

properties like discontinuity in GB sliding, diffusivity and mobility [391]. For example, the ductile to brittle transition of Al GBs in the presence of Li was attributed to two-dimensional phase transitions [392]. However, most of them lack the direct experimental observation at atomic scale to understand the structural change in GB that leads to discontinuity in the measured properties.

Faceting/roughening of GBs where the resultant facets have a different GB plane than the parent phase can be considered as one class of GB phase transitions. For example, Fe GBs were shown to be faceted in the presence of O and Te [393].  $\Sigma 19 \{331\}$  GB in Cu was shown to facet in the presence of Bi leading to embrittlement [394]. However, some more recent investigations reveal the atomic scale information. An asymmetric  $\Sigma 5$  GB in Cu was shown to facet at atomic scale into Ag-rich symmetric facets and Ag-lean asymmetric facets, where each facet was only few nm long [191]. In the present work, similar GB faceting is observed at atomic scale, as seen in Fig. 4.30. The global  $\{11\bar{2}0\}$  asymmetric GB was observed to facet into two symmetric segments. This is the first experimental observation of such atomic scale faceting phenomenon in hcp metals.

A structural change of the GB core where the GB plane remains the same is termed as congruent phase transition [395]. The atomic structure of a high angle GB is ultimately decided by its excess properties. Addition of a solute modifies the excess properties, which may lead to structural transitions. Using MC-MD simulations, a first order GB phase transformation between a 'kite' and a 'split-kite' structure has been demonstrated in  $\Sigma 5 (310)$  GB in Cu at 800 K. The segregation pattern and the Ag-excess in both the structures were observed to vary. The first order GB phase transition was observed both with and without solute. The transition between monolayer and bilayer in the presence of solute was termed as segregation-induced phase transition [378]. To the best of our knowledge, the only other instance where segregation induced GB phase transition was reported was in a Pt(Ni) system. Using MC simulations, upon heating to 850 K,  $\Sigma 5$  twist GB in a single phase Pt-Ni solid solution was seen to result in ordering of Ni at the GB. This was thought to be a segregation induced first order GB phase transition [396]. Recently, DFT was used to compare the difference in binding energy for various solute elements in  $\Sigma 7$  GB in Mg [397]. Certain preferred sites of segregation were identified in the GB structural units, but no relation was proposed between the CSL sites and the observed segregation. In the present work, there are preferred sites in the GB where the Fe segregates, as seen by comparing Fig. 4.25 and Fig. 4.28. In Fig. 4.34, the 11 atoms that form the 'B' and the 'C' units are labeled. It appears that Fe substitutes Ti in the atomic site #4 that joins the 'B' and 'C' units.

The presence of Fe results in local rearrangement around #4 resulting in a 10-atomic cage-like structure around it. A roughly identical reconstruction of the  $\Sigma 13$  [0001] GB was observed using DFT in ZnO when doped with Bi [386]. The defect energy (segregation energy) of Bi in ZnO was shown to be negative, meaning that the GB energy is lowered due to the solute addition. Because of the similarity in the symmetry, we can expect the Ti GB to behave roughly similar. In both the cases, the GB plane remains the same while the GB structural units are modified by the addition of solute.

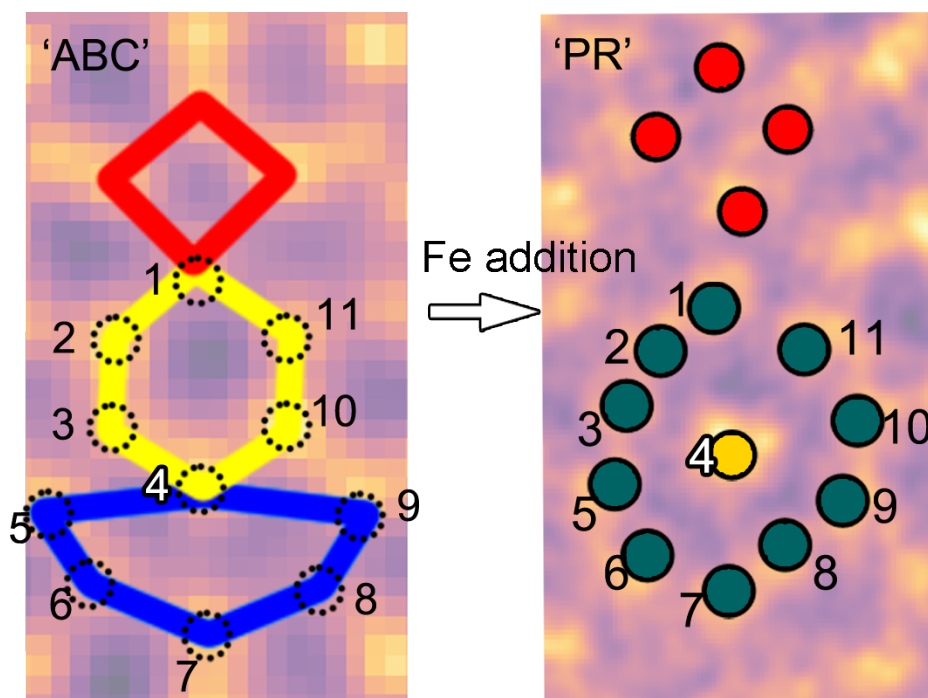


**Figure 4.34** The 'ABC' structure of the solute-free  $\Sigma 13$  [0001]  $\{\bar{7}520\}$  is magnified to label the 11 atoms that form the 'B' and the 'C' units. The addition of Fe transforms the GB unit 'P' and 'R' units where Fe-rich column is highlighted in yellow.



## Chapter 5

# Summary and conclusions

### 5.1 Ti thin film deposition using e-beam evaporation

In the first chapter, titanium thin films were successfully deposited using e-beam evaporation on substrates of  $\text{SiN}_x$ , NaCl and four orientations of sapphire. The substrate temperature and deposition rate were varied in order to study their influence on microstructure and texture. Following were the most crucial findings:

1. Nanocrystalline films were obtained for the first time on  $\text{SiN}_x$ . All depositions on NaCl substrate also led to nanocrystalline films. However, a difference in texture between the two was observed. The minimization of strain energy dominated for the film deposited on  $\text{SiN}_x$  substrate and led to a  $(10\bar{1}1)$  texture, while surface energy minimization promoted a  $(10\bar{1}0)$  texture for all films deposited on NaCl (100). All the films were nanocrystalline, which can be of great commercial interest for applications requiring high strength and corrosion resistance.
2. The film on C-plane sapphire grew as a single crystal with the (0002) plane surface normal in all cases. The six-fold symmetry of the oxygen sub-lattice of sapphire and the low lattice misfit are considered to be responsible for the formation of a SC film even at RT. Using cross-section HRTEM imaging the orientation relationship was determined to be  $(0002)_{Ti} \parallel (0006)_{Sapphire}, \langle 11\bar{2}0 \rangle_{Ti} \parallel \langle 03\bar{3}0 \rangle_{Sapphire}$ .
3. On C-plane sapphire with a  $2^\circ$  miscut and A-plane, a nanocrystalline film grew at RT and SC films were obtained by heating the substrate to  $200^\circ\text{C}$ . For the first time, a SC film was obtained on R-plane sapphire by heating the substrate to  $400^\circ\text{C}$ .
4. The resistivity of the 90 nm thick SC film was  $70 \mu \Omega \text{ cm}$  while 300 nm thick films displayed lower resistivity of  $60 \mu \Omega \text{ cm}$  owing to reduced surface scattering with increasing film thickness. The nanocrystalline film exhibited higher resistivity of  $95 \mu \Omega \text{ cm}$  because of additional scattering from grain boundaries.

Overall, we showed how a combination of deposition parameters and substrates can be chosen to obtain nanocrystalline and single crystalline Ti thin films. These results pave the way to a controlled synthesis of Ti films with defined orientations having fundamental implications for micro-electronics and thin film industry.

## 5.2 Grain boundary evolution and anisotropic Fe segregation in (0001) textured Ti thin films

Following the deposition of bicrystalline Ti thin films, the faceting and Fe-segregation in  $\Sigma 13$  [0001] GBs of Ti thin films were explored in this chapter for the first time. Following were the important findings:

1. A novel template based thin film deposition pathway for obtaining columnar grains containing tilt GBs of Ti is established using pulsed magnetron sputtering on SrTiO<sub>3</sub> (001) substrates at 600°C followed by post-annealing at the same temperature for 2 h, 4 h and 8 h.
2. The ion current density during magnetron sputtering is seen to modify the texture from a mixture of (10 $\bar{1}$ 1) and (0002) to only (0002).
3. EBSD and TEM analysis reveals a bicrystalline film with continuously curved GBs having a very high fraction of  $\Sigma 13$  [0001] CSL GBs. Such a textured film with well defined CSL GBs is demonstrated for the first time.
4. Two orientation relationships (ORs) are identified, where OR I is one continuous grain spread over the entire substrate. The OR II grains are distributed across the film and are observed to shrink upon annealing of the films. The two ORs are given as:

$$\text{OR I: } (0002)_{Ti} \parallel (001)_{SrTiO_3}, [5\bar{7}20]_{Ti} \parallel [100]_{SrTiO_3}$$

$$\text{OR II: } (0002)_{Ti} \parallel (001)_{SrTiO_3}, [5\bar{4}\bar{1}0]_{Ti} \parallel [100]_{SrTiO_3}$$

5. (S)TEM imaging revealed GBs faceted frequently into symmetric  $\{\bar{7}520\}$  and  $\{\bar{4}310\}$ , and sporadically asymmetric  $\{10\bar{1}0\} // \{2\bar{1}\bar{1}0\}$  facets. The selection of GB planes during faceting is considered to be a combination of high planar coincidence site density and high effective interplanar spacing ( $d_{eff}$ ).
6. EDS analysis reveals a distinct preferential Fe segregation in every  $\{\bar{7}520\}$  GB facet while every  $\{\bar{4}310\}$  GB remains Fe-lean. A similar behavior was verified

by atom probe tomography and the Fe solute excess at the Fe-rich facets was determined to be 1.25 at/nm<sup>2</sup>.

In this chapter, we established a novel route to obtain bicrystalline Ti thin film that opens the path to investigate its GBs in detail. Phenomenon such as faceting and segregation of GBs are known to influence their properties. For most polycrystalline materials, its failure and strengthening is directly associated with these GB phenomenon. The Fe segregation investigated here is of added interest because it a common impurity present in all lower grades of titanium that are often used due to their lower cost.

### 5.3 (S)TEM investigation of $\Sigma 13$ grain boundaries in Ti

The thin film having columnar grains and tilt GBs was selected to be the optimal thin film required for atomic scale investigation of the GBs.

1. A symmetric  $\Sigma 13$  [0001]  $\{\bar{7}520\}$  GB that was observed to constitute periodic structural units, termed 'ABC'.
2. A dichromatic pattern was utilized to find out the defect content of the structural units using topological theory. One repeating unit was found to have the same defect content as two basal plane edge dislocations. Using the same dichromatic pattern it was verified that no disconnections / secondary defects were present at the investigated GB.
3. In another instance, Fe segregation was observed in the symmetric  $\Sigma 13$  [0001]  $\{\bar{7}520\}$  GB. Atomic columns rich in Fe distinctly appear bright when imaged using HAADF detector and decorated the GB periodically. The observed repeating structural units were termed 'PQ'.
4. The presence of Fe in the brighter atomic columns was verified using near-atomically resolved EDS.
5. The spacing between two 'ABC' and 'PQ' units is similar. This indicates that 'ABC' transforms into 'PQ' upon Fe-segregation. As the GB structure modifies entirely due to segregation, this is to the best of our knowledge the first example of the direct observation of GB structural transition due to segregation in a hcp material.

6. An asymmetric  $\{10\bar{1}0\} // \{11\bar{2}0\}$  GB was observed to facet into the two symmetric variants,  $\{\bar{7}520\}$  and  $\{13\bar{4}0\}$ , at atomic scale upon segregation.
7. Another similar asymmetric  $\{10\bar{1}0\} // \{11\bar{2}0\}$  GB was observed to have a rather continuous curvature instead of facets. The curvature was accommodated by a mixture of both 'ABC' and 'PQ' structural units.

To conclude, in this final chapter of results, we observe  $\Sigma 13$   $[0001]$  GB in hcp materials at the atomic scale. We prove the applicability of the structural unit model to both symmetric and asymmetric GBs in hcp metals. Additionally, we show the periodic nature of segregation leading to structural transitions in hcp GBs for the first time.



## Chapter 6

# Conclusions and outlook

In this thesis, a large portion of the work deals with thin films of Ti. Thin film deposition of metals is a commercially heavily used technique. Many studies have shown how a minor change in deposition parameters can change the microstructure of the thin films. Therefore, the present work helps to fill the gaps in the understanding of growing Ti thin films. We describe in depth a number of methods for obtaining diverse microstructures, including single crystalline, bicrystalline, and nanocrystalline, each of which has unique properties. The single crystalline Ti thin films can act as a diffusion barrier while also exhibiting improved fatigue and wear resistance owing to its single crystallinity. The nanocrystalline Ti on the other hand is widely known for its high strength and resistance against grain coarsening at higher temperatures. Since bulk Ti is expensive, thin coatings of Ti can be used for several cost-effective applications.

The second half of the thesis is focused on investigating the  $\Sigma 13$  [0001] GBs that are commonly observed in many (0001) textured hcp materials. The atomic structure of the GB was found to have many commonalities with the structure of the same GB observed in ZnO and GaN. Although the latter have dominant covalent bonds and the bonding characteristics are determined by the charge transfers, the GB structure in the (0001) projection appears to be similar. This indicates that the GB structure in hcp materials, and perhaps in other close packed structures, depends strongly on the local coordination more than anything else. It is noteworthy that the 5,7-atom ring structures observed in hexagonal 2D materials such as graphene also highly resemble the structure observed in the present work, although this is only limited to the projected view from (0001). This serves as a further indication of how much the structure depends on the local geometry. Similar findings were also reported for fcc materials where  $\Sigma 5$  GB was found to have identical structural units for Au, Ag, Ni, and Cu [341].

GB multiplicity has been demonstrated theoretically and more recently experimentally in Cu. Several GBs are expected to exhibit similar behaviour. However, observing the high-temperature high-pressure phases experimentally is challenging. Therefore, for our enhanced understanding of the interfaces, theoretical computations using DFT

and MC-MD simulations are necessary. Furthermore, some important questions remain unanswered in the present work. Although the spacing between the Fe-rich columns was seen to be identical to the spacing between CSL points, we need theoretical calculations to determine the variation in GB energy depending on various solute segregation sites. It would be also of great interest to investigate the difference in GB energy values that result from the clustering of 'P' units to form '4P' units upon a change in solute content. These clusters are probably the nucleating sites for Ti-Fe intermetallic compounds, which makes their better understanding even more critical. Furthermore, such experiments can never provide an exhaustive answer to the possible number of favoured GBs and if any particular GB is stable or meta-stable.

EDS was used in the present work to verify that the bright contrast in the HAADF corresponded to Fe-rich columns. However, it is extremely challenging to determine the actual concentration of the Fe in individual atomic columns. This makes correlating GB structure/ properties to the solute content difficult. Also, the Fe-rich columns were detected to always have an the increased projected width when compared to pure-Ti columns. Fe has a smaller atomic size than Ti, yet the Fe-rich columns appeared wider. This could be related to higher free volume at the GB that de-channels the probe. Answers to several such questions lie in the 3-dimensional nature of the structural units, which can only be revealed using simulations. Therefore, like in every scientific study, the present work has led to a number of new questions that will need to be answered in the future.

# Bibliography

1. Forrester, R. *History of Metallurgy* tech. rep. ID 2864178 (Rochester, NY, 2016).
2. Mould, R. F. The early history of X-ray diagnosis with emphasis on the contributions of physics 1895-1915. *Physics in Medicine and Biology* **40**, 1741–1787 (1995).
3. Priester, L. *Grain boundaries: from theory to engineering* (Springer Science & Business Media, 2012).
4. Lejček, P. *Grain Boundaries: Description, Structure and Thermodynamics* (ed Lejcek, P.) 239 pp. (Springer, Berlin, Heidelberg, 2010).
5. Vitek, V., Sutton, A., Gui Jin Wang & Schwartz, D. On the multiplicity of structures and grain boundaries. *Scripta Metallurgica* **17**, 183–189 (1983).
6. Zhou, X., Yu, X.-x., Kaub, T., Martens, R. L. & Thompson, G. B. Grain Boundary Specific Segregation in Nanocrystalline Fe(Cr). *Scientific Reports* **6**, 34642 (2016).
7. Peter, N. J., Liebscher, C. H., Kirchlechner, C. & Dehm, G. Beam-induced atomic migration at Ag-containing nanofacets at an asymmetric Cu grain boundary. *Journal of Materials Research* **32**, 968–982 (2017).
8. Meiners, T., Frolov, T., Rudd, R. E., Dehm, G. & Liebscher, C. H. Observations of grain-boundary phase transformations in an elemental metal. *Nature* **579**, 375–378 (2020).
9. Greene, J. E. Review Article: Tracing the recorded history of thin-film sputter deposition: From the 1800s to 2017. *Journal of Vacuum Science & Technology A* **35**, 05C204 (2017).
10. Seshan, K. *Handbook of Thin Film Deposition* (ed Seshan, K.) 408 pp. (Elsevier, 2012).
11. Rasic, D. & Narayan, J. *Crystal Growth* (ed Glebovsky, V.) chap. 5 (IntechOpen, Rijeka, 2019).
12. Bunshah, R. F. & Deshpandey, C. V. Evaporation Processes. *MRS Bulletin* **13**, 33–39 (1988).

13. Reichelt, K & Jiang, X. The preparation of thin films by physical vapour deposition methods. **191**, 91–126 (1990).
14. Radzinski, Z. J., Posadowski, W. M., Rosnagel, S. M. & Shingubara, S. Directional copper deposition using dc magnetron self-sputtering. *Journal of Vacuum Science & Technology B: Microelectronics and Nanometer Structures Processing, Measurement, and Phenomena* **16**, 1102–1106 (1998).
15. Campbell, D. S. (eds Dupuy, C. H. S. & Cachard, A.) 9–48 (Springer US, Boston, MA, 1976).
16. Mattox, D. M. & Mattox, V. *Vacuum coating technology* (Elsevier, 2003).
17. Shah, S. I., Jaffari, G. H., Yassitepe, E. & Ali, B. *Evaporation: Processes, Bulk Microstructures, and Mechanical Properties* (ed Martin, P. M.) 135–252 (William Andrew Publishing, Boston, 2010).
18. Zhang, J. X. J. & Hoshino, K. (eds Zhang, J. X. J. & Hoshino, K.) 43–111 (Academic Press, 2019).
19. Savale, P. A. Physical Vapor Deposition (PVD) Methods for Synthesis of Thin Films: A Comparative Study. *Archives of Applied Science Research* **8**, 1–8 (2016).
20. Adachi, H. & Wasa, K. Thin films and nanomaterials. *Handbook of Sputter Deposition Technology: Fundamentals and Applications for Functional Thin Films, Nano-Materials and MEMS*: 3–39 (2012).
21. Zalm, P. C. Energy dependence of the sputtering yield of silicon bombarded with neon, argon, krypton, and xenon ions. *Journal of Applied Physics* **54**, 2660–2666 (1983).
22. West, G. T. & Kelly, P. J. Influence of inert gas species on the growth of silver and molybdenum films via a magnetron discharge. *Surf. Coat. Technol.* **206**, 1648–1652 (2011).
23. Laegreid, N. & Wehner, G. K. Sputtering Yields of Metals for Ar<sup>+</sup> and Ne<sup>+</sup> Ions with Energies from 50 to 600 eV. *Journal of Applied Physics* **32**, 365–369 (1961).
24. Gobbi, A. L. & Nascente, P. A. P. *D.C. Sputtering* (eds Wang, Q. J. & Chung, Y.-W.) 699–706 (Springer US, Boston, MA, 2013).
25. Gudmundsson, J. T. Physics and technology of magnetron sputtering discharges. *Plasma Sources Science and Technology* **29**, 113001 (2020).
26. Freund, L. B. & Suresh, S. *Thin Film Materials. Stress, Defect Formation and Surface Evolution* (Cambridge University Press, 2004).

27. Schiller, S. *et al.* Pulsed magnetron sputter technology. *Surface and Coatings Technology* **61**, 331–337 (1993).
28. Kelly, P. J & Arnell, R. D. Magnetron sputtering: a review of recent developments and applications. *Vacuum* **56**, 159–172 (2000).
29. Kouznetsov, V., Macák, K., Schneider, J. M., Helmersson, U. & Petrov, I. A novel pulsed magnetron sputter technique utilizing very high target power densities. *Surface and Coatings Technology* **122**, 290–293 (1999).
30. Gudmundsson, J. T., Brenning, N., Lundin, D. & Helmersson, U. High power impulse magnetron sputtering discharge. *Journal of Vacuum Science & Technology A* **30**, 030801 (2012).
31. Schneider, J. M., Sproul, W. D., Voevodin, A. A. & Matthews, A. Crystalline alumina deposited at low temperatures by ionized magnetron sputtering. *Journal of Vacuum Science & Technology A: Vacuum, Surfaces, and Films* **15**, 1084–1088 (1997).
32. Arnell, R. D., Kelly, P. J. & Bradley, J. W. Recent developments in pulsed magnetron sputtering. *Surface and Coatings Technology. Proceedings of the 31<sup>st</sup> International Conference on Metallurgical Coatings and Thin Films* **188-189**, 158–163 (2004).
33. Boyer, R. R. An overview on the use of titanium in the aerospace industry. *Materials Science and Engineering: A* **213**, 103–114 (1996).
34. *Mineral commodity summaries 2022* USGS Numbered Series. IP-135364 (U.S. Geological Survey, Reston, VA, 2022), 202.
35. Banerjee, D. & Williams, J. Perspectives on Titanium Science and Technology. *Acta Materialia* **61**, 844–879 (2013).
36. Van Noort, R. Titanium: The implant material of today. *Journal of Materials Science* **22**, 3801–3811 (1987).
37. Boyer, R. Titanium airframe applications: Brief history, present applications and future trends. *Materials Science Forum* **426**, 643–648 (2003).
38. *Titanium: Physical Metallurgy, Processing, and Applications* (ed Froes, F.) (ASM International, 2015).
39. Wood, R. M. The Lattice Constants of High Purity Alpha Titanium. *Proceedings of the Physical Society* **80**, 783–786 (1962).
40. Leyens, C. & Peters, M. *Titanium and Titanium Alloys: Fundamentals and Applications* (eds Leyens, C. & Peters, M.) (John Wiley & Sons, 2003).

41. Donachie, M. J. *Titanium: A Technical Guide, 2<sup>nd</sup> Edition* (ASM International, 2000).
42. Levinger, B. W. Lattice Parameter of Beta Titanium at Room Temperature. *JOM* **5**, 195 (1953).
43. Nakajima, H. & Koiwa, M. Diffusion in Titanium. *ISIJ International* **31**, 757–766 (1991).
44. Raabe, D., Sander, B., Friák, M., Ma, D. & Neugebauer, J. Theory-guided bottom-up design of  $\beta$ -titanium alloys as biomaterials based on first principles calculations: Theory and experiments. *Acta Materialia* **55**, 4475–4487 (2007).
45. Polmear, I., StJohn, D., Nie, J.-F. & Qian, M. *Light Alloys* 544 pp. (Elsevier Science & Technology, 2017).
46. Earlam, M. R. *Extractive Metallurgy of Titanium* (eds Fang, Z. Z., Froes, F. H. & Zhang, Y.) 97–112 (Elsevier, 2020).
47. Aksyonov, D. & Lipnitskii, A. Solubility and grain boundary segregation of iron in hcp titanium: A computational study. *Computational Materials Science* **137**, 266–272 (2017).
48. Bläsius, A. & Gonser, U. Precision Phase Analysis. *Le Journal de Physique Colloques* **37**, C6–397–C6–399 (1976).
49. Devaraj, A. *et al.* A low-cost hierarchical nanostructured beta-titanium alloy with high strength. *Nature Communications* **7**, 1–8 (2016).
50. Matyka, J., Faudot, F. & Bigot, J. Study of iron solubility in  $\alpha$  titanium. *Scripta Metallurgica* **13**, 645–648 (1979).
51. Raub, E. *et al.* The  $\alpha$ -Ti-Fe solid solution and its superconducting properties. *Journal of The Less-Common Metals* **12**, 36–40 (1967).
52. Liu, Y. *et al.* Design of powder metallurgy titanium alloys and composites. *Materials Science and Engineering: A* **418**, 25–35 (2006).
53. Pan, D., Liu, B., Xu, R., Qiu, J. & Liu, C. Predicting workability of a low-cost powder metallurgical Ti-5Al-2Fe-3Mo alloy using constitutive modeling and processing map. *Materials* **14**, 1–19 (2021).
54. Peng, Y., Zhu, Q., Luo, T. & Cao, J. Enhancement of the tensile strength by introducing alloy element Fe for Ti based alloy. *Solid State Communications* **318**, 113982 (2020).

55. Reverte, E., Tsipas, S. A. & Gordo, E. Oxidation and Corrosion Behavior of New Low-Cost Ti-7Fe-3Al and Ti-7Fe-5Cr Alloys from Titanium Hydride Powders. *Metals* **10** (2020).
56. Boyer, R. R. & Briggs, R. D. The use of  $\beta$  titanium alloys in the aerospace industry. *Journal of Materials Engineering and Performance* **14**, 681–685 (2005).
57. Raghunathan, S. L., Stapleton, A. M., Dashwood, R. J., Jackson, M. & Dye, D. Micromechanics of Ti-10V-2Fe-3Al: In situ synchrotron characterisation and modelling. *Acta Materialia* **55**, 6861–6872 (2007).
58. Jones, N. G., Dashwood, R. J., Jackson, M. & Dye, D.  $\beta$  Phase decomposition in Ti-5Al-5Mo-5V-3Cr. *Acta Materialia* **57**, 3830–3839 (2009).
59. Levi, I. & Shechtman, D. The microstructure of rapidly solidified Ti-Fe melt-spun ribbons. *Metallurgical Transactions A* **20**, 2841–2845 (1989).
60. Louzguine, D. V., Kato, H., Louzguina, L. V. & Inoue, A. High-strength binary Ti-Fe bulk alloys with enhanced ductility. *Journal of Materials Research* **19**, 3600–3606 (2004).
61. Bermingham, M., McDonald, S., StJohn, D. & Dargusch, M. Segregation and grain refinement in cast titanium alloys. *Journal of Materials Research* **24**, 1529–1535 (2009).
62. Simonelli, M. *et al.* The Influence of Iron in Minimizing the Microstructural Anisotropy of Ti-6Al-4V Produced by Laser Powder-Bed Fusion. *Metallurgical and Materials Transactions A* **51**, 2444–2459 (2020).
63. Wu, Y., Wu, X., Qin, S. & Yang, K. Compressibility and phase transition of intermetallic compound Fe<sub>2</sub>Ti. *Journal of Alloys and Compounds* **558**, 160–163 (2013).
64. Illarionov, A. G., Ushakova, A. S. & Vodolazsky, F. V. ThermoCalc Modelling of the Effect of Chemical Composition on the Phase Transformations Temperatures of Ti-0.4Al Alloy. *IOP Conference Series: Materials Science and Engineering* **969**, 012029 (2020).
65. Ray, R., Giessen, B. C. & Grant, N. J. The constitution of metastable titanium-rich Ti-Fe alloys: An order-disorder transition. *Metallurgical and Materials Transactions B* **3**, 627–629 (1972).
66. Sakintuna, B., Lamari-Darkrim, F. & Hirscher, M. Metal hydride materials for solid hydrogen storage: A review. *International Journal of Hydrogen Energy* **32**, 1121–1140 (2007).

67. Reilly, J. J. & Wiswall, R. H. Formation and properties of iron titanium hydride. *Inorganic Chemistry* **13**, 218–222 (1974).
68. Chu, B.-L., Lee, S.-M. & Perng, T.-P. Formation of amorphous Ti-Fe alloys by mechanical alloying. *Journal of Applied Physics* **69**, 4211–4215 (1991).
69. Louzguine-Luzgin, D. V. High-Strength Ti-Based Alloys Containing Fe as One of the Main Alloying Elements. *Materials Transactions* **59**, 1537–1544 (2018).
70. Pelloth, J., Brand, R. A. & Keune, W. Local magnetic properties of the Fe<sub>2</sub>Ti Laves phase. *Journal of Magnetism and Magnetic Materials. International Conference on Magnetism* **140-144**, 59–60 (1995).
71. Santhy, K. & Hari Kumar, K. C. Thermodynamic modelling of magnetic laves phase in Fe–Ti system using first principle method. *Intermetallics* **128**, 106978 (2021).
72. Murray, J. L. The Fe- Ti (iron-titanium) system. *Bulletin of Alloy Phase Diagrams* **2**, 320–334 (1981).
73. Savvakina, D. G. *et al.* Effect of Iron Content on Sintering Behavior of Ti-V-Fe-Al Near- $\beta$  Titanium Alloy. *Metallurgical and Materials Transactions A* **43**, 716–723 (2012).
74. Raynova, S., Yang, F. & Bolzoni, L. The effect of thermomechanical treatments on the properties of powder metallurgy Ti–5Fe alloy. *Materials Science and Engineering: A* **801**, 140389 (2021).
75. Bodunrin, M. O., Chown, L. H., van der Merwe, J. W. & Alaneme, K. K. On the substitution of vanadium with iron in Ti–6Al–4V: Thermo-Calc simulation and processing map considerations for design of low-cost alloys. *Materials Science and Engineering: A* **791**, 139622 (2020).
76. Esteban, P. G., Bolzoni, L., Ruiz-Navas, E. M. & Gordo, E. PM processing and characterisation of Ti–7Fe low cost titanium alloys. *Powder Metallurgy* **54**, 242–252 (2011).
77. Carman, A. *et al.* Role of alloying elements in microstructure evolution and alloying elements behaviour during sintering of a near- $\beta$  titanium alloy. *Materials Science and Engineering A* **528**, 1686–1693 (2011).
78. Straumal, B. B. *et al.* Phase Transformations in Ti-Fe Alloys Induced by High-Pressure Torsion. *Advanced Engineering Materials* **17**, 1835–1841 (2015).



79. Straumal, B. *et al.* Diffusive and displacive phase transitions in Ti-Fe and Ti-Co alloys under high pressure torsion. *Journal of Alloys and Compounds* **735**, 2281–2286 (2018).
80. Kilmametov, A. *et al.* Transformations of  $\alpha'$  martensite in Ti-Fe alloys under high pressure torsion. *Scripta Materialia* **136**, 46–49 (2017).
81. Kilmametov, A. *et al.* The  $\alpha \rightarrow \omega$  and  $\beta \rightarrow \omega$  phase transformations in Ti-Fe alloys under high-pressure torsion. *Acta Materialia* **144**, 337–351 (2018).
82. Kriegel, M. J. *et al.* Thermal Stability of Athermal  $\omega$ -Ti(Fe) Produced upon Quenching of  $\beta$ -Ti(Fe). *Advanced Engineering Materials* **21**, 1800158 (2019).
83. Kriegel, M. J. *et al.* Formation and thermal stability of  $\omega$ -Ti(Fe) in  $\alpha$ -phase-based Ti(Fe) alloys. *Metals* **10** (2020).
84. Wasz, M. L., Brotzen, F. R., McLellan, R. B. & Griffin, A. J. Effect of oxygen and hydrogen on mechanical properties of commercial purity titanium. *International Materials Reviews* **41**, 1–12 (1996).
85. Chong, Y. *et al.* Mechanistic basis of oxygen sensitivity in titanium. *Science Advances* **6**, eabc4060 (2020).
86. Cancarevic, M., Zinkevich, M. & Aldinger, F. Thermodynamic description of the Ti–O system using the associate model for the liquid phase. *Calphad* **31**, 330–342 (2007).
87. Xia, Y., Zhao, J., Tian, Q. & Guo, X. Review of the Effect of Oxygen on Titanium and Deoxygenation Technologies for Recycling of Titanium Metal. *JOM* **71**, 3209–3220 (2019).
88. Guo, J., Zhang, Q., Bian, J. & Zhang, J. Laser gas oxidizing of titanium surface in a dilute oxygen environment. *Surface and Coatings Technology* **424**, 127653 (2021).
89. Luo, S. D. *et al.* High oxygen-content titanium and titanium alloys made from powder. *Journal of Alloys and Compounds* **836**, 155526 (2020).
90. Aksyonov, D. A., Hickel, T, Neugebauer, J & Lipnitskii, A. G. The impact of carbon and oxygen in alpha-titanium : ab initio study of solution enthalpies and grain boundary segregation. *Journal of Physics: Condensed Matter*, 385001 (2016).
91. Tarnawski, Z. & Kim-Ngan, N.-T. T. Hydrogen storage characteristics of Ti and V based thin films. *Journal of Science: Advanced Materials and Devices* **1**, 141–146 (2016).

92. Hofmann, K, Spangenberg, B, Luysberg, M & Kurz, H. Properties of evaporated titanium thin films and their possible application in single electron devices. *Thin Solid Films* **436**, 168–174 (2003).
93. Gablech, I. *et al.* Stress-free deposition of [001] preferentially oriented titanium thin film by Kaufman ion-beam source. *Thin Solid Films* **638**, 57–62 (2017).
94. Aoh, J.-N. & Chuang, C.-L. Thermosonic Bonding of Gold Wire onto a Copper Pad with Titanium Thin-Film Deposition. *Journal of electronic materials* **33**, 290–299 (2004).
95. Yu, J. *et al.* Characteristics of hexagonal c-oriented titanium film as the template for GaN epitaxy on glass substrate by electron beam evaporation. *Thin Solid Films* **624**, 160–166 (2017).
96. Bernhardt, G *et al.* Performance of Zr and Ti adhesion layers for bonding of platinum metallization to sapphire substrates. *Sensors and Actuators B: Chemical* **77**, 368–374 (2001).
97. Vlasov, V. P., Muslimov, A. E., Butashin, A. V. & Kanevsky, V. M. Sapphire evolution of the vicinal (0001) sapphire surface upon annealing in air. *Crystallography Reports* **61**, 58–62 (2016).
98. Evans, J. W., Thiel, P. A. & Bartelt, M. C. Morphological evolution during epitaxial thin film growth: Formation of 2D islands and 3D mounds. *Surface Science Reports* **61**, 1–128 (2006).
99. Huang, J. C., Du, R. R. & Flynn, C. P. Nucleation processes in the growth of hcp titanium. *Physical Review Letters* **66**, 341–344 (1991).
100. Jung, M. J., Nam, K. H., Shaginyan, L. R. & Han, J. G. Deposition of Ti thin film using the magnetron sputtering method. *Thin Solid Films* **435**, 145–149 (2003).
101. Savaloni, H., Taherizadeh, A. & Zندهنام, A. Residual stress and structural characteristics in Ti and Cu sputtered films on glass substrates at different substrate temperatures and film thickness. *Physica B: Condensed Matter* **349**, 44–55 (2004).
102. Sonoda, T *et al.* Structure and mechanical properties of pure titanium film deposited onto TiNi shape memory alloy substrate by magnetron DC sputtering. **459**, 212–215 (2004).
103. Freibertshauser Pe & McCamont Jw. Electrical properties of Titanium, Zirconium and Hafnium films from 3000K to 1.30K. *J Vacuum Science & Technology* **6**, 184–187 (1969).

104. O'Neal, J., Wyatt, R. & Leonhard, F. The deposition of titanium on sapphire in ultrahigh vacuum. *Journal of Crystal Growth* **7**, 177–178 (1970).
105. Dehm, G., Edongué, H., Wagner, T. A., Oh, S. H. & Arzt, E. Obtaining different orientation relationships for Cu Films grown on (0001)  $\alpha$ -Al<sub>2</sub>O<sub>3</sub> substrates by magnetron sputtering. *Zeitschrift Fur Metallkunde* **96**, 249–254 (2005).
106. Huth, M. & Flynn, C. P. Titanium thin film growth on small and large misfit substrates. *Applied Physics Letters* **71**, 2466–2468 (1997).
107. Koyama, M., Arai, S., Suenaga, S & Nakahashi, M. Interfacial reactions between titanium film and single crystal  $\alpha$ -Al<sub>2</sub>O<sub>3</sub>. *Journal of Materials Science* **28**, 830–834 (1993).
108. Liu, Y.-l. *et al.* Effect of bias voltage on microstructure and nanomechanical properties of Ti films. *Transactions of Nonferrous Metals Society of China* **24**, 2870–2876 (2014).
109. Fontana, L. C. & Muzart, J. L. R. Characteristics of triode magnetron sputtering: the morphology of deposited titanium films. *Surface and Coatings Technology* **107**, 24–30 (1998).
110. Kavitha, A., Kannan, R. & Rajashabala, S. Effect of target power on the physical properties of Ti thin films prepared by DC magnetron sputtering with supported discharge. *Materials Science- Poland* **35**, 173–180 (2017).
111. Sadeghi-Khosravieh, S. & Robbie, K. Morphology and crystal texture in tilted columnar micro-structured titanium thin film coatings. *Thin Solid Films* **627**, 69–76 (2017).
112. Wen, Q., Wei, X., Jiang, F., Lu, J. & Xu, X. Focused Ion Beam Milling of Single-Crystal Sapphire with A-, C-, and M-Orientations. *Materials* **13**, 2871 (2020).
113. Wawner, F. E. & Lawless, K. R. Epitaxial Growth of Titanium Thin Films. *Journal of Vacuum Science and Technology* **6**, 588–590 (1969).
114. Graham, C. *et al.* NaCl substrates for high temperature processing and transfer of ultrathin materials. *Scientific reports* **10**, 1–7 (2020).
115. Campbell, G *et al.* The HCP To BCC Phase Transformation in Ti Characterized by Nanosecond Electron Microscopy. *Proceedings of an International Conference on Solid-Solid Phase Transformations in Inorganic Materials* **2** (2005).
116. Tal-Gutelmacher, E., Gemma, R., Pundt, A. & Kirchheim, R. Hydrogen behavior in nanocrystalline titanium thin films. *Acta Materialia* **58**, 3042–3049 (2010).

117. Badyal, J. P. S., Nix, R. M., Rayment, T. & Lambert, R. M. Chemistry and catalysis at the metal/metal oxide interface. *Faraday Discussions of the Chemical Society* **87**, 121–132 (1989).
118. Wagner, W. R., Tan, T. Y. & Balluffi, R. W. Faceting of high-angle grain boundaries in the coincidence lattice. *Philosophical Magazine A* **29**, 895–904 (1974).
119. Chen, G. S. *et al.* Evaluation of radio-frequency sputter-deposited textured TiN thin films as diffusion barriers between copper and silicon. *Journal of Vacuum Science & Technology A* **20**, 479–485 (2002).
120. Chakraborty, J., Kumar, K., Ranjan, R., Chowdhury, S. G. & Singh, S. R. Thickness-dependent fcc–hcp phase transformation in polycrystalline titanium thin films. *Acta Materialia* **59**, 2615–2623 (2011).
121. Ma, D. L. *et al.* Tailoring the texture of titanium thin films deposited by high-power pulsed magnetron sputtering. *International Journal of Modern Physics B* **33**, 1940017 (2019).
122. Checchetto, R. Titanium thin film deposition in a deuterium atmosphere. **302**, 77–83 (1997).
123. Lai, J., Chen, L. & Liu, C. Ion beam induced formation of metastable fcc-Ti phase in the epitaxial Ti/Cu/(111)Si structures. *Micron* **30**, 205–211 (1999).
124. Park, D.-S. & Kim, Y.-H. Texture enhancement of Al films on Ti underlayers by radio-frequency bias sputtering. *Journal of Electronic Materials* **31**, 1009–1015 (2002).
125. Sondergard, E., Kerjan, O., Barreteau, C. & Jupille, J. Structure and growth of titanium buffer layers on Al<sub>2</sub>O<sub>3</sub>(0001). *Surface Science* **559**. arXiv: cond-mat/0406376, 131–140 (2004).
126. Dehm, G., Scheu, C., Rühle, M. & Raj, R. Growth and structure of internal Cu/Al<sub>2</sub>O<sub>3</sub> and Cu/Ti/Al<sub>2</sub>O<sub>3</sub> interfaces. Paper presented at Sympos. Synergistic Synthesis of Inorganic Materials, March 1996, Schloß Ringberg, Germany. *Acta Materialia* **46**, 759–772 (1998).
127. Lu, H. *et al.* Study of the Ti/Al<sub>2</sub>O<sub>3</sub> interface. *Journal of Materials Science* **30**, 339–346 (1995).
128. Grünbaum, E. & Schwarz, R. Epitaxial growth of titanium films on mica. *Journal of Applied Physics* **40**, 3364–3369 (1969).
129. Gould, G. *et al.* Electrical resistivity of epitaxial titanium films. *Thin Solid Films* **13**, 61–66 (1972).

130. Naoe, M., Ono, S. & Hirata, T. Crystal orientation in titanium thin films deposited by the sputtering method without plasma damage. *Materials Science and Engineering A* **134**, 1292–1295 (1991).
131. Coxeter, H. Regular polytopes. *Reports of Mathematical Colloquium* **8**, 18 (1948).
132. Kronberg, M. & Wilson, F. Atomic Relationships in the Cubic Twinned State. *Trans. AIME* **185**, 501 (1949).
133. Dunn, C. *Annual AIME meeting, San Francisco* (San Francisco, USA, 1959).
134. Aust, K. & Rutter, u. J. Temperature dependence of grain migration in high-purity lead containing small additions of tin. *Trans TMS-AIME* **215**, 820–831 (1959).
135. Hornstra, J. Models of grain boundaries in the diamond lattice: II. Tilt about [001] and theory. *Physica* **26**, 198–208 (1960).
136. Brandon, D. G., Ralph, B., Ranganathan, S. & Wald, M. S. A field ion microscope study of atomic configuration at grain boundaries. *Acta Metallurgica* **12**, 813–821 (1964).
137. Brandon, D. The structure of high-angle grain boundaries. *Acta Metallurgica* **14**, 1479–1484 (1966).
138. Ranganathan, S. On the geometry of coincidence-site lattices. *Acta Crystallographica* **21**, 197–199 (1966).
139. Palumbo, G. & Aust, K. T. Structure-dependence of intergranular corrosion in high purity nickel. *Acta Metallurgica et Materialia* **38**, 2343–2352 (1990).
140. Lin, P., Palumbo, G., Erb, U. & Aust, K. T. Influence of grain boundary character distribution on sensitization and intergranular corrosion of alloy 600. *Scripta Metallurgica et Materialia* **33**, 1387–1392 (1995).
141. Gao, Y., Ritchie, R. O., Kumar, M. & Nalla, R. K. High-cycle fatigue of nickel-based superalloy ME3 at ambient and elevated temperatures: Role of grain-boundary engineering. *Metallurgical and Materials Transactions A* **36**, 3325–3333 (2005).
142. Was, G., Alexandreanu, B., Andresen, P. & Kumar, M. Role of Coincident Site Lattice Boundaries in Creep and Stress Corrosion Cracking. *MRS Online Proceedings Library* **819**, 21 (2004).
143. Field, D. P. & Adams, B. L. Interface cavitation damage in polycrystalline copper. *Acta Metallurgica et Materialia* **40**, 1145–1157 (1992).

144. Lehockey, E. M., Brennenstuhl, A. M. & Thompson, I. On the relationship between grain boundary connectivity, coincident site lattice boundaries, and intergranular stress corrosion cracking. *Corrosion Science* **46**, 2383–2404 (2004).
145. Aifantis, K. E. *Interfaces in crystalline materials Procedia Engineering* **1** (Elsevier Ltd, 2009), 167–170.
146. Kumar, M., Schwartz, A. J. & King, W. E. Microstructural evolution during grain boundary engineering of low to medium stacking fault energy fcc materials. *Acta Materialia* **50**, 2599–2612 (2002).
147. Schuh, C. A., Kumar, M. & King, W. E. Analysis of grain boundary networks and their evolution during grain boundary engineering. *Acta Materialia* **51**, 687–700 (2003).
148. Randle, V. The coincidence site lattice and the ‘sigma enigma’. *Materials Characterization* **47**, 411–416 (2001).
149. Sutton, A. P. & Balluffi, R. W. Overview no. 61 On geometric criteria for low interfacial energy. *Acta Metallurgica* **35**, 2177–2201 (1987).
150. Pond, R. C., Bollmann, W. & Frank, F. C. The symmetry and interfacial structure of bicrystals. *Philosophical Transactions of the Royal Society of London. Series A, Mathematical and Physical Sciences* **292**, 449–472 (1979).
151. Pond, R. C., Vlachavas, D. S. & Christian, J. W. Bicrystallography. *Proceedings of the Royal Society of London. A. Mathematical and Physical Sciences* **386**, 95–143 (1983).
152. Chen, K., Srolovitz, D. J. & Han, J. Grain-boundary topological phase transitions. *Proceedings of the National Academy of Sciences* **117**, 33077–33083 (2020).
153. Hirth, J. P., Wang, J. & Tomé, C. N. Disconnections and other defects associated with twin interfaces. *Progress in Materials Science* **83**, 417–471 (2016).
154. Pond, R. C. On the characterisation of interfacial defects using high resolution electron microscopy. *Interface Science* **2**, 299–310 (1995).
155. Pond, R. C. & Hirth, J. P. Topological model of type II deformation twinning. *Acta Materialia* **151**, 229–242 (2018).
156. Potin, V., Ruterana, P., Nouet, G., Pond, R. C. & Morkoç, H. Mosaic growth of GaN on (0001) sapphire: A high-resolution electron microscopy and crystallographic study of threading dislocations from low-angle to high-angle grain boundaries. *Physical Review B* **61**, 5587–5599 (2000).

157. Ruterana, P., Abouzaid, M., Béré, A. & Chen, J. Formation of a low energy grain boundary in ZnO: The structural unit concept in hexagonal symmetry materials. *Journal of Applied Physics* **103**, 033501 (2008).
158. Rosenhain, W. The Intercrystalline Cohesion of Metals. *Journal of the Institute of Metals* **10**, 119 (1913).
159. Mott, N. F. Slip at Grain Boundaries and Grain Growth in Metals. *Proceedings of the Physical Society* **60**, 391–394 (1948).
160. Read, W. T. & Shockley, W. Dislocation Models of Crystal Grain Boundaries. *Physical Review* **78**, 275–289 (1950).
161. Weinberg, F. Grain boundaries in metals. *Progress in Metal Physics* **8**, 105–146 (1959).
162. Bishop, G. H. & Chalmers, B. A coincidence — Ledge — Dislocation description of grain boundaries. *Scripta Metallurgica* **2**, 133–139 (1968).
163. Chalmers, B. & Gleiter, H. A re-interpretation of the ‘coincidence model’ for grain boundaries. *The Philosophical Magazine: A Journal of Theoretical Experimental and Applied Physics* **23**, 1541–1546 (1971).
164. Weins, M. J., Gleiter, H. & Chalmers, B. Computer Calculations of the Structure and Energy of High-Angle Grain Boundaries. *Journal of Applied Physics* **42**, 2639–2645 (1971).
165. Smith, D. A., Vitek, V. & Pond, R. C. Computer simulation of symmetrical high angle boundaries in aluminium. *Acta Metallurgica* **25**, 475–483 (1977).
166. Sutton, A. P., Vitek, V. & Christian, J. W. On the structure of tilt grain boundaries in cubic metals I. Symmetrical tilt boundaries. *Philosophical Transactions of the Royal Society of London. Series A, Mathematical and Physical Sciences* **309**, 1–36 (1983).
167. Sutton, A. P., Vitek, V. & Christian, J. W. On the structure of tilt grain boundaries in cubic metals II. Asymmetrical tilt boundaries. *Philosophical Transactions of the Royal Society of London. Series A, Mathematical and Physical Sciences* **309**, 37–54 (1983).
168. Wolf, D. Structure-energy correlation for grain boundaries in F.C.C. metals— III. Symmetrical tilt boundaries. *Acta Metallurgica et Materialia* **38**, 781–790 (1990).

169. Krivanek, O. L., Isoda, S. & Kobayashi, K. Lattice imaging of a grain boundary in crystalline germanium. *The Philosophical Magazine: A Journal of Theoretical Experimental and Applied Physics* **36**, 931–940 (1977).
170. Ichinose, H. & Ishida, Y. Observation of [110] tilt boundary structures in gold by high resolution HVEM. *Philosophical Magazine A: Physics of Condensed Matter, Structure, Defects and Mechanical Properties* **43**, 1253–1264 (1981).
171. Krakow, W., Wetzel, J. T., Smith, D. A. & Trafas, G. Characterization of Tilt Boundaries by Ultra High Resolution Electron Microscopy. *MRS Online Proceedings Library* **41**, 253–260 (1984).
172. Krakow, W., Wetzel, J. T. & Smith, D. A. Observation and interpretation of the atomic structure of a  $\Sigma = 19/[110]$  (331) tilt boundary in Au thin films. *Philosophical Magazine A* **53**, 739–754 (1986).
173. Krakow, W. Characterization of Grain Boundaries and Interfaces by High Resolution Transmission Electron Microscopy. *MRS Online Proceedings Library* **153**, 103–108 (1989).
174. Krakow, W. Multiplicity of atomic structure for  $\Sigma = 17/[001]$  symmetrical tilt boundaries in gold. *Acta Metallurgica et Materialia* **38**, 1031–1036 (1990).
175. Penisson, J. M., Nowicki, T. & Biscondi, M. Atomic structure of a tilt grain boundary in a molybdenum bicrystal studied by 400 kV high-resolution electron microscopy. *Philosophical Magazine A* **58**, 947–956 (1988).
176. Pénisson, J. M., Dahmen, U. & Mills, M. J. HREM study of a  $\Sigma=3\langle 112 \rangle$  twin boundary in aluminium. *Philosophical Magazine Letters* **64**, 277–283 (1991).
177. Cosandey, F., Chan, S.-W. & Stadelmann, P. Atomic structure of a  $\Sigma = 5$  (310) symmetric tilt boundary in Au. *Scripta Metallurgica* **22**, 1093–1096 (1988).
178. Ichinose, H., Ishida, Y., Baba, N. & Kanaya, K. Lattice imaging analysis of  $\Sigma 3$  coincidence-site-lattice boundaries in gold. *Philosophical Magazine A* **52**, 51–59 (1985).
179. Mills, M. J., Daw, M. S., Thomas, G. J. & Cosandey, F. High-resolution transmission electron microscopy of grain boundaries in aluminum and correlation with atomistic calculations. *Ultramicroscopy* **40**, 247–257 (1992).
180. Merkle, K. L. High-resolution electron microscopy of grain boundaries. *Interface Science* **2**, 311–345 (1995).



181. Hu, J. R, Chang, S. C, Chen, F. R & Kai, J. J. HRTEM investigation of a  $\Sigma=9$   $[01\bar{1}]/(122)$  symmetric tilt grain boundary in Cu. *Scripta Materialia* **45**, 463–469 (2001).
182. Muller, D. A. & Mills, M. J. Electron microscopy: probing the atomic structure and chemistry of grain boundaries, interfaces and defects. *Materials Science and Engineering: A* **260**, 12–28 (1999).
183. Subramanian, S., Muller, D. A., Silcox, J. & Sass, S. L. Chemistry, bonding and fracture of grain boundaries in Ni<sub>3</sub>Si. *Acta Materialia* **45**, 3565–3571 (1997).
184. Muller, D. A., Subramanian, S, Batson, P. E., Silcox, J & Sass, S. L. Structure, chemistry and bonding at grain boundaries in Ni<sub>3</sub>Al-I. The role of boron in ductilizing grain boundaries. *Acta Materialia* **44**, 1637–1645 (1996).
185. Browning, N., Arslan, I., Moeck, P. & Topuria, T. Atomic Resolution Scanning Transmission Electron Microscopy. *physica status solidi (b)* **227**, 229–245 (2001).
186. Saito, M., Wang, Z., Tsukimoto, S. & Ikuhara, Y. Local atomic structure of a near-sigma 5 tilt grain boundary in MgO. *Journal of Materials Science* **48**, 5470–5474 (2013).
187. Ma, S. *et al.* Grain boundary complexion transitions in WO<sub>3</sub>- and CuO-doped TiO<sub>2</sub> bicrystals. *Acta Materialia* **61**, 1691–1704 (2013).
188. Cantwell, P. R. *et al.* Grain boundary complexions. *Acta Materialia* **62**, 1–48 (2014).
189. Cantwell, P. R. *et al.* Grain Boundary Complexion Transitions. *Annual Review of Materials Research* **50**, 465–492 (2020).
190. Rohrer, G. S. The role of grain boundary energy in grain boundary complexion transitions. *Current Opinion in Solid State and Materials Science* **20**, 231–239 (2016).
191. Peter, N. J. *et al.* Segregation-Induced Nanofaceting Transition at an Asymmetric Tilt Grain Boundary in Copper. *Physical Review Letters* **121**, 255502 (2018).
192. Parajuli, P. *et al.* Misorientation dependence grain boundary complexions in  $\langle 111 \rangle$  symmetric tilt Al grain boundaries. *Acta Materialia* **181**, 216–227 (2019).
193. Wei, J. *et al.* Direct imaging of atomistic grain boundary migration. *Nature Materials* **20**, 951–955 (2021).

194. Solanki, K. N., Tschopp, M. A., Bhatia, M. A. & Rhodes, N. R. Atomistic Investigation of the Role of Grain Boundary Structure on Hydrogen Segregation and Embrittlement in  $\alpha$ -Fe. *Metallurgical and Materials Transactions A* **44**, 1365–1375 (2013).
195. Tschopp, M. A. & McDowell, D. L. Asymmetric tilt grain boundary structure and energy in copper and aluminium. *Philosophical Magazine* **87**, 3871–3892 (2007).
196. Yang, S., Zhou, N., Zheng, H., Ong, S. P. & Luo, J. First-Order Interfacial Transformations with a Critical Point: Breaking the Symmetry at a Symmetric Tilt Grain Boundary. *Physical Review Letters* **120**, 85702 (2018).
197. Pan, Z. & Rupert, T. J. Effect of grain boundary character on segregation-induced structural transitions. *Physical Review B* **93**, 1–15 (2016).
198. Mishin, Y., Asta, M. & Li, J. Atomistic modeling of interfaces and their impact on microstructure and properties. *Acta Materialia* **58**, 1117–1151 (2010).
199. Koju, R. K. & Mishin, Y. Atomistic study of grain-boundary segregation and grain-boundary diffusion in Al-Mg alloys. *Acta Materialia* **201**, 596–603 (2020).
200. Bacia, M., Morillo, J., Pénisson, J. M. & Pontikis, V. Atomic structure of the  $\Sigma = 5$ , (210) and (310), [001] tilt axis grain boundaries in Mo: a joint study by computer simulation and high-resolution electron microscopy. *Philosophical Magazine A* **76**, 945–963 (1997).
201. Campbell, G. H., Foiles, S. M., Gumbsch, P., Rühle, M. & King, W. E. Atomic structure of the (310) twin in niobium: Experimental determination and comparison with theoretical predictions. *Physical Review Letters* **70**, 449–452 (1993).
202. Campbell, G. H., Belak, J. & Moriarty, J. A. Atomic structure of the  $\Sigma 5$  (310)/[001] symmetric tilt grain boundary in molybdenum. *Acta Materialia* **47**, 3977–3985 (1999).
203. Bruggeman, G. A., Bishop, G. H. & Hartt, W. H. *The Nature and Behavior of Grain Boundaries: A Symposium held at the TMS-AIME Fall Meeting in Detroit, Michigan, October 18–19, 1971* (ed Hu, H.) 83–122 (Springer US, New York, NY, 1972).
204. Chen, F.-R. & King, A. H. The further geometry of grain boundaries in hexagonal close-packed metals. *Acta Crystallographica Section B: Structural Science* **43**, 416–422 (1987).
205. MacLaren, I. & Aindow, M. Reassessment of the constrained coincident-site-lattice model for reference structures in vicinal high-angle grain boundaries. *Philosophical Magazine Letters* **76**, 25–32 (1997).

206. MacLaren, I. & Aindow, M. Analysis of the reference structure adopted by a mixed tilt-twist vicinal high-angle grain boundary in titanium. *Philosophical Magazine A* **76**, 871–888 (1997).
207. Bhatia, M. A. & Solanki, K. N. Energetics of vacancy segregation to symmetric tilt grain boundaries in hexagonal close pack materials. *Journal of Applied Physics* **114**, 244309 (2013).
208. Farkas, D. & Cardozo, F. A. The multiplicity of possible grain boundary structures in Ni<sub>3</sub>Al. *Intermetallics* **6**, 257–268 (1998).
209. Fernández, J. R., Monti, A. M., Pasianott, R. C. & Vitek, V. An atomistic study of formation and migration of vacancies in (1121) twin boundaries in Ti and Zr. *Philosophical Magazine A* **80**, 1349–1364 (2000).
210. Wang, J. & Beyerlein, I. J. Atomic structures of [0110] symmetric tilt grain boundaries in Hexagonal Close-Packed (hcp) crystals. *Metallurgical and Materials Transactions A: Physical Metallurgy and Materials Science* **43**, 3556–3569 (2012).
211. Serra, A. & Bacon, D. J. Computer simulation of twin boundaries in the h.c.p. metals. *Philosophical Magazine A* **54**, 793–804 (1986).
212. Chen, F. R., King, A. H. & Chen, F. R. Large-angle grain-boundary structures in hexagonal close-packed metals. *Philosophical Magazine A: Physics of Condensed Matter, Structure, Defects and Mechanical Properties* **57**, 431–455 (1988).
213. Kenway, P. R. Calculated Structures and Energies of Grain Boundaries in  $\alpha$ -Al<sub>2</sub>O<sub>3</sub>. *Journal of the American Ceramic Society* **77**, 349–355 (1994).
214. Chen, F.-R., Chu, C.-C., Wang, J.-Y. & Chang, L. Atomic structure of  $\Sigma$ 7(0112) symmetrical tilt grain boundaries in  $\alpha$ -Al<sub>2</sub>O<sub>3</sub>. *Philosophical Magazine A* **72**, 529–544 (1995).
215. Kiselev, A. N. *et al.* High-resolution electron microscopy of ZnO grain boundaries in bicrystals obtained by the solid-phase intergrowth process. *Philosophical Magazine A* **76**, 633–655 (1997).
216. Ikuhara, Y., Watanabe, T., Saito, T., Yoshida, H. & Sakuma, T. Atomic structure and chemical bonding state of sapphire bicrystal. *Materials Science Forum* **294-296**, 273–276 (1999).
217. Nishimura, H., Matsunaga, K., Saito, T., Yamamoto, T. & Ikuhara, Y. Atomic Structures and Energies of  $\Sigma$ 7 Symmetrical Tilt Grain Boundaries in Alumina Bicrystals. *Journal of the American Ceramic Society* **86**, 574–80 (2003).

218. Matsunaga, K., Nishimura, H., Saito, T., Yamamoto, T. & Ikuhara, Y. High-resolution transmission electron microscopy and computational analyses of atomic structures of [0001] symmetric tilt grain boundaries of Al<sub>2</sub>O<sub>3</sub> with equivalent grain-boundary planes. *Philosophical Magazine* **83**, 4071–4082 (2003).
219. Oba, F. *et al.* Atomic structure of [0001]-tilt grain boundaries in ZnO: A high-resolution TEM study of fiber-textured thin films. *Physical Review B - Condensed Matter and Materials Physics* **70**, 2–11 (2004).
220. Sato, Y., Mizoguchi, T., Oba, F., Ikuhara, Y. & Yamamoto, T. Arrangement of multiple structural units in a [0001]  $\Sigma$ 49 tilt grain boundary in ZnO. *Physical Review B* **72**, 064109 (2005).
221. Sato, Y., Yamamoto, T. & Ikuhara, Y. Atomic structures and electrical properties of ZnO grain boundaries. *Journal of the American Ceramic Society* **90**, 337–357 (2007).
222. Lane, N. J. *et al.* First-principles study of dislocations in hcp metals through the investigation of the (11-21) twin boundary. *Physical Review B* **84**, 184101 (2011).
223. Wu, X. L. *et al.* Deformation twinning in a nanocrystalline hcp Mg alloy. *Scripta Materialia* **64**, 213–216 (2011).
224. Nie, J. F., Zhu, Y. M., Liu, J. Z. & Fang, X. Y. Periodic Segregation of Solute Atoms in Fully Coherent Twin Boundaries. *Science* **340**, 957–960 (2013).
225. Tu, J. *et al.* Structural characterization of  $\{101\bar{2}\}$  twin boundaries in cobalt. *Applied Physics Letters* **103**, 051903 (2013).
226. Ni, C., Ding, H., Asta, M. & Jin, X. Computational study of  $\langle 11\bar{0}0 \rangle$  symmetric tilt grain boundaries in Mg and Ti. *Scripta Materialia* **109**, 94–99 (2015).
227. Pei, Z. *et al.* Atomic structures of twin boundaries in hexagonal close-packed metallic crystals with particular focus on Mg. *npj Computational Materials* **3**, 1–7 (2017).
228. Ostapovets, A. & Sheikh-Ali, A. D. Misorientation dependence of atomic structure and energy of symmetric tilt boundaries in magnesium. *Philosophical Magazine* **98**, 3235–3246 (2018).
229. Xue, Z., Zhang, X., Qin, J., Ma, M. & Liu, R. Exploring the effects of solute segregation on the strength of Zr  $\{101\bar{1}\}$  grain boundary: A first-principles study. *Journal of Alloys and Compounds* **812**, 152153 (2020).

230. Inoue, K. *et al.* Arrangement of polyhedral units for [0001]-symmetrical tilt grain boundaries in zinc oxide. *Acta Materialia* **212**, 116864 (2021).
231. Sato, Y., Roh, J.-Y. & Ikuhara, Y. Grain-boundary structural transformation induced by geometry and chemistry. *Physical Review B* **87**, 140101 (2013).
232. Béré, A. & Serra, A. Atomic structure of dislocation cores in GaN. *Physical Review B* **65**, 205323 (2002).
233. Béré, A. & Serra, A. Structure of [0001] tilt boundaries in GaN obtained by simulation with empirical potentials. *Physical Review B* **66**, 085330 (2002).
234. Chen, J., Ruterana, P. & Nouet, G. The energy of tilt grain boundaries around  $\langle 0001 \rangle$  in GaN. *physica status solidi (a)* **203**, 247–258 (2006).
235. Cullity, B. D. *Elements of X-ray Diffraction* (Addison-Wesley Publishing, 1956).
236. Warren, B. E. *X-ray Diffraction* (Courier Corporation, 1990).
237. Mayadas, A., Shatzkes, M. & Janak, J. Electrical resistivity model for polycrystalline films: The case of specular reflection at external surfaces. *Applied Physics Letters* **14**, 345–347 (1969).
238. Sambles, J. R. The resistivity of thin metal films—Some critical remarks. *Thin Solid Films* **106**, 321–331 (1983).
239. Miccoli, I., Edler, F., Pfnür, H. & Tegenkamp, C. The 100<sup>th</sup> anniversary of the four-point probe technique: the role of probe geometries in isotropic and anisotropic systems. *Journal of physics. Condensed matter : an Institute of Physics journal* **27**, 223201 (2015).
240. Van der Pauw, L. J. A Method of Measuring Specific Resistivity and Hall Effect of Discs of Arbitrary Shape. *Philips Res. Rept.* **13**, 1–9 (1958).
241. Smits, F. M. Measurement of sheet resistivities with the four-point probe. *The Bell System Technical Journal* **37**, 711–718 (1958).
242. Reimer, L. *Scanning Electron Microscopy* 544 pp. (Springer Berlin Heidelberg, 1998).
243. Wilkinson, A. J., Meaden, G. & Dingley, D. J. High-resolution elastic strain measurement from electron backscatter diffraction patterns: new levels of sensitivity. *Ultramicroscopy* **106**, 307–313 (2006).
244. Liu, J. *et al.* Effect of Ion Irradiation Introduced by Focused Ion-Beam Milling on the Mechanical Behaviour of Sub-Micron-Sized Samples. *Scientific Reports* **10**, 10324 (2020).

245. Giannuzzi, L. A. & Stevie, F. A. A review of focused ion beam milling techniques for TEM specimen preparation. *Micron* **30**, 197–204 (1999).
246. Phaneuf, M. W. Applications of focused ion beam microscopy to materials science specimens. *Micron* **30**, 277–288 (1999).
247. Tomus, D. & Ng, H. P. In situ lift-out dedicated techniques using FIB–SEM system for TEM specimen preparation. *Micron* **44**, 115–119 (2013).
248. Williams, D. B. & Carter, C. B. *The transmission electron microscope* (Springer, 1996).
249. Pennycook, S. J. & Nellist, P. D. *Scanning transmission electron microscopy: imaging and analysis* (eds Pennycook, S. J. & Nellist, P. D.) (Springer Science & Business Media, 2011).
250. Reimer, L. *Transmission electron microscopy: physics of image formation and microanalysis* (Springer, 2013).
251. *Transmission Electron Microscopy* (eds Carter, C. B. & Williams, D. B.) 552 pp. (Springer International Publishing, 2016).
252. Van Aert, S., Chen, J. H. & Van Dyck, D. Linear versus non-linear structural information limit in high-resolution transmission electron microscopy. *Ultramicroscopy* **110**, 1404–1410 (2010).
253. Thust, A. *Transmission Electron Microscopy* (eds Carter, C. B. & Williams, D. B.) 233–266 (Springer International Publishing, Cham, 2016).
254. Zuo, J. M. & Spence, J. C. *Advanced transmission electron microscopy* (Springer, 2017).
255. Nellist, P. D. (eds Pennycook, S. J. & Nellist, P. D.) 91–115 (Springer, New York, NY, 2011).
256. Pennycook, S. J. (eds Pennycook, S. J. & Nellist, P. D.) 1–90 (Springer, New York, NY, 2011).
257. Pennycook, S. J. & Jesson, D. E. High-resolution incoherent imaging of crystals. *Physical Review Letters* **64**, 938–941 (1990).
258. Treacy, M. M. J., Howie, A & Wilson, C. J. Z contrast of platinum and palladium catalysts. *Philosophical Magazine A* **38**, 569–585 (1978).
259. Pennycook, S. J. & Boatner, L. A. Chemically sensitive structure-imaging with a scanning transmission electron microscope. *Nature* **336**, 565–567 (1988).
260. Hartel, P., Rose, H. & Dinges, C. Conditions and reasons for incoherent imaging in STEM. *Ultramicroscopy* **63**, 93–114 (1996).

261. Engel, A., Wiggins, J. & Woodruff, D. A comparison of calculated images generated by six modes of transmission electron microscopy. *Journal of Applied Physics* **45**, 2739–2747 (1974).
262. Kalinin, S. V. *et al.* Machine learning in scanning transmission electron microscopy. *Nature Reviews Methods Primers* **2**, 1–28 (2022).
263. Van Dyck, D. Is the frozen phonon model adequate to describe inelastic phonon scattering? *Ultramicroscopy* **109**, 677–682 (2009).
264. Hage, F., Kepaptsoglou, D., Ramasse, Q. & Allen, L. Phonon Spectroscopy at Atomic Resolution. *Physical Review Letters* **122**, 016103 (2019).
265. Nguyen, D. T., Findlay, S. D. & Etheridge, J. The spatial coherence function in scanning transmission electron microscopy and spectroscopy. *Ultramicroscopy* **146**, 6–16 (2014).
266. Egerton, R. F. (ed Egerton, R. F.) 27–55 (Springer US, Boston, MA, 2005).
267. Rose, H. *Advances in Imaging and Electron Physics* (ed Hawkes, P. W.) 3–39 (Elsevier, 2008).
268. Krivanek, O. L. *et al.* *Advances in Imaging and Electron Physics* (ed Hawkes, P. W.) 121–160 (Elsevier, 2008).
269. Hetherington, C. Aberration correction for TEM. *Materials Today* **7**, 50–55 (2004).
270. Zhou, W. *et al.* Single Atom Microscopy. *Microscopy and Microanalysis* **18**, 1342–1354 (2012).
271. Egerton, R. F. & Watanabe, M. Characterization of single-atom catalysts by EELS and EDX spectroscopy. *Ultramicroscopy* **193**, 111–117 (2018).
272. Russ, J. C. *Fundamentals of Energy Dispersive X-ray Analysis* (Elsevier, 1984).
273. Newbury, D. E. & Ritchie, N. W. M. Elemental mapping of microstructures by scanning electron microscopy-energy dispersive X-ray spectrometry (SEM-EDS): extraordinary advances with the silicon drift detector (SDD). *Journal of Analytical Atomic Spectrometry* **28**, 973–988 (2013).
274. Zaluzec, N. J. Quantitative Assessment and Measurement of X-ray Detector Performance and Solid Angle in the Analytical Electron Microscope. *Microscopy and Microanalysis* **28**, 83–95 (2022).
275. Notthoff, C., Winterer, M., Beckel, A., Geller, M. & Heindl, J. Spatial high resolution energy dispersive X-ray spectroscopy on thin lamellas. *Ultramicroscopy* **129**, 30–35 (2013).

276. Muller, D. A. *et al.* Atomic-Scale Chemical Imaging of Composition and Bonding by Aberration-Corrected Microscopy. *Science* **319**, 1073–1076 (2008).
277. Watanabe, M. *et al.* Improvements in the X-Ray Analytical Capabilities of a Scanning Transmission Electron Microscope by Spherical-Aberration Correction. *Microscopy and Microanalysis* **12**, 515–526 (2006).
278. Potapov, P. & Lubk, A. Optimal principal component analysis of STEM XEDS spectrum images. *Advanced Structural and Chemical Imaging* **5**, 4 (2019).
279. Fink, J. M. *et al.* Quantum electromechanics on silicon nitride nanomembranes. *Nature communications* **7**, 1–10 (2016).
280. Konstantinidis, S., Dauchot, J. P., Ganciu, M., Ricard, A. & Hecq, M. Influence of pulse duration on the plasma characteristics in high-power pulsed magnetron discharges. *Journal of Applied Physics* **99** (2006).
281. Schneider, J. M., Rohde, S., Sproul, W. D. & Matthews, A. Recent developments in plasma assisted physical vapour deposition. *Journal of Physics D: Applied Physics* **33**, R173–R186 (2000).
282. Greczynski, G., Mráz, S., Hultman, L. & Schneider, J. M. Venting temperature determines surface chemistry of magnetron sputtered TiN films. *Applied Physics Letters* **108**, 041603 (2016).
283. Khorashadizadeh, A. *et al.* Five-Parameter Grain Boundary Analysis by 3D EBSD of an Ultra Fine Grained CuZr Alloy Processed by Equal Channel Angular Pressing. *Advanced Engineering Materials* **13**, 237–244 (2011).
284. Saylor, D. M., El Dasher, B. S., Rollett, A. D. & Rohrer, G. S. Distribution of grain boundaries in aluminum as a function of five macroscopic parameters. *Acta Materialia* **52**, 3649–3655 (2004).
285. Krakauer, B. W. & Seidman, D. N. Absolute atomic-scale measurements of the Gibbsian interfacial excess of solute at internal interfaces. *Physical Review B* **48**, 6724–6727 (9 1993).
286. Schneider, C. A., Rasband, W. S. & Eliceiri, K. W. NIH Image to ImageJ: 25 years of image analysis. *Nature Methods* **9**, 671–675 (2012).
287. Hunter, J. D. Matplotlib: A 2D graphics environment. *Computing in Science & Engineering* **9**, 90–95 (2007).
288. De la Peña, F *et al.* *HyperSpy v1. 5.2 (Version v1. 5.2)*. Zenodo 2019.
289. Scherrer, P. *Kolloidchemie Ein Lehrbuch* 387–409 (Springer Berlin Heidelberg, Berlin, Heidelberg, 1912).



290. Tal-Gutelmacher, E., Pundt, A. & Kirchheim, R. The effect of residual hydrogen on hydrogenation behavior of titanium thin films. *Scripta Materialia* **62**, 709–712 (2010).
291. Enck, F. D. & Dommel, J. G. Behavior of the Thermal Expansion of NaCl at Elevated Temperatures. *Journal of Applied Physics* **36**, 839–844 (1965).
292. Narayan, J. & Larson, B. C. Domain epitaxy: A unified paradigm for thin film growth. *Journal of Applied Physics* **93**, 278–285 (2003).
293. Wurst, J. C. & Nelson, J. A. Lineal Intercept Technique for Measuring Grain Size in Two-Phase Polycrystalline Ceramics. *Journal of the American Ceramic Society* **55**, 109 (1972).
294. Vopsaroiu, M *et al.* Deposition of polycrystalline thin films with controlled grain size. *Journal of Physics D: Applied Physics* **38**, 490–496 (2005).
295. Bae, J. *et al.* Grain Size and Phase Transformation Behavior of TiNi Shape-Memory-Alloy Thin Film under Different Deposition Conditions. *Materials* **13** (2020).
296. Estel, J, Hoinkes, H, Kaarmann, H, Nahr, H & Wilsch, H. On the problem of water adsorption on alkali halide cleavage planes, investigated by secondary ion mass spectroscopy. *Surface Science* **54**, 393–418 (1976).
297. Cabrera-Sanfeliu, P., Arnau, A., Darling, G. R. & Sanchez-Portal, D. Water Adsorption and Diffusion on NaCl(100). *The Journal of Physical Chemistry B* **110**, 24559–24564 (2006).
298. Thompson, C. V. & Carel, R. Texture development in polycrystalline thin films. *Materials Science and Engineering B* **32**, 211–219 (1995).
299. Moskalenko, V. A., Smirnov, A. R. & Moskalenko, A. V. Cryomechanically obtained nanocrystalline titanium: microstructure and mechanical properties. *Low Temperature Physics* **35**, 905–907 (2009).
300. Chen, Y. *et al.* Plasma assisted molecular beam epitaxy of ZnO on c-plane sapphire: Growth and characterization. *Journal of Applied Physics* **84**, 3912–3918 (1998).
301. Wang, Y. *et al.* Effects of sapphire substrate annealing on ZnO epitaxial films grown by MOCVD. *Applied Surface Science* **253**, 1745–1747 (2006).
302. Brockman, J, Samant, M. G., Roche, K. P. & Parkin, S. S. P. Substrate-induced disorder in V<sub>2</sub>O<sub>3</sub> thin films grown on annealed c-plane sapphire substrates. *Applied Physics Letters* **101**, 51606 (2012).

303. Hayashi, T. *et al.* In-plane ordering of a dibenzo[b,t]phthalocyaninato-Zn(II) thin film due to the atomic step arrays on a sapphire (1-012) surface. *Journal of Crystal Growth* **156**, 245–251 (1995).
304. Grabow, M. H. & Gilmer, G. H. Thin film growth modes, wetting and cluster nucleation. *Surface science* **194**, 333–346 (1988).
305. Kakehi, Y. *et al.* Epitaxial growth of CuScO<sub>2</sub> thin films on sapphire a-plane substrates by pulsed laser deposition. *Journal of Applied Physics* **97**, 83535 (2005).
306. Gall, D. The search for the most conductive metal for narrow interconnect lines. *Journal of Applied Physics* **127**, 050901 (2020).
307. Day, M. E., Delfino, M., Fair, J. A. & Tsai, W. Correlation of electrical resistivity and grain size in sputtered titanium films. *Thin Solid Films* **254**, 285–290 (1995).
308. Caballero, J., Kremer, G. & Moraga, L. Electrical resistivity of very thin single-crystal titanium films as a function of temperature. *Thin Solid Films* **117**, 1–8 (1984).
309. Bel'skaya, E. A. & Kulyamina, E. Y. Electrical resistivity of titanium in the temperature range from 290 to 1800 K. *High Temperature* **45**, 785–796 (2007).
310. Schwarz, S., Houge, E., Giannuzzi, L. & King, A. Bicrystal growth and characterization of copper twist grain boundaries. *Journal of Crystal Growth* **222**, 392–398 (2001).
311. Westmacott, K. H., Hinderberger, S. & Dahmen, U. Physical vapour deposition growth and transmission electron microscopy characterization of epitaxial thin metal films on single-crystal Si and Ge substrates. *Philosophical Magazine A* **81**, 1547–1578 (2001).
312. Radetic, T., Ophus, C., Olmsted, D. L., Asta, M. & Dahmen, U. Mechanism and dynamics of shrinking island grains in mazed bicrystal thin films of Au. *Acta Materialia* **60**, 7051–7063 (2012).
313. Kluge-Weiss, P. M. & Bauer, C. L. Characterization of [001] tilt boundaries in bicrystalline thin films of copper. *physica status solidi (a)* **58**, 333–341 (1980).
314. Cosandey, F. & Bauer, C. L. Faceting of [001] grain boundaries in bicrystalline thin films of gold. *Acta Metallurgica* **28**, 601–605 (1980).
315. Yamada, I., Usui, H., Tanaka, S., Dahmen, U. & Westmacott, K. H. Atomic resolution study of the structure and interface of aluminum films deposited epitaxially on silicon by ionized cluster beam method. *Journal of Vacuum Science & Technology A* **8**, 1443–1446 (1990).

316. Sarakinos, K, Alami, J & Wuttig, M. Process characteristics and film properties upon growth of  $\text{TiO}_x$  films by high power pulsed magnetron sputtering. *Journal of Physics D: Applied Physics* **40**, 2108–2114 (2007).
317. Jing, F. J. *et al.* Titanium film deposition by high-power impulse magnetron sputtering: Influence of pulse duration. *Vacuum* **86**, 2114–2119 (2012).
318. Hilliard, J. E. Estimating grain size by the intercept method. *Metal Progress* **85**, 99–102 (1964).
319. Palmer, J. E., Thompson, C. V. & Smith, H. I. Grain growth and grain size distributions in thin germanium films. *Journal of Applied Physics* **62**, 2492–2497 (1987).
320. Dahmen, U. & Westmacott, K. H. Tem Characterization of Grain Boundaries in Mazed Bicrystal Films of Aluminum. *MRS Proceedings* **229**, 167 (1991).
321. Miller, M. & Hetherington, M. Local magnification effects in the atom probe. *Surface Science* **246**, 442–449 (1991).
322. Stoffers, A. *et al.* Grain boundary segregation in multicrystalline silicon: correlative characterization by EBSD, EBIC, and atom probe tomography. *Progress in Photovoltaics: Research and Applications* **23**, 1742–1753 (2015).
323. Sarakinos, K., Alami, J. & Konstantinidis, S. High power pulsed magnetron sputtering: A review on scientific and engineering state of the art. *Surface and Coatings Technology* **204**, 1661–1684 (2010).
324. Sittinger, V *et al.* High power pulsed magnetron sputtering of transparent conducting oxides. *Thin Solid Films* **516**, 5847–5859 (2008).
325. Petrov, I, Adibi, F, Greene, J. E., Hultman, L & Sundgren, J. Average energy deposited per atom: A universal parameter for describing ion-assisted film growth? *Applied Physics Letters* **63**, 36–38 (1993).
326. Hultman, L, Sundgren, J., Greene, J. E., Bergstrom, D. B. & Petrov, I. High-flux low-energy (20 eV)  $\text{N}^+2$  ion irradiation during TiN deposition by reactive magnetron sputtering: Effects on microstructure and preferred orientation. *Journal of Applied Physics* **78**, 5395–5403 (1995).
327. Rao, S. *et al.* Integration of epitaxial permalloy on Si (100) through domain matching epitaxy paradigm. *Current Opinion in Solid State and Materials Science* **18**, 1–5 (2014).

328. Thornton, J. A. Influence of apparatus geometry and deposition conditions on the structure and topography of thick sputtered coatings. *Journal of Vacuum Science and Technology* **11**, 666–670 (1974).
329. Barna, P. & Adamik, M. Fundamental structure forming phenomena of polycrystalline films and the structure zone models. *Thin solid films* **317**, 27–33 (1998).
330. Bishop, G. H., Hartt, W. H. & Bruggeman, G. A. Grain boundary faceting of 101-0 tilt boundaries in zinc. *Acta Metallurgica* **19**, 37–47 (1971).
331. Goodhew, P., Tan, T. & Balluffi, R. Low energy planes for tilt grain boundaries in gold. *Acta Metallurgica* **26**, 557–567 (1978).
332. Muschik, T., Laub, W., Wolf, U., Finnis, M. W. & Gust, W. Energetic and kinetic aspects of the faceting transformation of a  $\Sigma 3$  grain boundary in Cu. *Acta Metallurgica Et Materialia* **41**, 2163–2171 (1993).
333. Krzysztof Glowinski, A. M. Twist, tilt, and symmetric grain boundaries in hexagonal materials. *Journal of Material Science* **49**, 3936–3942 (2014).
334. Kelly, M. N., Glowinski, K., Nuhfer, N. T. & Rohrer, G. S. The five parameter grain boundary character distribution of  $\alpha$ -Ti determined from three-dimensional orientation data. *Acta Materialia* **111**, 22–30 (2016).
335. Farabi, E., Hodgson, P. D., Rohrer, G. S. & Beladi, H. Five-parameter intervariant boundary characterization of martensite in commercially pure titanium. *Acta Materialia* **154**, 147–160 (2018).
336. Ostapovets, A., Molnár, P. & Lejček, P. Boundary plane distribution for  $\Sigma 13$  grain boundaries in magnesium. *Materials Letters* **137**, 102–105 (2014).
337. Rohrer, G. S., El-Dasher, B. S., Miller, H. M., Rollett, A. D. & Saylor, D. M. Distribution of Grain Boundary Planes at Coincident Site Lattice Misorientations. *MRS Proceedings* **819**, N7.2 (2004).
338. Kim, C.-S., Hu, Y., Rohrer, G. S. & Randle, V. Five-parameter grain boundary distribution in grain boundary engineered brass. *Scripta Materialia* **52**, 633–637 (2005).
339. Randle, V., Hu, Y., Rohrer, G. S. & Kim, C.-S. Distribution of misorientations and grain boundary planes in grain boundary engineered brass. *Materials Science and Technology* **21**, 1287–1292 (2005).

340. Randle, V. Relationship between coincidence site lattice, boundary plane indices, and boundary energy in nickel. *Materials Science and Technology* **15**, 246–252 (1999).
341. Frolov, T., Olmsted, D. L., Asta, M. & Mishin, Y. Structural phase transformations in metallic grain boundaries. *Nature Communications* **4**, 1899 (2013).
342. Lejček, P., Kopeček, J. & Jarošová, M. Growth of oriented tricrystals of an Fe–Si alloy. *Journal of Crystal Growth. The 16<sup>th</sup> American Conference on Crystal Growth and Epitaxy* **287**, 262–266 (2006).
343. Hofmann, S. & Lejček, P. Solute segregation at grain boundaries. *Interface Science* **3**, 241–267 (1996).
344. Kirchheim, R. Reducing grain boundary, dislocation line and vacancy formation energies by solute segregation. I. Theoretical background. *Acta Materialia* **55**, 5129–5138 (2007).
345. Donald, A. & Brown, L. Grain boundary faceting in Cu–Bi alloys. *Acta Metallurgica* **27**, 59–66 (1979).
346. Peter, N. J., Duarte, M. J., Kirchlechner, C., Liebscher, C. H. & Dehm, G. Faceting diagram for Ag segregation induced nanofaceting at an asymmetric Cu tilt grain boundary. *Acta Materialia* **214**, 116960 (2021).
347. McLean, D. & Maradudin, A. Grain boundaries in metals. *Physics Today* **11**, 35 (1958).
348. Langmuir, I. The adsorption of gases on plane surfaces of glass, mica and platinum. *Journal of the American Chemical Society* **40**, 1361–1403 (1918).
349. Lejček, P., Hofmann, S. & Paidar, V. Solute segregation and classification of [100] tilt grain boundaries in  $\alpha$ -iron: consequences for grain boundary engineering. *Acta Materialia* **51**, 3951–3963 (2003).
350. Seah, M. P., Hondros, E. D. & Kelly, A. Grain boundary segregation. *Proceedings of the Royal Society of London. A. Mathematical and Physical Sciences* **335**, 191–212 (1973).
351. Wynblatt, P. & Ku, R. Surface energy and solute strain energy effects in surface segregation. *Surface Science* **65**, 511–531 (1977).
352. Seah, M. P. & Lea, C. Surface segregation and its relation to grain boundary segregation. *The Philosophical Magazine: A Journal of Theoretical Experimental and Applied Physics* **31**, 627–645 (1975).

353. Bozzolo, G., Ferrante, J. & Smith, J. R. Method for calculating alloy energetics. *Phys. Rev. B* **45**, 493–496 (1 1992).
354. Kwiatkowski da Silva, A. *et al.* Thermodynamics of grain boundary segregation, interfacial spinodal and their relevance for nucleation during solid-solid phase transitions. *Acta Materialia* **168**, 109–120 (2019).
355. Darvishi Kamachali, R. A model for grain boundary thermodynamics. *RSC Adv.* **10**, 26728–26741 (45 2020).
356. Ding, L. *et al.* Effect of Fe Content on the As-Cast Microstructures of Ti–6Al–4V–xFe Alloys. *Metals* **10**, 989 (2020).
357. Outlaw, R. A., Lee, W. S., Hoekje, S. J. & Sankaran, S. N. Sulfur segregation in titanium and selected titanium alloys. *Applied Surface Science* **81**, 143–150 (1994).
358. Suzuki, S., Abiko, K. & Kimura, H. Related to the grain boundary structure in an Fe-P alloy. *Scripta Metallurgica* **15**, 1139–1143 (1981).
359. Fukushima, H & Birnbaum, H. K. High resolution saes and sims studies of grain boundary segregation of S and Cl in Ni. *Scripta Metallurgica* **16**, 753–757 (1982).
360. Walther, T., Daneu, N. & Recnik, A. A new method to measure small amounts of solute atoms on planar defects and application to inversion domain boundaries in doped zinc oxide. *Interface Science* **12**, 267–275 (2004).
361. Doig, P & Flewitt, P. The detection of monolayer grain boundary segregations in steels using STEM-EDS X-ray microanalysis. *Metallurgical Transactions A* **13**, 1397–1403 (1982).
362. Keast, V. J. & Williams, D. B. Quantitative compositional mapping of Bi segregation to grain boundaries in Cu. *Acta Materialia* **47**, 3999–4008 (1999).
363. Liebscher, C. H., Stoffers, A., Alam, M., Lymperakis, L. & Cojocaru-mir, O. Strain-Induced Asymmetric Line Segregation at Faceted Si Grain Boundaries. *Phys. Rev. Lett.* **015702**, 1–5 (1 2018).
364. Raabe, D. *et al.* Grain boundary segregation engineering in metallic alloys: A pathway to the design of interfaces. *Current Opinion in Solid State and Materials Science* **18**, 253–261 (2014).
365. Babinsky, K. *et al.* Atom probe study of grain boundary segregation in technically pure molybdenum. *Materials Characterization* **87**, 95–103 (2014).

366. Herbig, M. Spatially correlated electron microscopy and atom probe tomography: Current possibilities and future perspectives. *Scripta Materialia* **148**, 98–105 (2018).
367. Murray, J. L. & Wriedt, H. A. The O-Ti (Oxygen-Titanium) system. *Journal of Phase Equilibria* **8**, 148–165 (1987).
368. Gunda, N. S. H., Puchala, B. & Van der Ven, A. Resolving phase stability in the Ti-O binary with first-principles statistical mechanics methods. *Phys. Rev. Materials* **2**, 033604 (3 2018).
369. Maugis, P. & Hoummada, K. A methodology for the measurement of the interfacial excess of solute at a grain boundary. *Scripta Materialia* **120**, 90–93 (2016).
370. Sumiyama, K., Ezawa, H. & Nakamura, Y. Metastable Fe<sub>1-x</sub>Ti<sub>x</sub> Alloys Produced by Vapor Quenching. *physica status solidi (a)* **93**, 81–86 (1986).
371. Nicholls, D. *et al.* Minimising damage in high resolution scanning transmission electron microscope images of nanoscale structures and processes. *Nanoscale* **12**, 21248–21254 (2020).
372. Han, J., Vitek, V. & Srolovitz, D. J. The grain-boundary structural unit model redux. *Acta Materialia* **133**, 186–199 (2017).
373. Sarrazit, F., Pond, F. R. C. & Kiselev, N. A. Structure transition in a ZnO grain boundary. *Philosophical Magazine Letters* **77**, 191–198 (1998).
374. Frank, F. C. On Miller–Bravais indices and four-dimensional vectors. *Acta Crystallographica* **18**, 862–866 (1965).
375. Pond, R. C., Clark, W. A. T. & Wagoner, R. H. On the crystallography of slip transmission in hexagonal metals. *Scripta Metallurgica* **20**, 1291–1295 (1986).
376. Pond, R. C., McAuley, N. A., Serra, A. & Clark, W. A. T. Transformation matrices for hexagonal and trigonal crystals. *Scripta Metallurgica* **21**, 197–202 (1987).
377. Devulapalli, V. *et al.* Microstructure, grain boundary evolution and anisotropic Fe segregation in (0001) textured Ti thin films. *Acta Materialia* **238**, 118180 (2022).
378. Frolov, T., Asta, M. & Mishin, Y. Segregation-induced phase transformations in grain boundaries. *Physical Review B - Condensed Matter and Materials Physics* **92** (2015).

379. Hondros, E. D. & Seah, M. P. Segregation to interfaces. *International Metals Reviews* **22**, 262–301 (1977).
380. Ma, S. *et al.* A grain boundary phase transition in Si–Au. *Scripta Materialia* **66**, 203–206 (2012).
381. Wang, G. J., Sutton, A. P. & Vitek, V. A computer simulation study of  $\langle 001 \rangle$  and  $\langle 111 \rangle$  tilt boundaries: the multiplicity of structures. *Acta Metallurgica* **32**, 1093–1104 (1984).
382. Aramfard, M. & Deng, C. Mechanically enhanced grain boundary structural phase transformation in Cu. *Acta Materialia* **146**, 304–313 (2018).
383. Cahn, J. W., Mishin, Y. & Suzuki, A. Coupling grain boundary motion to shear deformation. *Acta Materialia* **54**, 4953–4975 (2006).
384. Sutton, A. P. & Vitek, V. On the coincident site lattice and DSC dislocation network model of high angle grain boundary structure. *Scripta Metallurgica* **14**, 129–132 (1980).
385. Chen, J., Ruterana, P. & Nouet, G. Structural units and low-energy configurations of [0001] tilt grain boundaries in GaN. *Physical Review B* **67**, 205210 (2003).
386. Carlsson, J. M., Domingos, H. S., Bristowe, P. D. & Helling, B. An Interfacial Complex in ZnO and Its Influence on Charge Transport. *Physical Review Letters* **91**, 165506 (2003).
387. G.P. Dimitrakopoulos Ph. Komninou, R. P. Topological Analysis of Defects in Epitaxial Nitride Films and Interfaces. *physica status solidi (b)* **227**, 45–92 (2001).
388. Li, S., Chen, J. & Ruterana, P. The [10-10] edge dislocation in the wurtzite structure: A high-resolution transmission electron microscopy investigation of [0001] tilt grain boundaries in GaN and ZnO. *Acta Materialia* **175**, 457–465 (2019).
389. Hart, E. W. Two-dimensional phase transformation in grain boundaries. *Scripta Metallurgica* **2**, 179–182 (1968).
390. Sickafus, K. E. & Sass, S. L. Grain boundary structural transformations induced by solute segregation. *Acta Metallurgica* **35**, 69–79 (1987).
391. Straumal, B. B., Kogtenkova, O. A., Gornakova, A. S., Sursaeva, V. G. & Baretzky, B. Review: grain boundary faceting-roughening phenomena. *Journal of Materials Science* **51**, 382–404 (2015).



392. Lynch, S. P., Muddle, B. C. & Pasang, T. Mechanisms of brittle intergranular fracture in Al-Li alloys and comparison with other alloys. *Philosophical Magazine A* **82**, 3361–3373 (2002).
393. Menyhard, M., Rothman, B. & McMahon, C. J. Observations of segregation and grain-boundary faceting by tellurium and oxygen in iron. *Scripta Metallurgica et Materialia* **29**, 1005–1009 (1993).
394. Sigle, W., Ciiang, L.-S. & Gusr, W. On the correlation between grain-boundary segregation, faceting and embrittlement in Bi-doped Cu. *Philosophical Magazine A* **82**, 1595–1608 (2002).
395. Cahn, J. I. & Hoffman, D. I. A vector thermodynamics for anisotropic surfaces-II. Curved and faceted surfaces. *Acta Metallurgica* **22**, 1205–1214 (1974).
396. Udler, D. & Seidman, D. N. Congruent Phase Transition at a Twist Boundary Induced by Solute Segregation. *Phys. Rev. Lett.* **77**, 3379–3382 (1996).
397. Huber, L., Rottler, J. & Militzer, M. Atomistic simulations of the interaction of alloying elements with grain boundaries in Mg. *Acta Materialia* **80**, 194–204 (2014).



# Curriculum Vitae

## Personal Information

---

Name Vivek Devulapalli  
 Date of Birth 07.02.1995  
 Place of Birth Bhilai, India

## Education

---

2018–2022 **Doctoral Studies**  
 Dissertation *Microstructure and grain boundary evolution in titanium thin films*  
 Ruhr Universität Bochum – Fakultät für Maschinenbau  
 Advised by: Dr. Christian H. Liebscher  
 First thesis supervisor: Prof. Gerhard Dehm  
 Second thesis supervisor: Prof. Jochen M. Schneider

2016–2018 **Master Studies**  
 Thesis *Study of grain boundary segregation on heat treatment in Mg- 1 wt.% Gd alloy*  
 Indian Institute of Technology – Madras, India – Department of Metallurgical and Materials Engineering  
 Advised by: Prof. K. G. Pradeep & Prof. B S Murty  
 GPA: 8.4 / 10

2012–2016 **Bachelor Studies**  
 Thesis *Development of cost effective fly-ash/ alumina aluminium composite*  
 National Institute of Technology – Raipur, India – Department of Metallurgical Engineering  
 Advised by: Dr. Neha Gupta  
 GPA: 9.2 / 10.0